Integrated Self-Interference Cancellation for Full-Duplex and Frequency-Division Duplexing Wireless Communication Systems

Jin Zhou

Submitted in partial fulfillment of the
requirements for the degree
of Doctor of Philosophy
in the Graduate School of Arts and Sciences

COLUMBIA UNIVERSITY

2017

ABSTRACT

Integrated Self-Interference Cancellation for Full-Duplex and Frequency-Division Duplexing Wireless Communication Systems

Jin Zhou

From wirelessly connected robots to car-to-car communications, and to smart cities, almost every aspect of our lives will benefit from future wireless communications. While promise an exciting future world, next-generation wireless communications impose requirements on the data rate, spectral efficiency, and latency (among others) that are higher than those for today's systems by several orders of magnitude.

Full-duplex wireless, an emergent wireless communications paradigm, breaks the long-held assumption that it is impossible for a wireless device to transmit and receive simultaneously at the same frequency, and has the potential to immediately double network capacity at the physical (PHY) layer and offers many other benefits (such as reduced latency) at the higher layers. Recently, discrete-component-based demonstrations have established the feasibility of full-duplex wireless. However, the realization of *integrated full duplex radios*, compact radios that can fit into smartphones, is fraught with fundamental challenges. In addition, to unleash the full potential of full-duplex communication, a careful redesign of the PHY layer and the medium access control (MAC) layer using a *cross-layer approach* is required.

The biggest challenge associated with full duplex wireless is the tremendous amount of transmitter self-interference right on top of the desired signal. In this dissertation, new self-interference-cancellation approaches at both system and circuit levels are presented, contributing towards the realization of full-duplex radios using integrated circuit technology. Specifically, these new approaches involve elimination of the noise and distortion of the cancellation circuitry, enhancing the integrated cancellation bandwidth, and performing joint radio frequency, analog, and digital cancellation to achieve cancellation with nearly one part-per-billion accuracy.

In collaboration with researchers at higher layers of the stack, a cross-layer approach has been used in our full-duplex research and has allowed us to derive power allocation algorithms and to characterize rate-gain improvements for full-duplex wireless networks. To enable experimental characterization of full-duplex MAC layer algorithms, a cross-layered software-defined full-duplex radio testbed has been developed. In collaboration with researchers from the field of micro-electro-mechanical systems, we demonstrate a multi-band frequency-division duplexing system using a cavity-filter-based tunable duplexer and our integrated widely-tunable self-interference-cancelling receiver.

Table of Contents

List of Figures

List of Tables

Acknowledgments

What people can accomplish depends on those around them. My doctoral study and my time at Columbia would not have been fulfilling and memorable for me without the people with whom that I have been fortunate to interact. I wish to express my gratitude to them here.

It is hard to find a person like my doctoral advisor, Professor Harish Krishnaswamy, who has had such a profound influence on my career that will last a lifetime. I would like to thank Harish for his guidance over the years. His ambition, wisdom, vision, and enthusiasm have shown me how to become a successful researcher. He exposed me to many collaborative research opportunities which have widened my research horizons. As one of Harish's Ph.D. students and a student in his class, I am constantly amazed by his breadth and depth of knowledge, clarity, and patient; I hope that I have learned some of these from him. Writing and presentation in English sometimes can be challenging for an international non-native speaker, and I am deeply indebted to Harish for his effort on improving my English skills. Harish has been a considerate advisor. I appreciate that he tried to shield me from pressure and work when my family needed me. Finally, I am thankful to Harish for his support in my future career. After years working with Harish, I can't feel more proud that I was one of his students.

I would like to thank Professors Peter Kinget, Gil Zussman, Yannis Tsividis, and Dr. Paul Draxler for being on my dissertation committees. I appreciate their time and effort in reading my dissertation and providing valuable comments. In addition, I want to thank Gil for his guidance on our full-duplex project. Working with Gil (and his group) taught me how to work with researchers outside my field to collectively tackle a large problem. I also learned quite some proposal writing skills from Gil. I would like to thank Prof. Kinget for his valuable comments and feedbacks on the RF-FPGA project. As an internationally renowned scholar in my field, Peter's professionalism and his attitude towards research have inspired me to continuously improve myself. In addition, I would like to thank Professors Peter Kinget and Gil Zussman for their support in my future career.

I was fortunate to have the opportunities to interact with several experts in industry. I am thankful to Dr. Paul Draxler and Dr. Hua Wang from Qualcomm for their feedbacks on the full-duplex project during our regular Qualcomm Innovation Fellowship meetings. I got to know Dr. Osama Shanaa during my time with MediaTek before I joined Columbia, the encouragement and support from Osama over the years are greatly appreciated.

I am extremely proud to be a member of the Columbia high-Speed and Mm-wave IC (CoSMIC) Lab – a group where all members have excelled in their ways; I have learned a great deal from everyone of them over the years. I would like to thank Jahnavi Sharma especially for her assistance when I first came to Columbia. Every time I look at the layout of my first tapeout at Columbia, it always reminds me about my collaboration with Dr. Anandaroop Chakrabarti. Anandaroop set a great example to me during my formative year at Columbia. I continued to have wonderful collaboration experience with Jeffrey Chuang and Tolga Dinc on the project of frequency-domain-equalization-based RF self-interference cancellation. Both Jeffrey and Tolga put great effort into this project to ensure its success. I sincerely appreciate their time and effort. I cherish my collaboration with Negar Reiskarimian and am very proud of her work. It was my great pleasure to work with Ritesh Bhat on his digital power amplifier project, and I was genuinely excited about his great results! Linxiao Zhang and I shared quite some discussions on many interesting things from circuits to politics/culture/history. I admired Linxiao's sharp mind on many of these topics. Jose Bahamonde helped me a lot with Keysight's ADS. Jose also took a keen interest in my future career and gave me a lot of encouragement. In addition to work, I cherish very much about our friendship among the lab members. I thank all CoSMIC members for organizing many memorable group events. Finally, it is very nice to know Mahmood, Gurkaranjot, Aditya, Sohail, and Aravind, and thank you for your comments on my dissertation talk.

My doctoral research is a part of an interdisciplinary project (called the Columbia FlexICoN project) that tackles the cross-layer design of full-duplex wireless systems and networks. I learned a great deal about wireless systems and networks from this project. I want to thank Dr. Jelena Marašević and Tingjun Chen from Prof. Gil Zussman's lab for making our collaboration a memorable and productive one. I was fortunate to have the opportunity to work with Dr. Mohammad Abu Khater and Yu-Chen Wu from Professor Dimitrios Peroulis's group at Purdue University. I thank them for teaching me many things about microwave filters and I appreciate their effort on

our tunable frequency-division-duplexing system project.

My gratitude also goes to many others at Columbia for their friendship and help over the years, especially Jianxun Zhu, Yang Xu, Yu Chen, Ning Guo, Josh Kim, and Teng Yang. Finally, I want to thank all the graduate students and undergraduates that I have worked with for their effort on our various research projects, especially Yuhe Cao, Amit Singh, Rel Fogel, Nicole Grimwood, Preetish Tilak, Sean Holloway, Damla Dimlioglu, Sukanya Meher, and Sally Yu.

Some of my measurements required multiple expensive instruments and cannot be accomplished without the generous support of many labs at Columbia. Regarding this, I would like to thank Professors Ken Sherpad, Keren Bergman, and Peter Kinget.

There are times when I have to make last-minute purchase orders through our department. Arturo Lopez and Yoel Rio from our department office bore with me about this for years; I am indebted to their patient and assistance. I also owe a great deal of gratitude to the remaining people from our department office, especially Laura Castillo and Kington Chan.

Before Columbia, there was Fudan. I would like to acknowledge Professor Wei Li of Fudan University for introducing me to this field and her continuous support and encouragement throughout the years.

Finally, it is time to acknowledge the most important people in my life. Words, *in any language*, cannot express how much love my parents have given to me. No one knows better than me that what it had taken for my Mom to raise me up. No matter what had happened, my Mom was always at my side. Her tenacity and kind heart have shaped me into who I am today. I am deeply indebted to my Dad who has been providing me with an ideal environment for me to explore almost whatever I want. His wisdom and extreme attention towards details have set an example for me to follow for the rest of my life. My life wouldn't be the same without Yan Ying in it. She is my love, my best friend, and the mother of our son. Her support, companionship, and understanding have been the most important factors for me to make it through this entire journey. This dissertation is dedicated to my parents and Yan.

To Ba, Ma, and Ying Yan

Chapter 1

Introduction

Today, it is hard to imagine life without wireless communications. We use our smartphones to write emails, watch videos streaming, and catch up with our family and friends; the list of things that we do with our wireless devices is perhaps endless.

The evolution of wireless communications never stops. While there exists various perceptions about future wireless communications, it has generally been acknowledged that almost every facet of our lives will benefit from the next-generation wireless communications, from wirelessly connected robots to car-to-car communications, and to smart cities [14].

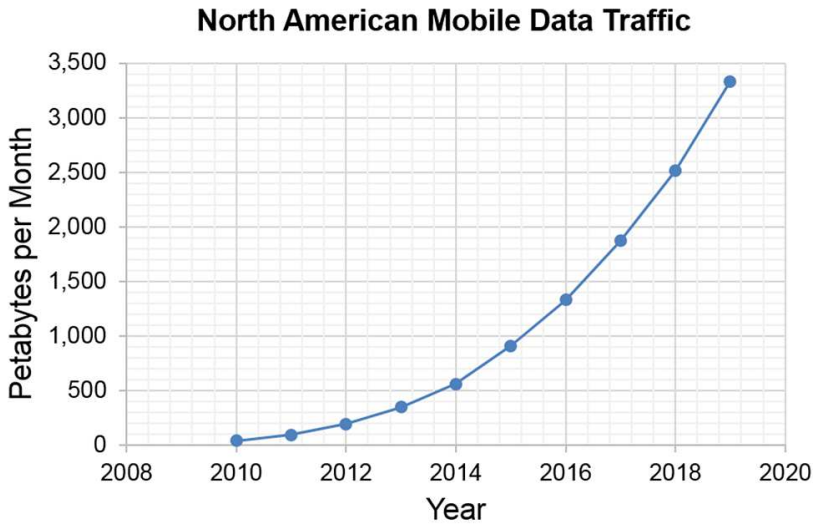

Figure 1.1: The North American mobile data traffic per month from 2010 to 2019 [1].

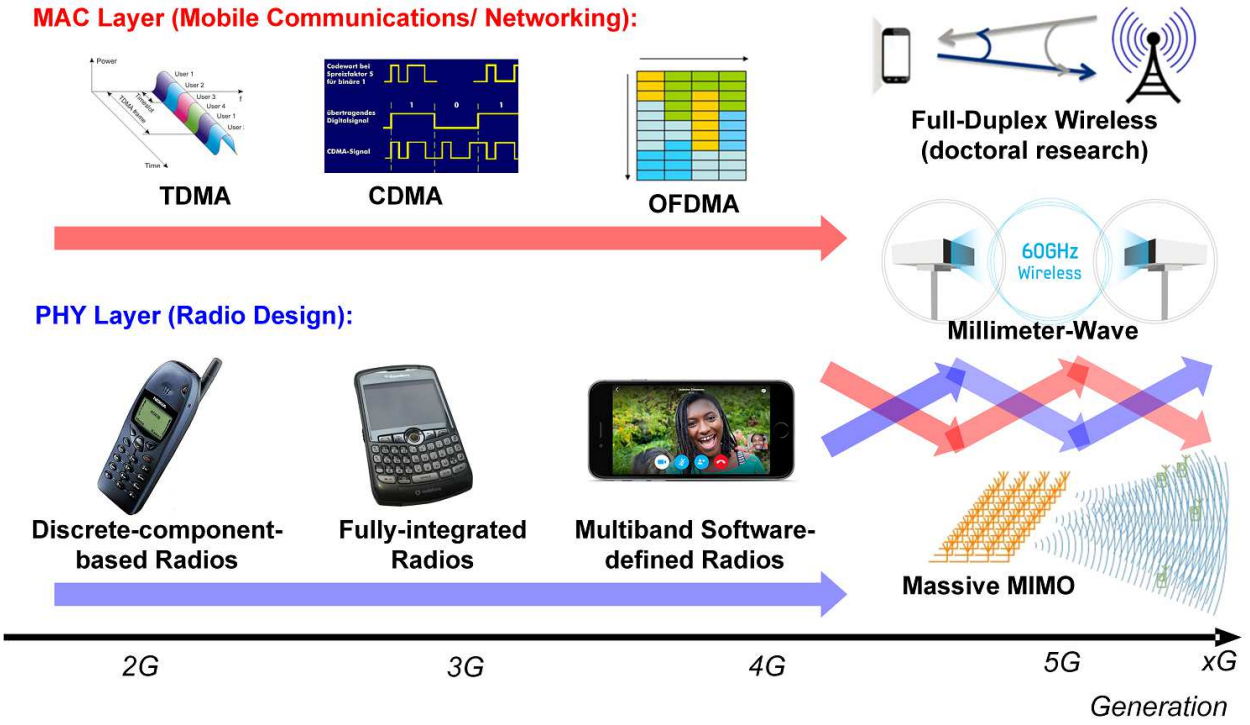

Figure 1.2: The evolution of mobile technologies at the MAC and PHY layers.

The next-generation wireless communications promise an exciting future, but at the same time, it imposes requirements that are higher than those for todays wireless systems by several orders of magnitude in things such as data rate and spectral efficiency. For instance, the north American mobile data traffic per month will increase by two orders of magnitude in nine years from 2010 to 2019 [1] (see Fig. 1.1). The natural question is how our technologies can realize the ever-increasing requirements for future wireless communications. To answer this question, let us first briefly review the evolution of mobile technologies in the past years.

The developments of mobile technologies at the Medium-Access Control (MAC) and Physical (PHY) layers followed relatively independent paths in the past (see Fig. 1.2). At the MAC layer, the representative system technologies for the second-, third- and fourth-generation mobile communications are Time-Division Multiple Access (TDMA), Code-Division Multiple Access (CDMA), and Orthogonal-Frequency-Division Multiple Access (OFDMA), respectively [15]; while at the PHY layer in terms of radio designs, the evolution has been towards higher integration levels, better

power efficiency, and enhanced flexibility [16].

Next-generation wireless technologies given by telecom experts include full-duplex wireless, massive Multi-In-Multi-Out (MIMO), and mm-wave mobile communications [17]: full-duplex wireless is based on novel radio designs that allow simultaneous transmission and reception at the same frequency, challenging our long held assumption about duplexing (see Section 1.1); massive MIMO and mm-wave mobile communications involve next-generation radios with orders of magnitude increase in the number of antennas and in carrier frequencies, reshaping our understandings about interference management and radio propagation for mobile applications [18][19][20]. *Therefore, unlike the MAC and PHY layer technologies developed in the past, these transformative next-generation paradigms involve a rethinking of the traditional assumptions about wireless communications, and require extensive interactions between the MAC and PHY layer designs. While the focus of this thesis is on integrated radios for full-duplex wireless, a cross-layer approach used in our collaborative research with theoreticians at higher layers of the stack has allowed us to make concrete steps towards practical full-duplex wireless networks:* based on the model of the proposed integrated full-duplex radios, the power control algorithms and the full-duplex rate gains have been derived and characterized [21]; to enable experimental characterization of full-duplex MAC layer algorithms, cross-layered software-defined testbeds have been developed and a practical real-time full-duplex wireless link have been demonstrated [22].

1.1 Full-Duplex Wireless

When Guglielmo Marconi launched the first commercial bi-directional radio link, he created the potential for Self-Interference (SI) – interference that comes from co-located transmitters. For Marconi's radios that used spark transmitters and coherer detectors [23], the transmission and reception were separated in different time slots so that the detectors could receive messages from the other user instead of being blocked by their own co-located transmitters. This separation between transmission and reception is called *duplexing* [24].

More than one hundred years later, today's wireless systems still rely on duplexing to avoid SI – many short range or local area radios, such as Bluetooth and WiFi transceivers, transmit and receive in non-overlapping time slots, essentially use Time-Division Duplexing (TDD), while other

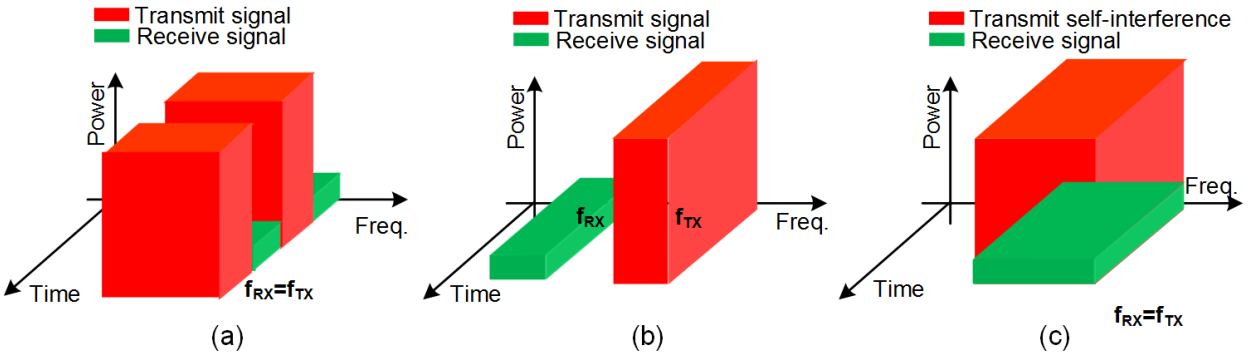

Figure 1.3: Separation of transmission and reception in (a) time (time-division duplexing) or (b) frequency (frequency-division duplexing). (c) Full-duplex wireless simultaneously transmit and receive at the same frequency, promising a significant enhancement in spectral efficiency.

modern wireless systems, such as the majority of today's cellular bands, use Frequency-Division Duplexing (FDD) to separate the transmission and reception in the frequency domain [25]. Both TDD and FDD are half-duplex, where the separation of the transmitted signal and the received signal of a single user in either frequency or time causes inefficient utilization of limited wireless resources (see Fig. 1.3(a) and (b)).

But today we are living in a very different world from what Guglielmo Marconi lived in. Wireless communications systems have woven themselves into the fabric of our everyday lives with applications well beyond wireless telegraphy. Despite advancements in wireless communications technologies such as MIMO, the abundance of wireless systems together with the ever-increasing demand for more communications bandwidths call for non-traditional spectrally-efficient duplexing approaches. *These changes and demand have sparked an emerging wireless communications paradigm which has been revolutionizing the concept of duplexing in existing wireless systems and networks; this new paradigm is called full-duplex wireless* [26],[2].

Without the separation in either time or frequency, full-duplex wireless involves simultaneous transmission and reception at the same frequency as illustrated in Fig. 1.3(c), promising a significant enhancement in spectral efficiency [26],[21]. *However, the biggest challenge associated with full-duplex wireless is the tremendous amount of SI right on top of the desired signal.* The SI has to be suppressed to the receiver noise floor through isolation and cancellation as filtering the SI is not an option. Given 0 to +20 dBm transmitter output power, 20 MHz receiver signal bandwidth

and 5 dB receiver noise figure, 0 dBm $-$ ($-$174 dBm/Hz + 5 dB + 10 lg 20M dB) = 96 dB to 20 dBm $-$ ($-$174 dBm/Hz + 5 dB + 10 lg 20M dB) = 116 dB dB SI suppression is required. For full-duplex radios, such a high degree of SI suppression must be performed across the antenna, Radio Frequency (RF), analog, and digital domains [26],[27]. In addition to the tremendous amount of SI, other challenges associated with full-duplex wireless include the changing wireless environment that requires adaptive Self-Interference Cancellation (SIC) control algorithms and unknown adjunct channel interference that comes from other transmitters in a full-duplex wireless network.

Recent demonstrations (such as those in [28],[29],[2],[7]) have established the feasibility of full-duplex wireless through SI suppression at the antenna interface and SIC in the analog/RF and digital domains. *Thanks to the advancement in Complementary Metal-Oxide-Semiconductor (CMOS) integrated circuit technology, complex digital SIC algorithms that reliably offer about 50 dB suppression can be readily implemented on commodity software-defined radios, such as WARP radios [30].* However, analog/RF SIC in existing full-duplex demonstrations rely on custom-designed cancellers using bulky off-the-shelf components that are not suitable for compact and low-cost integrated-circuit implementations.

The research presented in this thesis aims to build integrated SI-cancelling radios that bring the full-duplex functionality to handheld mobile devices, such as smartphones and tablets (see Fig. 1.4). A fully integrated CMOS implementation, on one hand, imposes constraints that render analog/RF SIC techniques proposed in prior discrete-component-based implementations not viable. *On the other hand, a CMOS implementation opens up new design spaces through the unprecedented integration level.* This thesis presents novel circuits and systems that leverage the true power of modern CMOS technologies for the implementation of integrated SIC for full-duplex wireless communications systems. The contribution of the research presented in this thesis includes the theoretical analysis, design, and experimental verification of the new findings. Based on the mathematical model of the proposed integrated full-duplex radios, our collaborators at higher layers of the stack have made concrete steps towards practical full-duplex wireless networks by deriving the power control algorithms and characterizing the full-duplex rate gains [21]. We also have developed cross-layered software-defined testbeds that enable experimental characterization of full-duplex MAC layer algorithms, and have demonstrated a practical real-time full-duplex wireless link [22].

Another significant impact of the integrated RF SIC techniques proposed in this thesis is related

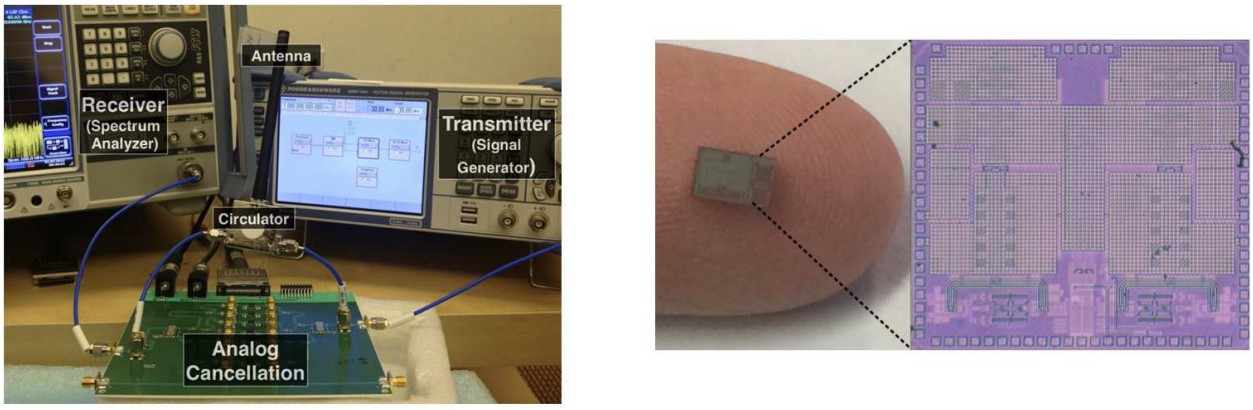

Figure 1.4: Full-duplex radios use (a) off-the-shelf components [2], and (b) a 65 nm CMOS technology with orders-of-magnitude lower cost and smaller form factor [3][4].

to today's FDD systems. Although TDD allows peer-to-peer communication and can assign more downlink capacity through a flexible resource allocation between uplink and downlink, the majority of cellular systems are based on FDD as FDD isolates receivers from signals produced by other mobile transmitters [31],[25]. However, transmitters and receivers operate simultaneously in FDD albeit at different frequencies; the transmitter SI can desensitize the receiver through cross- and inter-modulation, gain compression, noise figure degradation, and reciprocal mixing. In an FDD system, two front-end band-pass filters are combined to form a *duplexer filter* which isolates the powerful transmit signal from the receiver. To ensure sufficient isolation between transmitters and receivers, existing commercial compact duplexers are based on high order acoustic filters, such as Surface Acoustic Wave (SAW) filters [32]. However, each of these acoustic filters can only operate at a fixed frequency band. On the other hand, modern cellular standards (such as Long-Term Evolution (LTE)) often support numerous frequency bands [33], requiring wireless devices to support FDD operation across transmit-receive band pairs that range from several hundreds of megahertz to several gigahertz. Consequently, multi-band FDD operation requires numerous acoustic-filter-based duplexers as depicted in Fig. 1.5(a) which limit the cost and system form factor.

Recent research efforts have been making progress towards tunable duplexers [34],[35],[36]. However, the incorporation of tunability is typically associated with an increase in loss. Therefore,

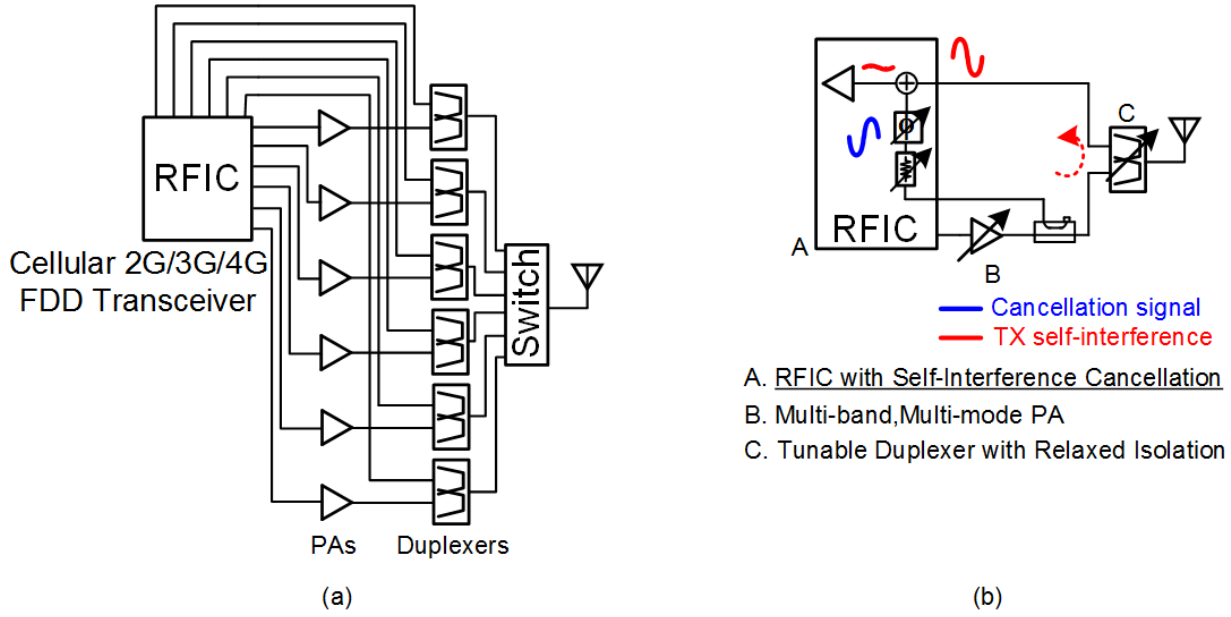

Figure 1.5: Multiband frequency-division duplexing systems utilizing (a) numerous fixed-frequency acoustic-filter-based duplexers and (b) a tunable duplexer with integrated RF self-interference cancellation.

tunable duplexers tend to have less transmitter-to-receiver isolation for the same insertion loss when compared with fixed-frequency duplexers. To relax transmitter-to-receiver isolation, SIC is required as depicted in Fig. 1.5(b). *The novel RF SIC techniques that we demonstrate can be employed together with tunable or low-cost duplexers to replace the numerous fixed-frequency acoustic-technology-based duplexers in next-generation multiband FDD systems.*

1.2 Organization

This thesis is organized as follows. A qualitative discussion about various SI mitigation strategies in full-duplex wireless communications systems is provided in Chapter 2 followed by a quantitative examination of the specifications and SIC requirements for a high-performance full-duplex wireless system. The impact of SI under reduced transmitter-to-receiver isolation at the antenna interface in multiband FDD systems is also discussed; a fundamental benefit of performing RF SIC over having an ultra-linear Receiver (RX) for FDD systems is unveiled.

Chapter 3 presents an overview of existing SI mitigation architectures and techniques. The

limitations of current SI suppression techniques are identified, motivating the need for integrated SIC solutions that can handle powerful SI with negligible RX desensitization, support a wide SIC bandwidth, and allow compact full-duplex radio implementations.

In Chapter 4, a Noise-Cancelling, Self-Interference-Cancelling (NC-SIC) receiver is presented. It breaks a fundamental trade-off between support for low antenna interface isolation levels (or equivalently, power of SI being cancelled) and receiver noise figure degradation through the insight that *unlike discrete-component-based designs that naturally utilize a block-by-block partitioned design strategy, the design of integrated SI-cancelling receivers enables co-design opportunities that can significantly enhance the system performance. In the proposed NC-SIC receiver, an SI canceller is embedded within a noise-cancelling low-noise amplifier.* After covering the evolution of the proposed NC-SIC receiver system architecture, a detailed theoretical analysis related to the simultaneous cancellation of the noise and distortion of the SIC circuitry at both circuit and system levels is provided. A prototype receiver that handles SI with a higher power level than that in prior art by three orders of magnitude is designed and implemented to verify the proposed architecture as well as the corresponding analysis. The 0.3-to-1.7 GHz NC-SIC receiver in 65 nm CMOS can cancel up to +2 dBm peak TX SI at the receiver input, resulting in an effective out-of-band IIP3 of +33 dBm, while the associated increase in receiver noise figure is less than 0.8 dB.

In order to emulate SI channels at RF over a wide frequency range for wideband SIC, Chapter 5 introduces a new concept called Frequency-Domain Equalization (FDE) in the RF domain. *This concept brings frequency-domain equalization, a functionality that is traditionally implemented in the digital signal-processing block, to the RF domain to ensure an SIC bandwidth that is wider than that using a conventional approach. The proposed FDE in the RF domain employs multiple RF bandpass filters with independent controls to emulate SI channels in different sub-bands. The realization of FDE in the RF domain is accomplished by leveraging today's ultra-scaled CMOS technology; with transistors that are able to be efficiently switched at high frequencies, high-quality factor RF BPFs can be realized based on Linear Periodically Time-Varying (LPTV) circuits [37][38][39][40][41].* Theoretical treatments of the proposed FDE-based SIC and the LPTV high-quality factor RF BPFs with embedded amplitude and phase adjustments capability are given. Experimental results of a 0.8-to-1.4 GHz SI-cancelling receiver with an FDE-based canceller in a 65 nm CMOS process validate the theoretical findings. In measurement, more than 20 MHz 20 dB

cancellation bandwidth is achieved across a couple of frequency-selective antenna interfaces.

A 0.6-to-0.8 GHz full-duplex radio with an integrated magnetic-free passive circulator and analog baseband (BB) SIC is presented in Chapter 6. The integrated circulator is based on a linear time-varying two-port N-path filter that breaks reciprocity via staggered commutation [42]. A joint-SIC methodology across the antenna and analog domains is proposed with enhanced performance when compared to a conventional approach where the antenna interface and the analog BB SI canceller are configured independently. Furthermore, the cancellation of the SI and its associated IM3 distortion in the digital domain is investigated. In conjunction with the digital SIC, the proposed integrated SI-cancelling full-duplex radio with the magnetic-free passive circulator in 65 nm CMOS *demonstrates 85 dB overall SI suppression, enabling a full-duplex link budget of* -7 *dBm Transmitter (TX) average output power and* -92 *dBm noise floor.*

Chapter 7 discusses the full-duplex cross-layered software-defined testbeds which consist of custom-designed RF SI cancellers and National Instruments (NI) Universal Software Radio Peripherals. The RF cancellers are implemented using discrete components and emulate our proposed integrated SI cancellers mentioned in previous Chapters. Digital SIC and adaptive canceller control algorithms are implemented in NI LabVIEW. *Using these testbeds, we demonstrate a practical real-time full-duplex wireless link consisting of two full-duplex transceivers [22].* Using the integrated SI-cancelling receiver described in Chapter 5 and a tunable duplexer based on cavity filters [43], a tunable FDD system demonstration is presented at the end of the Chapter 7.

Finally, Chapter 8 concludes the dissertation with a summary of the key technical contributions and a discussion of possible future research.

Chapter 2

Self-Interference and Its Mitigation in Wireless Communication Systems

TX SI mitigation in full-duplex wireless and FDD communication systems can be performed in different domains, including the wave propagation (at the antenna interface), analog/RF, and digital domains. Natural questions that arise are in which domain or domains should we perform SI suppression and how much suppression is required in each domain. The answers to these questions on SI mitigation strategies strongly depend on the performance specifications of the corresponding wireless systems. This chapter starts with a brief review of related wireless transceiver basics. After the review, a qualitative discussion on various SI mitigation strategies for full-duplex wireless communication systems is presented. This is followed by a quantitative examination of the specifications and SIC requirements in a high-performance (WiFi-like) full-duplex system. Finally, in section 2.3, the impact of SI under reduced transmitter-to-receiver isolation at the antenna interface in multiband FDD systems is discussed, and the fundamental benefit of performing SIC at RF over having an ultra-linear RX for FDD systems is unveiled.

2.1 A Brief Review of Wireless Transceiver Basics

With the proliferation of wireless applications and standards, modern radios have evolved into various categories that can be characterized based on specifications such as communication range, data rate, power consumption, modulation scheme, occupied bandwidth, interference tolerance, and

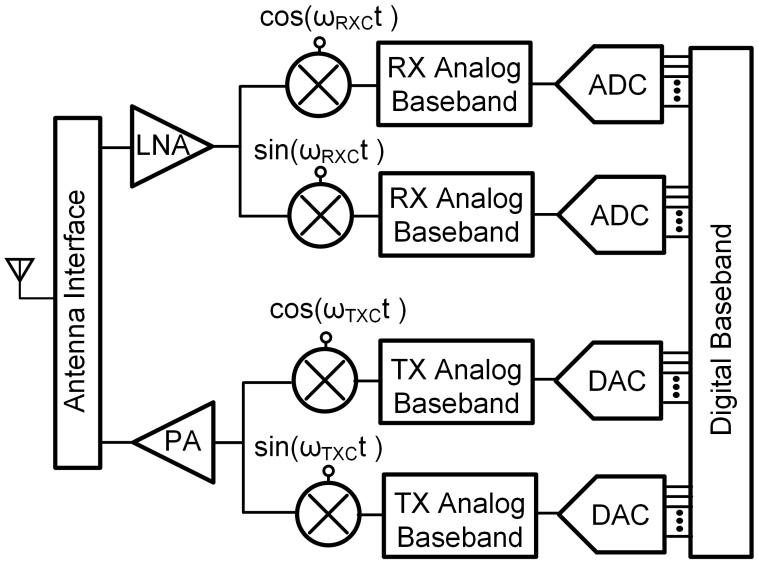

Figure 2.1: Block diagram of a wireless transceiver that employs the direct-conversion architecture. The direct-conversion architecture has been used for many today's high-performance cellular and WiFi radios[5][6]; those radios most likely will adopt full-duplex operation first in the near future [2][7].

so on. Here we present a brief review of the basics of modern high-performance wireless transceivers, specifically those for WiFi and cellular applications, as WiFi and cellular standards will most likely adopt full-duplex operation first when compared with other standards in the near future [2][7].

Modern high-performance wireless transceivers for cellular and WiFi standards such as wideband Wideband Code Division Multiple Access (WCDMA), LTE, and 802.11b/a/g often use a direct-conversion architecture for both TXs and RXs [5][6]. Despite having design issues related to local oscillator (LO) leakage, DC offset, and flicker noise, the direct-conversion architecture is a superior choice as it is compact and power efficient and has no image problem, resulting in low cost implementations with a simplified design process [25].

Fig. 2.1 depicts the block diagram of a direct-conversion wireless transceiver. The RX consists of an Low-Noise Amplifier (LNA), quadrature down-conversion mixers, analog BB circuits that include Variable-Gain Amplifiers (VGAs) and Low-Pass Filters (LPFs), and Analog-to-Digital Converters (ADCs). This architecture is called "direct-conversion" because its Local Oscillator (LO) frequency is set exactly to its incoming RF signal frequency. Quadrature down-conversion which

consists of two down-conversion paths driven by in-phase and quadrature-phase LOs is employed to avoid self-corruption of asymmetrically-modulated signals [25]. Many of today's modulations exhibit asymmetrical spectra around their carrier frequency, such as Frequency-Shift Keying (FSK), Quadrature Phase-Shift Keying (QPSK), and Quadrature Amplitude Modulation (QAM). BB VGAs and LPFs further amplify the signals and perform channel selection. Finally, ADCs convert received analog signals to digital bits.

A TX that utilizes direct up-conversion looks similar to a direct-conversion RX, except it operates in reverse order. TX digital BB signals are first converted into the analog domain by Digital-to-Analog Converters (DACs). Then TX BB LPFs suppress the quantization noise and aliasing spurs from the DACs. Quadrature up-conversion that includes two up-conversion pathes driven by in-phase and quadrature-phase LOs allows for quadrature modulations and transfers the analog BB signals to the carrier frequency. At the end of the TX chain, a Power Amplifier (PA) amplifies the transmitted signal to the desired power level.

2.1.1 TX Design Considerations

2.1.1.1 TX Linearity

Transmitters in high-performance wireless transceivers can operate at a relatively high output power level – the 802.11b WiFi standard stipulates a TX output power of +20 dBm [25]. Due to large signal operation, the nonlinearity of transmitters must be considered. In a typical TX design, the linearity performance of the TX is limited by the PA as it handles the largest voltage swing. PA nonlinearity leads to two effects: (1) distortion of the signal to be transmitted, and (2) high adjacent channel power as a result of spectral regrowth.

To understand the effect of distortion and spectral regrowth, let us consider an amplifier with a memoryless third-order nonlinearity as depicted in Fig. 2.2. The output ($y(t)$) of the amplifier can be written as a function of its input ($x(t)$) as $y(t) = \alpha_1 x(t) + \alpha_3 x^3(t)$, where α_1 and α_3 are the first- and third-order nonlinear coefficients. Assuming a single-tone signal $x(t) = A\cos\omega t$ passing through the amplifier, its output can be written as:

$$y(t) = \left(\alpha_1 + \frac{3}{4}\alpha_3 A^2\right) A\cos\omega t + \frac{1}{4}\alpha_3 A^3 A\cos 3\omega t. \tag{2.1}$$

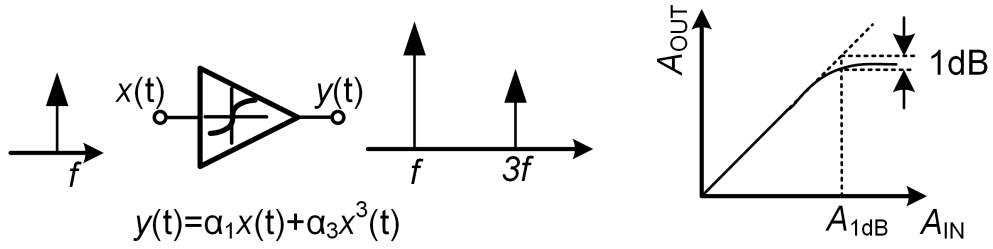

Figure 2.2: Amplitude compression of a single-tone signal passing through a memoryless nonlinear amplifier and the definition of the input 1 dB compression point A_{1dB}.

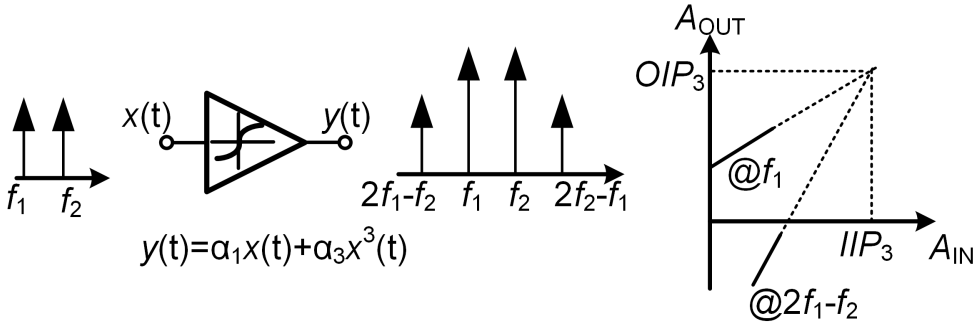

Figure 2.3: Inter-modulation of a two-tone signal passing through a memoryless nonlinear amplifier, and the definitions of the input and output third-order intercept points (IIP_3 and OIP_3).

As we can see from (2.1), the amplifier gain $\left(\alpha_1 + \frac{3}{4}\alpha_3 A^2\right)$ depends on the amplitude of the input single (A) – a larger input signal amplitude results in more severe amplitude compression assuming $\alpha_1\alpha_3 < 0$, which is typically the case for amplifiers. The input signal amplitude that corresponds to a 1 dB gain compression is called as the input 1 dB compression point A_{1dB} as illustrated in Fig. 2.2, and can be calculated as $A_{1dB} = \sqrt{0.145|\frac{\alpha_1}{\alpha_3}|}$.

Next, if a two-tone signal $x(t) = A_1 \cos\omega_1 t + A_2 \cos\omega_2 t$ appears at the input, the amplifier output can be calculated as:

$$\begin{aligned} y(t) = &\left(\alpha_1 + \frac{3}{4}\alpha_3 A_1^2 + \frac{3}{2}\alpha_3 A_2^2\right) A_1 \cos\omega_1 t + \left(\alpha_1 + \frac{3}{4}\alpha_3 A_2^2 + \frac{3}{2}\alpha_3 A_1^2\right) A_2 \cos\omega_2 t \\ &+ \frac{3}{4}\alpha_3 A_1^2 A_2 \cos(2\omega_1 - \omega_2)t + \frac{3}{4}\alpha_3 A_2^2 A_1 \cos(2\omega_2 - \omega_1)t + \\ &+ \frac{3}{4}\alpha_3 A_1^2 A_2 \cos(2\omega_1 + \omega_2)t + \frac{3}{4}\alpha_3 A_2^2 A_1 \cos(2\omega_2 + \omega_1)t + \\ &+ \frac{3}{4}\alpha_3 A_1^3 \cos(3\omega_1 t) + \frac{3}{4}\alpha_3 A_2^3 \cos(3\omega_2 t). \end{aligned} \tag{2.2}$$

indicating two side tones around the original two-tone signal as depicted in Fig. 2.3. These side tones or third-order inter-modulation (IM3) tones, representing the "spectral regrowth" when more complex modulation signals are considered, can corrupt the adjacent channels if the TX linearity performance doesn't meet the requirement prescribed in the wireless standard. Furthermore, from (2.2) we can see that for small A_1 and A_2, the IM3 tones grow three times as fast as the fundamental tones at ω_1 and ω_2 when the input amplitudes increase. Therefore, if we extrapolate the output-versus-input amplitude plots of the fundamental and IM3 tones for small A_1 and A_2, the plots will intersect as shown in Fig. 2.3. The input level at which this intersection happens is defined as the input third-order intercept point (IIP_3), while the corresponding output level is called the output third-order intercept point (OIP_3). IIP_3 can be calculated as $IIP_3 = \sqrt{\frac{4}{3}|\frac{\alpha_1}{\alpha_3}|} \approx A_{1dB} + 10\ dB$. Note that the third-order intercept point is obtained from an extrapolation and that the TX is never operated at that point (with very high power levels). Rather, third-order intercept point is a metric that allows one to calculate the IM3 levels at the actual point of operation.

2.1.1.2 TX Digital Predistortion

Digital predistortion is one of many techniques that have been employed for TX linearization, is closely related to SIC in the digital domain as we will see later in this thesis. The basic idea of digital predistortion is as follows: if the PA nonlinear characteristics are known, then it is possible to design a block that predistort the TX input signals such that a cascade of this block, called the predistortor, and the nonlinear PA exhibits an overall linear performance. The predistortor is often implemented in the digital domain due to the advancement of modern digital signal processing technology [44]. For instance, as illustrated in Fig. 2.4, if the PA has a nonlinear characteristic of $y = f(x)$, then the predistortor should have a response of $y = f^{-1}(x)$ to linearize the PA. As we will

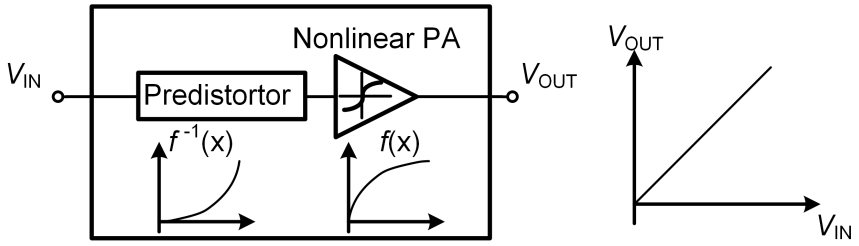

Figure 2.4: Basic idea of predistortion for TX linearization.

see later, digital predistortion is closely related to digital SIC as it involves the digital estimation and cancellation of spurious signals.

2.1.1.3 TX Noise

TX noise is often characterized in FDD systems as it can desensitize the RX. TX noise contributors include DAC quantization noise and thermal noise from the TX BB circuits and the quadrature modulator. In a typical design, the noise contribution from the PA can be assumed to be negligible. Given a typical TX noise floor of -156 dBc/Hz [45], and a signal bandwidth of 20 MHz, the TX noise integrated over the signal bandwidth is about 80 dB below the transmitted signals.

2.1.2 RX Design Considerations

2.1.2.1 RX Noise

The primary goal of receivers is to demodulate very weak signals from a noisy environment. The capability of detecting a weak signal in the presence of noise is quantified through RX sensitivity. The sensitivity is defined as the minimum signal level that an RX can detect with acceptable quality and can be calculated as $P_{sen} = P_{NoiseFloor} + SNR$, where SNR is the Signal-to-Noise Ratio (SNR) prescribed in the wireless communication standard and $P_{NoiseFloor}$ is the RX noise floor. The RX noise floor is further determined by the RX Noise Figure (NF) and the signal Bandwidth (BW), and can be calculated as: $P_{NoiseFloor} = -174\ dBm/Hz + NF + 10\log_{10}(BW)$.

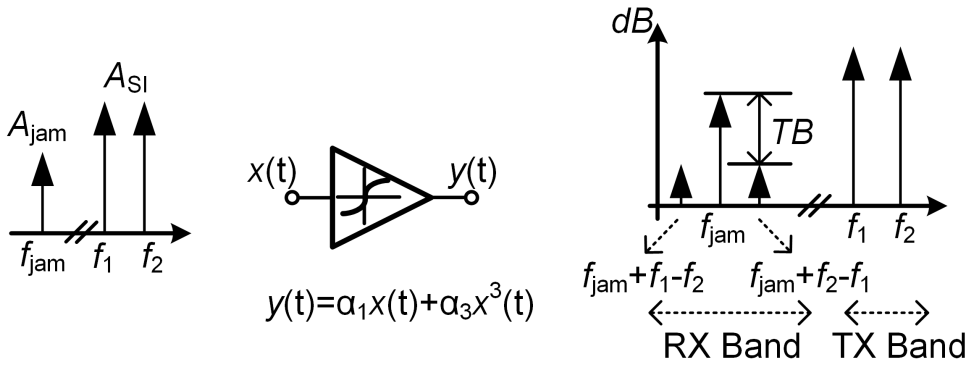

Figure 2.5: A continuous-wave (CW) unknown jammer with a two-tone TX self-interference signal passing through a nonlinear amplifier generating unknown cross-modulation distortion. Triple beat (TB) is defined as the difference (in dB) between the CW jammer and the cross-modulation distortion tone at the nonlinear system output.

2.1.2.2 RX Linearity

Interference from other wireless devices or devices located on the same platform can cause large voltage swings, resulting in nonlinear distortion. At RF, wireless transceivers today are largely interference limited, rather than noise limited, due to spectral congestion. Similar to transmitters, third-order intercept point (IP3) and 1 dB compression point are used to characterize the RX linearity performance. Depending on the interference frequency location with respect to the RX BW, Out-Of-Band (OOB) IP3 and 1 dB compression point and In-Band (IB) IP3 and 1 dB compression point are used. A key point of difference between receivers and transmitters is that for most receivers, the interference is an unknown signal, and therefore, techniques such as pre-distortion that compensate for the effects of nonlinearity cannot be applied. Full-duplex wireless, the focus of this thesis, represents a unique situation where the primary interference signal is from one's own transmitter and is known, thus enabling techniques such as SIC.

In existing FDD systems where transmitters and receivers operate simultaneously in different frequency bands, other more complex nonlinearity mechanisms exist that are characterized by other metrics. The TX signal can leak to the RX input through the antenna interface, which is typically an acoustic duplexer. This modulated SI can cross-modulate with an unknown jammer in the vicinity of the RX band, generating cross-modulation distortion and desensitizing the RX. To

understand this phenomenon, let us consider three tones passing through a memory-less nonlinear amplifier as depicted in Fig. 2.5. A Continuous-Wave (CW) signal at frequency f_{jam} represents the jammer, while a two-tone signal located at f_1 and f_2 models the TX SI. Due to the third-order nonlinearity, distortion tones $\frac{3}{2}\alpha_3 A_j A_{SI}^2 \cos[\omega_j + (\omega_1 - \omega_2)]t$ and $\frac{3}{2}\alpha_3 A_j A_{SI}^2 \cos[\omega_j - (\omega_1 - \omega_2)]t$ appear at the amplifier out around the CW jammer. It should be noted that the cross-modulation distortion involves an interaction between the unknown CW jammer and SI, and therefore the distortion cannot be predicted in the digital domain. To quantify the level of cross-modulation, the difference (in dB) between the CW jammer and the cross-modulation distortion tone is called Triple Beat (TB) as shown in Fig. 2.5, a specification that can be commonly found in literature describing FDD wireless transceiver designs [46][47]. Based on the definition and a power series analysis, TB can be related to IIP_3 as $TB = 2(IIP_3 - P_{SI,avg})$, where $P_{SI,avg}$ is the average SI power.

2.1.2.3 ADC Dynamic Range

ADCs on the RX side need to digitize complex modulated signals that have large peak-to-average ratio under fading conditions with sufficient SNR. In interference-limited scenarios, the ADC dynamic range must be sufficient to quantize the desired signal and the interference signal, without having the latter corrupt the former. Typically, a dynamic range of 60 dB is required for a ADC to support 64-QAM in a WiFi transceiver, of which about 30 dB is for SNR and another 30 dB for various margins [27]. Based on the ADC figure-of-merit defined in [48], a 6 dB increase in ADC dynamic range, or adding one more bit to the ADC, requires four times larger ADC power consumption. Considering a simple flash ADC, this can be understood as follows: adding one more bit to the ADC requires not only twice as many comparators as before but also higher performance from the comparators as the least significant bit is halved.

2.1.3 LO Design Considerations

2.1.3.1 LO Phase Noise

An LO circuitry is used to generate LO signals in a wireless transceiver for frequency conversion as depicted in Fig. 2.1. Typically, the core of an LO circuitry is a phase-locked loop that can generate a very precise clock frequency from an external crystal oscillator (see Fig. 2.6) [49]. An ideal phase-

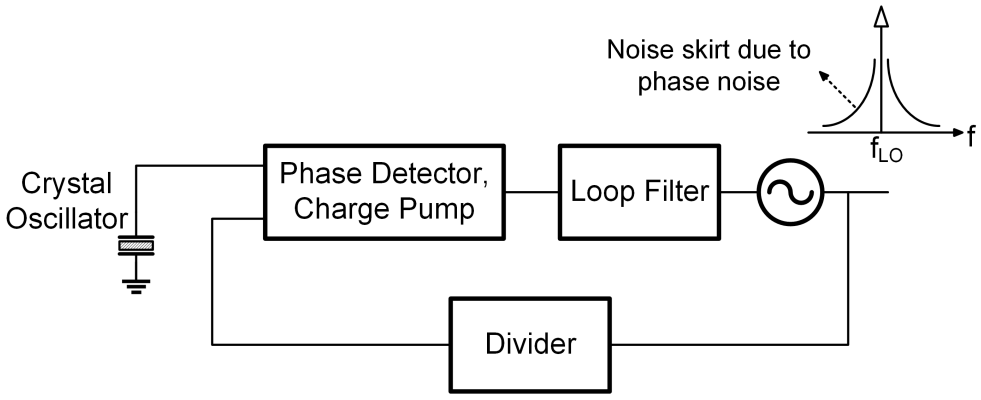

Figure 2.6: A typical phase-locked loop used in wireless transceiver LO circuitry with an illustration of the LO phase noise.

locked loop produces a perfectly-periodic output of the form $v_{LO}(t) = \cos(\omega_{LO}t + \psi_n)$. The zero crossings occur at exact integer multiples of the clock period. However, the noise of phase-locked loop circuits randomly perturbs the zero crossings or the phase ψ_n of the LO signal in reality. This perturbation in the zero crossings or the phase of the LO signal is called the "phase noise", and can be modeled as $v_{LO}(t) = \cos(\omega_{LO}t + \psi_n(t))$ in the time domain, where $\psi_n(t)$ represents the noisy LO phase [25][50]. In the frequency domain, the presence of phase noise creates a "noise skirt" around the ideal LO impulse as illustrated in Fig. 2.6.

2.1.3.2 Effect of Phase Noise

Phase noise is a critical design consideration in wireless transceiver designs as it can significantly affect the system performance. First of all, the mixing of a desired signal with a noisy LO signal in the TX or RX path can affect the information carried by the desired signal, degrading the bit error rate of the communication systems. Phase noise can also introduce interference issues in the TX or RX path. In transmitters, phase noise causes spectral spreading which can mask weak desired signals in adjacent channels. In receivers, the mixing of a noisy LO signal with an interferer results in a noise skirt that can corrupt the desired signal after down-conversion. This phenomenon is called reciprocal mixing [25].

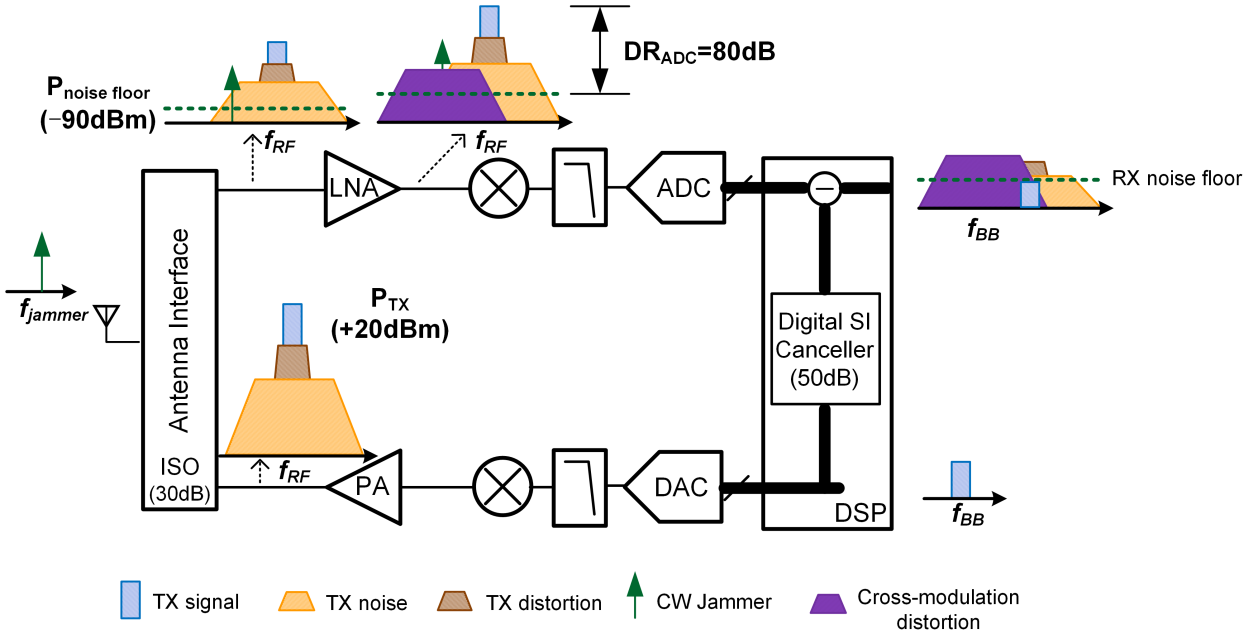

Figure 2.7: Illustration of a full-duplex wireless transceiver with self-interference isolation at the antenna interface and self-interference cancellation purely in the digital domain.

2.2 SI and Its Mitigation in Full-Duplex Systems

2.2.1 SI Suppression Across the Antenna, Analog/RF, and Digital Domains

Thanks to the advancements in the CMOS technology, sophisticated Digital Signal Processing (DSP) techniques, such as digital predistortion mentioned in Section 2.1.1 and digital beamforming in phased-array systems [51], can be utilized to enhance the performance of wireless systems. However, performing SIC only in the digital domain imposes extremely stringent requirements on the wireless system and is ineffective for unpredictable effects of the SI. The discussions presented here motivate an SI suppression strategy across the antenna, analog/RF, and digital domains.

Consider a full-duplex wireless transceiver depicted in Fig. 2.7. A direct-conversion architecture is assumed for both the TX and RX based on the reasons given at the beginning of Section 2.1. Quadrature conversion is not shown in Fig. 2.7 for simplicity. At the TX PA output, the transmitted signal contains not only the up-converted TX BB signal but also distortion and noise from the TX chain (see Section 2.1.1 and 2.1.3). The transmitted signals leak to the RX side after initial isolation from the antenna interface (e.g. a circulator or an antenna pair). A digital SI canceller emulates

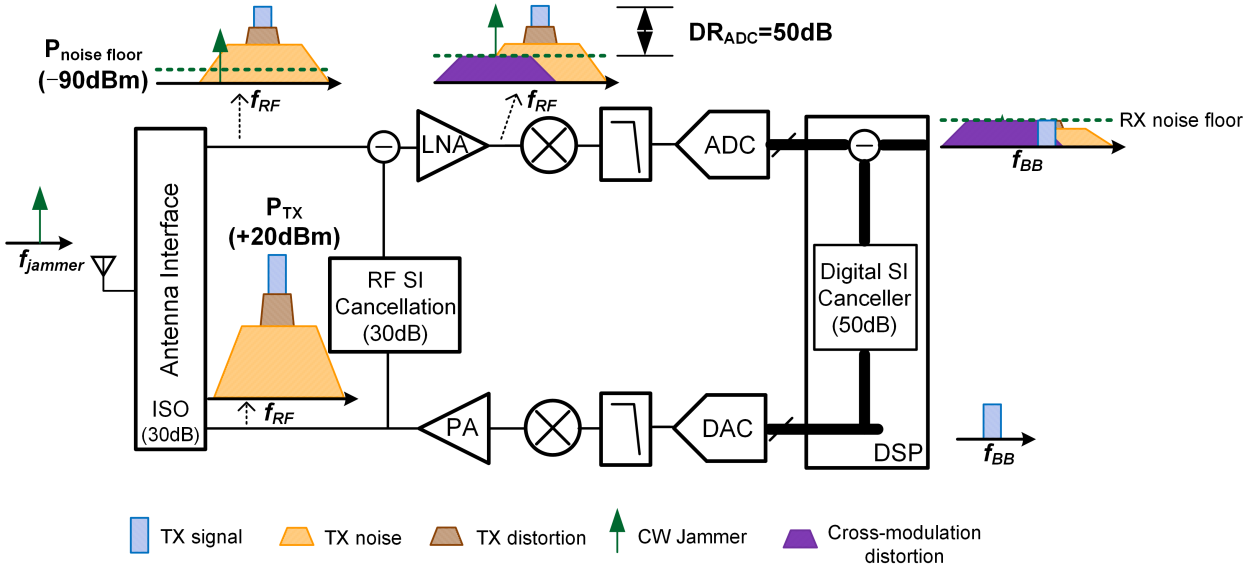

Figure 2.8: Illustration of a full-duplex wireless transceiver with self-interference mitigation across the antenna, RF, and digital domains.

the SI channel response, including both linear and nonlinear parts, to create a cancellation signal in the RX digital BB for SIC. *For SIC purely in the digital domain, the ADC acts as the major bottleneck.* Given a TX output power of +20 dBm, RX input-referred noise floor of −90 dBm, and SI isolation of 30 dB at the antenna interface, 80 dB digital SIC and hence ADC DR is required; this results in a 16-bit ADC [1] with an estimated power consumption of about 5 W at a sampling rate of 50 MS/s! In addition, the RF/analog receiver front-end must also exhibit the same DR. To relax the ADC and RF/analog front-end DR requirement and thus reduce their power consumption, SIC in the analog/RF domain is critical; given 30 dB SIC in the RF domain, the ADC would consume one thousand times less power (see Fig. 2.8). Furthermore, SI mitigation across the antenna, analog/RF, and digital domains is necessary for obtaining the 110 dB overall suppression as it is very challenging to achieve >100 dB precision from a single stage.

Even if we manage to have an ADC with the required DR performance, SIC purely in the digital domain can still be ineffective as *unpredictable effects of the SI, including RX gain compression of the desired signal, the resultant increase in RX noise floor, and cross-modulation between the SI*

[1] ADC effective DR can be roughly calculated as 6×(ENOB-2), where ENOB is the ADC effective number of bit. The factor 2 takes into account the signal peak-to-average ratio as well as a one-bit margin at the noise floor [26].

and an unknown incoming CW jammer, cannot be cancelled in digital. In addition, although it is possible to estimate the TX and RX distortion in the digital domain, similar to what is typically done for TX digital predistortion [44], the distortion cancellation is limited to 20-to-40 dB in practice [2][52] which can impose stringent requirements on the TX and RX linearity performance. On the other hand, consider SIC in the RF domain as illustrated in Fig. 2.8 where an RF SI canceller couples a fraction of the TX signal at the PA output, adjusts the TX replica signal based on the corresponding SI channel response, and subtracts the SI at the RX input. In this architecture, SI gets cancelled right at the receiver input, protecting the LNA and RX from gain compression and reducing the cross-modulation distortion by enhancing the effective input third-order intercept point (IIP3) of the LNA and RX. The SIC also includes the TX impairments and thus suppresses the powerful SI together with its associated TX distortion and noise, relaxing TX linearity and noise requirements.

2.2.2 Link Between SI Mitigation Strategies and System Specifications

SI mitigation strategies are strongly coupled with the performance and specifications of the corresponding wireless systems. The aforementioned SIC architecture depicted in Fig. 2.8 targets high-performance wireless transceivers with high PA output power and low RX NF. However, alternate SI mitigation architectures have been reported targeting other system performance envelopes. Note that the focus of this section is on highlighting the link between SIC architectures and the performance and specifications of the corresponding wireless systems; a comprehensive survey of full-duplex SIC architectures is deferred to Chapter 3.

One variant of the SIC architecture shown in Fig. 2.8 is depicted in Fig. 2.9. This architecture proposed in [8] adopts a passive mixer-first RX [53] for maintaining high IB linearity under strong SI. Due to the transparency of the passive mixer [54], the cancellation injection node is moved to the analog BB and the SI canceller phase shift, attenuation and downmixing can be combined in a single Vector Modulator (VM) as depicted in Fig. 2.9. Similar to the architecture presented in Fig. 2.8, this topology taps the TX signal at the PA output, including TX impairments in the cancellation, relaxing TX linearity and noise requirements. However, this mixer-first VM-downmixer-based architecture results in >10 dB RX NF in full-duplex mode due to the mixer-first RX and the strong coupling of the cancellation path to the analog BB, and thus aims for wireless

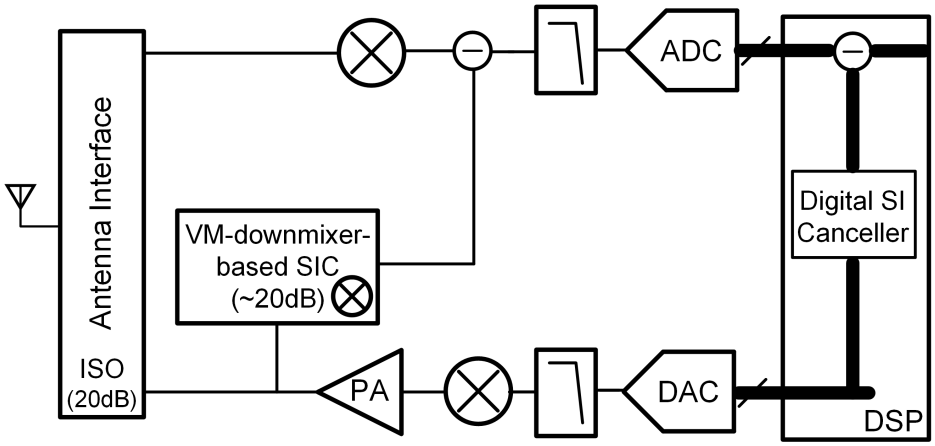

Figure 2.9: A full-duplex radio using a mixer-first receiver with a vector-modulator-downmixer-based self-interference canceller presented in [8].

applications with relaxed NF requirements.

For short-range wireless communications, the SIC budget can be relaxed resulting in another SIC architecture illustrated in Fig. 2.10 [9]. Since 80 dB overall SI suppression is budgeted (30 dB less when compared to the example shown in Fig. 2.8), SIC can be performed in the analog and digital domains without any isolation at the antenna interface. Baseband duplexing amplifiers are proposed that allow the TX and RX share one common mixer while providing 30 dB TX-to-RX isolation. This architecture leads to a highly integrated full-duplex implementation using a single antenna without having bulky and expensive off-chip components like circulators [2]. It should also be mentioned that the shared-antenna interface without any TX-RX isolation also limits the TX power to -17 dBm.

2.2.3 Example Full Duplex System-Level Analysis

After a qualitative overview of SI mitigation in full-duplex wireless transceivers, this section provides a quantitative examination of specifications and SIC requirements for a moderately-high-performance wireless transceiver with moderate PA output power and low RX NF. The system-level

[2]Recent research efforts have been making progress towards integrated magnetic-free circulators which also promise compact full-duplex system implementations with a single antenna but with potentially higher TX output power due to the extra isolation from the antenna interface [42]

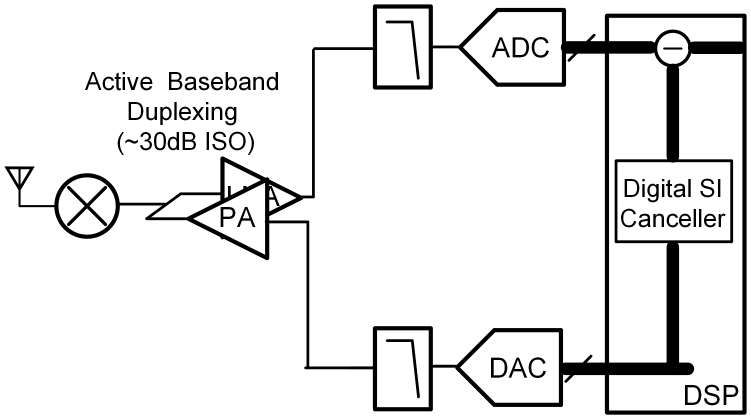

Figure 2.10: A compact short-range full-duplex radio using baseband duplexing amplifiers presented in [9].

analysis presented here are based on the integrated full-duplex radio presented in [3][4], but the analysis can be applied to other full-duplex radio designs with similar architectures.

2.2.3.1 Full Duplex System Considerations

In a full-duplex wireless transceiver as depicted in Fig. 2.11, the TX signal at the PA output includes the TX main signal ($P_{TX,main}$), TX nonlinear distortion signal ($P_{TX,dis}$), and TX noise ($P_{TX,noise}$). The TX signal leaks to the receiver input (becoming SI) through an antenna interface with certain TX-to-RX isolation (ISO).

Assuming a full-duplex wireless system with $P_{TX,main}$=+15 dBm, 20 MHz RX BW, and 5 dB RX NF (NF_{RX}), SIC of 15 $dBm - (-174\ dBm/Hz + 5\ dB + 73\ dBHz) + 6\ dB = 117\ dB$ is required. Additional 6 dB cancellation has been assumed to ensure that the residual SI is well below the RX noise floor. Such a large amount of isolation/cancellation must be achieved by combining suppression at the antenna, and in RF, analog and digital domains as mentioned in Section 2.2.1.

As mentioned earlier, SIC in the RF domain that taps from the PA output and cancels the SI at the RX front-end will cancel TX nonlinear distortion as well. However, the RF canceller might introduce its own nonlinear distortion ($P_{Canc,dis}$ in Fig. 2.11). Depending on how much cancellation is achieved, the RX will introduce nonlinear distortion on the TX signal as well ($P_{RX,dis}$ in Fig. 2.11). All these nonlinear distortions are predictable and can eventually be cancelled in the

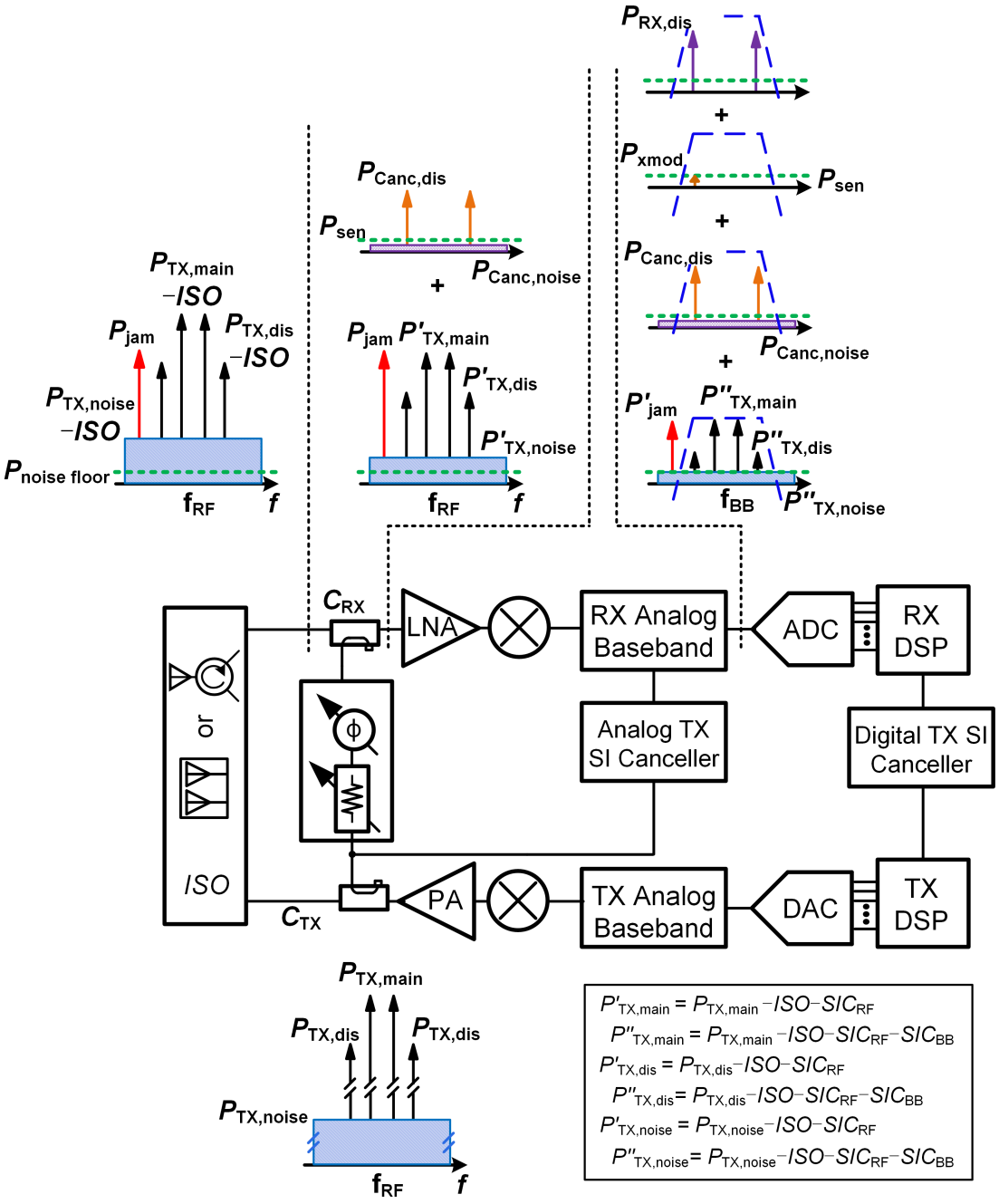

Figure 2.11: Full-duplex transceiver block diagram with TX self-interference cancellation in the RF, analog and digital domains. Various distortion mechanisms are also depicted.

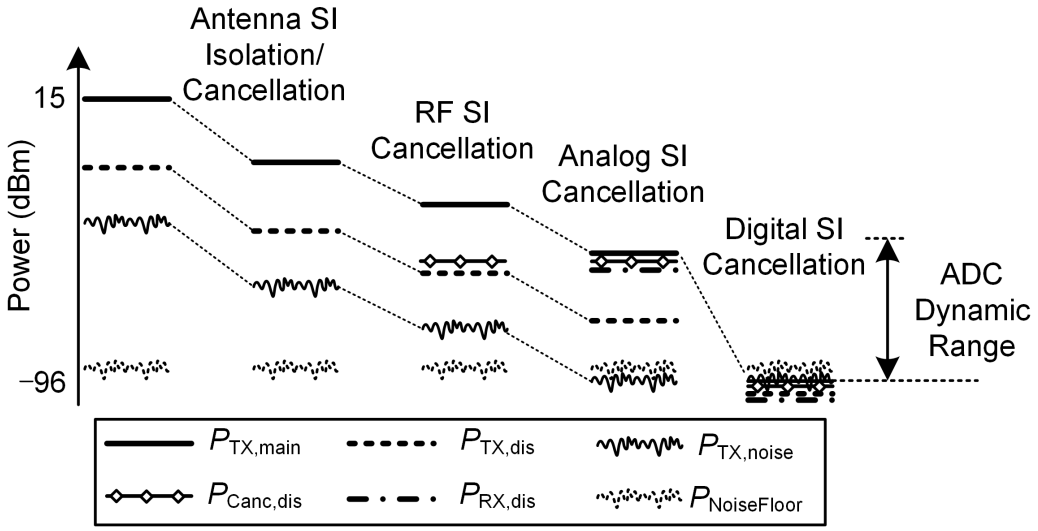

Figure 2.12: SIC budget of a full-duplex wireless system assuming +15 dBm PA output power ($P_{TX,main}$), 20 MHz RX BW, and 5 dB RX NF. RX noise floor is $P_{NoiseFloor} = -174dBm/Hz + 5dB + 73dBHz = -96dBm$.

digital domain [2][52]. What cannot be cancelled in the digital domain are unpredictable effects of the SI, including RX gain compression of the desired signal, NF increase and interaction between the SI and an unknown incoming CW jammer (P_{jam} in Fig. 2.11). We assume that RF SIC suppresses the SI sufficiently to prevent gain compression of the desired signal (verified by our prototype in [3][4]) and NF increase. Hence, we focus on cross-modulation between the SI and an unknown jammer.

Due to the stringent SIC requirement of almost 120 dB in this example, analog SIC is needed in addition to the SIC in the RF domain. The analog cancellation is depicted as tapping from the PA output (similar to [8]). Therefore, it will further suppress not only the TX main signal, but also the TX distortion and the TX noise. We assume that RF and analog SIC are sufficient to suppress the TX noise below the RX noise floor (see Fig. 2.11). RF canceller noise ($P_{Canc,noise}$ in Fig. 2.11) needs to be considered as well in establishing the final RX noise floor in the full-duplex system.

Figure 2.12 illustrates the aforementioned 117 dB full-duplex link budget enabled by SI isolation/cancellation across the various domains. The CW jammer and its associated cross-modulation distortion are not shown in Fig. 2.12 as they cannot be cancelled. We assume that the RX and RF canceller are designed so that their distortion ($P_{RX,dis}$ and $P_{Canc,dis}$) have the same power

level as the residual SI after RF and analog SIC. Therefore, the ADC DR is determined by the residual SI, RX distortion, canceller distortion, and RX noise floor ($P_{NoiseFloor}$) as $DR_{ADC} = (P_{TX,main} - ISO - SIC_{RF} - SIC_{BB} + 6) - (P_{NoiseFloor} - 6)$, where SIC_{RF} and SIC_{BB} are the amount of SIC achieved in the RF and analog domains, $P_{NoiseFloor}$ is the RX noise floor (-174 dBm/Hz+5 dB+73 dBHz=-96 dBm[3]) and we have included a 6 dB margin at both ends[4] [26]. Since we've assumed that the RX distortion has the same power as that of the residual SI after RF and analog SIC, we can compute the required RX linearity performance. The RX effective IB IIP3 (i.e. IIP3 under RF and analog cancellation of the SI) can be calculated as:

$$IIP_{3,RX,effective} = (P_{TX,main} - ISO - 3) + \frac{1}{2}(SIC_{RF} + SIC_{BB}). \tag{2.3}$$

Given 30 dB antenna isolation/cancellation [55], and 50 dB digital SIC [2], 37 dB SIC needs to be achieved in the RF and analog domains, resulting in $DR_{ADC} = 56\ dB$ and $IIP_{3,RX,effective} = +0.5\ dBm$.

One interesting question is how to distribute the 37 dB SIC between RF and analog domains. SIC must be judiciously distributed between the two to ensure that the required $IIP_{3,RX,effective}$ is achieved and gain compression and NF increase is prevented along the RX chain. Furthermore, as is discussed in the next subsection, RF SIC at the RX input is required to protect the RX front-end from cross-modulation distortion [56]. The amount of SIC that can be obtained at RF is also typically limited by the selectivity of the antenna interface and the required RF SIC BW (we will explain this in detail later in Chapter 3). We assume 20 dB cancellation can be achieved over >20 MHz BW (verified by our prototype in [3][4]). Therefore, analog SIC is required to meet the SIC budget.

2.2.3.2 RF Canceller Design Trade-offs

Here, we analyze the design trade-offs associated with the integrated canceller in the RF domain.

In Fig. 2.11, an adjacent channel unknown jammer (P_{jam}) together with SI is present at the

[3]This noise floor should also consider the NF increase due to the noise of the RF and analog cancellers, but we have neglected that here for simplicity.

[4]Part of the 12 dB margin can account for the addition of the residual SI, RX and canceller distortion, and the NF increase due to canceller noise for instance.

RX input. Due to the 3^{rd}-order nonlinearity of the LNA, SI cross-modulates with the jammer generating a distortion signal (P_{xmod}) that cannot be canceled:

$$P_{xmod} = 2(P_{TX,main} - ISO - SIC_{RF}) + P_{jam} - 2IIP_{3,LNA}, \tag{2.4}$$

where $P_{TX,main}$ is the average power of the two-tone TX signal, and $IIP_{3,LNA}$ is the LNA IIP3[5]. To ensure that RX noise floor is not degraded, the cross-modulation distortion needs to be well below (6 dB below in our calculation) the noise floor, resulting in a required SIC_{RF} of:

$$SIC_{RF} = P_{TX,main} - ISO - IIP_{3,LNA} + \frac{1}{2}(P_{jam} - P_{NoiseFloor} + 6). \tag{2.5}$$

Current-mode receivers typically employ complementary LNTAs that achieve $IIP_{3,LNA}$ values around +10 dBm. Assuming a conservative $IIP_{3,LNA}$ of +6 dBm, $P_{TX,main}$=+15 dBm, ISO=30 dB, $P_{NoiseFloor}$=−96 dBm, and P_{jam}=−33 dBm[6], SIC_{RF} of ¿14 dB is obtained.

Regarding the RF canceller's linearity requirement, the third-order inter-modulation (IM3) distortion signals ($P_{RX,dis}$) generated by the canceller are assumed to be at the power level of residual SI after RF and analog SIC (see Fig. 2.12). Thus, the required output third-order intercept point (OIP3) of the RF canceller is:

$$OIP_{3,Canc} + CP_{RX} = P_{TX,main} - ISO - 3 + \frac{1}{2}(SIC_{RF}+SIC_{BB}), \tag{2.6}$$

where CP_{RX} is the coupling strength at the RX side.

In Fig. 2.11, the RF SI canceller is a passive structure depicted as consisting of a variable attenuator and a phase shifter, although more sophisticated structures may be required to achieve wideband SIC and gain in the canceller may be required to support low antenna isolation. Since linearity is typically challenging to achieve in scaled CMOS, one may assume that the variable attenuator precedes the other building blocks in the canceller. Assuming the noise figure of the phase shifter is NF_{PS}, the NF of the RX including the RF canceller can be written as:

[5]We assume a current-mode receiver implementation so that the mixer following the LNA is highly linear, and that the jammer is filtered out in the analog baseband. Therefore, the LNA is the main source of cross-modulation distortion.

[6]No full-duplex wireless standard is currently available. P_{jam} is taken from current FDD systems (specifically CDMA [46]).

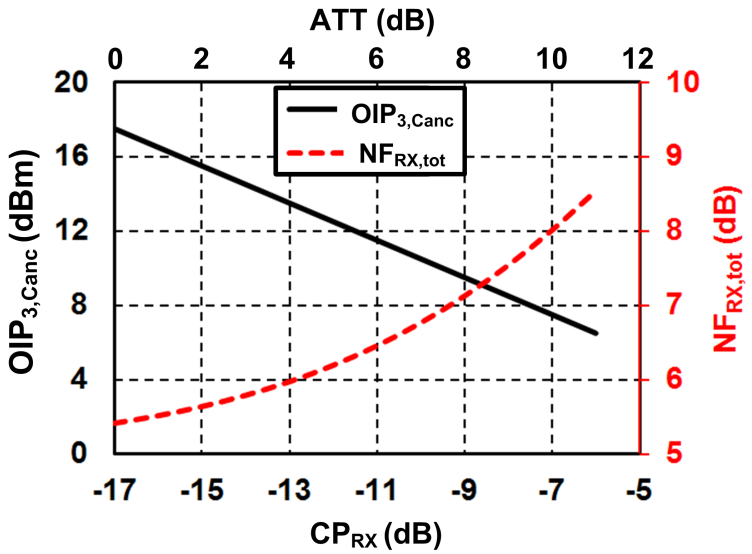

Figure 2.13: Canceller output IP3 ($OIP_{3,Canc}$) and RX overall NF ($NF_{RX,tot}$) including canceller noise versus the coupling strength at the RX side (CP_{RX}).

$$NF_{RX,tot} = 10\log_{10}(10^{NF_{RX}/10} + 10^{(NF_{PS}-IL+CP_{RX})/10}), \tag{2.7}$$

where IL is the implementation loss of the phase shifter. Furthermore, the attenuation of the RF canceller and CP_{RX} can be related to ISO and the TX-side coupling strength (CP_{TX}):

$$ISO = -CP_{TX} - CP_{RX} + ATT + IL, \tag{2.8}$$

where ATT is the attenuation from the variable attenuator. Equations (2.6), (2.7), and (3.1) indicate a design trade-off between the RX NF degradation and the RF canceller linearity requirement. Assuming CP_{TX}=−10 dB, ISO=30 dB, NF_{RX}=5 dB, IL=3 dB, and NF_{PS}=15 dB, canceller OIP3 requirement and receiver overall NF including the RF canceller are plotted in Fig. 2.13 versus CP_{RX}. The specifications used closely match our implementation in [3][4]. For a given ISO, the attenuation that must be achieved in the canceller can be partitioned between ATT and CP_{RX} based on (3.1). $OIP_{3,Canc} + CP_{RX}$ is fixed based on (2.6). As shown in Fig. 2.13, *stronger coupling at the RX side relaxes the canceller linearity requirement. Stronger coupling, however, degrades the RX overall NF performance as more canceller noise couples to the RX input* as seen in (2.7). In our design described in [3][4], CP_{RX}=−10 dB is chosen, resulting in a canceller OIP3 requirement

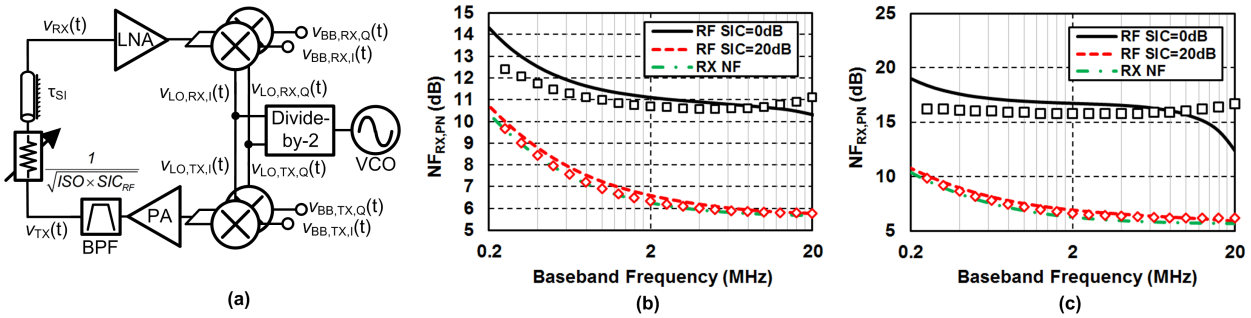

Figure 2.14: (a) Full-duplex transceiver block diagram with TX self-interference cancellation in the RF domain for phase noise analysis. $v_{LO,TX,I}(t)$, $v_{LO,TX,Q}(t)$, $v_{LO,RX,I}(t)$, and $v_{LO,RX,Q}(t)$ are the LO signals. $v_{BB,TX,I}(t)$ and $v_{BB,TX,Q}(t)$ are up-converted and amplified to $v_{TX}(t)$. A BPF at the TX output is assumed to suppress harmonic emissions. $v_{TX}(t)$ leaks to the RX input after antenna isolation and RF SIC through a response modeled as a combination of a magnitude response $1/\sqrt{ISO \times SIC_{RF}}$ and a time delay τ_{SI}. The SI present at RX input ($v_{RX}(t)$) is down-converted obtaining $x_{BB,RX,I}(t)$ and $x_{BB,RX,Q}(t)$. Simulated (lines) and calculated (markers) $NF_{RX,PN}$ for different amounts of SIC_{RF} are plotted in (b) with τ_{SI} =10 ns, and in (c) with τ_{SI} =25 ns. It is assumed that ISO=30 dB, f_{LO}=1.4 GHz, FoM_{VCO}=−185 dBc/Hz, and P_{TX}=15 dBm.

of 10.5 dBm and an expected NF degradation of less than 2 dB.

2.2.3.3 Impact of RF SIC on LO Phase Noise Requirements

Phase noise limits the overall achievable SIC in a full-duplex wireless system when separate local oscillators are used for TX and RX [57]. In an integrated full-duplex radio, a common LO can be shared between TX and RX, and thus phase noise in the TX and the RX path are fully correlated. In practical scenarios, however, there will be some delay between the transmission and reception of the SI introduced by the wireless channel. This delay reduces the correlation between the transmitted and received SI signal and hence limits the subsequent digital cancellation[57].

Fig. 2.14(a) depicts a full-duplex transceiver with SIC in the RF domain. A common LO is shared between the TX and the RX, and the LO signals appearing at the TX and RX mixers are $v_{LO,TX,I}(t)$, $v_{LO,TX,Q}(t)$, $v_{LO,RX,I}(t)$, and $v_{LO,RX,Q}(t)$. The TX BB signals $v_{BB,TX,I}(t) = \cos(\omega_{BB}t + \varphi)$ and $v_{BB,TX,Q}(t) = \sin(\omega_{BB}t + \varphi)$ are up-converted and amplified to $v_{TX}(t)$. The TX signal leaks to the RX input after antenna isolation and RF SIC through a response modeled

as a combination of a magnitude response[7] $1/\sqrt{ISO \times SIC_{RF}}$ and a time delay τ_{SI}. Finally, the SI present at the RX input ($v_{RX}(t)$) is down-converted obtaining the receiver BB signals $v_{BB,RX,I}(t)$ and $v_{BB,RX,Q}(t)$.

Assuming the phase noise at the TX and RX mixers are fully correlated, we have:

$$v_{LO,I}(t) = v_{LO,TX,I}(t) = v_{LO,RX,I}(t) = \cos\left(\omega_{LO}t + \psi_n(t)\right), \tag{2.9}$$

where $\psi_n(t)$ represents the noisy LO phase. Assuming complex up-conversion mixing,

$$v_{TX}(t) = A_{TX}\cos\left(\omega_{RF}t + \psi_n(t) + \varphi\right), \tag{2.10}$$

where A_{TX} is the amplitude of the TX signal and $\omega_{RF} = \omega_{LO} + \omega_{BB}$. The SI can be written as:

$$\begin{aligned} v_{RX}(t) &= \frac{1}{\sqrt{ISO \times SIC_{RF}}}\delta(t-\tau_{SI}) * v_{TX}(t) = \frac{1}{\sqrt{ISO \times SIC_{RF}}}v_{TX}(t-\tau_{SI}), \\ &= \frac{A_{TX}}{\sqrt{ISO \times SIC_{RF}}}\cos\left(\omega_{RF}(t-\tau_{SI}) + \psi_n(t-\tau_{SI}) + \varphi\right). \end{aligned} \tag{2.11}$$

The RX BB signal (normalized to the LNA gain) is:

$$\begin{aligned} v_{RX,BB,I}(t) = v_{RX}(t)\times v_{LO,I}(t) \approx{}& \frac{A_{TX}}{2\sqrt{ISO \times SIC_{RF}}}\cos(\omega_{BB}t - \omega_{RF}\tau_{SI} + \varphi) - \\ & \frac{A_{TX}}{2\sqrt{ISO \times SIC_{RF}}}\left(\psi_n(t-\tau_{SI}) - \psi_n(t)\right)\sin(\omega_{BB}t - \omega_{RF}\tau_{SI} + \varphi), \end{aligned} \tag{2.12}$$

where we've assumed $\psi_n(t-\tau_{SI}) - \psi_n(t) \ll 1$ rad and the presence of a low-pass filter to eliminate the component near the second harmonic. The first term in the RX baseband signal is perfectly correlated with $v_{TX,BB,I}(t)$ and $v_{TX,BB,Q}(t)$, and hence can be subsequently cancelled using analog or digital SIC. However, the second term is uncorrelated with the transmitter baseband signals due to the multiplication with the term $(\psi_n(t-\tau_{SI}) - \psi_n(t))$ that represents random phase noise. Hence, it cannot be cancelled in analog or digital, and will remain as residual SI.

[7] As required by the calculations, all variables represent their raw number (instead of decibel number) unless otherwise mentioned.

Modeling the phase noise as the peak sinusoidal jitter level Φ_n at a frequency offset $\Delta\omega$ ($\psi_n(t) = \Phi_n\cos(\Delta\omega t + \theta_n)$) [58] results in:

$$\psi_n(t-\tau_{SI}) - \psi_n(t) \approx \Phi_n \Delta\omega\tau_{SI}\sin(\Delta\omega t + \theta_n), \tag{2.13}$$

where we've assumed $\Delta\omega\tau_{SI} \ll 1$ rad. Substituting (2.13) into (2.12), the uncorrelated residual SI is

$$\begin{aligned} v_{RX,BB,I,n}(t) &= -\frac{A_{TX}}{2\sqrt{ISO \times SIC_{RF}}}\left(\psi_n(t-\tau_{SI}) - \psi_n(t)\right)\sin(\omega_{BB}t - \omega_{RF}\tau_{SI} + \varphi), \\ &= -\Phi_n\Delta\omega\tau_{SI}\frac{A_{TX}}{2\sqrt{ISO \times SIC_{RF}}}\sin(\Delta\omega t + \theta_n)\sin(\omega_{BB}t - \omega_{RF}\tau_{SI} + \varphi). \end{aligned} \tag{2.14}$$

For simplicity, let us assume ω_{BB}=0 as it eases the visualization of the creation of a phase-noise induced noise floor. The one-sided uncorrelated SI power at frequency offset $\Delta\omega$ is:

$$P_{n,I}(\Delta\omega) \approx \frac{\Phi_n^2\Delta\omega^2\tau_{SI}^2 P_{TX,main}}{8ISO \times SIC_{RF}}, \tag{2.15}$$

where we have used $A_{TX}^2/2 = P_{TX,main}$. Now, we consider phase noise with a power spectral density (PSD) of $\bar{\phi_n^2}$/Hz [50]. Then,

$$\frac{p_n(\Delta f)}{Hz} = \pi^2\frac{\bar{\phi_n^2}}{Hz}\frac{\Delta f^2\tau_{SI}^2 P_{TX,main}}{ISO \times SIC_{RF}} = \frac{2\pi^2\mathcal{L}\{\Delta f\}\Delta f^2\tau_{SI}^2 P_{TX,main}}{ISO \times SIC_{RF}}, \tag{2.16}$$

where $\frac{\Phi_n^2}{2}$ is replaced with $\frac{\bar{\phi_n^2}}{Hz}$, since Φ_n represents the peak jitter amplitude. By definition, the single-side band phase noise at frequency offset Δf is $\mathcal{L}\{\Delta f\} = \Phi_n^2/4 = \frac{\bar{\phi_n^2}/Hz}{2}$. Note that the resultant noise floor $p_n(\Delta f)/Hz$ is flat with respect to Δf if phase noise varies as $1/\Delta f^2$. Now, the RX NF including residual SI noise that arises from the delay-induced decorrelation of LO phase noise (and cannot be cancelled) ($NF_{RX,PN}$) can be calculated as:

$$NF_{RX,PN} = 10\log_{10}\left(10^{NF_{RX}/10} + \frac{4\pi^2\mathcal{L}\{\Delta f\}\Delta f^2\tau_{SI}^2 P_{TX,main}}{kT \times ISO \times SIC_{RF}}\right). \tag{2.17}$$

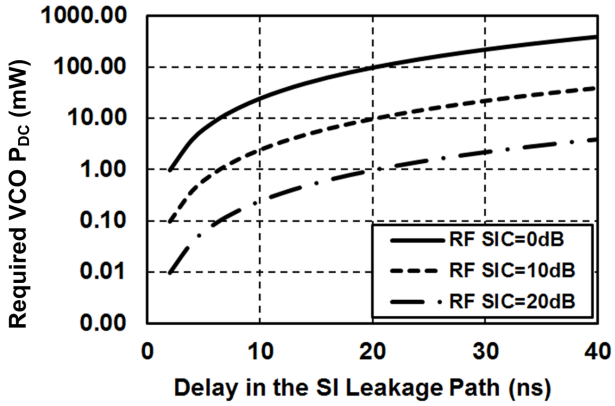

Figure 2.15: Calculated required VCO P_{DC} that ensures that the noise floor resulting from LO phase noise is 6 dB below the RX noise floor versus the amount of delay in the SI leakage path for SIC_{RF}=0 dB, 10 dB, and 20 dB. ISO=30 dB, f_{LO}=1.4 GHz, FoM_{VCO}=−185 dBc/Hz, and P_{TX}=15 dBm.

Both $NF_{RX,PN}$ and NF_{RX} are in decibels. Given 30 dB isolation from the antenna interface (ISO=30 dB), the simulated and calculated $NF_{RX,PN}$ for different amounts of SIC_{RF} are plotted in Fig. 2.14(b) and Fig. 2.14(c) with τ_{SI} =10 ns and τ_{SI} =25 ns, respectively. In simulation, an ideal full-duplex transceiver chain is constructed at 1.4 GHz with $P_{TX,main}$ =+15 dBm. A 2^{nd}-order BPF is included at the TX output to filter out harmonic content and has a quality factor of about 10. As shown in Fig. 2.14, the SI delay is modeled in simulation using an LC-based quasi-distributed transmission line. The RX has a NF of 5.6 dB. 4-phase passive mixers are used at both TX and RX sides. A cross-coupled LC-VCO designed in 65nm CMOS followed by the divide-by-2 divider and 25% duty-cycle LO generation circuitry used in our prototype is used to drive both TX and RX mixers. The 2.8 GHz LC-VCO has a phase noise of −121 dBc/Hz at 1 MHz offset with a DC power consumption of 3.2 mW, resulting in a figure-of-merit (FoM_{VCO}) [59] of −185 dBc/Hz. The VCO $1/f^3$ noise corner is about 100 kHz. As shown in Fig. 2.14(b) and Fig. 2.14(c), the simulation matches calculation well. Without RF SIC, the RX NF is degraded by about 5 dB/10 dB for τ_{SI} =10 ns/25 ns. With 20 dB RF SIC, negligible degradation is observed.

$p_n(\Delta f)/Hz$ can be related to the VCO FoM_{VCO} as:

$$\frac{p_n(\Delta f)}{Hz} = \frac{2\pi^2 f_{LO}^2 \tau_{SI}^2 P_{TX,main}}{ISO \times SIC_{RF}} \frac{FOM_{VCO}}{P_{DC}}, \tag{2.18}$$

where P_{DC} is the VCO power consumption. By setting $p_n(\Delta f)/Hz$ to be 6 dB below the noise floor (i.e. the second term inside the bracket of (2.17) to be 4× below the first term), we can obtain the required P_{DC} (given FoM_{VCO}) such that the LO phase noise will not limit the overall achievable SIC in the full-duplex transceiver. Given ISO=30 dB, f_{LO}=1.4 GHz, FoM_{VCO}=−185 dBc/Hz, P_{TX}=+15 dBm, the required P_{DC} is plotted versus the amount of delay in the SI leakage path in Fig. 2.15, for SIC_{RF}=0 dB, 10 dB, and 20 dB. It can be seen that increasing the SIC_{RF} relaxes the VCO phase noise and power consumption requirement. From Fig. 2.15, 20 dB SIC at RF relaxes the VCO DC power requirement from 24 mW to 0.24 mW assuming 10 ns delay in the SI channel.

Larger delays in the self-interference channel for a given ISO increase the VCO phase noise (and hence power consumption) requirement. For reflections off environmental objects, typically paths that incur larger delay are weaker. In our measurements presented in [4] using a 1.4 GHz antenna pair, the direct coupling path between the TX and RX antennas inside an anechoic chamber has a peak isolation magnitude of 32 dB and peak isolation group delay of 9 ns[8]. While a single reflection or delay path has been considered here for simplicity, in reality, multiple reflections resulting in a delay spread need to be considered. Characterization of the delay spread of typical wireless SI channels, and its usage in conjunction with the formulation presented here to establish the requirements on integrated VCOs and synthesizers is an important future research direction.

Finally, Table 2.1 summarizes the system-level analyses and specifications presented in section 2.2.2.

2.3 SI and Its Mitigation in Multiband FDD Systems

Existing multiband FDD systems rely on numerous fixed-frequency acoustic-filter-based duplexers as depicted in Fig. 1.5(a) which limit the cost and system form factor. Recent research efforts have been making progress towards tunable duplexers [34][35][36] that can be employed to replace the numerous fixed-frequency duplexers. However, the tunable duplexers tend to have less TX-to-RX isolation for the same insertion loss when compared with the fixed-frequency duplexers. This reduced TX-to-RX isolation can result in stringent wireless transceiver requirements.

[8]Due to the tuned nature of the antenna, this group delay is larger than the time delay associated with the physical separation.

Table 2.1: Summary of the specifications for an example full-duplex system.

		Specifications		Measurement Results
		Requirements	Comments	
System Definition	$P_{TX,main}$ (TX output power)	+15 dBm		+15 dBm[1]
	Self-Interference (SI) Bandwidth	20 MHz	BW for LTE	>20 MHz[2]
	NF_{RX} (RX NF without SIC)	5 dB		4.8 to 5.8 dB
	$P_{NoiseFloor}$ (RX noise floor)	-96 dBm	Calculated from NF_{RX} and BW	-96.2 to -95.2 dBm
	P_{jam} (CW jammer power)	-33 dBm	Referred from CDMA standard [46]	-33 dBm
	Total SI Cancellation (SIC)	117 dB	To suppress SI 6 dB below RX noise floor	~52 dB over 27 MHz (ISO + RF SIC)[9]
SIC Budget	ISO (antenna isolation)	30 dB		32 dB[3]
	SIC_{RF}	20 dB	Determined by eq. (2.5)	20 dB over 27 MHz SI BW[9]
	SIC_{BB}	37 dB - SIC_{RF}	Assuming 117dB required total SIC, 30 dB ISO and 50 dB $SIC_{digital}$	Not implemented
	$SIC_{digital}$	50dB	Based on [2][52]	Not implemented
	SI Delay τ_{SI} (SI delay from the direct coupling path)	10 ns		9 ns[3]
Circuit Performance	DR_{ADC}	56 dB	Determined by DR_{ADC}= ($P_{TX,main}$−ISO−SIC_{RF}−SIC_{BB}+6) −($P_{NoiseFloor}$−6)	Not implemented
	In-band $IIP_{3,RX,effective}$ (RX IIP3 with respect to SI under SIC)	+0.5 dBm	Determined by eq. (2.3)	+2 dBm[5]
	$IIP_{3,LNA}$	+6 dBm	Typical value for LNTA.	+17 dBm[6]
	CP_{TX} (coupling strength at TX side)	-10 dB	10% reduction of TX efficiency	-10 dB
	CP_{RX} (coupling strength at RX side)	-10 dB	Determined by eq. (2.6) (2.7) (2.8).	-10 dB[4]
	$OIP_{3,Canc}$ (canceller OIP3)	+10.5 dBm	Determined by eq. (2.6).	N/A[8]
	NF_{filter} (canceller filter noise figure)	15 dB	From filter implementation.	16 dB[4]
	NF degradation under RF SIC	< 2 dB	Determined by eq. (2.7)	1.1 to 1.3 dB
	ATT+IL (total attenuation or loss from the canceller in the RF domain)	10 dB	Determined by eq. (2.8).	12 dB[7]

1. Transmitted power in the RF SIC demonstration measurement shown in Fig. 24. This is also the transmitter power at which other table parameters are reported. Note that higher levels of SI can be canceled at the RX input assuming ISO=30 dB.
2. Maximum achieved 20 dB RF SIC BW in Fig. 20(b) is 25 MHz and the wireless demonstration in Fig. 24 uses 27 MHz.
3. This represents the peak isolation magnitude and group delay of the 1.4GHz antenna pair's direct coupling path.
4. Based on the simulations of the design. 5. Includes canceller IM3 distortion as well. 6. Estimated from RX OOB IIP3 measurement.
7. Calculated as ISO+CP_{TX}+CP_{RX}=32-10-10 dB=12 dB. 8. Canceller IM3 distortion is included in the measured in-band effective IIP3 ($IIP_{3,RX,effective}$).

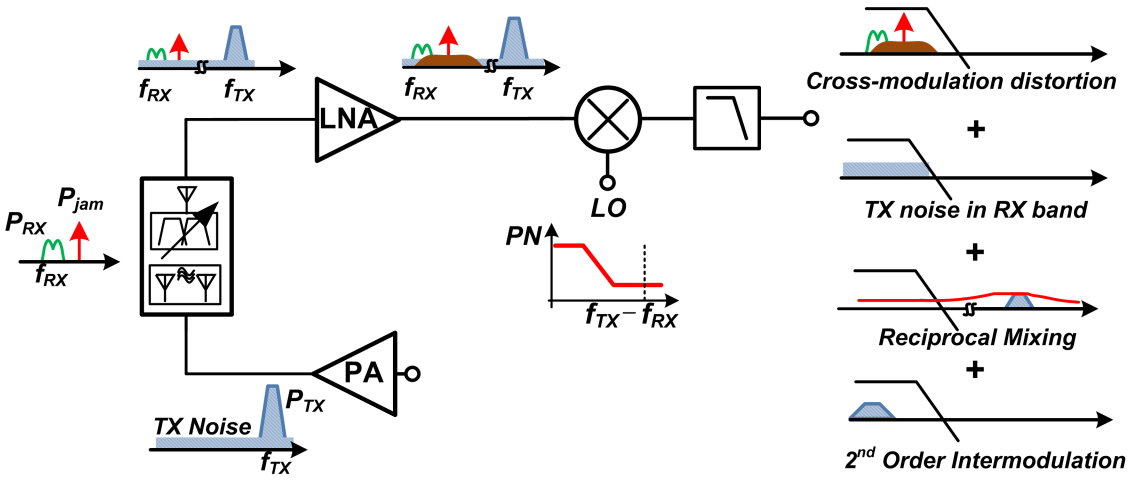

Figure 2.16: Frequency-division duplexing receiver challenges in the presence of strong transmitter self-interference.

To derive the system requirements under reduced TX-to-RX isolation, let us consider a simplified direct conversion RX front-end in Fig. 2.16 detecting a weak signal P_{RX}. The output of a TX on the same platform couples to the RX input through the antenna interface. The TX generates a powerful signal P_{TX} that is outside the RX band as well as a noise floor that extends to the RX band. The TX SI can degrade the receiver performance in several ways (Fig. 2.16). In this thesis, we focus on cross-modulation distortion and TX noise in the RX band. The TX SI can cross-modulate with an in-band CW jammer (P_{jam} in Fig. 2.16), desensitizing the receiver [60; 61]. Modeling the TX signal as two tones, the input-referred cross-modulation product can be calculated as:

$$P_{xmod,in} = 2(P_{TX,avg} - ISO) - 2IIP_3 + P_{jam}, \tag{2.19}$$

where $P_{TX,avg}$ is the average transmitted power, ISO is the TX-to-RX isolation, and IIP_3 is the RX OOB input-referred third-order intercept point. Note that all quantities are expressed in dB scale. We assume a desired SNR of 7 dB, signal bandwidth of 2 MHz, in-band jammer power of -30 dBm and peak PA output power of $+24$ dBm. For a receiver with 5 dB NF, the sensitivities based on the individual contributions of cross-modulation distortion and TX noise in the RX band are plotted in Fig. 2.17. For 55 dB isolation, offered by current fixed-frequency duplexers, OOB IIP_3 of $+10$ dBm is sufficient for -100 dBm sensitivity. However, for a reduced isolation of 25 dB,

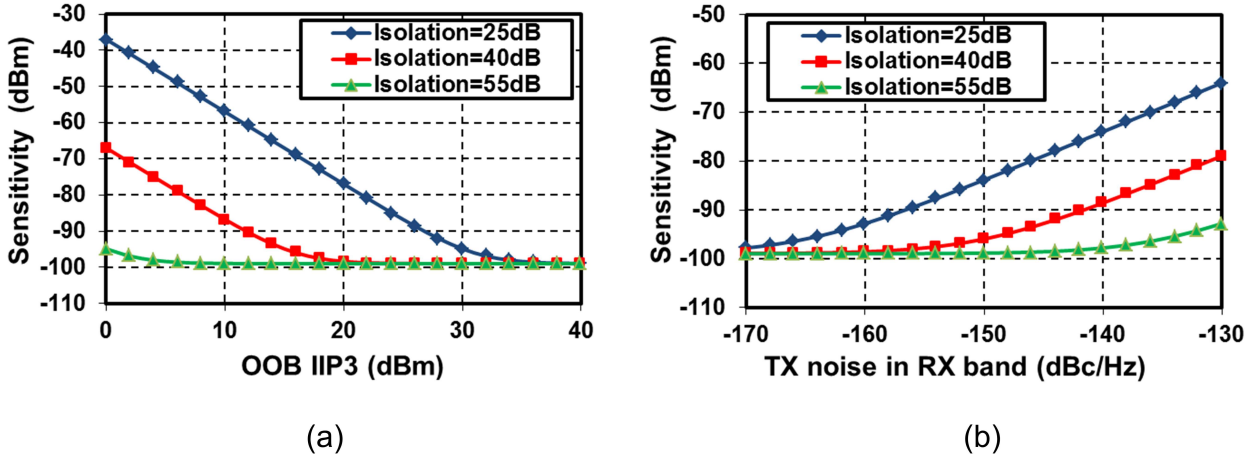

Figure 2.17: Receiver sensitivity with varying TX-to-RX isolation for different (a) out-of-band IIP3 levels and (b) levels of TX noise in RX band. Desired SNR of 7 dB, signal BW of 2 MHz, an in-band CW jammer power of −30 dBm, peak PA output power of +24 dBm and RX NF of 5 dB are assumed.

enabling low-cost/compact/tunable front-end modules, receiver OOB IIP_3 greater than +30 dBm is required. A stringent requirement of −170 dBc/Hz is seen for the RX-band TX noise as well.

2.3.1 Trade-offs and Benefits Associated with RF SIC for FDD

Knowledge of the SI enables SIC in the RF domain that can relax the aforementioned stringent wireless transceiver requirements in FDD systems. A natural question is whether the active canceller DC power consumption may be used in the original RX to achieve equivalent performance [9]. We investigate this fundamental question in this section.

First, let us consider a RX without RF SIC in Fig. 2.18(a) and assume a two-tone signal for the TX signal. Using (2.19) and assuming that the receiver is linear enough to keep the cross-modulation distortion products at the RX sensitivity level, the required OOB IIP_3 is:

$$IIP_3 = (P_{TX,avg} - ISO) + \frac{1}{2}(P_{jam} - P_{sen}), \tag{2.20}$$

where P_{sen} is the receiver sensitivity and we've assumed that only one of the two cross-modulation

[9] As discussed in Chapter 3, active RF SIC has the advantages of being area efficient, more amenable to silicon integration, and widely tunable when compared with passive SIC approaches.

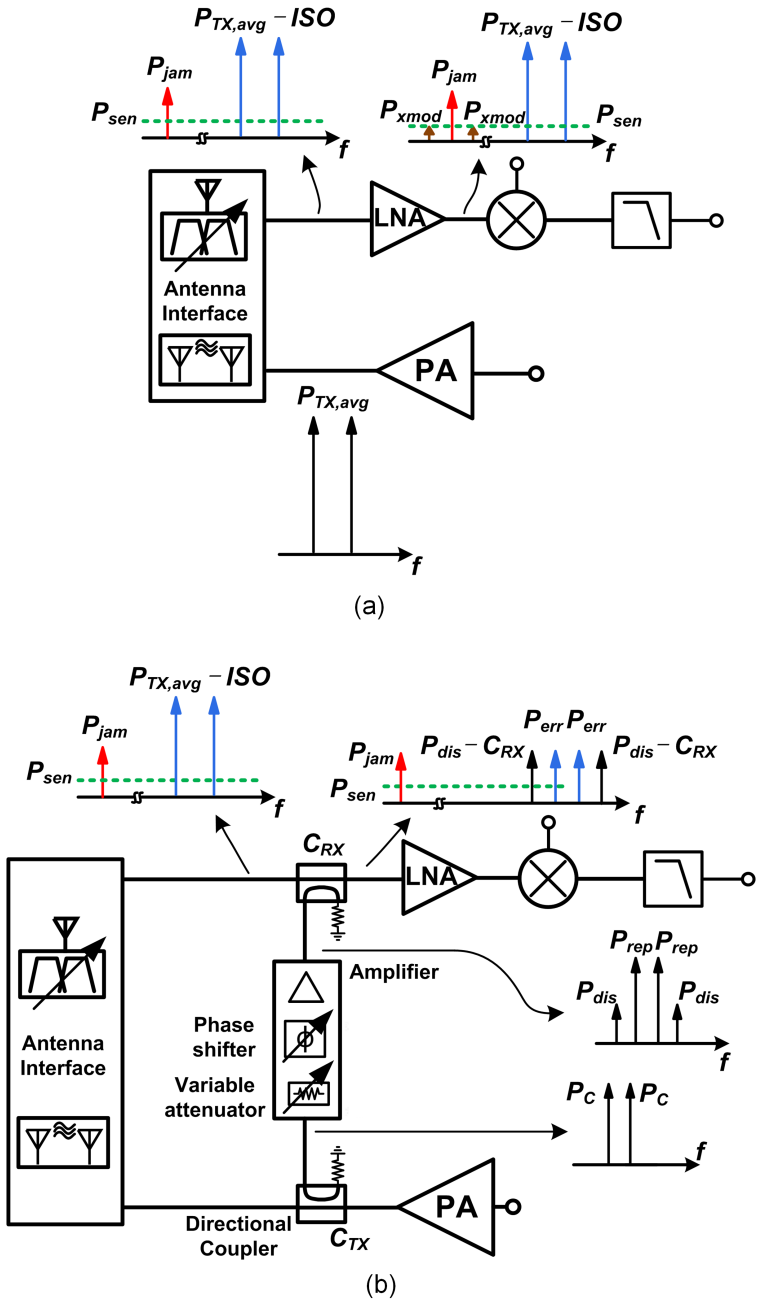

Figure 2.18: Transceiver block diagram with a two-tone TX self-interference signal along with an in-band CW jammer at the input of the receiver: (a) without RF self-interference cancellation, and (b) with a generic RF self-interference cancellation.

tones falls on top of the desired signal.

Now consider a RX with RF SIC shown in Fig. 2.18(b). A portion of the TX signal is coupled from the PA output. The TX replica signal is then adjusted in amplitude and phase, and subtracted at the RX input using another coupler. The total gain of the canceller which consists of a lossy variable attenuator, a phase shifter, and an amplifier is $G_{Canceller}$. The amplifier is used to partially compensate for the coupling ratios of the couplers (C_{TX} and C_{RX}) and implementation losses in the canceller. C_{TX} must be high to avoid degrading PA efficiency and is assumed to be 15 dB. The finite linearity of the canceller will generate IM3 tones at the RX input. These IM3 tones as well as the residual TX SI due to finite SIC can still cross-modulate with the jammer. The canceller should have sufficient linearity to keep the distortion tones at the level of the residual SI – a further increase in the canceller power consumption would not help, since the sensitivity would dominated by cross modulation products generated by the residual SI. Note that the extent of RF SIC is limited by the selectivity of the antenna interface and we will explain this in detail later in Chapter 3. Nevertheless, with these design guidelines, the canceller IIP_3 is:

$$IIP_{3,Canceller} = P_C + \frac{1}{2}(P_{rep} - P_{dis}) \approx P_{TX,avg} - ISO - 3 + C_{RX} - G_{Canceller} + \frac{1}{2}SIC_{RF}, \quad (2.21)$$

where P_C is the coupled signal power from the PA at the input of the canceller, P_{rep} is the power of the cancellation signal at the output of the canceller, and P_{dis} is the power of the 3^{rd} order distortion produced by the canceller. Each of them represents the power of one tone of a two-tone signal. We have assumed that the cancellation signal has approximately the same power as the SI ($P_{rep} \approx P_{TX,avg} - ISO - 3 + C_{RX}$). The gain of the canceller $G_{Canceller} = P_{rep} - P_C$, and consequently $P_C \approx P_{TX,avg} - ISO - 3 + C_{RX} - G_{Canceller}$. $SIC_{RF} = P_{TX,avg} - ISO - 3 - P_{err}$ is the amount of SIC in dB scale. The canceller is designed so that the 3^{rd} order distortion tone at the RX input ($P_{dis} - C_{RX}$) is equal to the residual TX leakage (P_{err}). Therefore, we have $SIC_{RF} \approx P_{rep} - P_{dis}$.

At the same time, the relaxed receiver OOB IIP_3 after the RF SIC is:

$$IIP_{3,relaxed} = P_{TX,avg} - ISO - SIC_{RF} + 3 + \frac{1}{2}(P_{jam} - P_{sen}). \quad (2.22)$$

The additional 3 dB in (2.22) comes from the cross-modulation distortion produced by P_{dis}.

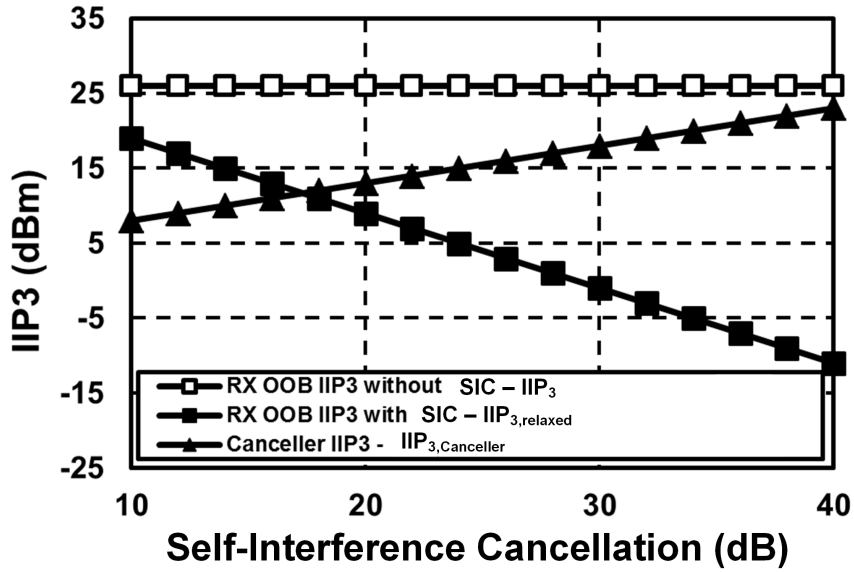

Figure 2.19: Required RX OOB IIP3 with or without RF self-interference cancellation and required canceller IIP3 ($P_{TX,avg}$ = +21 dBm, ISO = 25 dB, IL = 5 dB, G_{Amp} = 5 dB, C_{RX} = 10 dB, C_{TX} = 15 dB, P_{jam} = −30 dBm and P_{sen} = −90 dBm).

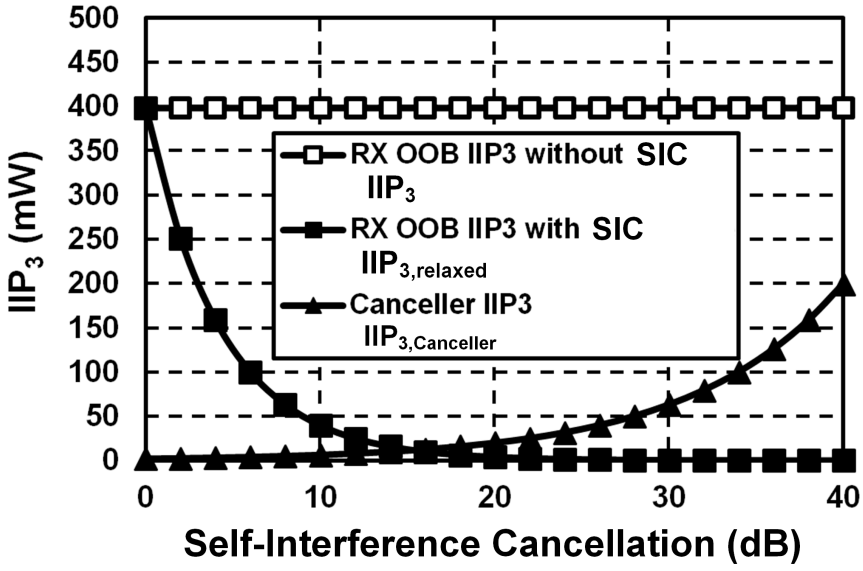

Figure 2.20: Required RX OOB IIP3 plotted in a linear scale with or without RF self-interference cancellation and required canceller IIP3.

Given $P_{TX,avg} = +21$ dBm, $ISO = 25$ dB, $G_{Canceller} = 0$ dB, $C_{RX} = 10$ dB, $P_{jam} = -30$ dBm and $P_{sen} = -90$ dBm, we plot (2.20), (2.21) and (2.22) as a function of RF SIC in Fig. 2.19. In Fig. 2.19, the calculated RX OOB IIP_3 without RF SIC is +26 dBm, while with RF SIC of 20 dB, the RX OOB IIP_3 is relaxed to +9 dBm, while the canceller IIP_3 must be +13 dBm. Assuming that the linearity performance of the RX and RF SI canceller can be traded with their power consumption in a linear fashion based on a RX figure-of-merit (FoM) defined in [62], we plot Fig. 2.19 again using a linear scale as shown in Fig. 2.20. Assuming similar NF requirements for the RX and RF SI canceller with and without SIC (which will be verified later in Chapter 3), it is clear that the combination of a RX and a RF SI canceller consumes much less power than a RX alone that is designed to handle the powerful TX SI. *Fundamentally, this is because the RF SI canceller dramatically relaxes the RX linearity requirement. While the canceller has to handle a large replica signal, it has a significantly lower DR requirement than a RX without SIC as it does not handle the weak desired signal. Hence its distortion does not need to be below the sensitivity level.* Another advantage of active cancellation is that the canceller can be deactivated to save power when the TX is off or operating at low output power levels.

Chapter 3

A Review of Self-Interference Cancellation Techniques

A variety of SIC architectures have been reported for full-duplex and FDD wireless communication systems. A review of reported SIC architectures is presented in Section 3.1. Section 3.2 discusses the existing implementations of SIC in the RF domain. Finally, the fundamental challenges associated with the existing SIC techniques are identified, motivating the need for integrated SIC solutions that can handle powerful SI with negligible receiver desensitization, support a wide SIC bandwidth, and allow compact full-duplex radio implementations with SIC across the antenna, analog/RF, and digital domains.

3.1 Self-Interference Cancellation Architectures

A generic self-interference-cancelling full-duplex transceiver with SI isolation at the antenna interface is depicted in Fig. 3.1. For SIC, a replica of the transmitted signal is first obtained from the TX side, then the TX replica is adjusted based on the SI channel response, and finally the processed replica is injected at the RX side. As depicted in Fig. 3.1, the tapping points at the TX side can be freely chosen in the RF, analog, and digital domains, and so can the injection nodes at the RX side; this freedom results in a variety of SIC architectures.

Several recently-reported SIC architectures are shown in Fig. 3.2. As is shown in Fig. 3.2(a)-(c), the TX replica signal is often tapped at the output of the PA so that the replica contains

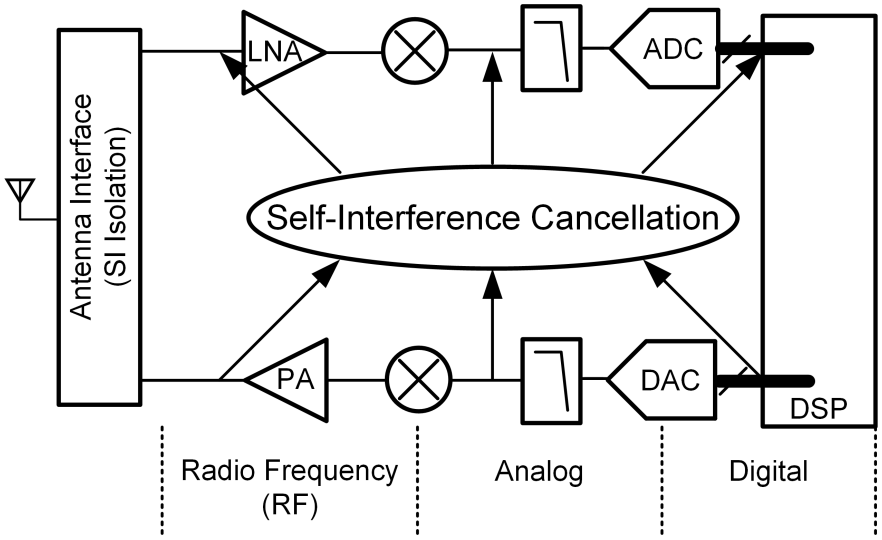

Figure 3.1: A generic self-interference-cancelling full-duplex transceiver with self-interference isolation at the antenna interface.

the distortion and noise from the entire TX chain, allowing cancellation of the TX nonidealities at the RX side. Figure 3.2(a) depicts a common SIC architecture employed in full-duplex radios that aim for $>+15$ dBm TX output power and a < -90 dBm noise floor [2][7][4]. Given moderate (20-to-30 dB) isolation from the antenna interface, residual SI of at least -15 dBm to -5 dBm can be present at the RX input, imposing an extremely stringent linearity requirement on the RX. To relax the RX linearity requirement, cancellation signals are injected at the input of the RX as depicted in Fig. 3.2(a). For full-duplex radios that target wireless applications with relaxed noise figure requirements, the cancellation signal can be injected at the output of a passive mixer in a mixer-first RX as shown in Fig. 3.2(b) [8]. This topology results in superior RX in-band linearity performance thanks to the mixer-first RX [54]. A TX noise cancellation architecture is reported in [63] where the cancellation signal tapped at the PA output is injected in the digital domain at the RX side (see Fig. 3.2(c)). Note that [63] targeted the cancellation of TX noise in the RX band for FDD applications. It is unlikely that such an architecture is viable for FD as the entire RF/analog portion of the RX chain is exposed to the residual SI after the antenna isolation.

Alternatively, TX replica signals can be obtained from the digital domain, resulting in a mixed-signal SIC architecture as depicted in Fig. 3.2(d) [29]. In this mixed-signal SIC architecture, a separate SIC chain that consists of a DAC and an up-conversion-based SI canceller is used to

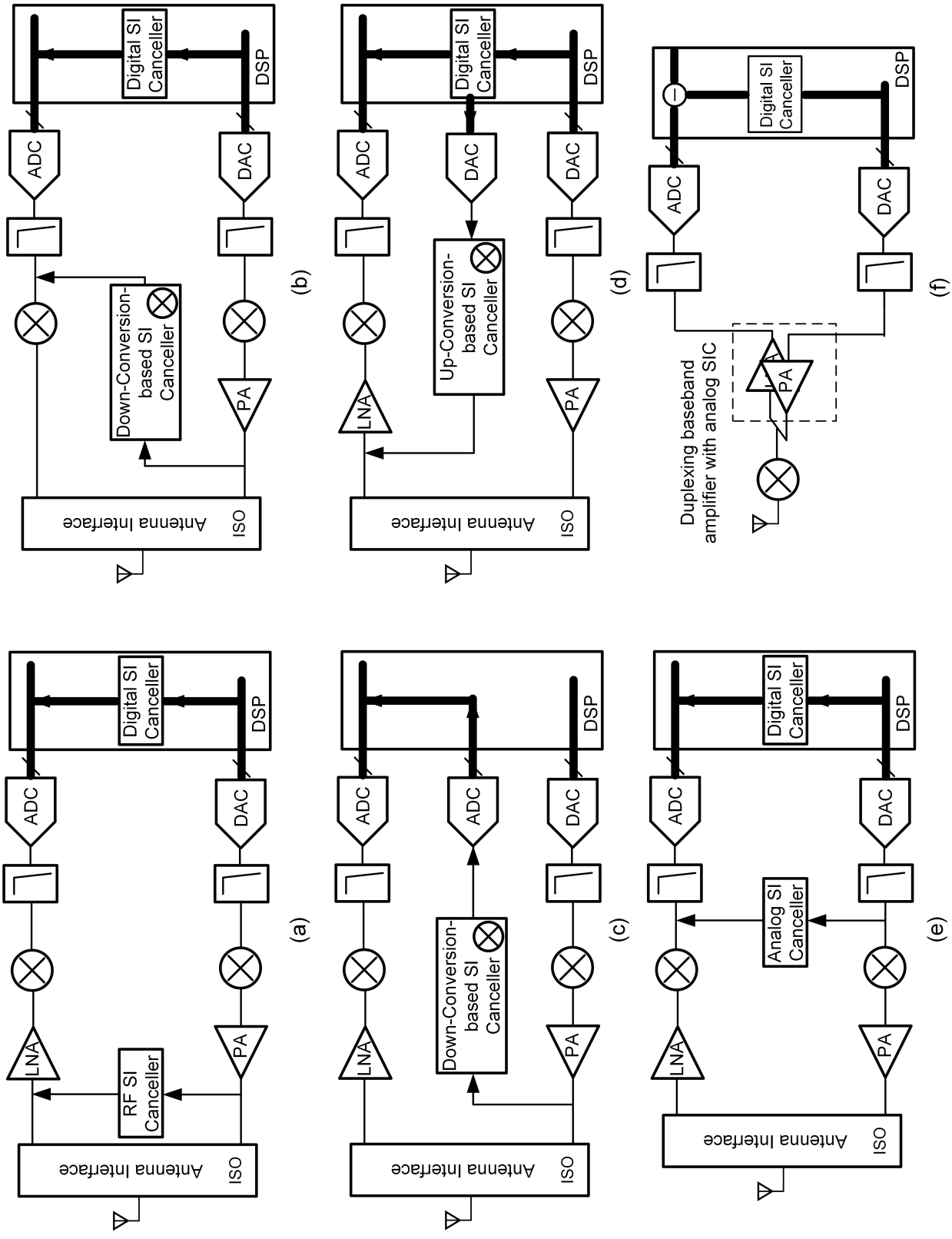

Figure 3.2: Recently-reported SIC architectures.

perform SIC at the RX input. TX replica signals are processed in the digital domain to emulate the SI channel response; therefore, this architecture can leverage the capability of modern CMOS technology nodes to implement efficient digital signal processing. However, this mixed-signal SIC requires estimation and recreation of the nonlinearity of the entire TX chain, which can be power hungry, and cannot cancel TX noise. It should be mentioned that the passive mixer output stage limits the output power and the efficiency achievable in the TX. The lack of isolation in the antenna interface also limits the TX power at which effective duplexing can be achieved.

Figures 3.2(e) and (f) illustrate SIC architectures that have been reported for short-range full-duplex applications [52][9]. With reduced TX output power (and correspondingly reduced PA distortion), an analog SI canceller which taps from the TX analog baseband and injects cancellation signals at the RX analog baseband can be utilized to replace an RF SI canceller, resulting in lower RX NF and TX efficiency degradation. Fig. 3.2(f) shows a short-range full-duplex radio with relaxed SIC budget (overall 80 dB SIC is budgeted in [9]). The TX and the RX share a passive mixer as the (common) antenna interface, resulting in a compact and widely tunable full-duplex implementation. To relax the RX and analog-to-digital converter dynamic range requirements, analog SIC is performed within an analog baseband duplexing amplifier [9].

3.2 Self-Interference Cancellation in the RF Domain

Among the SIC architectures discussed in the previous section, SIC in the RF domain (such as the RF SIC in Fig. 3.2(a)), where a replica signal is tapped from the TX output and injected prior to RX down-conversion, has been used in many full-duplex and FDD wireless systems [2][7][4][64][65][66][67]. The benefit of SIC in the RF domain (as discussed in Chapter 2) is that the cancellation signal includes all the nonidealities coming from the TX chain. Furthermore, the earlier the SIC, the more relaxed is the RX front-end linearity requirement.

3.2.1 RF SIC with Passive or Active Circuitry

SIC in the RF domain may be pursued using passive or active circuitry. Passive RF SIC (Fig. 3.3(a)) requires bulky LC-based [65] or transmission line-based [68] cancellation paths that are not amenable to silicon integration and wideband/tunable operation. Absence of some gain in the cancellation

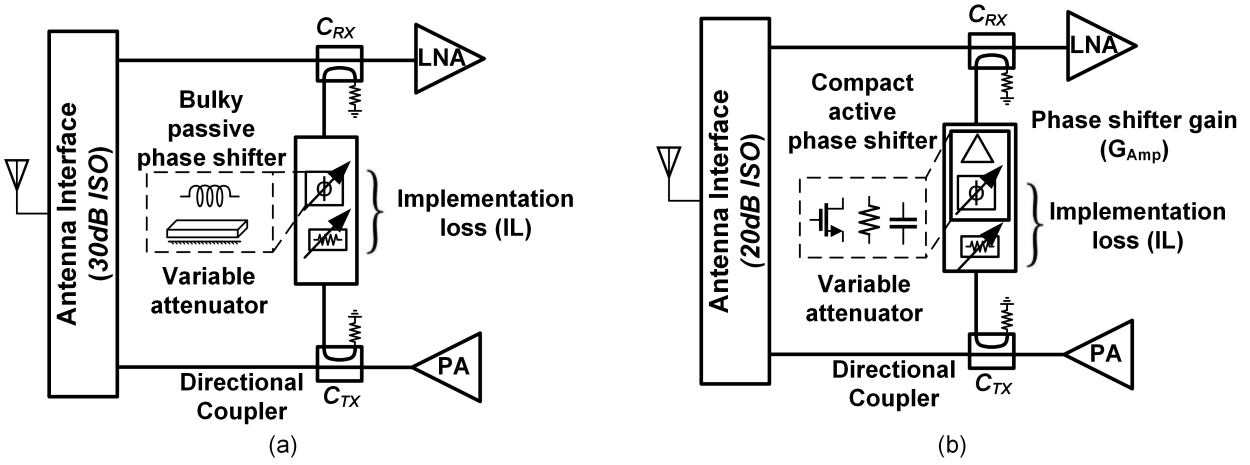

Figure 3.3: SIC in the RF domain using (a) passive circuitry with a variable attenuator and a bulky passive phase shifter, or (b) active circuitry with a variable attenuator, a compact active phase shifter. The presence of some gain in the cancellation path enables cancellation across antenna interfaces with low inherent isolation.

path also prevents support for antenna interfaces with low inherent isolation due to inevitable losses in coupling a replica signal out of the TX and into the RX and in the canceller itself. Active RF SIC (Fig. 3.3(b)) has the advantages of being area efficient, more amenable to silicon integration and widely tunable when compared with passive SIC approaches. Furthermore, the presence of some gain in the cancellation path enables cancellation across antenna interfaces with low inherent isolation. Note that an antenna interface typically can trade its TX-to-RX isolation for a more compact size and/or lower cost.

A generic active RF SIC approach is shown in Fig. 3.3(b), where a portion of the TX signal is coupled from the PA output. The TX replica signal is then adjusted in amplitude and phase, and subtracted at the RX input using another coupler. To partially compensate for the coupling ratios of the couplers (C_{TX} and C_{RX}) and implementation losses (IL) in the canceller, the active phase shifter includes amplification of G_{Amp}. Thus, the total gain of the canceller can be written as $G_{Canceller} = G_{Amp} - IL$. C_{TX} must be high to avoid degrading PA efficiency[1] and is assumed to be 15 dB. The required gain G_{Amp} can be related to ISO in the dB scale as

[1]In this discussion, the coupling ratios and the antenna isolation are assumed to be positive numbers.

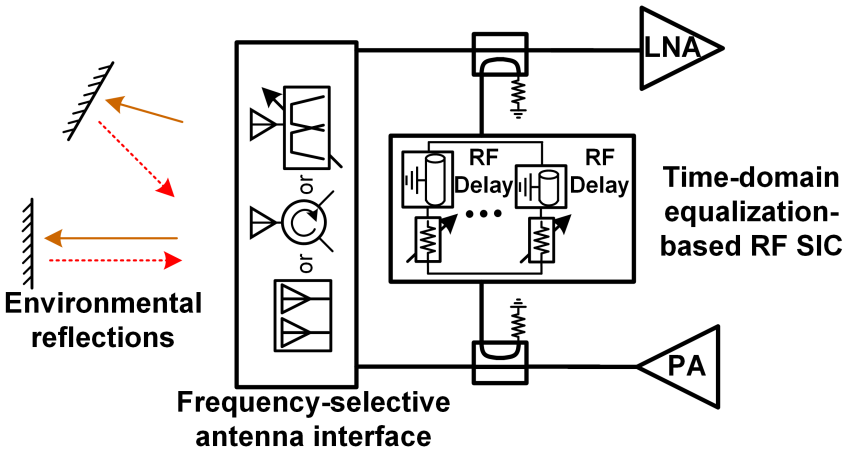

Figure 3.4: SIC in the RF domain based on time-domain equalization using true time delays [2]

$$ISO = C_{TX} + C_{RX} - G_{Canceller} = C_{TX} + C_{RX} - G_{Amp} + IL. \tag{3.1}$$

Assuming C_{TX}=15 dB, C_{RX}=10 dB, and IL=5 dB, 10 dB gain is required to support antenna interfaces with as low as 20 dB isolation (for instance, the miniature circulator in [13]). On the other hand, if passive SIC is used, the minimum supported antenna interface isolation is 30 dB (G_{Amp}=0 dB).

3.2.2 Equalization-based Wideband RF SIC

The SI channel at RF often includes a frequency-selective antenna interface (a circulator, an antenna pair, or a duplexer) and environmental reflections as depicted in Fig. 3.4. Because of the frequency selectivity difference, a frequency-flat amplitude- and phase-based RF canceller shown in Fig. 3.3 cannot emulate a frequency-selective SI channel over a wide frequency range, resulting in a limited RF SIC BW [64][56]. Equalization of a frequency-selective SI channel can be performed based on time-domain equalization. In [2] and as illustrated in Fig. 3.4, multiple on-PCB transmission-line delays and variable attenuators are used in a time-domain equalization approach, essentially implementing an RF Finite Impulse Response (FIR) filter.

3.3 Fundamental Challenges Associated with Self-Interference Cancellation

3.3.1 Noise and Distortion Associated with Active RF SIC

As mentioned earlier, RF SIC using active circuitry is more amenable to silicon integration and can support antenna interfaces with less TX-to-RX isolation when compared with SIC using passive circuitry. However, previously reported integrated (CMOS-based) active RF SIC works typically do not relax the RX input linearity requirement and/or are limited to SI levels of -25 to -28 dBm [64][67].

The fundamental challenge associated with active RF SIC is the degradation of RX performance due to the noise and distortion of the active devices in the canceller, particularly when designed to handle powerful SI and performed at the RX input. Consider the generic active RF SIC shown in Fig. 3.3(b). If the NFs of the canceller and the RX are $NF_{Canceller}$ and NF_{RX} respectively, the NF of the RX including the canceller can be calculated as

$$NF_{RX,tot} = 10log_{10}(10^{NF_{RX}/10} + 10^{(NF_{Canceller}+G_{Amp}-IL-C_{RX})/10}), \tag{3.2}$$

From (3.2) and (3.1), a larger value of C_{RX} protects the receiver from NF degradation due to the canceller but requires greater ISO to be achieved in the antenna interface. Assuming $NF_{RX} = 3\ dB$, $NF_{Canceller} = 12\ dB$, $C_{TX} = 15\ dB$, $C_{RX} = 10\ dB$, $IL = 5\ dB$, the $NF_{RX,tot}$ and ISO are plotted versus G_{Amp} in Fig. 3.5. In order to support antenna interfaces with as low as 25-20 dB isolation (for instance, the miniature circulator in [13]), 5-10 dB gain is required in the canceller amplifier but the overall NF will degrade by 2.5-5.5 dB. *Therefore, there exists a fundamental trade-off between support for low antenna interface isolation levels (or equivalently, power of TX SI being cancelled) and RX NF degradation.*

3.3.2 Bandwidth Limits for Integrated RF SIC

Equalization-based RF SIC has the advantage of being able to emulate frequency-selective SI channel responses over a wide frequency range for wideband cancellation. *However, for time-domain-equalization-based RF SIC (e.g., the one in [2]), generation of significant (nanosecond-scale) true*

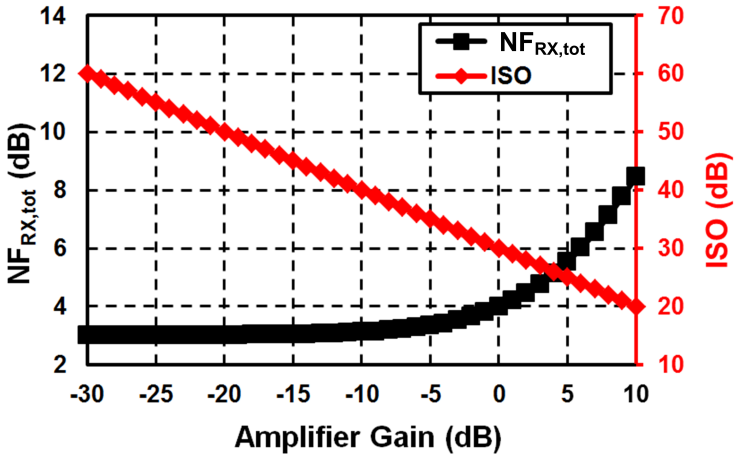

Figure 3.5: Total RX NF and minimum supported inherent antenna interface isolation as a function of canceller amplifier gain. There exists a fundamental trade-off between support for low antenna interface isolation levels and RX NF degradation.

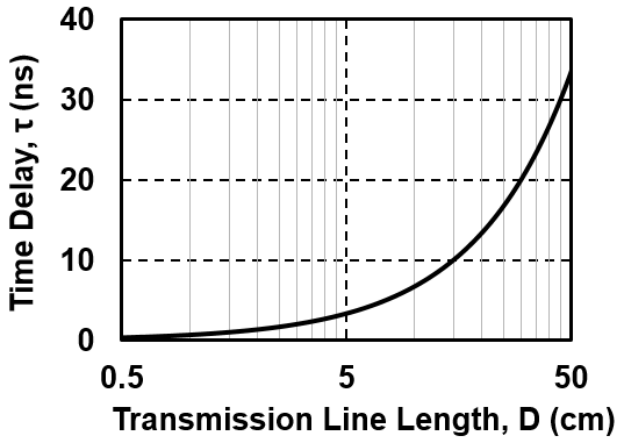

Figure 3.6: The amount of time delay versus required transmission line length in silicon dioxide. To have 10 ns delay, a transmission line with length of 15 cm is needed which is too bulky and lossy to be integrated on silicon.

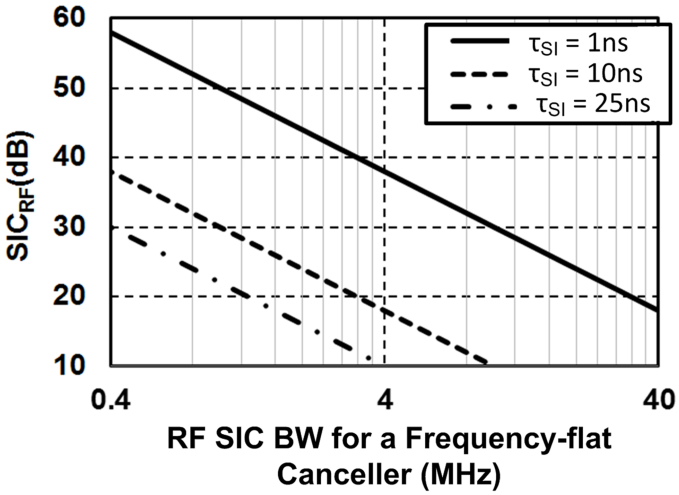

Figure 3.7: Calculated RF SIC BW for a given worst-case RF SIC and a frequency-flat amplitude- and phase-based canceller using (3.3) across various SI channel delays.

time delay on silicon is fundamentally challenging due to the length of the transmission lines required and the lossy nature of the silicon substrate [69]. Figure 3.6 plots the amount of time delay versus required transmission line length in silicon dioxide; to have 10 ns delay, a transmission line with length of 15 cm is needed which is too bulky and lossy to be integrated on silicon.

Equalization of a frequency-selective SI channel can be performed in the digital domain as well, and a dedicated cancellation path can up-convert the TX replica signal to RF to perform SIC (see Fig. 3.2(d)) [29]. However, to suppress the TX distortion signals, this approach requires a re-creation of the nonlinearity characteristics of the entire TX chain. Moreover, this approach is not able to cancel the noise from the TX chain.

Because of the aforementioned fundamental challenges associated with existing equalization-based RF SIC techniques, most reported *integrated* RF SI cancellers don't have equalization functionality and purely rely on amplitude-and-phase scaling. Consider a wireless transceiver with a frequency-selective antenna interface (such as an antenna pair, a circulator or a duplexer) and a frequency-flat amplitude- and phase-based RF canceller depicted in Fig. 3.3. For simplicity, let us model the antenna interface response ($H_{SI,model}(j\omega)$) with a flat magnitude response but a constant group delay as $H_{SI,model}(j\omega) = A_0\exp(-j(\omega-\omega_0)\tau_{SI} + j\phi_0)$. A_0 is the flat magnitude response, τ_{SI} is the isolation group delay, and ϕ_0 is the phase at frequency ω_0. For the frequency-flat RF

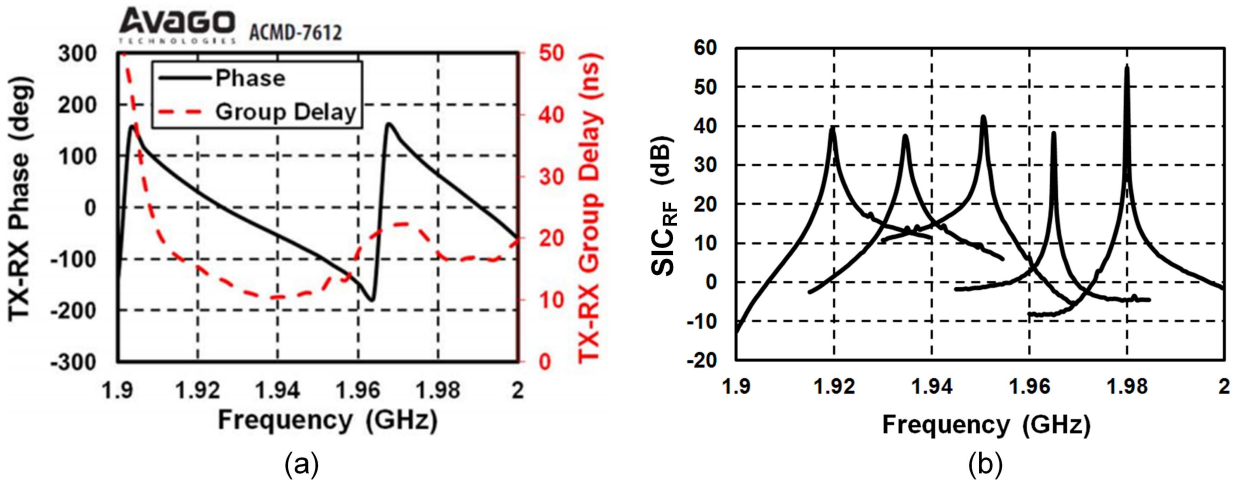

Figure 3.8: (a) Measured isolation phase and group delay of an Avago ACMD-7612 miniature UMTS band-I duplexer, and (b) measured small-signal RF SIC across the entire TX passband of the Avago duplexer.

canceller, the transfer function (TF) $\hat{H}_{flat}$ can be written as $\hat{H}_{flat}(j\omega) = A_C \exp(+j\phi_C)$[2]. A_C and ϕ_C are the frequency-flat magnitude and phase responses of the canceller. To achieve RF SIC centered at ω_0, one needs to set $A_C = A_0$ and $\phi_C = \phi_0$. One can then write an equation for the residual SI across ω, and assuming $(\omega - \omega_0)\tau_{SI} \ll 1$ rad, write an equation for the RF BW (ω_{BW}) within which the worst case SIC is SIC_{RF}. We obtain:

$$\omega_{BW} = \frac{2}{\sqrt{SIC_{RF}}\tau_{SI}}. \tag{3.3}$$

SIC_{RF} is plotted versus f_{BW} in Fig. 3.7 for τ_{SI} =1 ns, 10 ns, and 25 ns. For SIC_{RF}=20 dB, the supported SI RF BWs are 31 MHz, 3 MHz, and 1.2 MHz, respectively.

To verify the theoretical analysis, small-signal SIC is measured across the entire TX pass-band of an Avago ACMD-7612 miniature UMTS band-I duplexer [70] using our self-interference-cancelling RX reported in [56]. In the TX band (1.92-1.98 GHz) of this Avago duplexer, we measured an isolation magnitude that varies from 40-50 dB with 10-20 ns group delay[3] (as shown in Fig. 3.8(a)).

[2]The hat above the transfer function is used to signify a canceller that is attempting to approximate an antenna interface.

[3]Although such a duplexer does not require SIC due to its high initial isolation, duplexers with relaxed isolation

Table 3.1: Comparison of antenna interfaces for full-duplex radios.

	Antenna Pair [55][71]	Shared-Antenna Interface		
		Reciprocal electrical-balance duplexer [72][73]	Non-reciprocal ferrite circulator [13]	Non-reciprocal active circulator [9][74]
Form Factor	✗	✓	✗	✓
Insertion Loss	✓	✗	✓	✓
Noise/ Linearity	✓	✗ / ✓	✓	✗
Channel Reciprocity	✗	✓	✓	✓
CMOS Integration	✓	✓	✗	✓

In Fig. 3.8(b), the measured 20 dB SIC BW ranges from 1 to 7 MHz which matches reasonably well with the predictions from (3.3).

3.3.3 SIC Across Multiple Domains

Suppressing the tremendous amount of TX SI below the RX noise floor in full-duplex wireless systems is fundamentally challenging. Short-range wireless applications relax FD system requirements [8][9][52], but a full-duplex system with −6 dBm transmit power, 10 MHz signal bandwidth and 12 dB NF budget still requires 86 dB of SI suppression to reach the −92 dBm noise floor. To achieve such a high degree of SI suppression, cancellation must be performed across the antenna[71][55], analog/RF[56][4][65][66][8][71], and digital domains[52][2] as discussed in Chapter 2.

While across-domain SIC breaks a formidable amount of overall cancellation into several manageable pieces, it has several challenges. In a cascaded across-domain SIC system, the successive cancellation can become a difficult task if the previous cancellation is optimized individually, as the successive cancellers work on the extremely frequency-selective residual SI. A joint-SIC approach that unites all SI cancellers across domains is desirable. In addition, it has been shown in [57] that phase noise can limit the overall suppression for across-domain SIC. Therefore, SIC must be judiciously distributed across all domains based on the transceiver architecture and the LO phase noise performance to ensure that the required total SIC is achieved.

3.3.4 Integrated Antenna Interface For Full-Duplex Wireless

Another fundamental challenge is related to the full-duplex antenna interface. As shown in Table 3.1, reported full-duplex antenna interfaces can be divided into three categories, namely antenna pairs[71][55], electrical-balance duplexers[72][73] and non-reciprocal circulators[13][74][9]. Among them, shared-antenna interfaces such as the electrical-balance duplexers and circulators are more favorable as they enable compact form factor, translate easily to MIMO and antenna diversity applications, and ease system design through channel reciprocity. However, reciprocal full-duplex shared-antenna interfaces, such as electrical-balance duplexers [72][73], feature a fundamental minimum of 3 dB loss (typically higher when parasitic losses are factored in). Passive non-reciprocal circulators typically require the use of magnetic materials (ferrites [13]), making them bulky, expensive, and not amenable to CMOS integration. Circulators that exploit the inherent non-reciprocity of active devices [74][9] are limited by the noise and nonlinearity introduced by the active devices [75]. In other words, *the realization of compact CMOS-compatible full-duplex shared-antenna interfaces with low loss, low noise, high linearity, and high TX-to-RX isolation is an important open challenge.*

of 20-30 dB can still exhibit >10 ns group delay (such as the one reported in [4]).

Chapter 4

A Noise-Cancelling and Self-Interference-Cancelling Receiver

As discussed in Chapter 3, SIC in the RF domain using active circuitry has the advantages of being area efficient, more amenable to silicon integration and widely tunable when compared with passive SIC approaches. The fundamental challenge associated with active RF SIC is the degradation of RX performance due to the noise and distortion of the active devices, and there exists a fundamental trade-off between support for low antenna interface isolation levels (or equivalently, the power of TX SI being cancelled) and receiver sensitivity degradation. This chapter introduces a noise-cancelling, self-interference-cancelling (NC-SIC) RX [76][56] that breaks this fundamental trade-off through the insight that *unlike discrete-component-based designs that naturally utilize a block-by-block partitioned design strategy, the design of integrated SI-cancelling RXs enables co-design opportunities that can result in enhanced system performance. In the NC-SIC receiver, an active SI canceller is embedded and co-designed within a noise-cancelling receiver.*

This Chapter is organized as follows. The block-by-block partitioned design strategy is briefly discussed in Section 4.1. Section 4.2 presents the evolution of the NC-SIC RX architecture for multi-band FDD wireless communications systems. Noise analysis of the NC-SIC RX is described in Section 4.3. Section 4.4 discusses distortion cancellation in the proposed NC-SIC RX based on a current-mode receiver OOB linearity analysis. Sections 4.5 and 4.6 discuss circuit implementations and measurement results, respectively. Section 4.7 summarizes the Chapter. While the NC-SIC

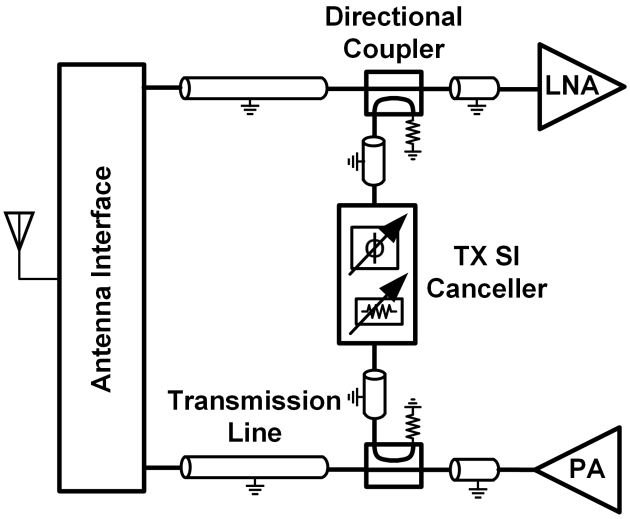

Figure 4.1: Diagram of a discrete-component-based RF front-end that adopts a block-by-block partitioned design methodology. On one hand, this methodology enables the experimental determination of input and output port parameters without the need to know the internal block details. On the other hand, this methodology misses many degrees of design freedom as it ignores the low-level device/component characteristics.

RX prototype presented here aimed at multi-band FDD applications, variants of the NC-SIC architecture based on a similar co-design methodology (such as the one in [9] which has been developed in parallel) can be employed for full-duplex wireless communications systems.

4.1 Block-by-Block Partitioned Design Methodology

Many RF system designs adopt a block-by-block partitioned design methodology [77]. As depicted in Fig. 4.1, an RF front-end is partitioned into major building blocks including an antenna interface, an LNA, a PA, and a TX SI canceller. In a partitioned design methodology, each building block is treated as a "black box" and is reduced to a simple input-output relation. One of the most prominent advantages associated with this design methodology is the experimental determination of input and output port parameters without the need to know the internal block details [77]. Discrete-component-based RF system designs almost exclusively use this partitioned design methodology as only the component input and output ports are available or the distributed nature of discrete-

component-based RF systems makes it challenging to utilize the component internal nodes.

On the other hand, the block-by-block partitioned methodology misses many degrees of design freedom as it ignores the lower-level device/component characteristics, resulting in fundamental design trade-offs, such as the one between support for low antenna interface isolation levels (or equivalently, the power of TX SI being cancelled) and receiver sensitivity degradation. *An integrated implementation of RF systems allows easy access and utilization of device internal nodes, opening doors to co-design opportunities that can substantially enhance the system performance.*

4.2 NC-SIC Receiver: A Co-Design Between the Receiver and SI Canceller

The idea of the NC-SIC RX starts from noise-cancelling LNAs. The concept of noise cancelling in wideband LNAs uses a voltage-sensing stage [the common-source transistor M_{CS} shown in Fig. 4.2(a)] in addition to a matching stage [common-gate transistor M_{CG} in Fig. 4.2(a)] so that when the outputs of the two stages are combined (differentially in this case), the noise from the matching device adds destructively while the desired signals are added constructively [10][78][79]. Therefore, broadband input matching is accomplished through the matching device without its associated noise penalty thanks to the noise cancellation mechanism. The condition to cancel the Common-Gate (CG) device's noise and generate a balanced desired signal at the LNA output is:

$$g_{m,CG}R_{CG} = g_{m,CS}R_{CS}, \tag{4.1}$$

where we've assumed that $g_{m,CG}R_S = 1$ for input matching.

The NC-SIC technique [76] involves a co-design between the noise-cancelling LNA and a TX SI canceller by repurposing the CG device of the noise-cancelling LNA as part of the TX SI canceller as in Fig. 4.2(b). By driving the gate node of the CG device – an LNA internal node that ties to a fixed voltage bias in conventional designs – with an appropriately scaled TX replica signal, the SI can be cancelled right at the input of the LNA. A TX-replica signal is injected at the gate of the CG device through a phase shifter and VGA, while the desired signal and the SI are both present at the LNA input.

Applying KCL at the LNA input and considering only the SI, we have

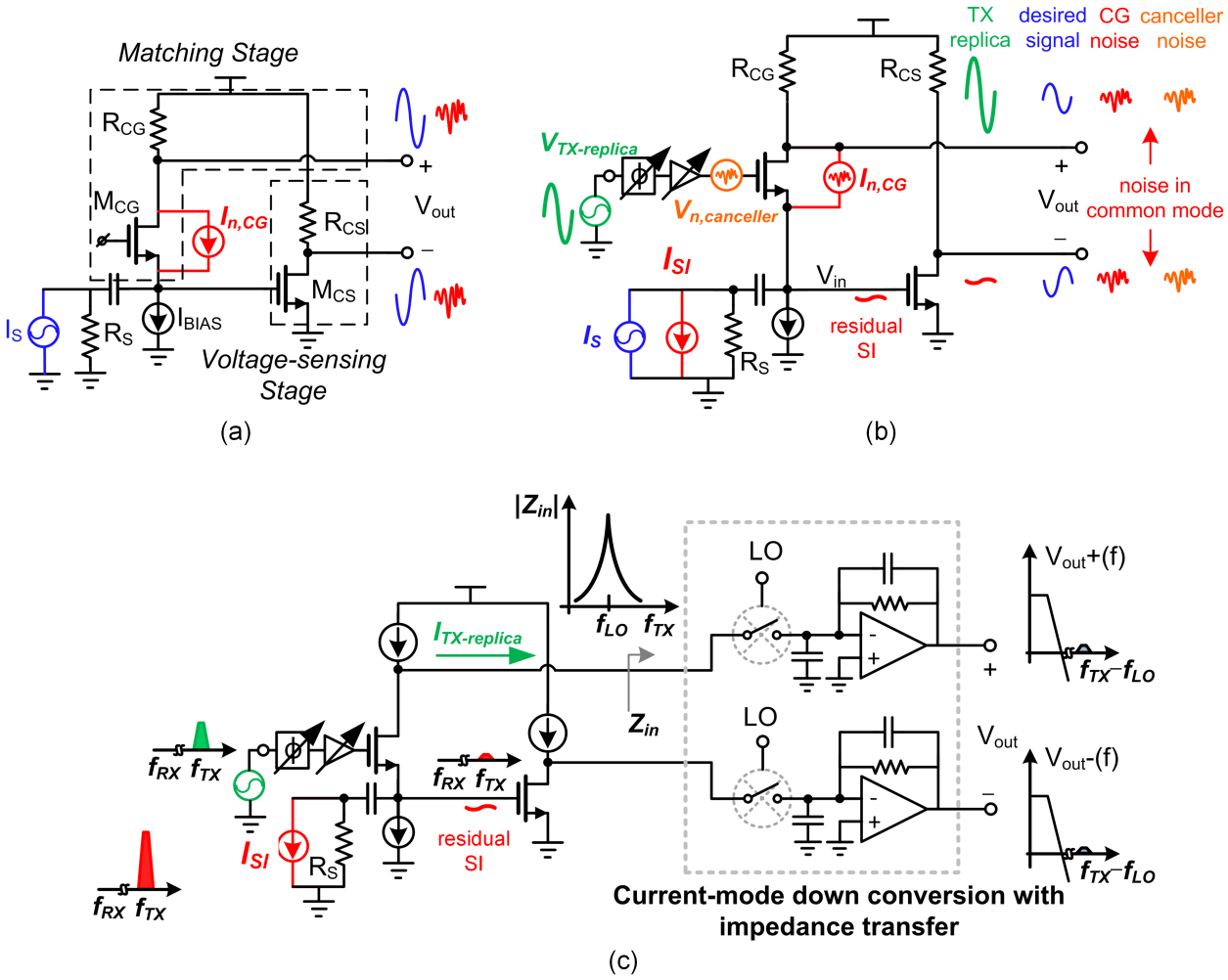

Figure 4.2: Evolution of the proposed Noise-Cancelling, Self-Interference Cancelling Receiver (NC-SIC RX): (a) noise-cancelling LNA in [10], (b) noise-cancelling LNA with embedded RF SIC, and (c) NC-SIC RX with current-mode downconversion to alleviate the output-side linearity challenge in the CG path.

$$g_{m,CG}(A_{canceller}V_{TX-replica} - V_{in}) = I_{SI} + V_{in}/R_S. \tag{4.2}$$

where $A_{canceller}$ is the voltage gain of the phase shifter and VGA. If the VGA and phase shifter are adjusted so that $g_{m,CG}A_{canceller}V_{TX-replica} = I_{SI}$, then $V_{in} = 0$, indicating the SI voltage swing is eliminated at the LNA input. It is interesting to note that under SIC, the source node of the CG device is a virtual ground for the TX-replica signal, and therefore the CG device is not degenerated by the source resistance.

Meanwhile, interestingly, the entire noise from the active canceller, namely the transistor M_{CG}, variable-gain amplifier and phase shifter, gets completely cancelled through the noise cancelling property, as the common source device M_{CS} senses the noise from the canceller and then subtracts it at the output. Therefore, in the proposed scheme, SIC is achieved right at the LNA input with ideally no noise penalty, while the desired signal appears differentially at the LNA output. A detailed noise analysis will be presented in the next sub-section.

Unlike in a conventional RF SIC architecture such as the one shown in Fig. 4.1, in the proposed architecture, while the SI is cancelled at the input, a large SI current still flows down the CG device producing a large voltage swing ($I_{SI}R_{CG}$) at its output. To mitigate this, in Fig. 4.2(c), a current-mode down conversion stage with impedance transfer from baseband consisting of passive mixers and baseband transimpedance amplifiers (TIAs) is inserted before the combining network to filter out the large OOB SI current before the achievement of voltage gain. The structure has evolved into the NC-SIC RX. It should be noted that the NC-SIC RX prototype presented here aimed for multiband FDD applications, but variants of the NC-SIC architecture based on a similar co-design methodology (such the one in [9] which has been developed in parallel) can be employed for full-duplex wireless communications systems.

While the Low-Noise Transconductance Amplifier (LNTA) Common-Source (CS) device is protected due to the SIC at the input, the CG device still experiences large voltage swing at its gate node due to the CG canceller injection, and can generate cross-modulation distortion together with an incident in-band CW jammer. The cross-modulation distortion generated by the CG device appears at the input as well as in the CG path of the receiver as depicted in Fig. 4.3. Interestingly, in the proposed scheme, the cross-modulation distortion of the CG device gets cancelled as well upon baseband recombination, as the cross-modulation distortion is sensed by the CS device, generating

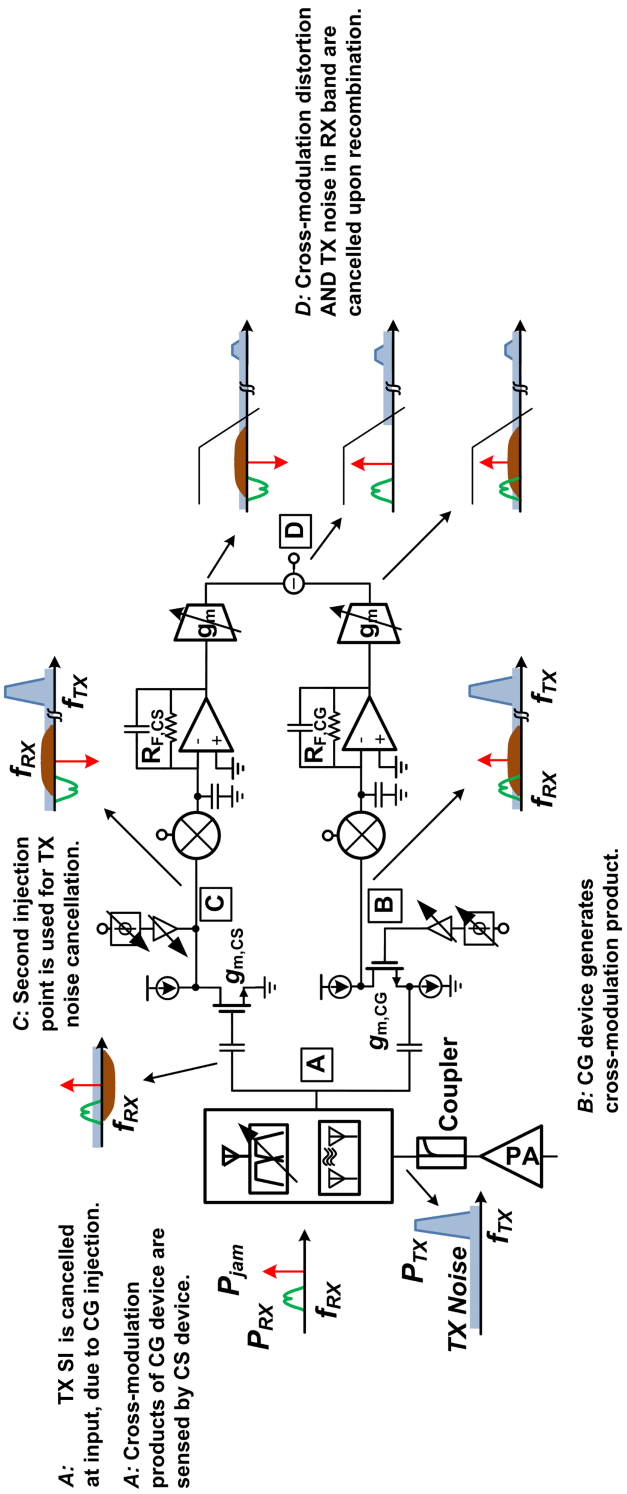

Figure 4.3: Cancellation of the cross-modulation distortion of the CG device in the proposed NC-SIC RX, and the second injection point in the CS path for RX-band TX noise cancellation.

a distortion current that is in phase with the distortion current in the CG path. This is similar to the distortion cancellation property of noise-cancelling LNAs [78][80] and implies that *SIC in the RF domain has been achieved with no noise or distortion penalty, thus breaking the fundamental trade-off between support for low antenna interface isolation levels (or equivalently, power of TX SI being cancelled) and receiver sensitivity degradation in a block-by-block partitioned design. This is essentially accomplished by the co-design between the active SI canceller and the RX that introduces more degrees of design freedom.*

It is interesting to take a more general view of the proposed scheme as an active combining circuit that has ideally no noise penalty, and is able to handle large signals without generating distortion. Consequently, the scheme can be used to cancel any interference signal for which a replica can be generated. For instance, spatial interference is mitigated through a similar scheme in MIMO/digital beamforming arrays in [81].

Although the discussion and analysis presented in this Section assume a 50Ω source impedance from the antenna interface, the canceller noise in the proposed NC-SIC RX may be mitigated even in the presence of source impedance variation. This is possible because that the noise cancellation occurs at the RX analog baseband upon recombination of the quadrature baseband signals which can be used to support a complex antenna impedance. As depicted in Fig. 4.21, we have investigated the optimum RX baseband recombination conditions in the presence of antenna impedance variation in both simulation and measurement. An adaptive control algorithm that can find the optimum recombination conditions in real time is an important topic for future research. In FDD systems where transmission and reception are separated into different frequency bands, cancellation of the SI at the RX input does not guarantee cancellation of the RX-band TX noise at the input, as their transfer functions through the antenna interface will be different. Consequently, the TX noise remains in both the CG and CS paths, and can desensitize the receiver. Since noise is small, TX noise can be cancelled down the receiver chain [63]. A second injection point is introduced in current mode at the output of the CS device (Fig. 4.3). With appropriate scaling using the CS canceller, TX noise can be nulled upon baseband recombination. The noise penalty of the CS canceller is alleviated by the CS gain. At this second injection node, the main TX-band signal is injected together with the RX-band TX noise, and flows down the receiver CS down-conversion path. This main TX-band signal is filtered out in the baseband TIAs, and current mode design

mitigates the potential linearity issues caused by it.

The SI currents flowing down the CG and CS paths to baseband can degrade receiver performance through mixer impairments such as the generation of second-order inter-modulation (IM2) products. It should be noted that these SI currents are similar to the currents in these paths in the absence of cancellation. IM2 challenges can be mitigated through mixer calibration techniques [82],[83].

4.3 Noise Analysis

In this section, the noise performance of the NC-SIC RX is analyzed. A subtle mechanism of NF penalty is revealed, produced by the fact that the optimal baseband recombination condition for cancellation of the CG canceller noise is different from the condition that minimizes receiver NF in the absence of SIC circuitry. The CS canceller noise contribution is not included in the noise analysis, since the CS canceller is only activated when TX noise in the RX band dominates. Furthermore, since noise is a small signal, TX noise cancellation can be performed further down the receiver chain, minimizing the noise impact even further.

Based on the noise model in Fig. 4.4, the NF for the entire receiver can be calculated as:

$$NF = K_{Fold}\left[1+\frac{(R_{F,CG}\delta - R_S g_{m,CS}R_{F,CS})^2\left(\gamma g_{m,CG}+\overline{V_{n,canc}^2}\frac{g_{m,CG}^2}{4kT}\right)+\gamma g_{m,CS}R_{F,CS}^2(1+g_{m,CG}R_S)^2}{(g_{m,CG}R_{F,CG}\delta+g_{m,CS}R_{F,CS})^2R_S}\right] + \pi^2\frac{(1+g_{m,CG}R_S)^2\left[\left(4kTR_{F,CG}+\overline{V_{n,eq,CG}^2}\right)\delta^2+4kTR_{F,CS}+\overline{V_{n,eq,CS}^2}\right]}{4kT(g_{m,CG}R_{F,CG}\delta+g_{m,CS}R_{F,CS})^2R_S}, \tag{4.3}$$

where $K_{Fold} \approx 0.9dB$ is a constant that factors in the noise folding effect of 4-phase mixing, $\delta = g_{CGI}/g_{CSI}$ is the ratio between the recombination weights on receiver's CG and CS paths, $\overline{V_{n,canc}^2}$ is the output noise of the CG canceller, and $\overline{V_{n,eq,CG}^2}$ and $\overline{V_{n,eq,CS}^2}$ are the input-referred noise of the OTAs. The noise has been computed at the output v_{OUTI}. Also, g_{CSQ} and g_{CGQ} are assumed to be zero for a purely resistive source impedance. Complex recombination weights may be required to compensate for complex source impedance and other sources of signal path phase-shift differences between the CS and CG paths but such cases are not considered here for simplicity. Note

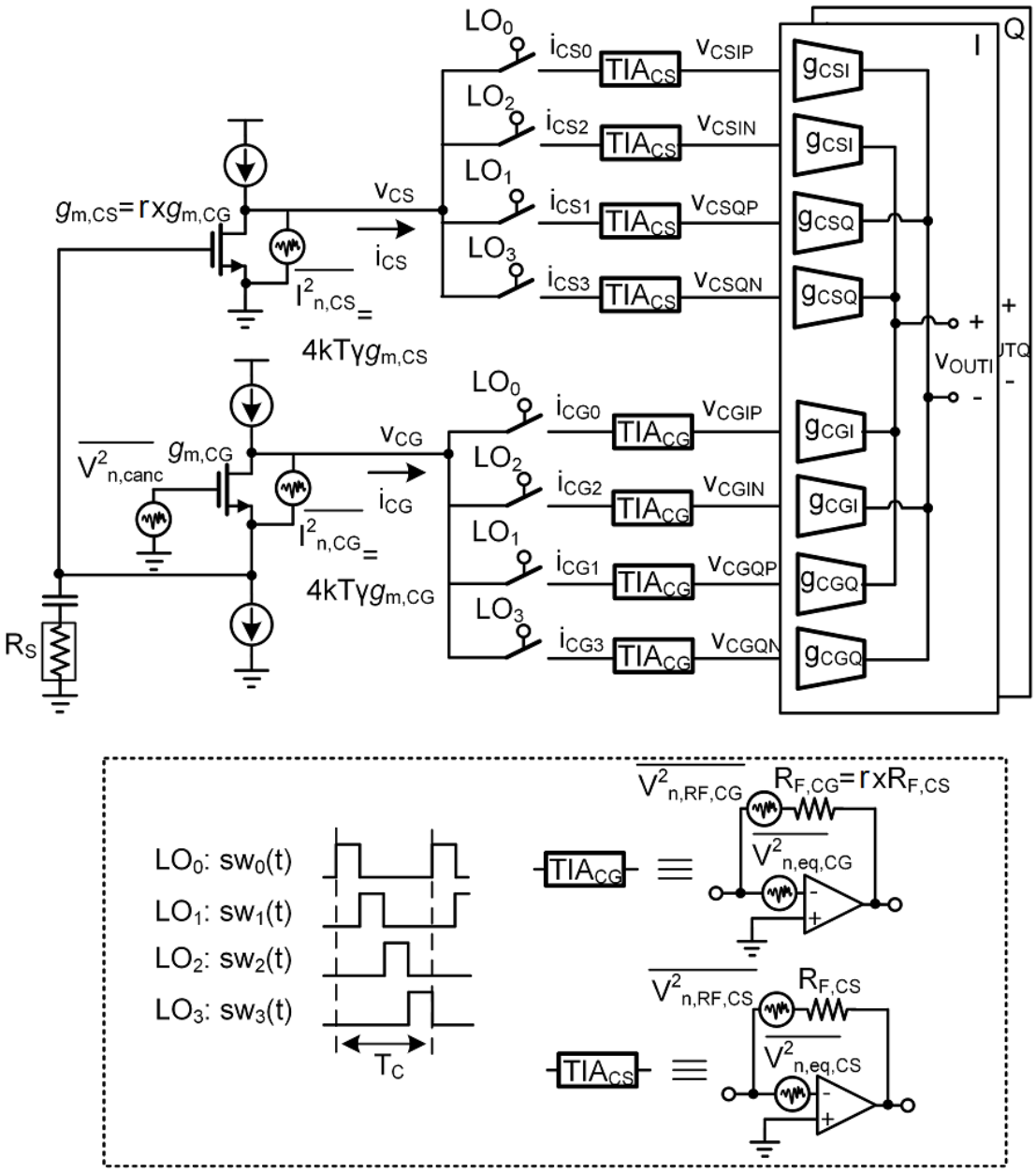

Figure 4.4: NC-SIC RX model for noise and distortion analysis.

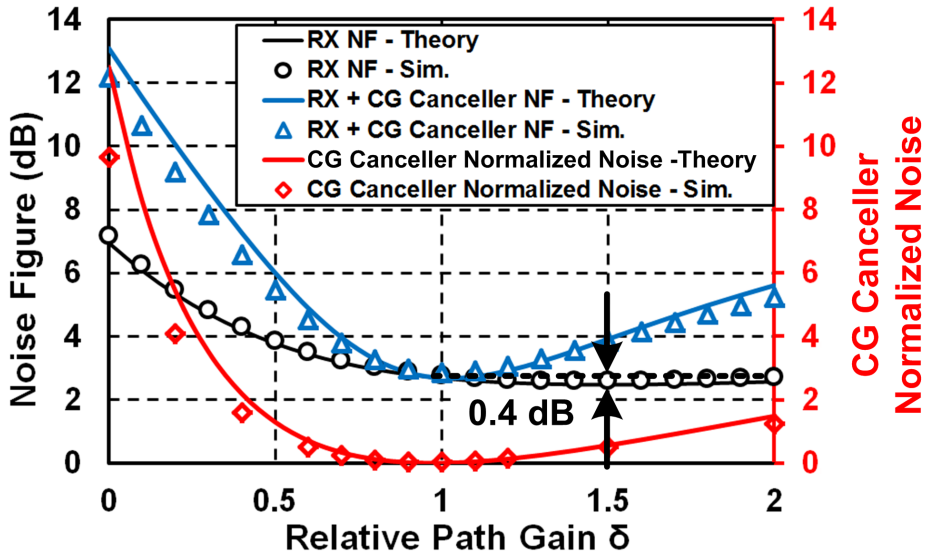

Figure 4.5: Receiver NF with and without the CG canceller active and normalized CG canceller noise as a function of the (real) relative path gain setting in the baseband recombination block. Markers depict simulation results for the actual receiver implementation at 500 MHz LO frequency. Solid lines depict theoretical results calculated using eq. (4.3).

that the weighting to compensate for the ratio of the LNTA CG and CS device transconductance has been performed in baseband TIAs ($R_{F,CG}$=$r \times R_{F,CS}$ where $r = g_{m,CS}/g_{m,CG}$). The NF in (4.3) includes three contributors: the CG device and CG canceller noise, CS device noise and the noise of the TIAs. Fig. 4.5 depicts the calculated and simulated NF when the canceller is inactive ($\overline{V_{n,canc}^2} = 0$) across δ. The simulations presented in this section are for the actual receiver implementation described in the following subsection at 500 MHz LO frequency, but without layout parasitics to ease simulation time and with ideal mixer switches and LO drive. Hence, the final performance numbers are close to the measured values but are slightly lower. As indicated by (4.3), the noise from the CG device gets cancelled when relative path gain $\delta = R_S g_{m,CS} R_{F,CS}/R_{F,CG} = 1$ (assuming $g_{m,CG}R_S = 1$ for input matching). However, the optimum relative path gain for the receiver NF is around 1.5 in Fig. 4.5 as this optimizes the contributions from other noise sources ([80]), including the CS device and baseband TIAs. On the other hand, the CG canceller noise ($\overline{V_{n,canc}^2}$) still gets cancelled when the δ equals 1 as is indicated by the CG canceller normalized noise (i.e., CG canceller NF component, calculated as the noise contribution from the canceller divided by that from the source impedance R_S) in Fig. 4.5. Therefore, when CG canceller is active, the relative path gain δ is very close to 1, as the noise from the CG canceller dominates. This change in the optimal baseband recombination condition is an indirect source of NF penalty in the proposed scheme. However, the resultant NF penalty is only 0.3-0.4 dB in Fig. 4.5.

4.4 Linearity Analysis and Simultaneous Noise and Distortion Cancellation

As discussed earlier, the noise cancelling architecture also cancels the distortion of the CG device. In this section, the linearity analysis of the NC-SIC RX is presented with a focus on cross-modulation distortion as it typically is the linearity performance bottleneck of RF front-ends (see Chapter 2). Next, the distortion cancellation condition under RF SIC is given and compared with the noise cancellation condition, unveiling the feasibility of simultaneous noise and distortion cancellation in the NC-SIC RX.

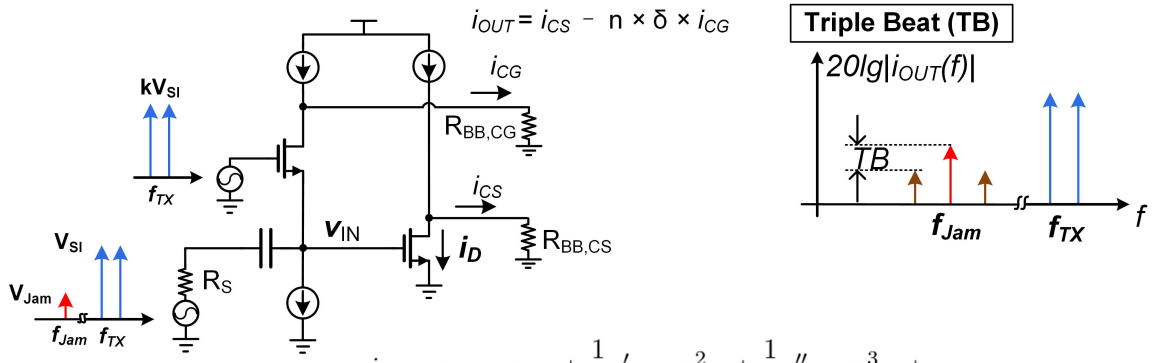

$$i_D = g_{m,CS}v_{IN} + \frac{1}{2}g'_{m,CS}v_{IN}^2 + \frac{1}{6}g''_{m,CS}v_{IN}^3 + \cdots .$$

$$v_{IN} = \alpha_{1T}v_{SI} + \alpha_{2T^2}v_{SI}^2 + \alpha_{3T^3}v_{SI}^3 + \alpha_{1S}v_{Jam} + \alpha_{2S^2}v_{Jam}^2 + \alpha_{3S^3}v_{Jam}^3 + \alpha_{2TS}v_{SI}v_{Jam} + \alpha_{3T^2S}v_{SI}^2v_{Jam} + \alpha_{3TS^2}v_{SI}v_{Jam}^2 + \cdots .$$

Figure 4.6: Circuit model for the analysis of cross-modulation distortion in the NC-SIC LNTA in the presence of the TX SI and an in-band CW jammer.

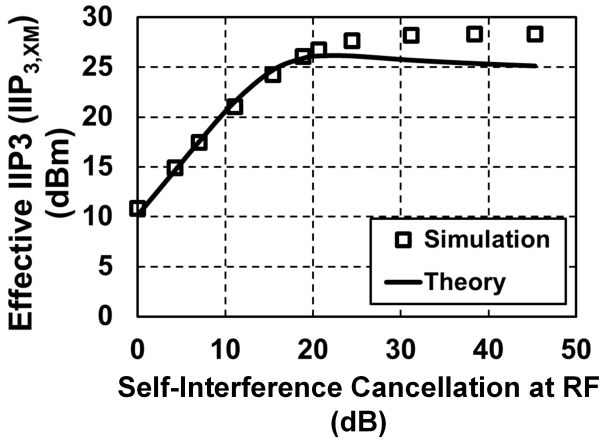

Figure 4.7: Effective IIP_3 of the implemented NC-SIC LNTA across SIC in the RF domain from simulations and theory. The in-band jammer and the two-tone TX SI signal (peak power of -6dBm) are located at 500 MHz and 600/605 MHz, respectively. The TX replica signal at the gate of the CG device is swept to vary RF SIC.

4.4.1 LNTA Cross-Modulation Distortion Analysis

In current-mode receivers, the OOB linearity is typically limited and determined by the LNTA when the SI (or any interference in general) is located sufficiently outside the BW of the RX analog baseband circuits [84]. In order to perform the LNTA linearity analysis under RF SIC, two excitations are included as depicted in Fig. 4.6 – one at the input of the LNTA containing the SI v_{SI} and the jammer signal v_{Jam}, and the other at the gate of the LNTA CG device containing a scaled TX replica signal. To model the CG device nonlinearity, we expand the input voltage v_{IN} into a 2-variable power series of the SI and the jammer signals.

$$\begin{aligned} v_{IN} =& \alpha_{1T} v_{SI} + \alpha_{2T^2} v_{SI}^2 + \alpha_{3T^3} v_{SI}^3 + \alpha_{1S} v_{Jam} + \alpha_{2S^2} v_{Jam}^2 + \alpha_{3S^3} v_{Jam}^3 \\ &+ \alpha_{2TS} v_{SI} v_{Jam} + \alpha_{3T^2S} v_{SI}^2 v_{Jam} + \alpha_{3TS^2} v_{SI} v_{Jam}^2 + \cdots . \end{aligned} \tag{4.4}$$

The device current is assumed to depend (nonlinearly) on gate-source voltage primarily. The first number in the subscripts of the α coefficients represents the order of the nonlinearity arising from the LNTA CG device and the exponents of T and S in the subscripts denote the exponents of the TX SI and the jammer signal in that term respectively. For instance, α_{3T^2S} arises from the 3^{rd} order nonlinearity of the CG device and is the coefficient of the $v_{SI}^2 v_{Jam}$ term. To model the CS device nonlinearity, its drain current is expanded into a power series of its gate voltage.

$$i_D = g_{m,CS} v_{IN} + \frac{1}{2} g'_{m,CS} v_{IN}^2 + \frac{1}{6} g''_{m,CS} v_{IN}^3 + \cdots . \tag{4.5}$$

Memory elements such as capacitive parasitics as well as off-chip biasing inductors and capacitors have been ignored. Consequently, the analysis is valid within the RF bandwidth of the receiver where these memory elements are ineffectual.The output is defined as $I_{CS} - n \times \delta \times I_{CG}$ where n is the nominal (real) weighting achieved in the baseband TIAs (= 4 in our implementation) and δ is the programmable recombination weighting.

Now, assuming a two-tone signal for the TX SI (each with amplitude of V_{SI}), the TB [46] is defined as the ratio of the jammer power to the power of the cross-modulation distortion tones in the output as shown in Fig. 4.6 (also see Chapter 2). Circuit analysis along with (4.4) and (4.5) can be used to obtain the following expression for the LNTA TB.

$$TB_{LNTA}^{-1} \approx \frac{\left[(g_{m,CS}R_S - r\delta)\alpha_{3T^2S} + g'_{m,CS}(\alpha_{2T^2}\alpha_{1S} + \alpha_{2TS}\alpha_{1T})R_S + \frac{1}{2}g''_{m,CS}\alpha_{1T}^2\alpha_{1S}R_S\right]A_{SI}^2}{2\alpha_{1S}g_{m,CS}R_S + 2(1-\alpha_{1S})r\delta}$$
$$\approx \frac{g'_{m,CS}\alpha_{2T^2}A_{SI}^2}{4g_{m,CS}} \text{ (if } g_{m,CS}R_S = r\delta \text{ , } \alpha_{1T} = 0 \text{ and } \alpha_{1S} = 0.5), \tag{4.6}$$

The TB has three contributors: 3^{rd} order nonlinearity of the CG device ($\frac{(g_{m,CS}R_S - r\delta)\alpha_{3T^2S}V_{SI}^2}{2\alpha_{1S}g_{m,CS}R_S + 2(1-\alpha_{1S})r\delta}$), 3^{rd} order nonlinearity of the CS device ($\frac{\frac{1}{2}g''_{m,CS}\alpha_{1T}^2\alpha_{1S}R_SV_{SI}^2}{2\alpha_{1S}g_{m,CS}R_S + 2(1-\alpha_{1S})r\delta}$), and an interaction between the 2^{nd} order nonlinearities of the CG and CS devices ($\frac{g'_{m,CS}(\alpha_{2T^2}\alpha_{1S} + \alpha_{2TS}\alpha_{1T})R_SV_{SI}^2}{2\alpha_{1S}g_{m,CS}R_S + 2(1-\alpha_{1S})r\delta}$). The 3^{rd} order distortion of the CG device gets cancelled upon baseband recombination due to the simultaneous noise and distortion cancellation property of the noise-canceling architecture as indicated in Fig. 4.3. This corresponds to the condition $g_{m,CS}R_S = r\delta$ in (4.6) as $g_{m,CG} = 1/R_S$ for input matching and $\delta = 1$ for cancellation of the CG device and CG canceller noise. Under TX SI cancellation, the CS device is protected ($\alpha_{1T} \approx 0$), and so the 3^{rd} order distortion from the CS device is also minimized. From (4.6), we note that part of the distortion arising from the interaction between the 2^{nd} order nonlinearities gets cancelled as well since $\alpha_{1T} \approx 0$ under TX SI cancellation. Therefore, the final residual TB after TX SI and distortion cancellation is limited by the 2^{nd} order nonlinearity of the CG and the CS devices.

A complementary topology is used for the implemented LNTA (Fig. 4.13) for achieving high 2^{nd} and 3^{rd} order linearity simultaneously [79][85]. Fig. 4.7 shows the simulated LNTA effective IIP_3 across RF SIC. The in-band jammer and the two-tone TX SI signal (peak power of -6dBm) are located at 500 MHz and 600/605 MHz, respectively. The relative strength of the TX replica signal (represented by k in Fig. 4.6) at the gate of the CG device is swept to vary TXRR. The significance of the effective IIP_3, which is calculated from the TB, is that it represents the IIP_3 requirement that a conventional LNTA/receiver without TX SI cancellation must achieve to have the same TB ([46]):

$$IIP_{3,XM} = \frac{1}{2}TB + P_{TX,avg}. \tag{4.7}$$

In simulation, the recombination weight is chosen to satisfy the CG device and canceller noise cancellation condition [$\delta = 1$ in eq. (4.6)] , so that the CG device's 3^{rd}-order distortion is cancelled. As shown in Fig. 4.7, the LNTA effective IIP_3 starts from approximately +10 dBm, and keeps

increasing as TXRR increases until the effective IIP_3 saturates at almost +30 dBm, where it is limited by the finite 2^{nd} order nonlinearity of the CG and CS devices. A good match between simulation and theory [equation (4.6)] is also observed. This effective IIP_3 level also agrees well with the measurements detailed later in this paper.

4.4.2 Receiver Cross-Modulation Distortion

For the NC-SIC RX, the cross-modulation distortion analysis in the previous subsection takes into account only the broadband nonlinearity of the LNTA with embedded RF SIC. Such an analysis is accurate for FDD systems with a large normalized TX/RX frequency separation[1] (e.g. ≈ 8). For small normalized TX/RX frequency separation (e.g. 2.05 in LTE FDD band 20[2]), the distortion introduced by the baseband filtering TIA must be considered. This subsection presents a current-mode RX OOB linearity analysis that factors in not only the LNTA but also the frequency-selective baseband TIA. It should be noted that this linearity analysis is applicable to current-mode receivers in general [86][87], such as the NC-SIC RX presented here and the Frequency-Translational Noise Cancelling (FTNC)-RX in [87][88].

Fig. 4.4 depicts a model for our RX linearity analysis. The noise-cancelling LNTA is modeled by a CG device and a CS device with ideal current source loads. Memory elements in the LNTA as well as in the source impedance have been ignored. The current outputs in the LNTA CG and CS paths are i_{CG} and i_{CS}, respectively. The four-phase passive mixers are modeled by ideal switches driven by 25% non-overlapping LO signals with a period of T_0. The current outputs of the CG and CS path passive mixers are i_{CGx} and i_{CSx} respectively, where $x = 0, 1, 2, 3$. v_{CSIP}, v_{CSIN}, v_{CSQP}, and v_{CSQN} are the voltage outputs of the TIAs in the RX CS path, while v_{CGIP}, v_{CGIN}, v_{CGQP}, and v_{CGQN} are the outputs in the RX CG path. The TIA in the CS path is an $r\times$ scaled version of the TIA in the CG path to compensate for the ratio of the LNTA CG and CS device transconductance ($g_{m,CS} = r \times g_{m,CG}$).Finally, the outputs of the TIAs from CG and CS paths are combined through the recombination circuits to create the RX voltage outputs of v_{outI} and v_{outQ}.

[1]The normalized TX/RX frequency separation is defined as TX/RX frequency separation divided by the TIA BW.

[2]Assume 20 MHz TIA BW to support 20 MHz LTE channel BW. LTE FDD band 20 has a TX/RX frequency separation of 41 MHz

g_{CGI}, g_{CGQ}, g_{CSI}, and g_{CSQ} are the transconductances of the recombination circuits.

The I-channel RX's output is:

$$\begin{aligned}\frac{v_{outI}(t)}{R_L} &= (v_{CGIP} - v_{CGIN})g_{CGI} + (v_{CGQP} - v_{CGQN})g_{CGQ} \\ &\quad + (v_{CSIN} - v_{CSIP})g_{CSI} + (v_{CSQN} - v_{CSQP})g_{CSQ}.\end{aligned} \tag{4.8}$$

Since the TIA is a nonlinear circuit with memory, its output can be expanded into a Volterra series as [89][90]:

$$\begin{aligned}v_{out}(t) &= \sum_{k=1}^{\infty} \mathbf{Q_k}[i_{in}(t)], \\ \text{where} \\ \mathbf{Q_k}[x(t)] &= \int \cdots \int_{-\infty}^{\infty} q_k(\tau_1, \ldots, \tau_k) x(t-\tau_1) \ldots x(t-\tau_k)\, d\tau_1 \ldots d\tau_k.\end{aligned} \tag{4.9}$$

$\mathbf{Q_k}[\cdot]$ is the k-th order Volterra operator, i_{in} and v_{out} are the input current and the output voltage of a TIA respectively. Substituting (4.9) into (4.8) gives:

$$\begin{aligned}\frac{v_{outI}(t)}{R_L} &= \left(\sum_{k=1}^{\infty} \mathbf{Q_k}(i_{CG0}) - \sum_{k=1}^{\infty} \mathbf{Q_k}(i_{CG2})\right) g_{CGI} \\ &\quad + \left(\sum_{k=1}^{\infty} \mathbf{Q_k}(i_{CG1}) - \sum_{k=1}^{\infty} \mathbf{Q_k}(i_{CG3})\right) g_{CGQ} \\ &\quad + \left(\sum_{k=1}^{\infty} \mathbf{Q_k}(\frac{i_{CS2}}{r}) - \sum_{k=1}^{\infty} \mathbf{Q_k}(\frac{i_{CS0}}{r})\right) g_{CSI} \\ &\quad + \left(\sum_{k=1}^{\infty} \mathbf{Q_k}(\frac{i_{CS3}}{r}) - \sum_{k=1}^{\infty} \mathbf{Q_k}(\frac{i_{CS1}}{r})\right) g_{CSQ}\end{aligned} \tag{4.10}$$

The 25% duty-cycle LO waveforms $sw_x(t)$ driving the passive mixer can be expanded into a Fourier series as:

$$sw_x(t) = \sum_{n=-\infty}^{\infty} \frac{1}{4} sinc\left(\frac{n\pi}{4}\right) e^{-j\frac{xn\pi}{2}} e^{jn\omega_C t}, \tag{4.11}$$

where $x = 0, 1, 2, 3$. Since the LOs are non-overlapping, i_{CGx} and i_{CSx} can be written as:

$$\begin{aligned} i_{CGx}(t) &= sw_x(t) i_{CG}(t), \\ i_{CSx}(t) &= sw_x(t) i_{CS}(t). \end{aligned} \tag{4.12}$$

This further gives that,

$$\sum_{k=1}^{\infty} \mathbf{Q_k}(i_{CG0}) = \sum_{k=1}^{\infty} \mathbf{Q_k} \left(i_{CG} \sum_{n=-\infty}^{\infty} \frac{1}{4} sinc\left(\frac{n\pi}{4}\right) e^{jn\omega_C t} \right). \tag{4.13}$$

Due to the low-pass filtering nature of the TIA, only components at baseband frequency after down-conversion need to be considered in (4.13). Thus, (4.13) can be simplified as,

$$\sum_{k=1}^{\infty} \mathbf{Q_k}(i_{CG0}) \approx \sum_{k=1}^{\infty} \mathbf{Q_k} \left(\frac{i_{CG}}{4} sinc\left(\frac{\pi}{4}\right) \left(e^{j\omega_C t} + e^{-j\omega_C t}\right) \right). \tag{4.14}$$

Since we focus on cross-modulation distortion analysis for FDD here, only 1^{st}- and 3^{rd}-order kernels are of concern. This further simplifies (4.14) to,

$$\sum_{k=1}^{\infty} \mathbf{Q_k}(i_{CG0}) \approx \mathbf{Q_1}(i_{CG} M_I) + \mathbf{Q_3}(i_{CG} M_I), \tag{4.15}$$

where $M_I = \frac{1}{4} sinc\left(\frac{\pi}{4}\right) \left(e^{j\omega_C t} + e^{-j\omega_C t}\right)$. Similarly, we have:

$$\begin{aligned} \sum_{k=1}^{\infty} \mathbf{Q_k}(i_{CG2}) &\approx -\mathbf{Q_1}(i_{CG} M_I) - \mathbf{Q_3}(i_{CG} M_I), \\ \sum_{k=1}^{\infty} \mathbf{Q_k}(i_{CG1}) &\approx \mathbf{Q_1}(i_{CG} M_Q) + \mathbf{Q_3}(i_{CG} M_Q), \\ \sum_{k=1}^{\infty} \mathbf{Q_k}(i_{CG3}) &\approx -\mathbf{Q_1}(i_{CG} M_Q) - \mathbf{Q_3}(i_{CG} M_Q), \end{aligned} \tag{4.16}$$

where $M_Q = -\frac{j}{4} sinc\left(\frac{\pi}{4}\right) \left(e^{j\omega_C t} - e^{-j\omega_C t}\right)$.

Similarly, for the RX CS path we have:

$$\begin{aligned}
\sum_{k=1}^{\infty}\mathbf{Q_k}\left(\frac{i_{CS0}}{r}\right) &\approx \mathbf{Q_1}\left(\frac{i_{CS}M_I}{r}\right)+\mathbf{Q_3}\left(\frac{i_{CS}M_I}{r}\right),\\
\sum_{k=1}^{\infty}\mathbf{Q_k}\left(\frac{i_{CS2}}{r}\right) &\approx -\mathbf{Q_1}\left(\frac{i_{CS}M_I}{r}\right)-\mathbf{Q_3}\left(\frac{i_{CS}M_I}{r}\right),\\
\sum_{k=1}^{\infty}\mathbf{Q_k}\left(\frac{i_{CS1}}{r}\right) &\approx \mathbf{Q_1}\left(\frac{i_{CS}M_Q}{r}\right)+\mathbf{Q_3}\left(\frac{i_{CS}M_Q}{r}\right),\\
\sum_{k=1}^{\infty}\mathbf{Q_k}\left(\frac{i_{CS3}}{r}\right) &\approx -\mathbf{Q_1}\left(\frac{i_{CS}M_Q}{r}\right)-\mathbf{Q_3}\left(\frac{i_{CS}M_Q}{r}\right).
\end{aligned} \tag{4.17}$$

Now, (4.10) can be simplified by substituting in (4.15), (4.16), and (4.17). This results in:

$$\begin{aligned}
\frac{v_{outI}(t)}{R_L} \approx & 2\left[\mathbf{Q_1}(i_{CG}M_I)+\mathbf{Q_3}(i_{CG}M_I)\right]g_{CGI}\\
&+2\left[\mathbf{Q_1}(i_{CG}M_Q)+\mathbf{Q_3}(i_{CG}M_Q)\right]g_{CGQ}\\
&-2\left[\mathbf{Q_1}\left(\frac{i_{CS}M_I}{r}\right)+\mathbf{Q_3}\left(\frac{i_{CS}M_I}{r}\right)\right]g_{CSI}\\
&-2\left[\mathbf{Q_1}\left(\frac{i_{CS}M_Q}{r}\right)+\mathbf{Q_3}\left(\frac{i_{CS}M_Q}{r}\right)\right]g_{CSQ}.
\end{aligned} \tag{4.18}$$

Based on (4.18), one can derive the RX TB as (see Appendix A for detailed derivation steps):

$$\begin{aligned}
TB^{-1} = |&\frac{(g_{m,CS}R_S - r\delta)\alpha_{3T^2S}+XR_S}{2(1-\alpha_{1S})r\delta+2g_{m,CS}R_S\alpha_{1S}}+\\
&\frac{rY\left[(1-\alpha_{1S})(1-\alpha_{1T})^2\delta+\left(\frac{g_{m,CS}R_S}{r}\right)^3\alpha_{1S}\alpha_{1T}^2\right]e^{j\phi}}{32[(1-\alpha_{1S})r\delta+g_{m,CS}R_S\alpha_{1S}]|Q_1(\omega_{1B})|R_S^2}|\cdot V_{SI}^2,
\end{aligned} \tag{4.19}$$

where $X = g'_{m,CS}(\alpha_{2T^2}\alpha_{1S}+\alpha_{2TS}\alpha_{1T})+\frac{1}{2}g''_{m,CS}\alpha_{1T}^2\alpha_{1S}$, $Y = 3(\mathrm{sinc}\frac{\pi}{4})^2|Q_{3,sym}(\omega_{1B},\omega_{2B},-\omega_{3B})|$, $\phi = \angle Q_{3,sym}(\omega_{1B},\omega_{2B},-\omega_{3B})-\angle Q_1(\omega_{xB})$, $\delta = \frac{g_{CGI}-jg_{CGQ}}{g_{CSI}-jg_{CSQ}}$, ω_{1B}, ω_{2B}, ω_{3B} are the baseband frequencies of a CW jammer and a two-tone SI, and ω_{xB} is the baseband frequency of the cross-modulation distortion. It should be noted that, when normalized TX/RX frequency separation is larger, $|Q_{3,sym}(\omega_{1B},\omega_{2B},-\omega_{3B})|$ is small, and the second term in (4.19) is negligible compared to the first term. Therefore, 4.19 can be simplified as follows:

$$\begin{aligned}
TB^{-1} &\approx |\frac{(g_{m,CS}R_S - n\delta)\alpha_{3T^2S}+XR_S}{2(1-\alpha_{1S})n\delta+2g_{m,CS}R_S\alpha_{1S}}|\cdot V_{SI}^2,\\
&= TB_{LNTA}^{-1}.
\end{aligned} \tag{4.20}$$

Therefore, for large normalized TX/RX frequency separation, (4.20) is simplified to (4.6) where only the broadband LNTA's nonlinearity is taken into account.

4.4.3 Simultaneous Noise and Distortion Cancellation

In the NC-SIC RX, both the noise and distortion associated with the SI canceller can be cancelled. A natural question is whether the noise and distortion cancellation mechanisms share the same RX baseband recombination condition. In this section, the recombination condition for the distortion cancellation is derived which matches well with the noise cancellation condition derived in our noise analysis, showing the feasibility of simultaneous noise and distortion cancellation.

By letting (4.19) to be zero, we can find the real part and the imaginary part of δ in (4.21) and (4.22), which result in perfect cancellation of the cross-modulation distortion product. In deriving (4.21) and (4.22), we've assumed cancellation of the SI, so that the cross-modulation products from the TIAs in the RX CS path can be ignored.

$$\mathrm{Re}\{\delta\} \approx 16(g_{m,CS}\alpha_{3T^2S} + X)|Q_1(\omega_{xB})|R_S^3 \cdot \left[G + \frac{((1-\alpha_{1S})(1-\alpha_{1T})^2 rY sin\phi)^2}{G}\right]^{-1}, \quad (4.21)$$

$$\mathrm{Im}\{\delta\} \approx \frac{(1-\alpha_{1S})(1-\alpha_{1T})^2 rY sin\phi}{G}\mathrm{Re}\{\delta\}, \quad (4.22)$$

where $G = 16r\alpha_{3T^2S}|Q_1(\omega_{xB})|R_S^2 - (1-\alpha_{1S})(1-\alpha_{1T})^2 rY cos\phi$.

For a large normalized TX/RX frequency separation, we have $|Q_{3,sym}(\omega_{1B}, \omega_{2B}, -\omega_{3B})| \approx 0$. Furthermore, assuming $g_{m,CS}R_S = r$ and $X \approx 0$ (negligible LNTA 2^{nd}-order nonlinearity), (4.21) and (4.22) can be reduced to $\mathrm{Re}\{\delta\} = 1$ and $\mathrm{Im}\{\delta\} = 0$ which are exactly the same as the optimum noise cancellation condition derived before.

4.5 Design Example and Simulation Results

Fig. 4.8 shows an implementation example of an NC-SIC RX using a 65 nm CMOS process. LNTA uses complementary topology for high 2nd-order linearity. The SI cancellation circuitry is modeled as voltage-controlled voltage source at the gate of the CG device of the LNTA. Thick-oxide MOSFET is adopted for the CG devices to handle powerful SI. Due to the discontinuity of the 2nd-derivative of MOSFET drain current in BSIM model, ideal switch with finite on-resistance is used

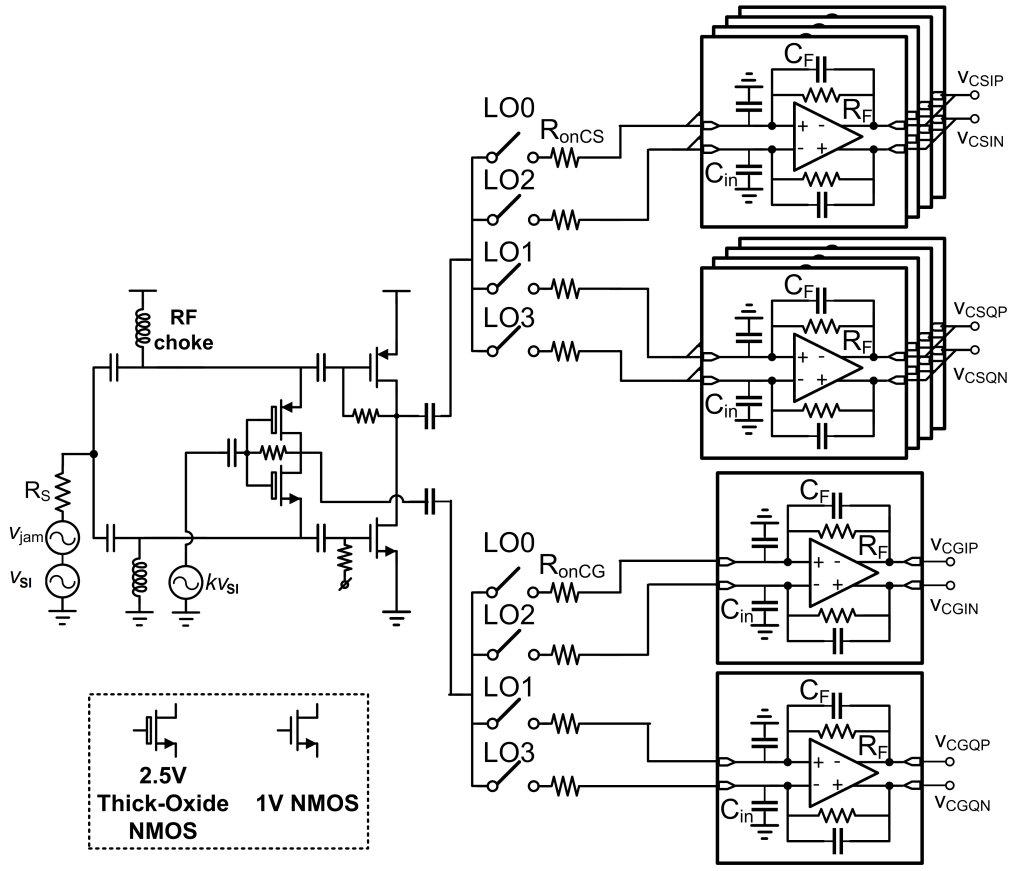

Figure 4.8: An NC-SIC RX design example using a 65 nm CMOS process. LNTA uses complementary topology for high 2nd-order linearity. Ideal switch with finite on-resistance is used for passive mixer for linearity simulation. LNTA and passive mixer are AC-coupled through large capacitors.

for passive mixer for linearity simulation[91]. In [91], +30 dBm IIP_3 is measured for current commutating passive mixer with 800 Ω source impedance and 5 Ω load impedance. LNTA and passive mixer are AC-coupled through large capacitors. Baseband TIAs use two-stage Miller-compensated OTA based on [92][86]. Class-AB output stage is used to handle large voltage swing for high OOB linearity.

4.5.1 Cross-Modulation Distortion Results

The NC-SIC receiver depicted in Fig. 4.8 reduces to an FTNC RX [84][88], by turning off the SIC, i.e. setting k in Fig. 4.8 to zero. The jammer at 520 MHz has a power of −30 dBm, while a two-tone SI is located at various frequencies based on the normalized TX/RX frequency separation with a peak power of −6 dBm. The TIA has a BW of 20 MHz. The two tones are separated by 10 MHz, and the LO frequency is 500 MHz. Fig. 4.9 shows the simulated and calculated FTNC RX $IIP_{3,XM}$ calculated from RX TB using (4.7)[46], together with calculated distortion contributions from the LNTA and from the TIA. From Fig. 4.9 we can see that with small TX/RX frequency separations, the current-mode RX OOB linearity performance can be limited by the baseband TIAs. Therefore, higher order TIA [93] or large-signal blocker robust TIA [94] may be required. While with large TX/RX frequency separations, the FTNC RX OOB linearity is ultimately limited by the LNTA input linearity. The LNTA broadband IIP_3 is typically below +20 dBm (even with input linearity enhancement techniques, e.g. in [95][79]). Therefore, to support low-cost/compact/tunable antenna interface with powerful TX SI, cancellation is required to achieve >+30 dBm RX OOB IIP_3.

Now, we activate the gate injection of the CG device of the LNTA, so that the SI is cancelled right at the input of the receiver. The scaling factor k in Fig. 4.8 is set to be −1.22, resulting in about 25 dB SIC across all duplexing ratios. Fig. 4.10 shows the simulated and calculated $IIP_{3,XM}$ of the RX depicted in Fig. 4.8. The jammer at 504 MHz has a power of −30 dBm, while a two-tone SI is located at various frequencies based on the normalized TX/RX frequency separation with a peak power of −6 dBm. The TIA has a BW of 25 MHz. The two tones are separated by 2.5 MHz, and the LO frequency is 500 MHz. The nominal baseband recombination setting ($\delta = 1$) is used. Similarly, calculated RX $IIP_{3,XM}$ results contributed by LNTA and TIA are plotted separately. Different from the FTNC RX without SIC, the LNTA linearity is improved significantly thanks to the TX-leakage cancellation at its input. This indicates the linearity performance of the NC-SIC

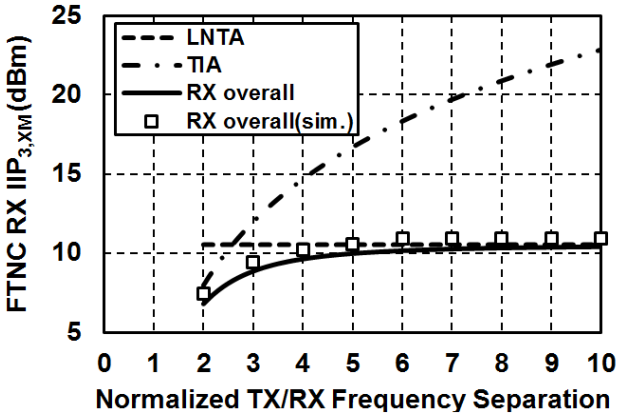

Figure 4.9: Simulated and calculated TB of the FTNC RX. The jammer at 520 MHz has a power of −30 dBm, while a two-tone SI is located at various frequencies based on the normalized TX/RX frequency separation with a peak power of −6 dBm. The TIA has a BW of 20 MHz. The two tones are separated by 10 MHz, and the LO frequency is 500 MHz.The nominal baseband recombination setting ($\delta = 1$) is used.

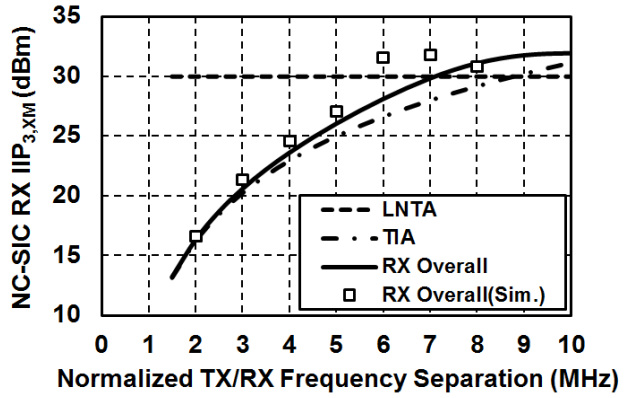

Figure 4.10: Simulated and Calculated NC-SIC RX TB under cancellation of TX SI. The jammer at 504 MHz has a power of −30 dBm, while a two-tone SI is located at various frequencies based on the normalized TX/RX frequency separation with a peak power of −6 dBm. The TIA has a BW of 25 MHz. The two tones are separated by 2.5 MHz, and the LO frequency is 500 MHz. The nominal baseband recombination setting ($\delta = 1$) is used.

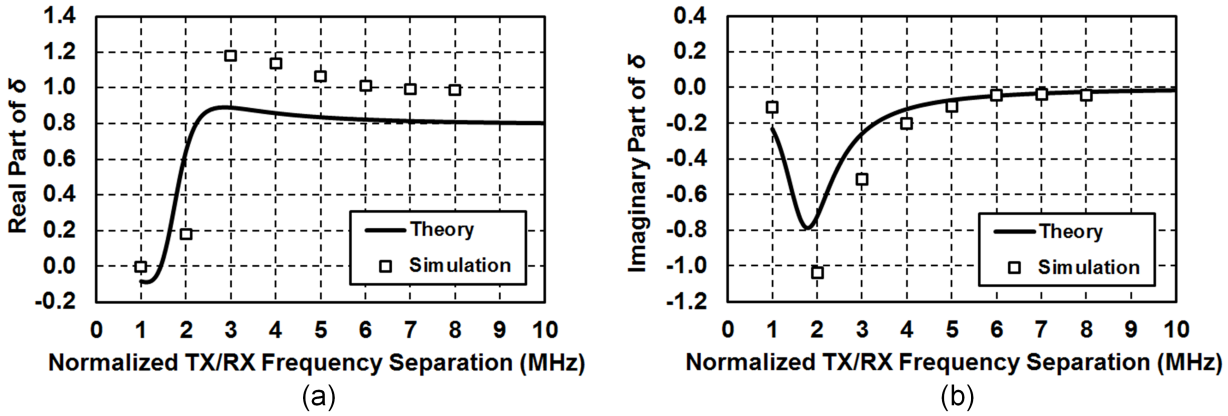

Figure 4.11: Simulated and calculated δ values for infinite large TB across various duplexing ratios: (a) real part of δ, and (b) imaginary part of δ.

receiver can be severely limited by the baseband TIAs, if nominal recombination settings are used at small TX/RX frequency offset.

Optimum conditions for the cross-modulation distortion cancellation (4.21) and (4.22) together with simulation results are plotted in Fig. 4.11. As from Fig. 4.11, given a normalized TX/RX frequency separation larger than 3, the NC-SIC RX baseband recombination conditions are within about 20% range to the nominal baseband recombination setting that correspond to the canceller noise cancellation cancellation condition. To support small TX/RX separation frequencies, TIAs with higher-ordering filtering [93] or large-signal blocker robust TIAs [94] are required.

4.5.2 Optimum Conditions for Simultaneous Noise and Distortion Cancellation

As shown in the previous subsection, the optimum baseband recombination conditions for the noise cancellation and for the distortion cancellation can be different. Thus, the overall receiver performance and ultimate baseband recombination setting should be determined jointly by both. A sensitivity defined in (4.23)[96], which includes the effects of cross-modulation distortion, is used to quantify the overall NC-SIC receiver performance under cancellation of strong TX SI. By substituting (4.6) and (4.3) into (4.23), we plot the RX sensitivity across the baseband recombination settings in Fig. 4.12. Signal bandwidth $BW = 2.5$ MHz, and $SNR = 10$ dB. The same interferences condition as for Fig. 4.10 is applied here. The sensitivity are plotted with normalized

TX/RX frequency separation set to be 4. In Fig. 4.12(a), for a sensitivity< -90 dBm, the real and imaginary part of δ can have a tolerance of about ± 0.25. Fig. 4.12(b) plots the sensitivity without cross-modulation distortion effects by setting TB to be infinite large. In this case, the tolerance in δ is significantly increased, indicating that the RX sensitivity here is more sensitive to the distortion cancellation.

$$\text{Sensitivity(dBm)} = 10\log_{10}\left[10^{\frac{P_j - TB}{10}} + kTB \cdot 10^{\frac{NF}{10}}\right] + SNR. \tag{4.23}$$

4.6 Circuit Implementation

The NC-SIC receiver (Fig. 4.13) is implemented in 65 nm CMOS. The LNTA uses a complementary topology for high linearity as was discussed in Section 4.4.1. The LNTA CG and CS devices are sized to have 20 mS and 80 mS transconductance, respectively. The 4-phase current-driven passive mixers are driven by 25% non-overlapping LO signals and are followed by baseband Rauch TIAs [93]. 8-phase mixing [84] would lower the receiver NF further by reducing noise folding effects, and would enable harmonic rejection. The 3^{nd} order Rauch TIAs offer high selectivity and low in-band impedance [93]. Large input shunt capacitors are used to help sink OOB TX SI current in the TIAs. The Rauch TIAs in the CS path are scaled by a factor of 4 to provide the nominal CG-CS recombination weighting. In addition, programmable recombination circuits combine the receiver outputs from the CG and CS paths for noise and cross-modulation distortion cancellation. They consist of eight 5-bit binary-weighted transconductance cells for programmable complex recombination weights, as each (I/Q) receiver output is driven by 5-bit cells from the CS and CG I and Q paths. Under large TX SI and TX noise, CG and CS cancellers are activated, respectively.

Both CG and CS cancellers adopt a Cartesian phase rotator topology which consists of two (I/Q) 6-bit variable-gain transconductance amplifiers (VGAs) as depicted in Fig. 4.13. For the CG canceller, an RF variable-gain TIA (VG-TIA) is inserted between the LNTA CG device and the phase rotator for gain variation and current-to-voltage conversion. Note that in the Cartesian phase rotators, the magnitude of the output current can also be modified through the VGAs at the expense of phase resolution. The phase-rotator VGAs are built using inverter-based transconductance

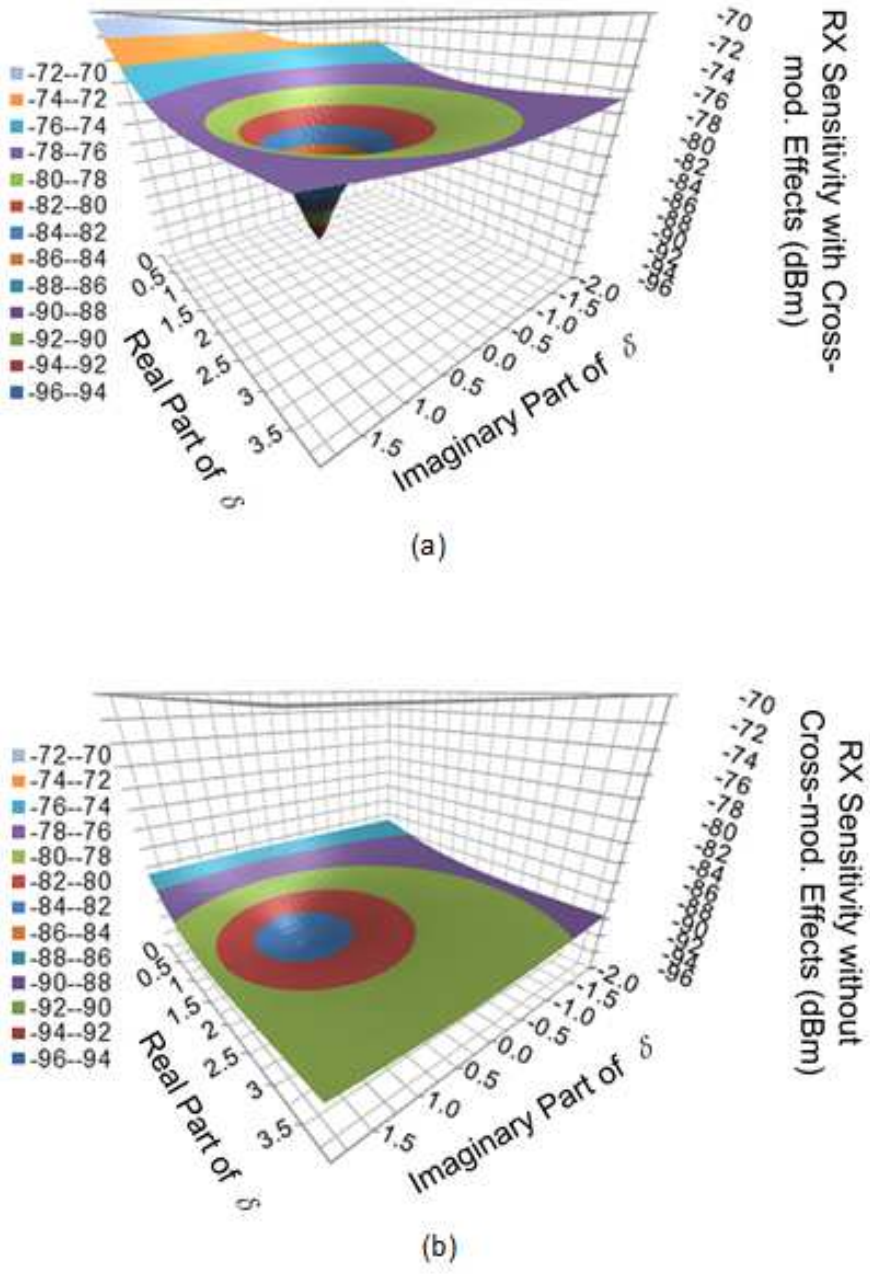

Figure 4.12: Simulated NC-SIC RX sensitivity across various baseband recombination settings: (a) with cross-modulation distortion effects, for a sensitivity< -90 dBm, the real and imaginary part of δ can have a tolerance of about ± 0.25; (b) without cross-modulation distortion effects, the tolerance in δ is significantly increased, indicating that the RX sensitivity here is more sensitive to the distortion cancellation.

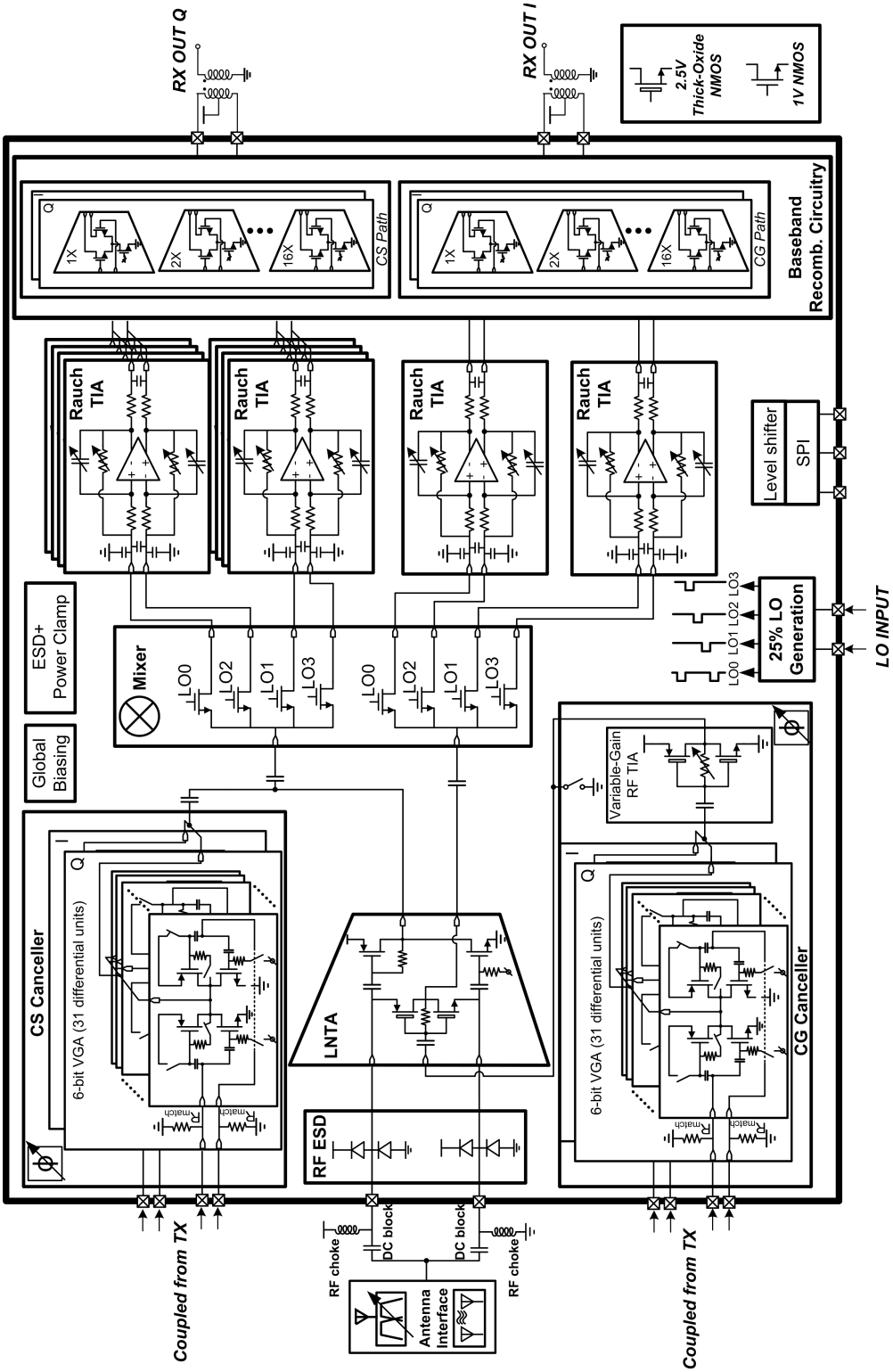

Figure 4.13: Block diagram and schematic for the implemented 65nm CMOS 0.3-1.7GHz NC-SIC receiver.

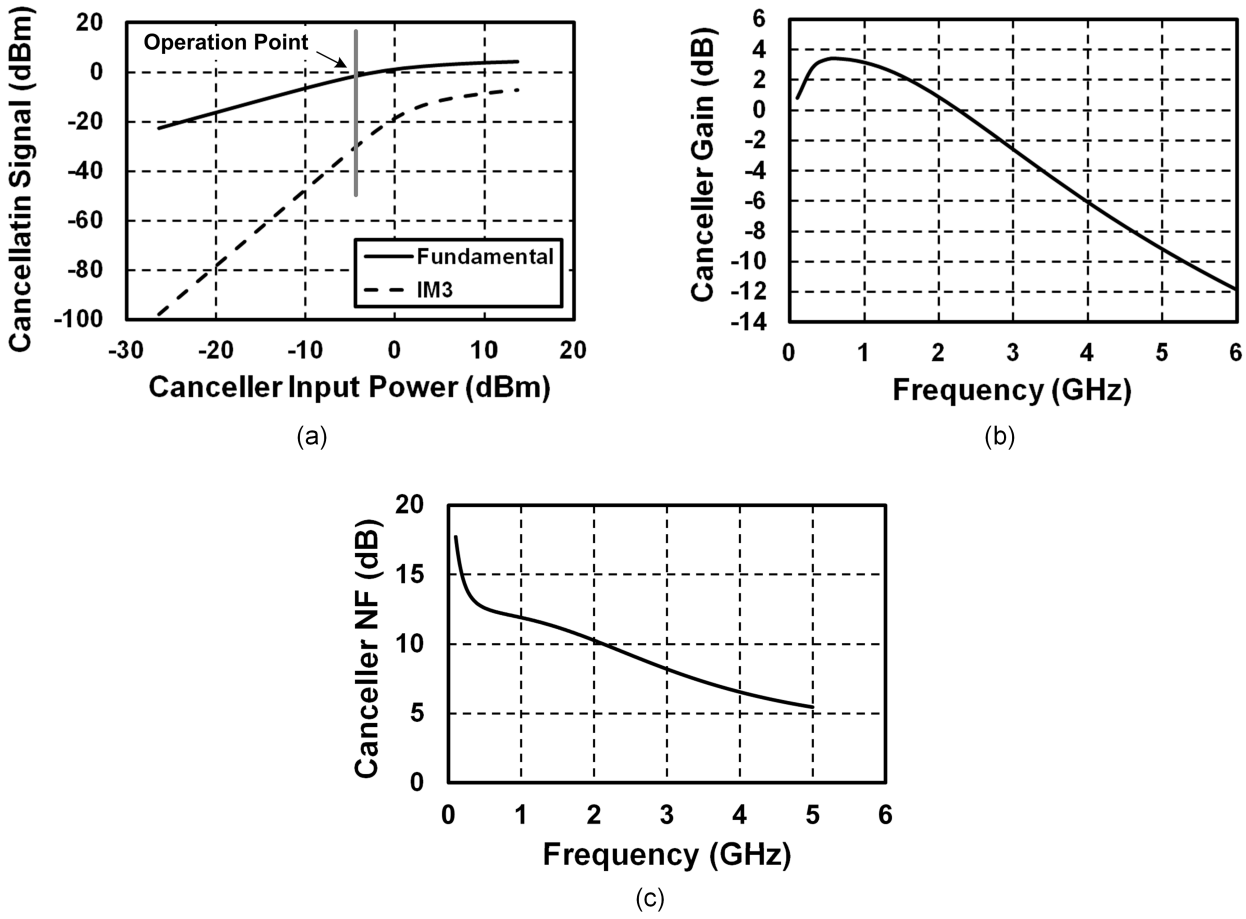

Figure 4.14: Simulated CG canceller performance at the highest gain setting: (a) two-tone large signal simulation where the output cancellation signal is the current generated by the CG device, represented in terms of the incident average TX SI power that can be cancelled, (b) AC small signal CG canceller power gain, and (c) CG canceller NF at the RX input.

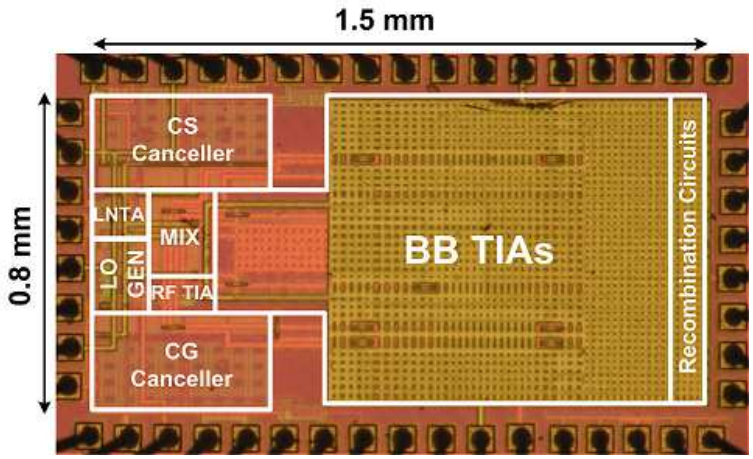

Figure 4.15: Chip microphotograph of the 65nm CMOS 0.3-1.7GHz NC-SIC receiver.

cells for high linearity. Both the RF VG-TIA and the LNTA CG device use thick oxide devices to handle large TX SI as shown in Fig. 4.13. Note that the CS canceller must be designed to deliver more current than the CG canceller by a factor equal to the CS device gain (4 in our prototype). The phase rotators require broadband quadrature signal generation which has not been implemented on chip in this prototype, but the proposed low-noise active cancellation scheme eases their implementation. Passive or active Polyphase Filters (PPFs) [97][98] may be employed. The loss of cascaded broadband passive PPFs can be compensated by the gain of the active canceller, while the noise of the broadband/reconfigurable active PPFs would be cancelled using the proposed scheme.

The simulated CG canceller performance is shown in Fig. 4.14 for peak gain setting. Fig. 4.14(a) depicts a two-tone simulation where the output cancellation signal is the current generated by the CG device, and is represented in terms of incident average TX SI power that can be cancelled (the peak TX SI power is 3dB higher). The CG canceller is able to generate a ¿0dBm cancellation signal (+3 dBm peak TX SI) while generating distortion products that are less than -30 dBm. Consequently, a TXRR of more than 30 dB is achievable before the CG canceller nonlinearity starts dominating the cross-modulation performance. Fig. 4.14(b) shows the small signal power gain of the CG canceller. It has a peak power gain of approximately 4 dB and a 3 dB bandwidth of approximately 2 GHz which is mainly limited by the thick oxide devices and is more than sufficient to cover the operating range. Finally, the simulated CG canceller NF is shown in Fig. 4.14(c).

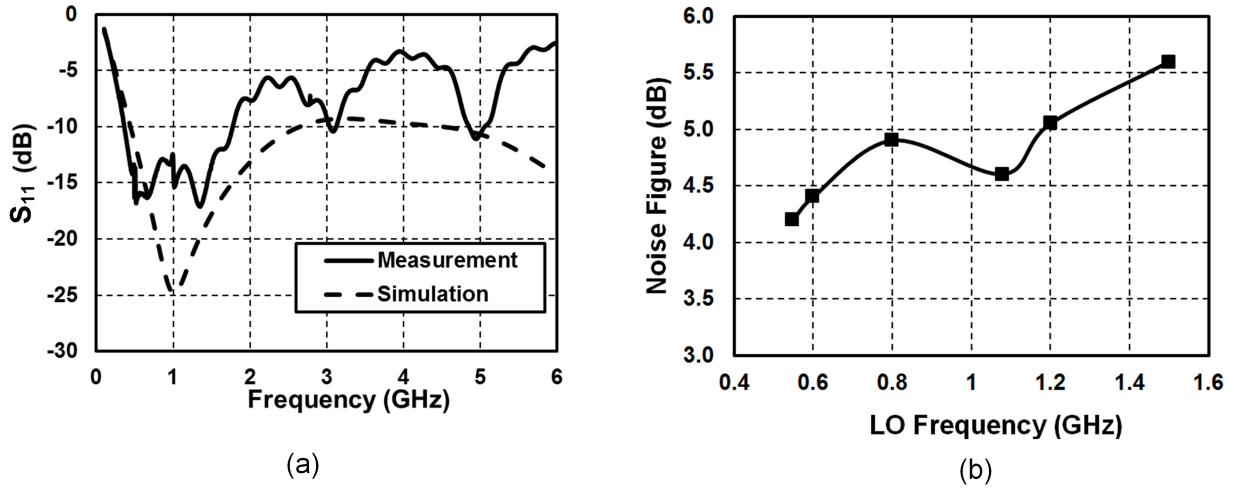

Figure 4.16: (a) Measured receiver S11, and (b) measured receiver NF across LO frequency with the cancellers inactive.

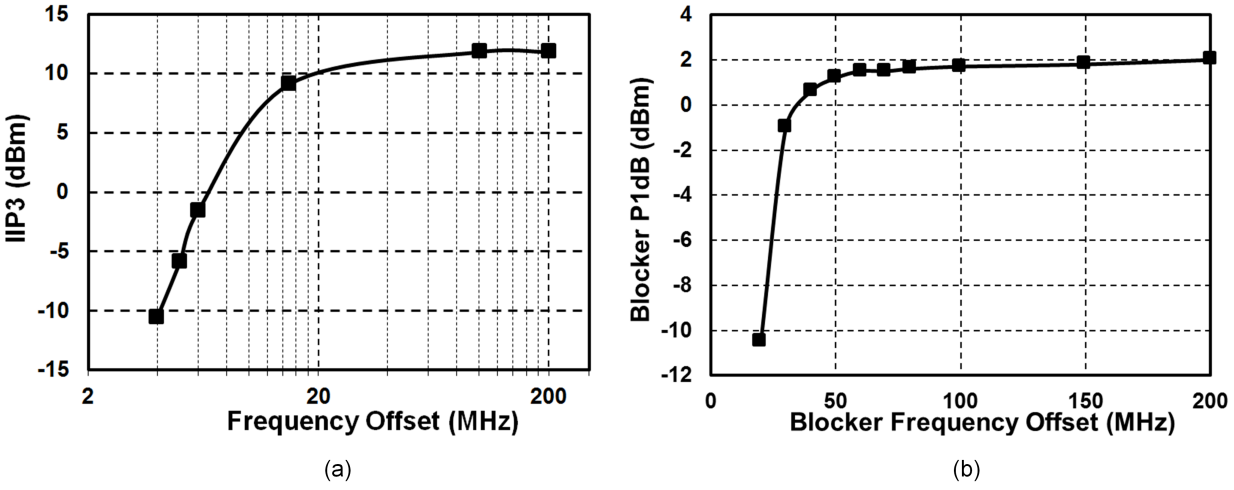

Figure 4.17: Measured receiver linearity with cancellers inactive: (a) receiver IIP3 versus offset frequency of the first tone of the two-tone input, and (b) receiver input-referred blocker P1dB.

4.7 Measurement Results

The chip micrograph is shown in Fig. 4.15. It has an active area of 1.2 mm^2. The chip is wire bonded and packaged in a 48-pin QFN package, and mounted on a 4-layer FR-4 PCB.

Generic receiver measurements are performed with both cancellers inactive, and without TX SI. The measured and simulated receiver S_{11} is plotted in Fig. 4.16(a) [3]. The measured receiver noise figure (Fig. 4.16(b)) ranges from 4.2 to 5.6 dB. The recombination weighting is optimized for NF in this measurement. Larger LNTA CS device transconductance and 8-phase mixing would further lower the receiver NF below 4.2dB at the low end of frequency. Simulations reveal that the degradation of NF versus frequency can be mitigated by optimizing the LO path design. The receiver has a measured OOB IIP_3 of +12 dBm, and OOB blocker-induced P1dB of +2 dBm (Fig. 4.17). While high OOB linearity is achieved through current-mode design, it is insufficient to tolerate >0 dBm TX SI.

Next, the receiver is measured in the presence of TX SI and with the CG canceller active (Fig. 4.18(a)). A two-tone signal with 1 MHz separation is fed into an off-the-shelf +30 dBm power amplifier. Couplers are used to couple a fraction of the transmitted power to the cancellers for TX SI and RX-band TX noise cancellation. A PCB-based planar antenna pair is used to model a co-existence environment with measured 30 dB isolation[99]. To measure cancellation at higher TX SI levels, an attenuator-based measurement setup is also used. Approximately 30 dB suppression is measured at the receiver input across a peak SI level ranging from −24 dBm to +2 dBm (Fig. 4.18(b)).

Next, the TB is measured by introducing an in-band jammer together with the two-tone OOB TX signal. Without cancellation, reducing our receiver to a generic current-mode receiver, the TB decreases at 20 dB/decade as TX SI power increases (Fig. 4.19(b)). The effective IIP_3 (calculated from the TB using eq. (4.7)) remains at +12-14 dBm, which matches the receiver OOB IIP_3 measurement shown in Fig. 4.17(a). Leakage cancellation is then enabled using the CG canceller. The baseband recombination circuits adjust the weights on the CG and CS paths for optimum TB performance. Currently, this adjustment is performed manually using trigonometric calculations

[3]The difference between the measured and simulated S_{11} is due to an erroneous RF SMA connector landing pad design on the PCB.

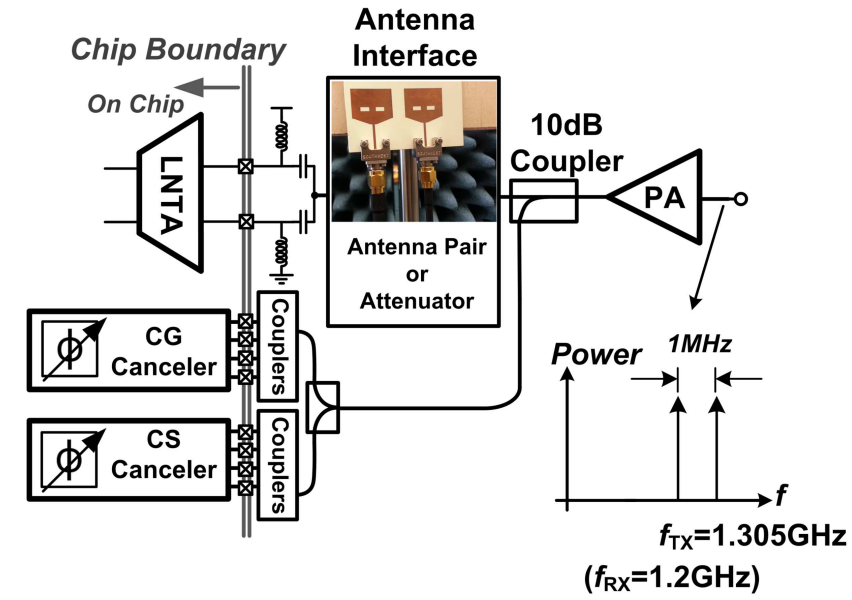

Figure 4.18: (a) Setup for TX SI cancellation measurements, and (b) cancellation of TX SI at the receiver input using the CG canceller using an antenna-pair based setup as well as an attenuator-based setup for higher SI levels.

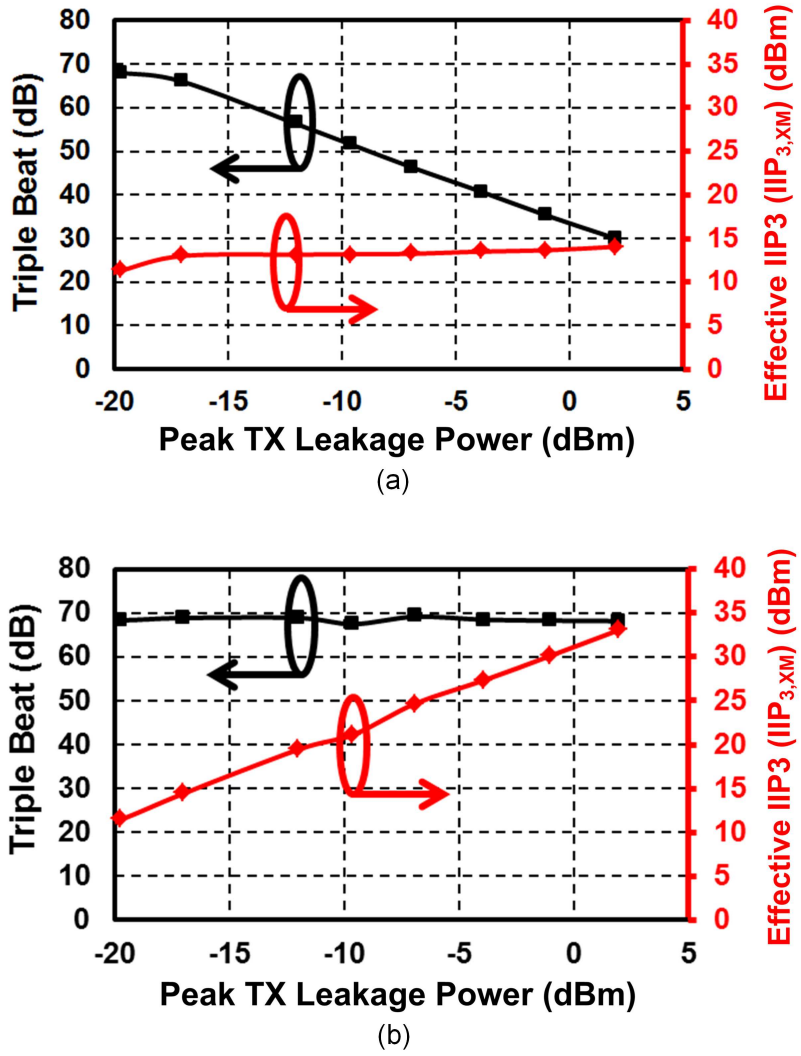

Figure 4.19: Receiver triple beat and effective IIP3 measurement: (a) without cancellation, and (b) with TX SI cancellation using the CG canceller. The baseband recombination circuits adjust the weights on the CG and CS paths for optimum TB performance.

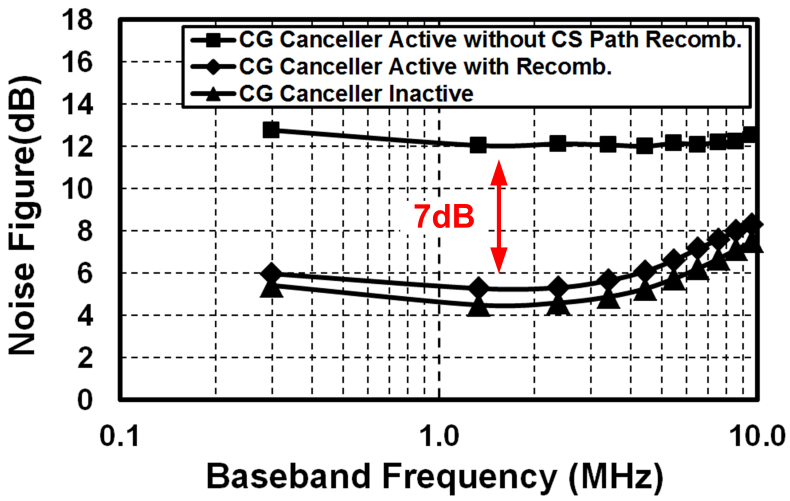

Figure 4.20: Measured receiver NF without the CG canceller active, with the CG canceller active, configured for cancelling +2 dBm peak TX SI and recombination cells configured for optimum TB performance, and with the CG canceller active but with noise cancellation disabled by turning off the recombination circuits in the CS path.

based on the cross-modulation product levels in the individual I and Q outputs of the CG and CS paths. The TB with TX SI cancellation remains constant at around 68 dB independent of the peak TX SI level ranging from −22 dBm to +2 dBm (Fig. 4.19(b)). The calculated receiver effective IIP_3 is as high as +33 dBm at +2 dBm peak TX SI. These TB and effective IIP_3 levels represent enhancements of 38 dB and 19 dB respectively over the RX performance in the absence of cancellation.

Fig. 4.20 shows the receiver NF when the CG-canceller is active and configured for cancelling +2 dBm peak TX SI. The recombination cells are also configured for optimum TB performance as was the case for Fig. 4.19(b). The noise figure degradation is less than 0.8 dB when compared to the receiver with the canceller disabled and with recombination cells configured for optimum NF. The analyses in Sections 4.3 and 4.4.1 quantify the achievable TB when the recombination is configured for optimum NF, but here we have measured the NF when the recombination is configured for optimum TB since TB typically limits the sensitivity in the presence of strong modulated TX SI. Hence, the NF increase is slightly higher than the theoretical result in Section 4.3. In addition, the receiver noise figure with the CG canceller active but with noise cancellation disabled by turning

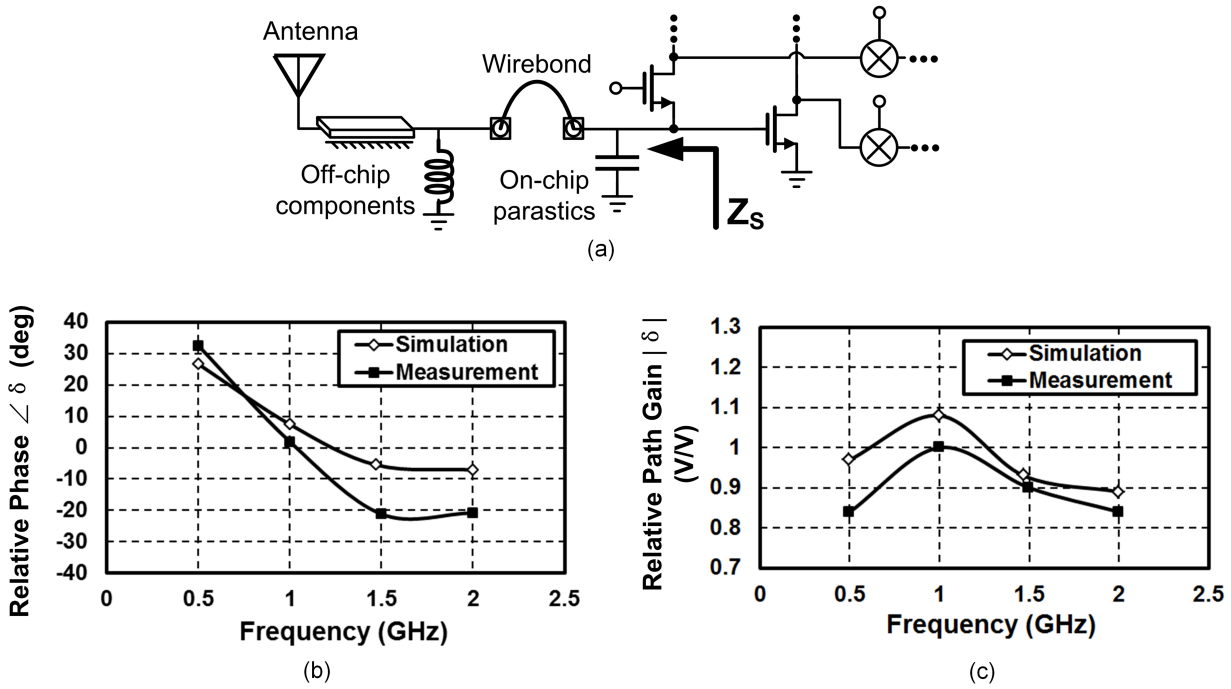

Figure 4.21: (a) Mechanisms of variation in source impedance. (b) Measured and simulated relative path gain in the baseband recombination cells for optimum noise performance of the receiver with CG canceller active and configured for maximum gain across frequency. (c) Measured and simulated relative phase adjustment in the baseband recombination cells for optimum noise performance.

off the recombination circuits in the CS path is measured. The noise figure is degraded by almost 7 dB, representing the penalty of performing active cancellation at the receiver input without our approach.

The SI, noise and cross-modulation cancellation have a dependence on the source impedance, which can deviate from 50 ohms due to on-chip and package parasitics, off-chip biasing components, as well as variations in the antenna impedance (Fig. 4.21(a)). The recombination condition for optimum receiver NF across frequency with CG canceller active and configured for maximum gain is measured to quantify the impact of the varying source impedance caused by package parasitics and off-chip biasing components (Fig. 4.21(b) and Fig. 4.21(c)). The optimum relative path gain for overall receiver NF is close to the nominal condition with less than 20% variation, while the optimal relative path phase varies from 32 to -22 degrees. They are relatively robust with respect to varying source impedance, and closely match simulations. While antenna tuner modules (ATMs) [100] somewhat limit antenna impedance variation, it is expected that adaptive digital calibration techniques will be required in practical scenarios.

Finally, both CG and CS cancellers are activated for simultaneous TX SI and TX noise cancellation. The TX SI is fixed at -6 dBm peak power[4] with varying RX band noise level. The effective TX noise in RX band after cancellation is computed from the measured total receiver noise after subtracting the contribution of the receiver itself. The CS-canceller's noise is not subtracted for a fair calculation. From Fig. 4.22, despite the CS canceller adding noise, up to 13 dB reduction of effective TX noise in the RX band is observed.

Table 4.1 summarizes the performance of the proposed receiver. When compared with the receivers with TX SI cancellation or suppression, our work exhibits wider operation bandwidth, higher OOB linearity and 30 dB improvement in maximum handled TX SI with less than 0.8 dB noise figure degradation. The NF degradation is even smaller than prior works where the TX SI is 30 dB weaker. When compared with highly linear software-defined receivers[54][101][93], our work has higher OOB linearity in the face of powerful modulated TX SI. Finally, our work also alleviates

[4] The reduced TX SI power level in this measurement is partly due to the measurement setup and partly due to the current delivery capability of the CS canceller. An auxiliary current-mode downconversion path for the cancellation of PA noise (similar to [63]) with independent baseband gain control would enable power-efficient cancellation at higher power levels.

Table 4.1: Performance summary and comparison with the state of the art.

	[46]	[64]	[54]	[101]	[93]	This work
Architecture	TX SI Cancellation/Suppression		Highly-Linear Software-Defined Radio			Current-Mode Receiver with active two-point low-noise TX-SI cancellation.
	Active TX Self-Interference Suppression After LNA	Active TX Self-Interference Cancellation After LNA	High Linearity Passive Mixer-First	Mixer First with Distortion Cancellation	Current-Mode RX with Highly-Linear LNTA	
CMOS Technology	180nm	250nm	65nm	65nm	40nm	65nm
RF Frequency	1.96GHz	800MHz	0.1-2.4GHz	0.2-2.6GHz	1.8-2.4(TDD)/ 1.8-2.1(FDD) GHz	0.3-1.7GHz
Gain	45dB	14.8dB (LNA)	40-70dB	26.5dB	45.5dB	19-34dB
Baseband BW	N/A	N/A	20MHz[1]	12MHz	1.4(TDD)/ 3.4(FDD) MHz	2-76MHz
DSB NF	3.1dB	1.4dB (LNA)	4dB	7.5dB	3.8(TDD)/ 3.1(FDD) dB	4.2dB
Blocker P1dB	N/A	N/A	+4dBm[2]	N/A	N/A	>+2dBm[3]
Out-of-band IIP3	N/A	N/A	+25dBm	+10/+18dBm[4]	+18(TDD)/ +16(FDD) dBm	**+12dBm/+33dBm[5]**
Maximum Handled Peak TX Leakage	-28dBm[6]	-28dBm[7]	N/A	N/A	N/A	**+2dBm[6]**
NF Degradation due to Leakage Cancellation	1.8dB	1.3dB (LNA)	N/A	N/A	N/A	**<0.8dB**
TB_{2dBm}[8]	9dB[9]	N/A	52dB[10]	22/38dB[10]	38(TDD)/ 34(FDD) dB[10]	**30dB (without cancellation) 68dB (with cancellation)**
TX Noise Cancellation	N/A	N/A	N/A	N/A	N/A	**13dB**
RX Power Consumption	114mW	N/A	37-70mW	17.3-36.7mW	30.7mW	74.6-83.0mW
Canceller Power Consumption	48mW	43mW	N/A	N/A	N/A	13-72mW
Active Area	N/A	N/A	2mm²	0.2 mm²	0.74 mm²	1.2 mm²

[1] Maximum BW [2] Blocker at 40MHz offset [3] Blocker at >60MHz offset [4] First tone at 135MHz/>450MHz offset
[5] Effective IIP3 for TX leakage under cancellation of +2dBm peak TX SI [6] 3dB Peak-to-average ratio
[7] 6dB Peak-to-average ratio [8] Triple beat at +2dBm peak TX leakage power [9] Calculated from reported TB at -28dBm TX leakage level
[10] Calculated from reported IIP3 (IIP3=0.5×TB+$P_{TX,avg}$) *Metrics related to the TX leakage cancellation are highlighted with*

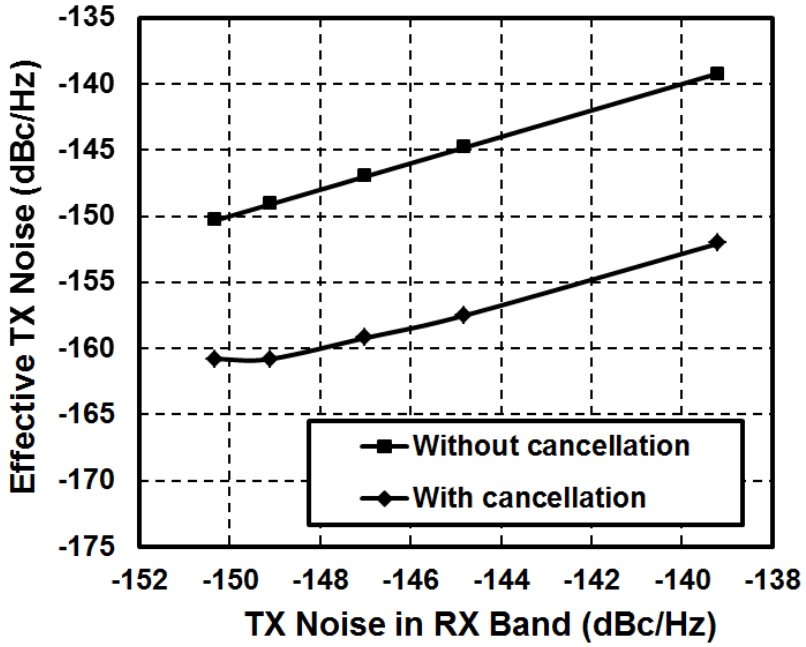

Figure 4.22: Measured TX noise cancellation results when both CG and CS cancellers are activated. The TX SI is fixed at −6 dBm peak power with varying RX band noise level.

the TX's RX-band noise requirement.

4.8 Summary

We presented an NC-SIC RX technique which breaks a fundamental trade-off between support for low antenna interface isolation levels (or equivalently, the power of TX SI being cancelled) and RX sensitivity degradation. This is accomplished through the insight that an active canceller that is integrated with the RX on the RFIC can be co-designed with the RX – by embedding the canceller within a noise-cancelling LNTA, the noise and distortion of the cancellation path is cancelled. Fundamentally, this co-design strategy introduces more degrees of design freedom when compared to a block-by-block partitioned design methodology where RF system building blocks are treated as "black boxes" with only input-output relations being defined.

The NC-SIC RX scheme can also be viewed as an active combining circuit that has ideally no noise penalty, and is able to handle large signals without generating distortion. Consequently, the scheme can be used to cancel any interference signal for which a replica can be generated.

A 0.3-1.7 GHz NC-SIC RX prototype was implemented in 65 nm CMOS for multiband FDD applications. It can cancel up to +2 dBm peak TX SI at the receiver input. The triple beat at +2 dBm peak TX SI is 68 dB and the effective IIP3 is +33 dBm, representing increases of 38 and 19 dB, respectively, over the receiver without cancellation. The associated increase in receiver NF is less than 0.8 dB. In addition, the scheme effectively suppresses TX noise in RX band by up to 13 dB. It should be noted that the NC-SIC RX prototype presented here aimed for multiband FDD applications, but variants of the NC-SIC architecture based on a similar co-design methodology (such the one in [9] which has been developed in parallel) can be employed for full-duplex wireless communication systems.

Chapter 5

Frequency-Domain Equalization at RF for Integrated Wideband Self-Interference Cancellation

One of the fundamental challenges associated with SIC in the RF domain as discussed in Chapter 3 is the cancellation BW due to the frequency selectivity of the antenna interface. Conventional integrated SI cancellers have frequency-flat magnitude and phase response, and thus can only emulate the antenna interface isolation at a single frequency point, resulting in narrowband SIC. In this Chapter, we introduce *integrated* wideband SIC in the RF domain based on *frequency-domain equalization (FDE)* of the wireless SI channel. *This concept brings FDE, a functionality that is traditionally implemented in the digital signal-processing block, to the RF domain – multiple RF bandpass filters (BPFs) are included in the SI canceller that channelize the desired signal bandwidth; within each channel, the BPF mimics the wireless SI channel in the frequency domain. The applicability of this technique to integrated wideband SIC in the RF domain is enabled by recent advances in the implementation of tunable, reconfigurable, high quality factor (high-Q) RF BPFs in nanoscale CMOS, namely N-path filters [12][37][39][40][102][41].*

This Chapter is organized as follows. Section 5.1 discusses the division of classic RF system functional domains and an emerging trend of unifying the different functional blocks to enable new wireless communications paradigms. Section 5.2 presents the integrated FDE-based wideband SIC

technique in the RF domain. For the realization of high-Q, widely-tunable RF BPFs, a two-port N-path G_m-C filter with embedded variable attenuation and phase shifting is introduced in Section 5.3. Sections 5.4 discusses the implementation of a 0.8-to-1.4 GHz 65 nm CMOS receiver that employed the FDE-based canceller for full-duplex and multi-band FDD wireless communications systems. Measurement results are given in Section 5.5 using a pair of frequency-selective antenna interfaces: (i) a custom-designed LTE-like 0.780/0.895 GHz LC-based duplexer for FDD with 30 dB peak TX/RX isolation, 11 ns peak isolation group delay and 7 dB isolation magnitude variation across the TX band, and (ii) a 1.4 GHz antenna pair for full-duplex with 32 dB peak TX/RX isolation, 9 ns peak isolation group delay and 3 dB isolation magnitude variation over 1.36 GHz to 1.38 GHz. Finally, Section 5.6 summaries this Chapter.

5.1 Classic RF System Functional Domains

RF systems are divided into several functional domains, namely the antenna, RF, analog, and digital domains as illustrated in Fig. 5.1. There are several reasons for this classic RF system division. One reason is that historically different technologies were used in different domains for performance or cost considerations. For instance, amplifiers and mixers at RF front-end used III-V compound semiconductor technology [103][104], analog baseband circuitry (such as filters and variable amplifiers) adopted bipolar process [105], and digital signal processing unit employed CMOS technology [106]. Another reason for this division is that different disciplines are applied to these domains – electromagnetics is required in designing antennas, microwaving engineering guides the RF front-end design, circuits theory is applied to analog baseband circuitry, and signal processing techniques are employed in the digital domain.

Today, ultra-scaled CMOS technology allows increasing functional integration onto a single silicon platform. This integration potential opens up a plethora of new design spaces, where a holistic approach that unifies the different functional blocks in a traditional RF system is emerging. For instance, channel selection that is conventionally performed in the analog and digital domains has been brought to RF for the simplicity that it affords in RX design and the promise of emerging concepts like cognitive radio [107][95][79]. In the following sections, we will demonstrate how equalization, a functionality that is traditionally implemented in the digital domain, can be realized

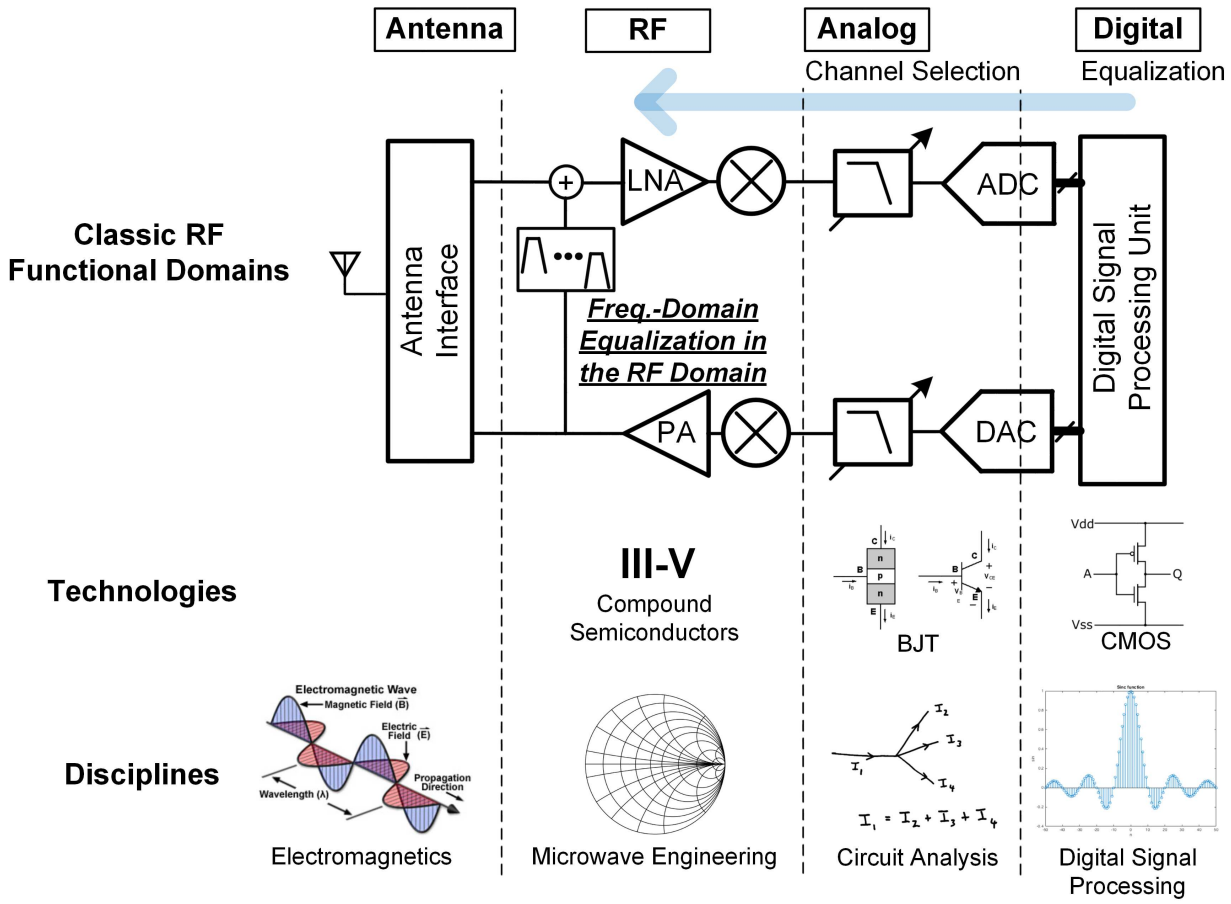

Figure 5.1: Classic RF system functional domains and an emerging trend of unifying the different functional blocks. In this Chapter, we will demonstrate how equalization, a functionality that is traditionally implemented in the digital domain, can be realized at RF, enabling wideband SIC for full-duplex and multiband frequency-division duplexing wireless applications.

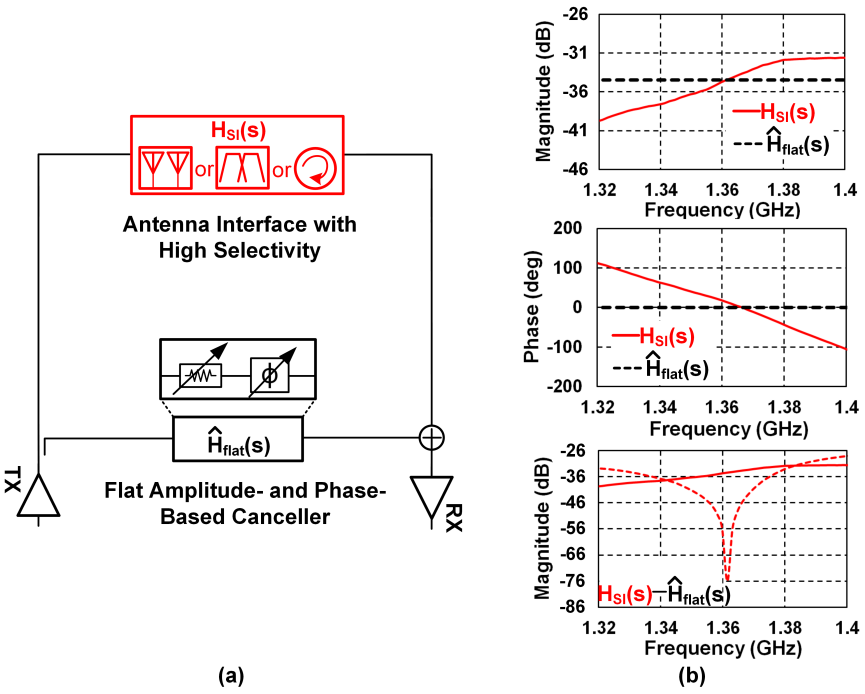

Figure 5.2: Conventional frequency-flat RF canceller based on amplitude-and-phase scaling: (a) block diagram and (b) frequency responses of an antenna interface and the RF canceller and the resultant SIC. Measured isolation transfer function (TF) of a 1.4 GHz antenna pair (see Fig. 5.24) is used for $H_{SI}(s)$.

at RF, enabling wideband SIC for full-duplex and multiband frequency-division duplexing (FDD) wireless applications.

5.2 Frequency-Domain-Equalization-based SIC in the RF Domain

5.2.1 Concept

As discussed in Chapter 3, RF SIC BW is typically limited by the frequency selectivity of the antenna interface isolation (such as that of a T/R antenna pair, duplexer or circulator and including environmental reflections for full-duplex). Figure 5.2(a) illustrates a full-duplex transceiver with a conventional frequency-flat RF canceller based on amplitude-and-phase scaling. Fig. 5.2(b) plots

the measured isolation Transfer Function (TF) [1] of a 1.4 GHz antenna pair (see Fig. 5.24) $H_{SI}(j\omega)$ with 32 dB peak TX/RX isolation, 9 ns peak isolation group delay and 3 dB isolation magnitude variation over 1.36 GHz to 1.38 GHz. The TF of a frequency-flat amplitude-and-phase-based RF canceller is also plotted in Fig. 5.2(b). The conventional RF canceller can only emulate the frequency selective antenna interface at a single cancellation frequency, resulting in a 20 dB SIC BW of about 3 MHz in Fig. 5.2(b). This matches very well with the result in (3.3) given in Chapter 3.

To enhance the cancellation BW, 2^{nd}-order reconfigurable BPFs with amplitude and phase control in each path are introduced in the RF canceller [Fig. 5.3(a)]. The reconfigurable BPFs can be modeled using a 2^{nd}-order RLC BPF as shown in Fig. 5.4, where transconductance g_i and phase ϕ_i present the amplitude and phase control in the i^{th} path. The short termination at the canceller output represents the virtual ground created by SIC. The TF of the i^{th} path is:

$$\hat{H}_i(j\omega) = \frac{A_i \exp(-j\phi_i)}{1 - jQ_i\frac{\omega_i}{\omega}(1 - \frac{\omega^2}{\omega_i^2})}, \tag{5.1}$$

where $Q_i = \frac{R||R_{p,i}}{\omega_i L_i}$ represents the quality factor, $\omega_i = 1/\sqrt{L_i C_i}$ is the center frequency, and $A_i = \frac{g_i R_{p,i}}{R_{p,i}+R}$ and ϕ_i are the magnitude and phase settings of the i^{th} BPF, respectively. *Thus, an RF canceller with a reconfigurable 2^{nd} order RF BPF features four degrees of freedom (A_i, ϕ_i, Q_i, and ω_i) and enables the replication of not just the magnitude and phase of the antenna interface isolation at a frequency point, but also the slope of the magnitude and the slope of the phase (or group delay),* enhancing the 20 dB SIC BW from 3 MHz to 19 MHz as shown in Fig. 5.3(b).

The use of a filter bank with independent BPF parameters enables such replication at multiple points in different frequency sub-bands, further enhancing SIC BW. In Fig. 5.3(c), the use of two filters enhances the 20 dB SIC BW to 32 MHz, respresenting a 10× improvement over a conventional RF canceller. *Essentially, this approach is frequency-domain equalization (FDE) in the RF domain.*

[1] To obtain this isolation TF, the antenna pair S-parameters are first measured. Using the measured S-parameters, the RX port output current is simulated with a short-circuit termination at the RX port The short represents the virtual ground created by SIC at the RX port. The isolation TF is then computed by multiplying the short-circuit output current by the reference resistance.

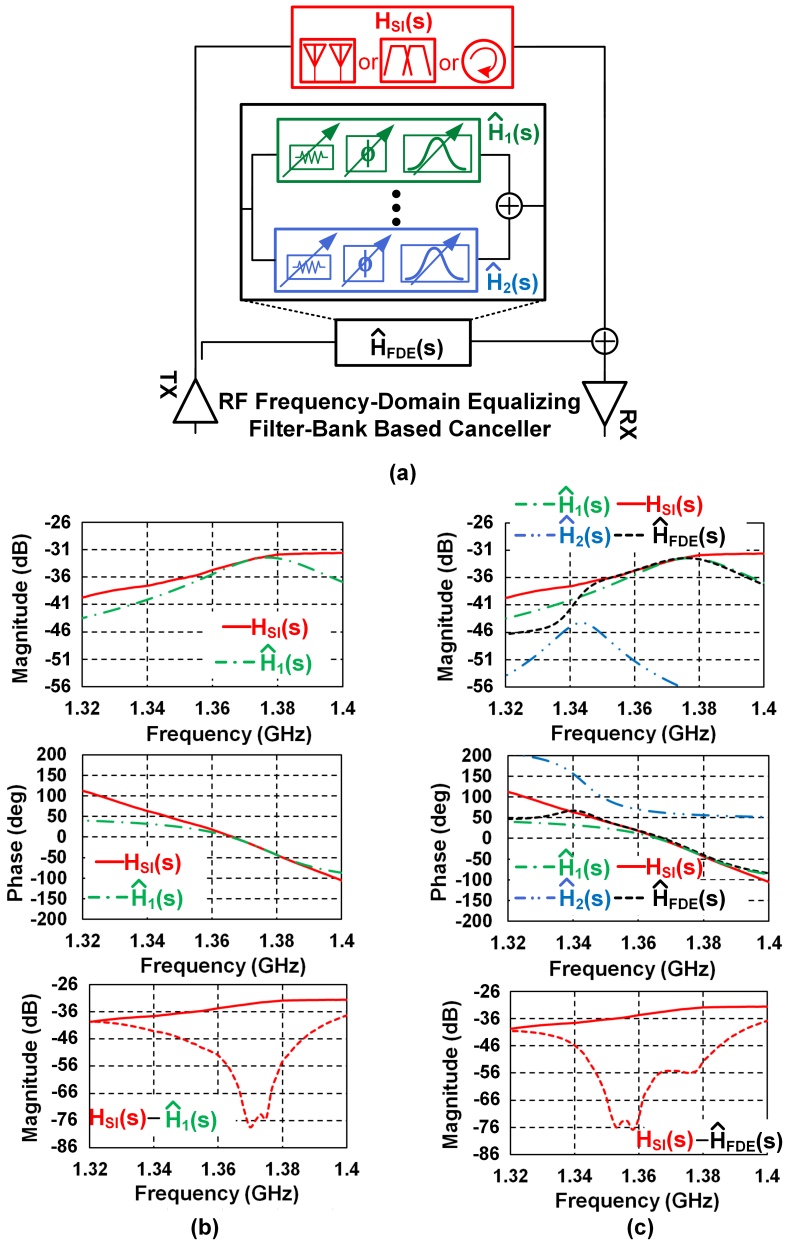

Figure 5.3: Proposed RF canceller based on frequency-domain equalization: (a) block diagram, (b) frequency responses of the antenna interface and the RF canceller with one filter and the resultant SIC, and (c) frequency responses of the antenna interface and the RF canceller with two filters and the resultant SIC. The $H_{SI}(s)$ is the same as in Fig. 5.2. The TFs of the canceller filters $\hat{H}_1$ and $\hat{H}_2$ follow (5.1). The canceller filter settings are mentioned in the text.

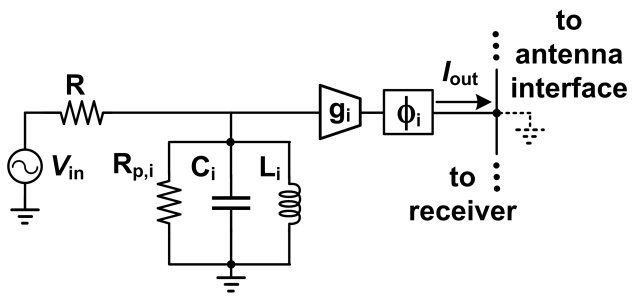

Figure 5.4: The equivalent 2^{nd}-order RLC BPF model for the BPF in Fig. 5.3(a). Transconductance g_i and phase ϕ_i represent the amplitude and phase control. The short termination at the canceller output represents the virtual ground created by SIC.

5.2.2 RF SIC Equalizer Coefficient Derivation

Similar to traditional FDE in digital (e.g., [108]), the RF SIC equalizer coefficient (A_i, ϕ_i, Q_i, and ω_i) can be derived from the SI channel transfer function $H_{SI}(j\omega)$. Furthermore, an iterative successive approach is employed to configure the RF BPFs in the equalizer.

From the RF BPF transfer function (5.1), we have the i^{th} BPF magnitude, phase, magnitude slope, and phase slope (group delay) as:

$$\begin{aligned}
|\hat{H}_i(j\omega)| &= \frac{A_i}{\sqrt{1+K(\omega)^2}}, \\
\angle\hat{H}_i(j\omega) &= \arctan K(\omega) - \phi_i, \\
\frac{d|\hat{H}_i(j\omega)|}{d\omega} &= \frac{K(\omega)}{1+K(\omega)^2}\frac{Q_i\omega_i}{\omega^2}(1+\frac{\omega^2}{\omega_i^2})|\hat{H}_i(j\omega)|, \\
\frac{d\angle\hat{H}_i(j\omega)}{d\omega} &= -\frac{1}{1+K(\omega)^2}\frac{Q_i\omega_i}{\omega^2}(1+\frac{\omega^2}{\omega_i^2}),
\end{aligned} \tag{5.2}$$

where $K(\omega) = Q_i\frac{\omega_i}{\omega}(1-\frac{\omega^2}{\omega_i^2})$. Using i^{th} BPF to emulate the antenna interface isolation magnitude, phase, magnitude slope, and phase slope (group delay) at the i^{th} BPF cancellation frequency $\omega_{SIC,i}$ results in:

$$\begin{aligned}
|\hat{H}_i(j\omega_{SIC,i})| &= |H_{SI}(j\omega_{SIC,i})|, \\
\angle\hat{H}_i(j\omega_{SIC,i}) &= \angle H_{SI}(j\omega_{SIC,i}) + \pi, \\
\frac{d|\hat{H}_i(j\omega)|}{d\omega}|_{\omega=\omega_{SIC,i}} &= \frac{d|H_{SI}(j\omega)|}{d\omega}|_{\omega=\omega_{SIC,i}}, \\
\frac{d\angle\hat{H}_i(j\omega)}{d\omega}|_{\omega=\omega_{SIC,i}} &= \frac{d\angle H_{SI}(j\omega)}{d\omega}|_{\omega=\omega_{SIC,i}}.
\end{aligned} \tag{5.3}$$

Therefore, the coefficients of the equalizer RF BPF can be solved from (5.2) and (5.3) as:

$$\begin{aligned}
\phi_i &= \angle H_{SI}(j\omega_{SIC,i}) + \arctan\frac{B}{|H_{SI}(j\omega_{SIC,i})|} + \pi, \\
\omega_i &= \sqrt{\frac{1+P}{1-P}}\omega_{SIC,i}, \\
Q_i &= -\frac{B}{|H_{SI}(j\omega_{SIC,i})|}\frac{1+P}{2P}, \\
A_i &= \sqrt{1+K(\omega_{SIC,i})^2}|H_{SI}(j\omega_{SIC,i})|,
\end{aligned} \tag{5.4}$$

where $\omega_{SIC,i}$ is the cancellation frequency for the i^{th} BPF, and B, P, and K are shorthand notations defined as:

$$\begin{aligned}
B &= \frac{\frac{d|H_{SI}(j\omega)|}{d\omega}|_{\omega=\omega_{SIC,i}}}{\frac{d\angle H_{SI}(j\omega)}{d\omega}|_{\omega=\omega_{SIC,i}}}, \\
K(\omega_{SIC,i}) &= -B/|H_{SI}(j\omega_{SIC,i})|, \\
P &= \frac{B^2|H_{SI}(j\omega_{SIC,i})|}{(B^2+|H_{SI}(j\omega_{SIC,i})|^2)}\left(\frac{d|H_{SI}(j\omega)|}{d\omega}|_{\omega=\omega_{SIC,i}}\omega_{SIC,i}\right)^{-1}.
\end{aligned} \tag{5.5}$$

In Fig. 5.3(b), $\omega_{SIC,1}$ is chosen to be $2\pi\times1.370$ Grad/sec. Based on (5.4), $\omega_1 = 2\pi\times1.377$ Grad/sec, $Q_1 = 40.6$, $A_1 = -32.4\ dB$ and $\phi_1 = -33.3°$.

As mentioned before, an iterative successive cancellation approach is used for FDE in the RF domain. In Fig. 5.3(c), $\hat{H}_1$ first emulates the antenna interface H_{SI} at $\omega_{SIC,1} = 2\pi\times1.370$ Grad/sec, then $\hat{H}_2$ replicates the residual response $(H_{SI} - \hat{H}_1)$ at $\omega_{SIC,2} = 2\pi\times1.350$ Grad/sec. Since the introduction of $\hat{H}_2$ will adversely affect the cancellation originally achieved at $\omega_{SIC,1}$, iteration of $\hat{H}_1$ and $\hat{H}_2$ is required. In Fig. 5.3(c), the filter parameters calculated using (5.4) in an iterative successive fashion are: $\omega_1 = 2\pi \times 1.377$ Grad/sec, $Q_1 = 40.6$, $A_1 = -32.4\ dB$, $\phi_1 = -33.3°$, $\omega_2 = 2\pi \times 1.343$ Grad/sec, $Q_2 = 81.2$, $A_2 = -44.2\ dB$, $\phi_2 = 133.3°$.

5.3 Bandpass Filters for the RF SIC Equalizer

As shown in the previous Section, reconfigurable RF BPFs with high quality factor (e.g. as high as 81.2 in the example shown in Fig. 5.3) are required to channelize the SI signal bandwidth for FDE in the RF domain. However, integrated RF BPFs have been notoriously difficult to implement. In this section, we first review two popular approaches to the implementations of integrated RF BPFs and then introduce our proposed two-port N-path G_m-C filter with embedded variable attenuation and phase shifting.

5.3.1 Integrated RF Bandpass Filters

This sub-section discusses and compares two commonly used approaches for the design of integrated high-Q RF BPFs, namely the Q-enhanced LC-based technique [109][11][110][111] and N-path filters [12][37][39][40][102][41] [2].

RF BPFs can be realized by using LC circuitry. However, the qualify factor of integrated RF BPFs based on LC topology is limited by the inductor qualify factor. To compensate the loss in the LC tank, the Q-enhanced LC-based technique has been proposed [109][11][110]. Fig. 5.5 shows a basic RF BPF design using the Q-enhanced technique. A negative resistor R_N that can be implemented as a transconductor with positive feedback is introduced to offset the LC tank loss represented by R_P [11]. In theory, the achievable quality factor for Q-enhanced RF BPFs can be as high as desired. However, at large quality factor enhancements, the negative resistance R_N must be carefully controlled to avoid oscillation, limiting the achievable quality factor. While a Q-factor of 400 at 2.4 GHz has been reported in [111], Q-enhanced LC RF BPFs have several disadvantages such as the need for inductors which are not friendly with process scaling, limited frequency tuning range, and poor dynamic range performance. In addition, phase shifting capability that is required by the RF equalizer BPF cannot be easily embedded within a Q-enhanced BPF.

The idea of N-path filters dates back to the 1940s and was demonstrated by using an electromechanical circuit [12]. As depicted in Fig. 5.6(a), a mechanical wheel holding a number of capacitors is rotated by the rotating brushes, making each capacitor charge to the input first through R_1 and then discharge at the output through R_2. The magnitude response of the circuit is shown in

[2] A review of the implementations of integrated high-Q analog/RF BPFs can be found elsewhere (such as [112]).

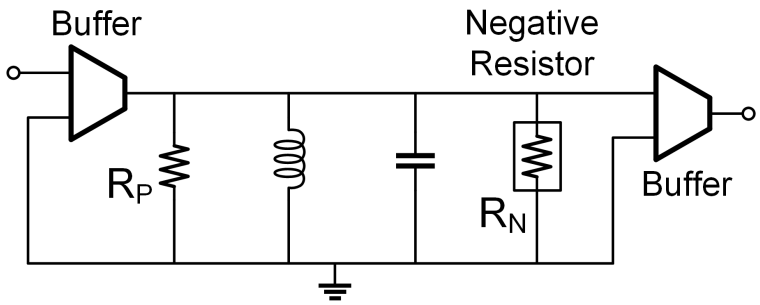

Figure 5.5: A basic Q-enhanced RF BPF design with a lossy LC tank and a negative resistor [11].

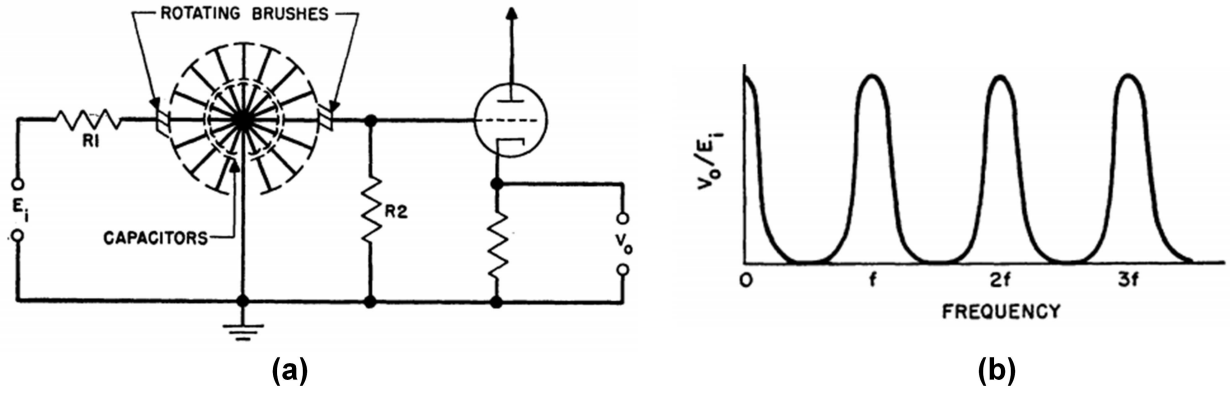

Figure 5.6: (a) A 1948 electromechanical circuit that produces a "comb filter" type of frequency response and (b) the type of frequency response produced. The mechanical rotational frequency fixes the location of the pass bands of the "comb filter", and the RC time constant fixes the width of each pass band [12].

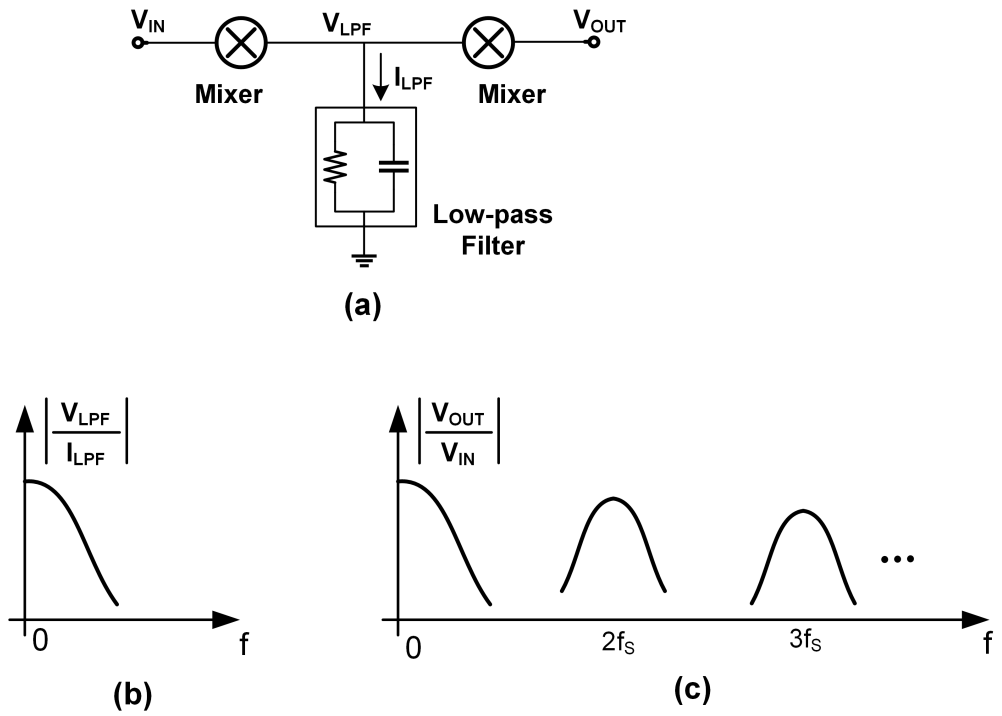

Figure 5.7: Intuitive explanation of N-path filters operation: (a) N-path filters conceptual diagram; (b) low-pass response at the intermediate node of N-path filters; and (c) the bandpass response of N-path filters that can be intuitively understood as the low-pass response being upconverted to RF by the mixer switching actions.

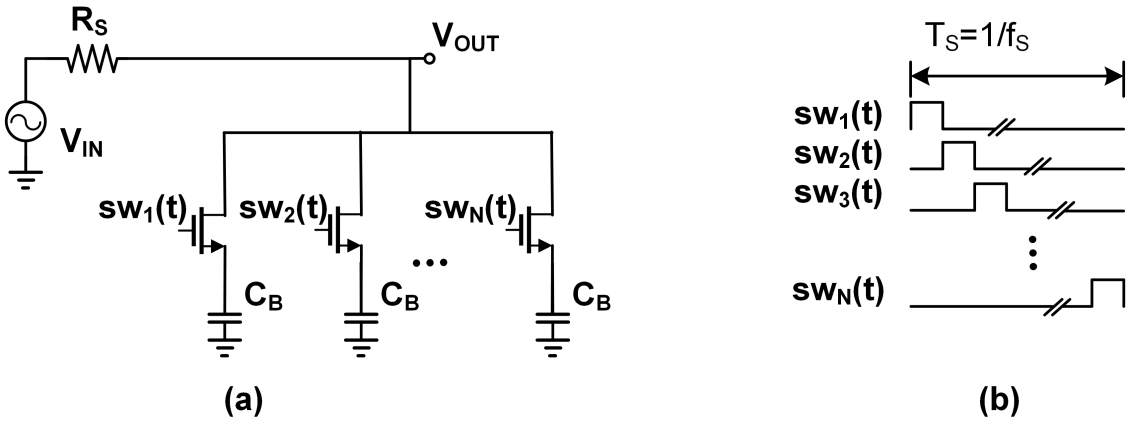

Figure 5.8: One-port N-path filter in CMOS: (a) schematic and (b) clock timing diagram.

Fig. 5.6(b) revealing a "comb filter" type of response. The mechanical rotational frequency fixes the location of the pass bands of the "comb filter", and the RC time constant fixes the width of each pass band.

The operation of N-path filters can be understood intuitively. The two rotating brushes in Fig. 5.6(a) can be treated as two sets of mixers at the input and output sides as shown in Fig. 5.7(a), and the resistors and capacitors form a low-pass filter between the mixers. An input signal is first downconverted to a baseband frequency, then processed by the RC low-pass filter, and finally upconverted back to the RF frequency. This process essentially transfers an RC low-pass response [Fig. 5.7(b)] to a bandpass response [Fig. 5.7(c)] centered around the mixer switching frequency and its harmonics. For exact modelings of N-path filters, linear periodically time-variant (LPTV) analyses can be applied [38][39][41].

Thanks to the advancement in modern ultra-scaled CMOS technology, transistors are able to efficiently switched at gigahertz frequency range, making N-path filters a promising solution for the implementation of integrated widely-tunable high-Q RF filters as shown in Fig. 5.8 [39][40]. When compared to the Q-enhanced LC-based RF BPFs, N-path filters in CMOS have more compact size, wider frequency tuning range, and better dynamic range performance that is decoupled with Q-factors [112]. Furthermore, as we will discuss in the next subsection, phase shifting can be embedded within a two-port N-path filter, making N-path filters a viable solution for the RF FDE technique.

5.3.2 Proposed Two-Port N-path Canceller Filter with Embedded Phase Shifting

As discussed in the previous subsection, N-path filters in CMOS have advantages of being area efficient, widely tunable, and having better dynamic range performance when compared to other approaches to the design of integrated RF BPFs (such as the Q-enhanced LC RF BPF). Here, we introduce a two-port N-path G_m-C filter that has embedded variable attenuation and phase shifting for the realization of RF equalizer BPFs.

Fig. 5.9(a) depicts a two-port N-path filter, where R_S and R_L are the resistive loads at the TX and RX sides, respectively. C_C weakly couples the cancellation signal to the receiver input for self-interference cancellation. The quality factor of an N-path filter may be reconfigured via the baseband capacitor C_B, given fixed R_S and R_L. LPTV analysis yields [38]:

$$Q = 4\pi f_S((R_S + R_{on})||(R_L + R_{on}))C_B, \tag{5.6}$$

where R_{on} is the on-resistance of the N-path switches, f_S is the switching frequency, and we have ignored the loading effect of C_C. Through clockwise/counter-clockwise [only counter-clockwise connection is shown in Fig. 5.9(a) for simplicity] connected baseband reconfigurable transconductors (G_m), an upwards/downwards frequency offset with respect to the switching frequency can be obtained [113]. The frequency offset of the center frequency to the switching frequency is given by $\Delta\omega = \frac{G_m}{C_B}$[113]. Variable attenuation can be introduced by reconfiguring R_S and R_L relative to each other [Fig. 5.9(b)]. The magnitude response at the center frequency is:

$$|H(j\omega_S)| = \left|\frac{I_{canceller}}{V_{in}}\right|_{\omega=\omega_S} R_0 = \left|\frac{V_{out}}{V_{in}}\right|_{\omega=\omega_S} \times \omega_S C_C R_0 \approx \frac{8}{\pi^2}\frac{(R_L + R_{on})\omega_S C_C R_0}{R_S + R_L + 2R_{on}}, \tag{5.7}$$

where we have ignored the loading effect of C_C when calculating V_{out}. It should be noted that once cancellation is performed, V_{RX} is a virtual ground. The canceller transfer function is computed by finding the $I_{canceller}$ that flows into the virtual ground and multiplying it by the reference resistance R_0. Also, in (5.7), the center frequency is assumed to be ω_S, i.e. G_m=0, for simplicity.

Interestingly, phase shifting can be embedded in a two-port N-path filter by phase shifting the LOs driving the switches on the output side as in Fig. 5.9. A complete LPTV analysis of a two-port N-path filter with embedded phase shifting in [41] reveals that phase shifting the LOs driving the

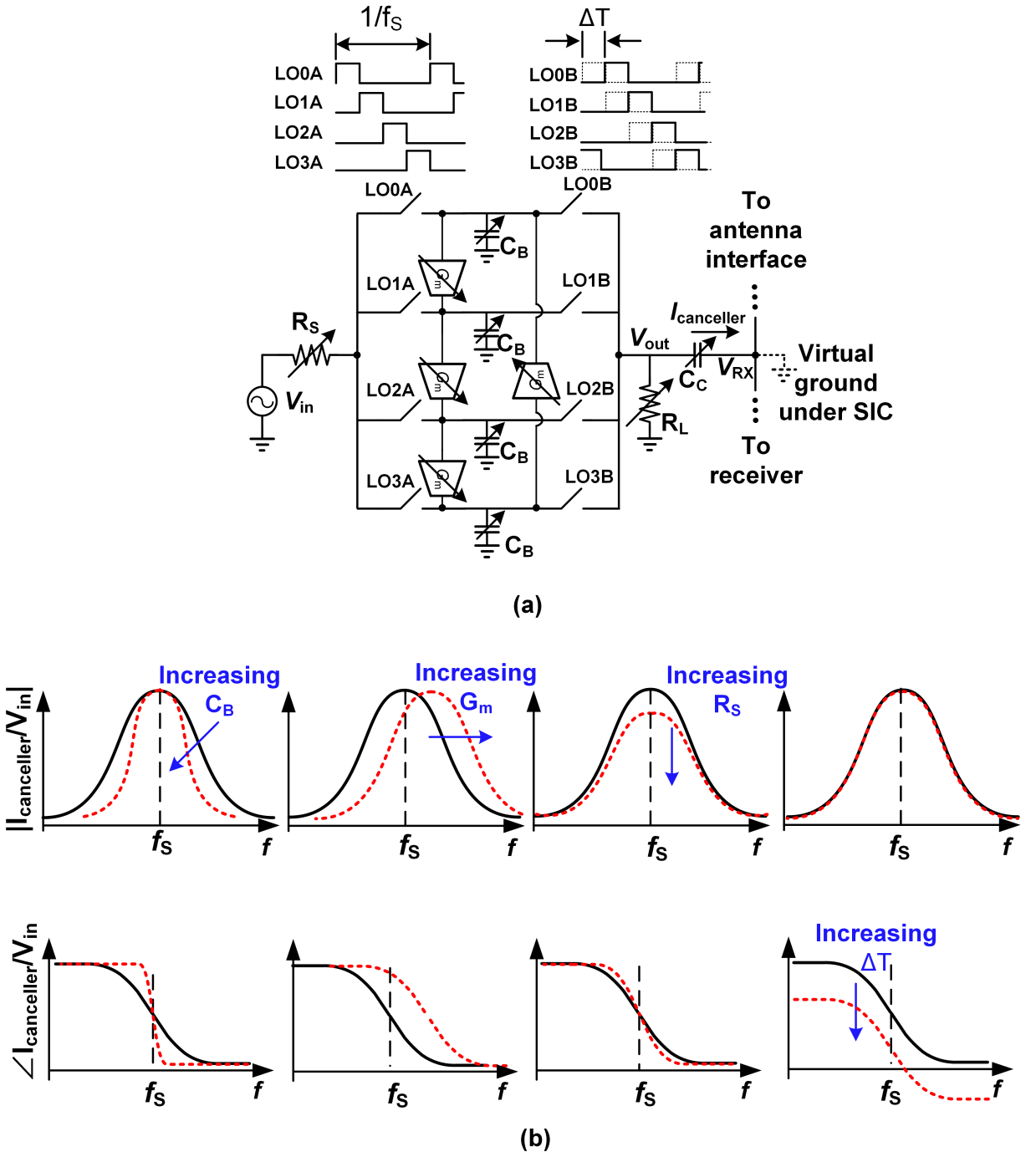

Figure 5.9: A two-port G_m-C N-path filter implementation with embedded variable attenuation and phase shift: (a) block diagram, and (b) illustration of variable quality-factor (group delay), frequency shift, attenuation, and phase shift.

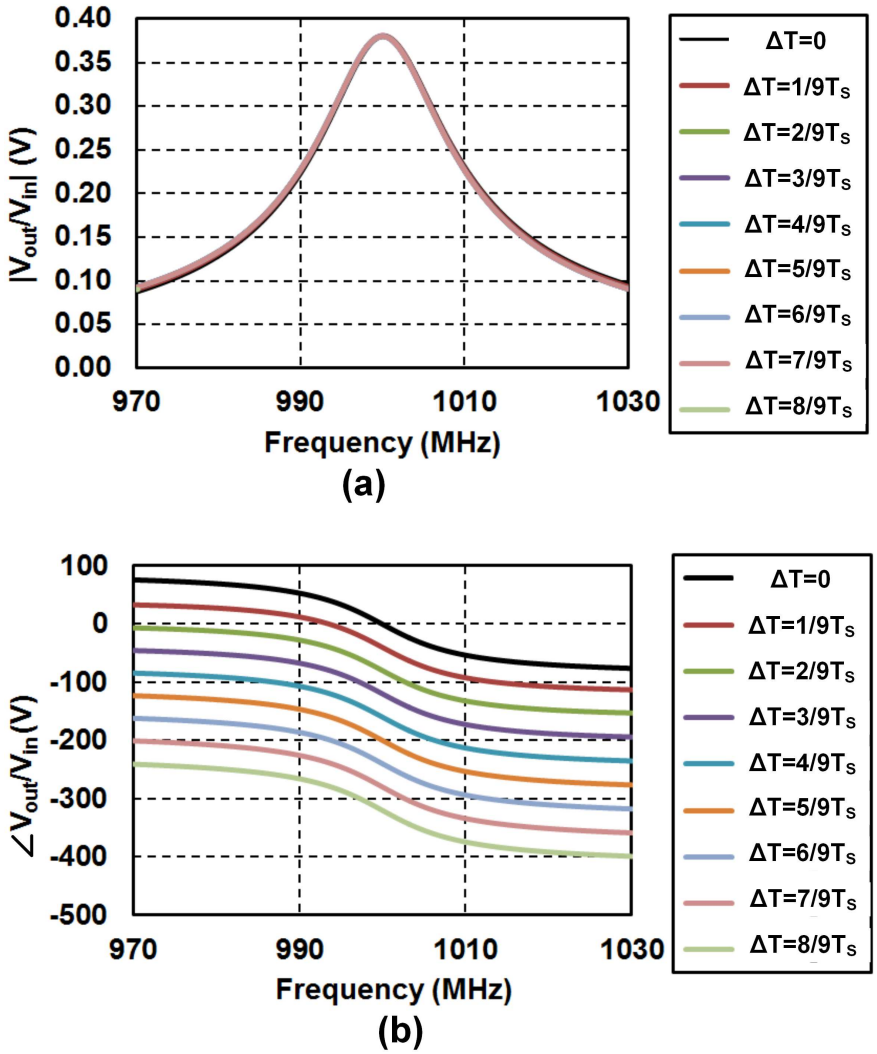

Figure 5.10: Simulated (a) magnitude and (b) phase responses of the two-port N-path filter shown in Fig. 5.9(a). In simulation, ideal 25% non-overlapping LOs drive ideal N-path switches with $R_{on} = 3.3\ \Omega$, $R_S = R_L = 50\ \Omega$, $C_B = 200\ pF$, $C_C = 0\ pF$. All $G_m = 0\ S$ and do not load the N-path filter.

output-side switches imparts constant phase shifts to the two-port N-path filter frequency response with no other impact on close-in response. Fig. 5.10 plots the simulated magnitude and phase responses of the two-port N-path filter shown in Fig. 5.9(a) with embedded phase shifting. In simulation, 25% non-overlapping LOs are used with $R_{on} = 3.3\ \Omega$, $R_S = R_L = 50\ \Omega$, $C_B = 200\ pF$, $C_C = 0\ pF$. All $G_m = 0\ S$ and do not load the N-path filter.

5.4 Circuit Implementation

A canceller bank of two reconfigurable 2^{nd}-order G_m-C N-path filters together with a 0.8-1.4 GHz reconfigurable current-mode receiver is implemented in a 65 nm standard CMOS process. The block diagram is shown in Fig. 5.11. The canceller filters have separate LO and TX replica signal inputs, lending flexibility in their use (e.g. cancellation of two separate TX signals for MIMO applications). The receiver uses a noise-cancelling CG, CS LNTA followed by 4-phase current-driven passive mixers and baseband TIAs [56]. Programmable baseband recombination circuits combine the receiver outputs from the CG and CS paths for noise cancellation [56][84].

For each canceller filter as illustrated in Fig. 5.12, the coupling capacitor C_C bank is designed to enable a -10 dB coupling across the operating frequency range based on our discussion in Section II-A. In addition, a relatively weak coupling is important for SIC at the RX input to not degrade the RX input matching as well as to prevent N-path filters from interacting with each other and with the receiver. Next, R_{RX} (nominal value 50 Ω) is sized to be smaller than $|\omega C_C|^{-1}$, so that the capacitive loading effect of C_C on the N-path filter is weak. Based on the required attenuation range and (5.7), the resistance range of R_{TX} can be obtained. Once R_{TX} and R_{RX} are set, using (5.6), the N-path filter baseband capacitance range is determined by the required group delay or quality-factor range. Finally, the transconductance range of the baseband G_m is designed using $\Delta\omega = \frac{G_m}{C_B}$ based on the required frequency shift range as well as the C_B capacitance range. Based on the aforementioned design principles, both canceller filters are designed to have a digitally-controlled peak group delay that ranges from 1 to 28 ns, a frequency shift that ranges from -10 MHz to $+10$ MHz under the peak group delay setting, full 360°phase shift range, and an attenuation range from 20 to 40 dB including the 10 dB RX-side capacitive coupling. The capacitive load present at the receiver input due to the capacitive coupling is resonated out using a combination of wirebond

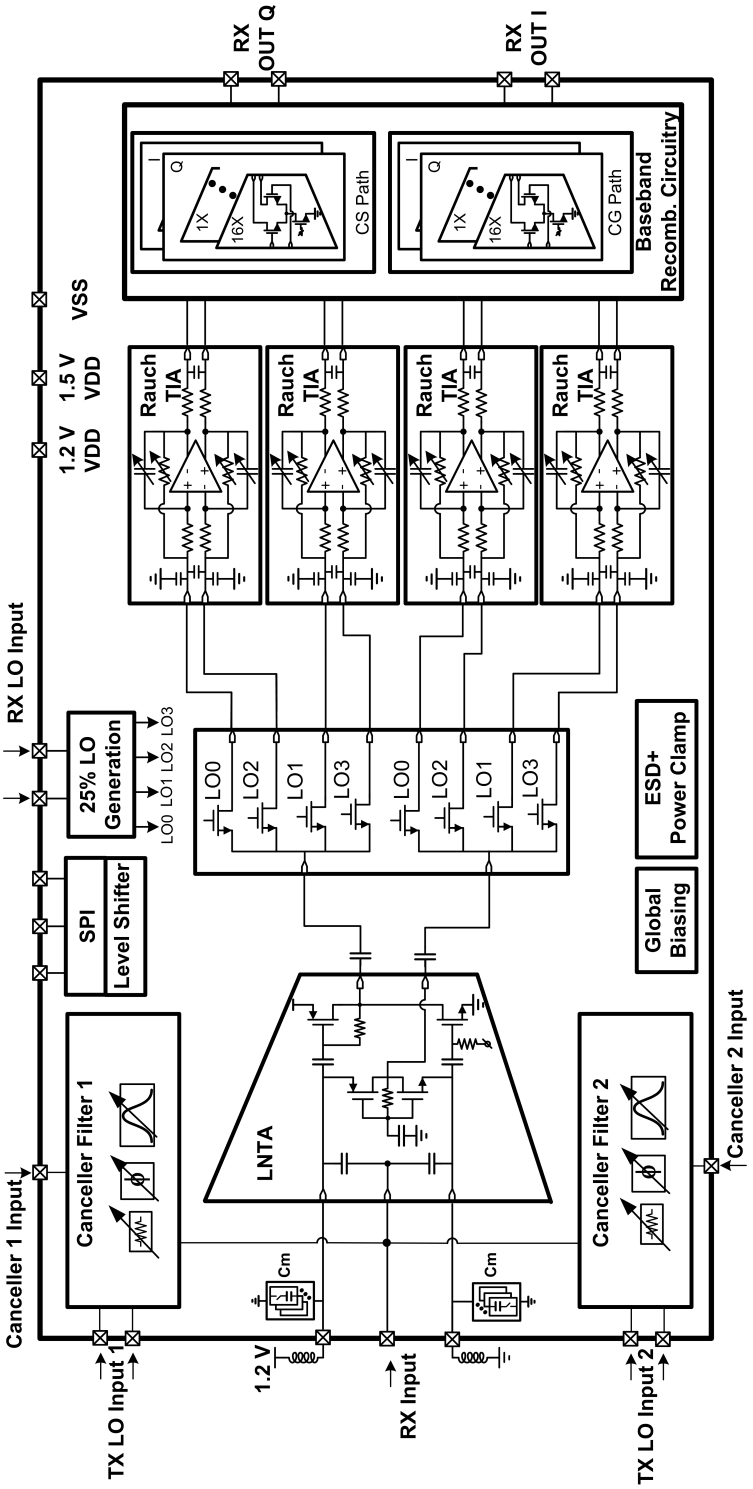

Figure 5.11: Block diagram and schematic of the implemented 0.8-1.4 GHz 65 nm CMOS receiver with FDE-based SIC in the RF domain featuring a bank of two filters.

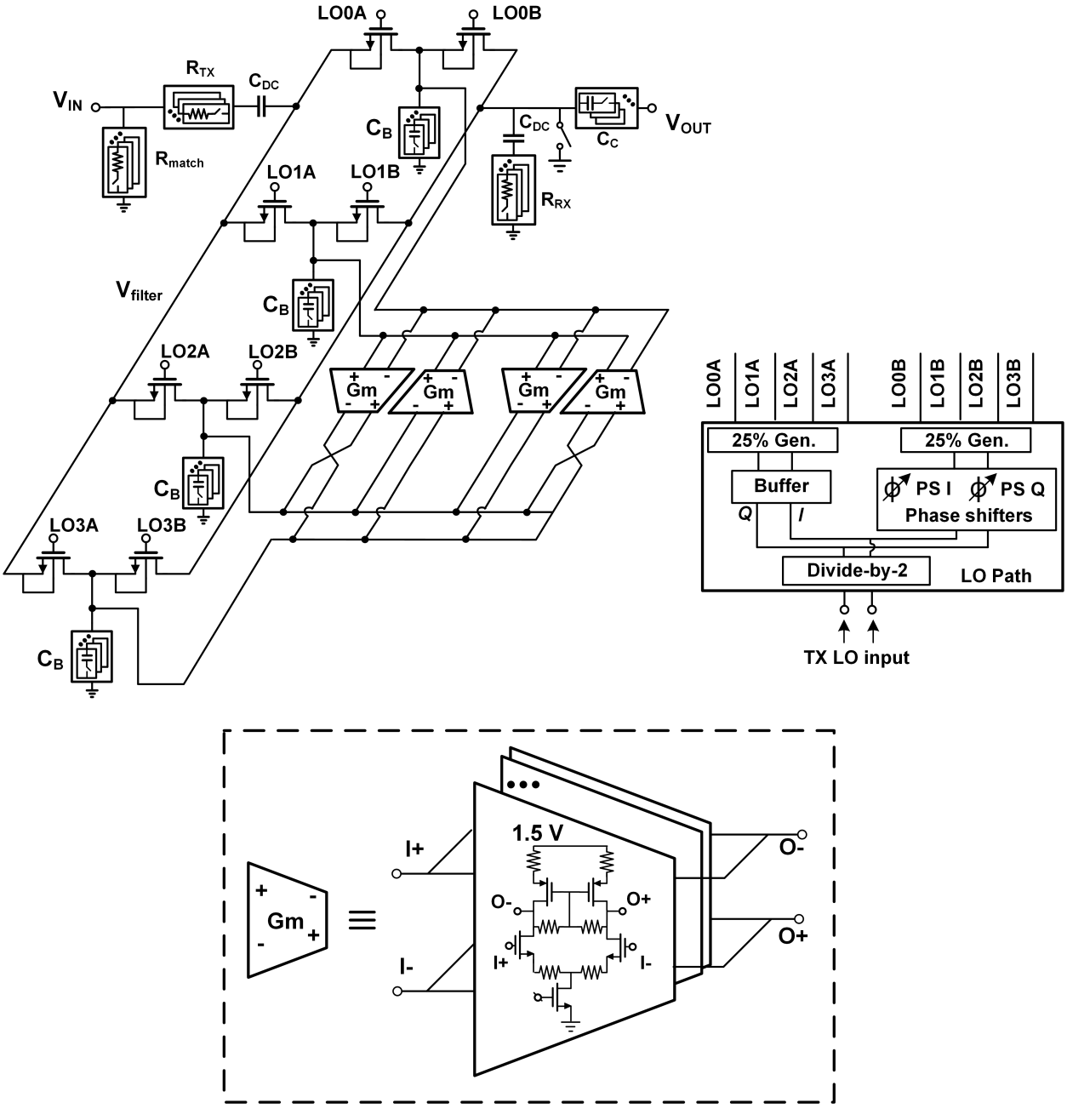

Figure 5.12: Block diagram and schematic of each canceller filter.

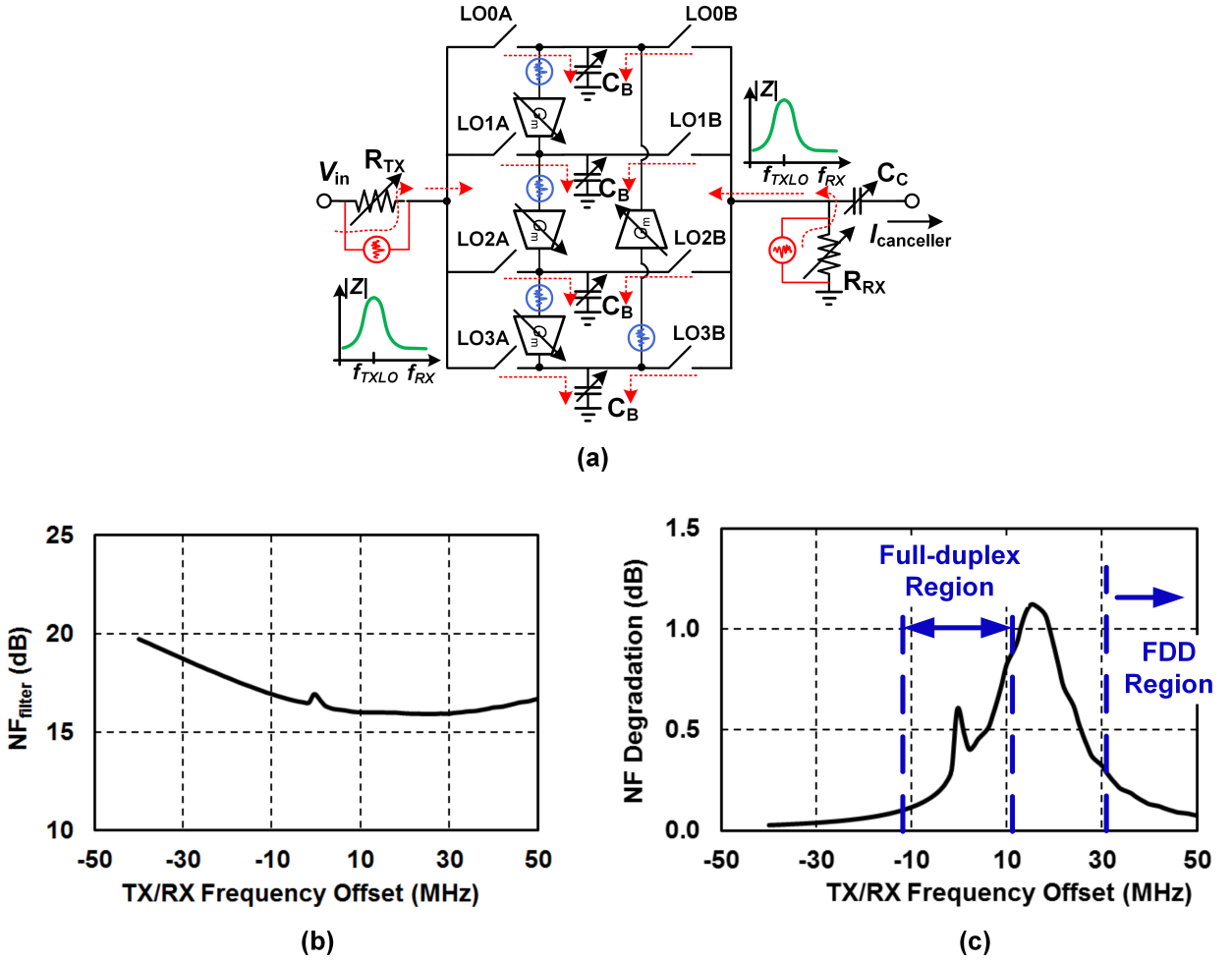

Figure 5.13: (a) Illustration of noise filtering for FDD, (b) the simulated canceller filter noise figure NF_{filter}, and (c) receiver NF degradation due to one canceller filter assuming NF_{RX}=6 dB. To obtain the NF_{filter}, the attenuation that precedes the filter input has been simulated and de-embedded. ($R_{TX} = R_{RX} = 50\ \Omega$, $R_{match} = 60\ \Omega$, $C_B = 200\ pF$, $G_m = 26\ mS$, $C_C = 2.5\ pF$, $f_S = 1\ GHz$, resulting in a total attenuation of about 20 dB including RX-side coupling, frequency shift of 15 MHz, phase shift of 0°, and Q of about 67.)

and off-chip inductance. Furthermore, programmable capacitor banks (C_m) are included to tune the input match to the desired frequency.

The schematic of the G_m cells is shown in Fig. 5.12. To ensure a high canceller linearity, the G_m cells of the canceller filters are source-degenerated and operate under slightly higher supply voltage (1.5 V) than the rest of the chip (1.2 V). In addition, the on-resistance (R_{on}) of the N-path switches is designed to be 3.3 Ω (much smaller than R_{TX} and R_{RX}), so that its impact on overall canceller linearity is minimized. The bulk nodes of the switches are connected to the source nodes to allow optimum DC biasing conditions. Linearity simulations of the canceller filters (and N-path filters in general) are challenging due to discontinuities in the higher order derivatives of drain current and terminal charges in BSIM models for MOSFET devices operating as switches [91]. Measurements of in-band RX effective IIP3 under cancellation of full-duplex SI described in the following section confirm that the IM3 distortion of the canceller filters remains within the performance specifications discussed in Section II-B.

An interesting benefit for FDD applications of using a frequency-selective reciprocal canceller is noise-filtering. In this work, for FDD, we target the cancellation of the powerful main SI signal in the TX band at the RX input. Cancellation of the TX noise in the RX band can be performed later in the RX chain [56] or even in the digital domain [63]. Since the filter banks are tuned to the TX frequency, the RX band noise of R_{TX}, G_m cells and even R_{RX} will be filtered by the low RX-band impedance of the N-path filter (see Fig. 5.13(a)). Using the canceller filter settings annotated in the caption, the simulated canceller filter noise figure NF_{filter} and RX NF degradation (given NF_{RX}=6 dB) is shown in Fig. 5.13(b) and Fig. 5.13(c). To obtain the NF_{filter}, the attenuation that precedes the filter has been simulated and de-embedded. As shown in Fig. 5.13(c), for TX/RX frequency offset >30 MHz, the NF degradation is less than 0.3 dB. NF degradation for TX/RX frequency offsets between −10 MHz and +10 MHz ranges from 0.1 dB to 0.8 dB and the maximum NF degradation is only slightly higher than 1 dB, thanks to the weak coupling at the RX side. In addition, the G_m cells use channel length of 200 nm to lower the flicker noise.

The LO path of each filter includes a divide-by-2 quadrature divider, LO slew-rate-control filters, I/Q vector-interpolation phase shifters and 25% duty-cycle generators. The slew-rate-control RC filters attenuate the harmonics to ensure the linearity of the subsequent vector interpolators.

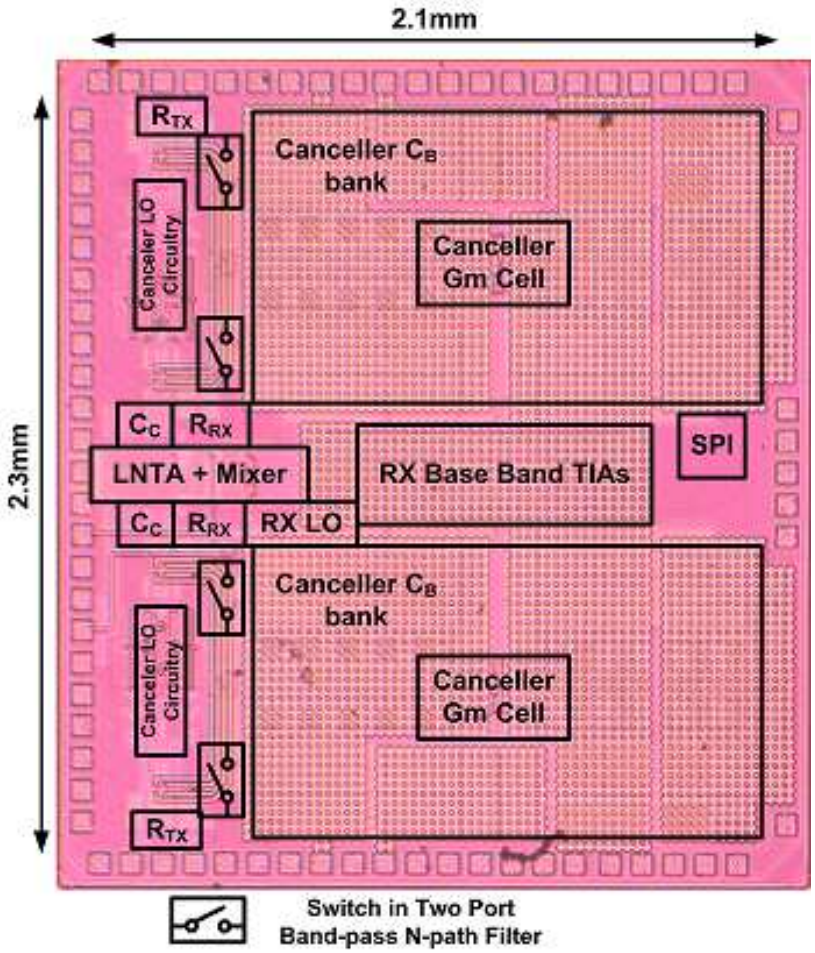

Figure 5.14: Chip microphotograph of the 65 nm CMOS 0.8-1.4 GHz self-interference-cancelling receiver.

5.5 Measurement Results

The chip microphotograph is shown in Fig. 5.14 and has an active area of 4.8 mm^2. The chip is wire bonded and packaged in a QFN package, and mounted on a PCB for all measurements.

5.5.1 Receiver without SIC

Basic receiver measurements are performed with the canceller inactive and without SI. The receiver has a measured programmable conversion gain that ranges from 27 to 42 dB. The measured receiver noise figure [Fig. 5.15(a)] ranges from 4.8 to 5.8 dB over the operating frequency range. The receiver

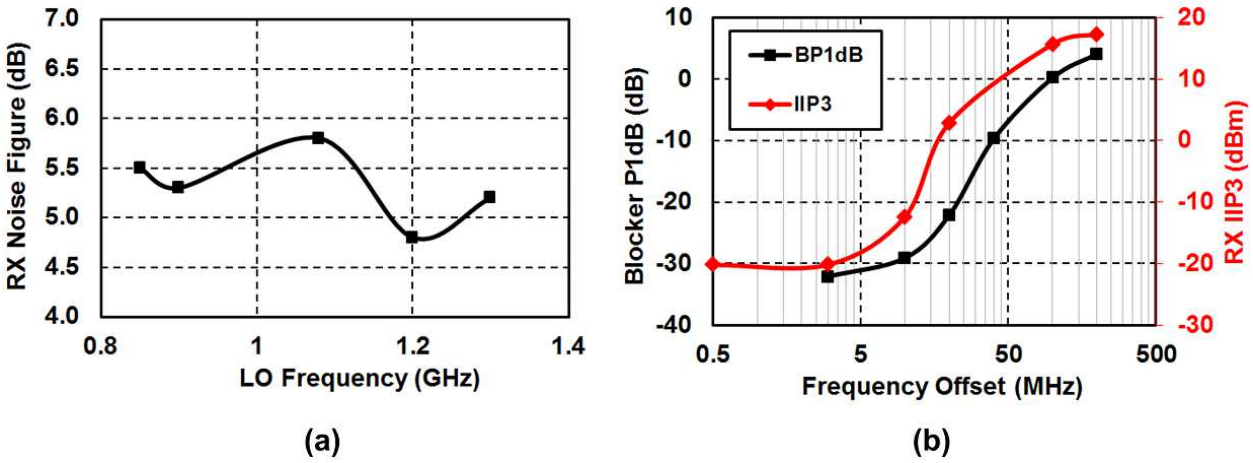

Figure 5.15: Measured receiver performance with canceller inactive and without SI: (a) noise figure, and (b) IIP3 and blocker-induced 1 dB compression point. IIP3 is plotted versus the frequency offset of the first tone in the two-tone test.

has a measured out-of-band (OOB) and in-band (IB) IIP_3 of +17 dBm and −20 dBm, respectively [Fig. 5.15(b)]. The measured receiver OOB and IB blocker-induced 1 dB gain compression points (blocker P1dB) are +4 dBm and −30 dBm, respectively.

5.5.2 SIC with a 30 dB TX/RX Isolation Duplexer for FDD

For FDD, the SI canceller enables the usage of a custom-designed LTE-like duplexer employing surface-mount-device-based 2^{nd}-order LC filters with TX band isolation as small as 30 dB, which is 25 dB relaxed compared to commercial SAW/FBAR duplexers[70]. The TX and RX 1 dB bandwidths are 762 to 798 MHz and 872 to 918 MHz (Fig. 5.16). The highly-selective duplexer has a peak isolation group delay of 11 ns and 7 dB magnitude variation across the TX band.

An iterative successive cancellation approach as described in Section 5.1 is used for canceller calibration[3]. The measured TX/RX isolation with SIC is shown in Fig. 5.17. The SI canceller achieves a 20 dB cancellation BW of 17/24 MHz for one/two filters enabled, while a conventional frequency-flat amplitude-and-phase-based canceller has a 20 dB SIC BW of only 3 MHz. Note that in measurement, the two canceller filters share the same LO, namely the TX LO frequency which

[3]The calculated parameters using (5.4) are used as initial settings. Subsequent manual tuning is used for optimal SIC BW.

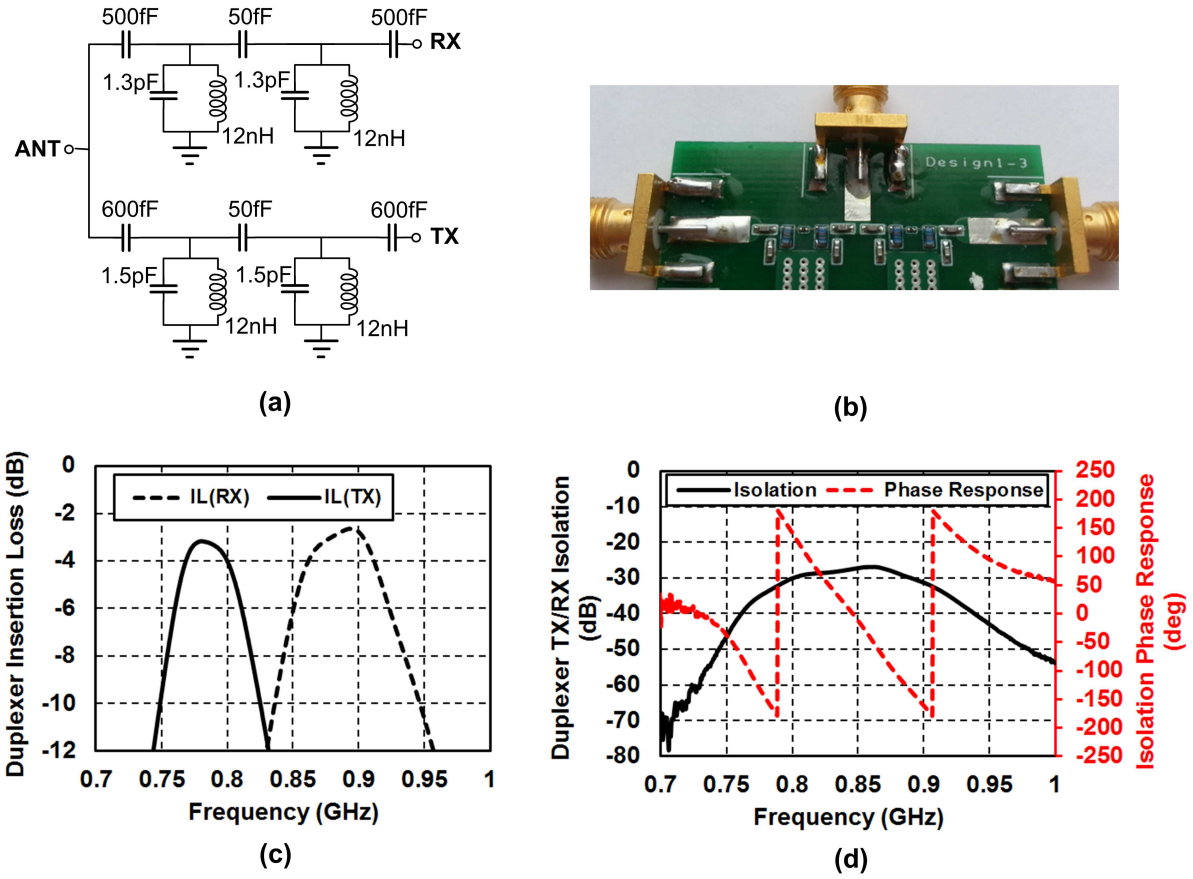

Figure 5.16: A custom-designed LTE-like 0.780/0.895 GHz duplexer employing surface-mount-device-based 2^{nd}-order LC filters: (a) schematic, (b) duplexer photo, (c) measured duplexer insertion loss, and (d) measured duplexer TX/RX isolation magnitude and phase response.

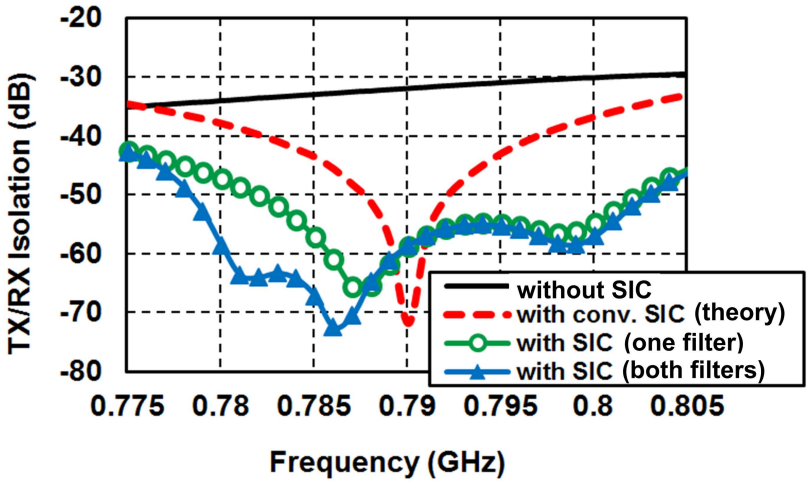

Figure 5.17: Measured TX/RX isolation of the FDD LTE-like duplexer shown in Fig. 5.16 without SIC, and with the proposed SIC. The proposed SI canceller achieves a 20 dB cancellation BW of 17/24 MHz for one/two filters enabled, while a conventional frequency-flat amplitude-and-phase-based canceller has a theoretical 20 dB SIC BW of only 3 MHz.

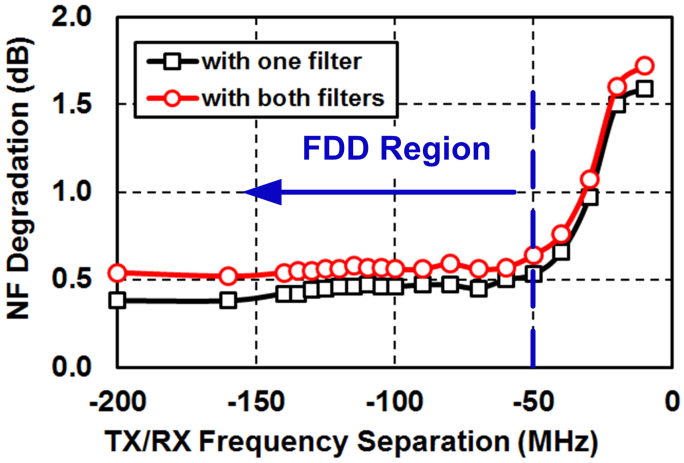

Figure 5.18: Measured RX NF degradation with one/two filters enabled versus TX/RX frequency offset. In other words, the RX LO frequency is swept with respect to the TX LO frequency used for the cancellers. Canceller settings for the FDD SIC measurement in Fig. 5.17 are used.

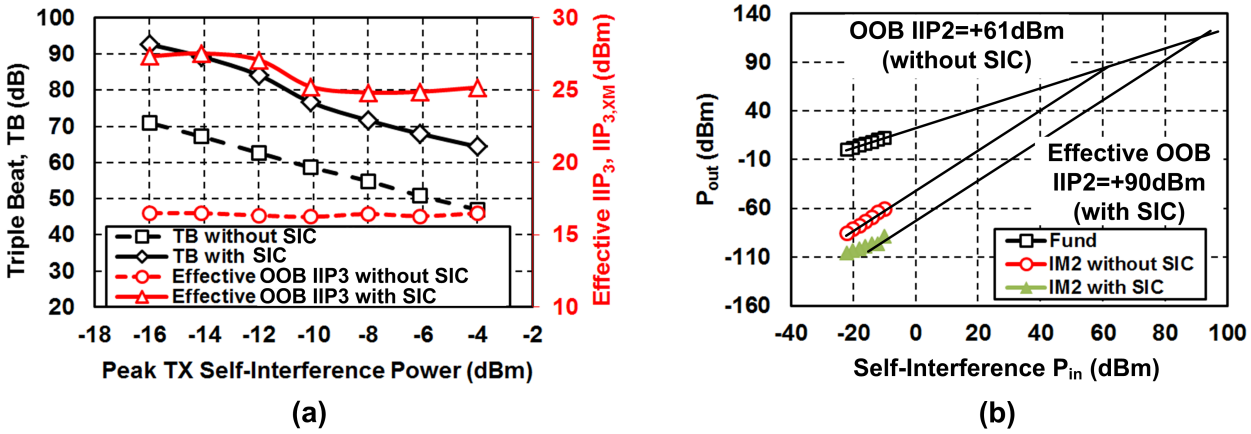

Figure 5.19: FDD linearity measurement:(a) TB and (b) IIP2 measurements with and without SIC with a two-tone OOB SI of varying power. For TB measurement, a −33 dBm in-band CW jammer is present at the RX input. To be fair, we ensure that the two-tone TX signal undergoes a cancellation of not more than 25 dB for these measurements (the average cancellation over the 24 MHz 20 dB SIC BW in Fig. 5.17).

is set at the center of the TX band, and the G_m cells are used to impart frequency shifts.

The associated NF increase is only 0.5 dB/0.6 dB due to noise filtering (Fig. 5.18), as the NF degradation is lower in the FDD region i.e. in the vicinity of the RX frequency than in the vicinity of the TX frequency. In measurement, SIC of up to −4 dBm of peak OOB TX leakage at the RX input is demonstrated. The SIC enhances the receiver effective OOB IIP3 from +17 dBm to +25 to +27 dBm from cross-modulation (triple-beat) measurements (Fig. 5.19(a)) and OOB IIP2 from +61 dBm to an effective +90 dBm (Fig. 5.19(b)). To be fair, we ensure that the two-tone TX signal undergoes a cancellation of not more than 25 dB (the average cancellation over the 24 MHz 20 dB SIC BW).

5.5.3 SIC across an Antenna Pair for Full-Duplex Wireless

For same-channel full-duplex, we use a 1.4 GHz narrowband antenna-pair interface with peak isolation group delay of 9 ns, peak isolation magnitude of 32 dB[4] and 3 dB of isolation magnitude

[4]More than 30 dB antenna isolation is achieved through physical separation here, but can also be obtained through antenna cancellation in practice [27][55]. It should be noted that the 9 ns group delay significantly exceeds the delay associated with the physical separation (about 0.4 m) due to the tuned nature of the antennas.

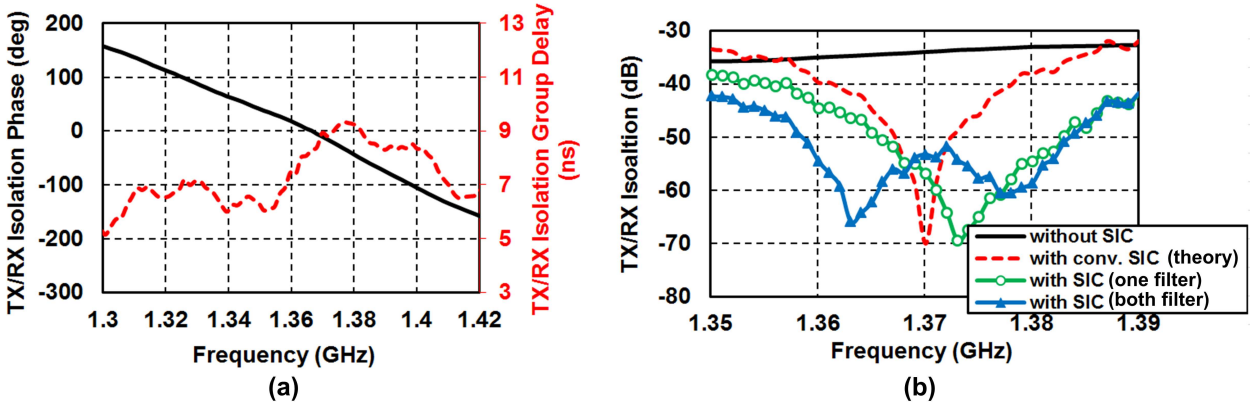

Figure 5.20: Measured TX/RX isolation of the 1.4 GHz full-duplex antenna pair shown in Fig. 5.24 with and without the proposed SIC: (a) TX/RX isolation phase and group delay, and (b) TX/RX isolation magnitude without SIC, with conventional SIC (theoretical), and with the proposed SIC. The proposed SI canceller achieves a 20 dB cancellation BW of 15/25 MHz for one/two filters enabled, while a conventional frequency-flat amplitude-and-phase-based canceller has a 20 dB SIC BW of only 3 MHz.

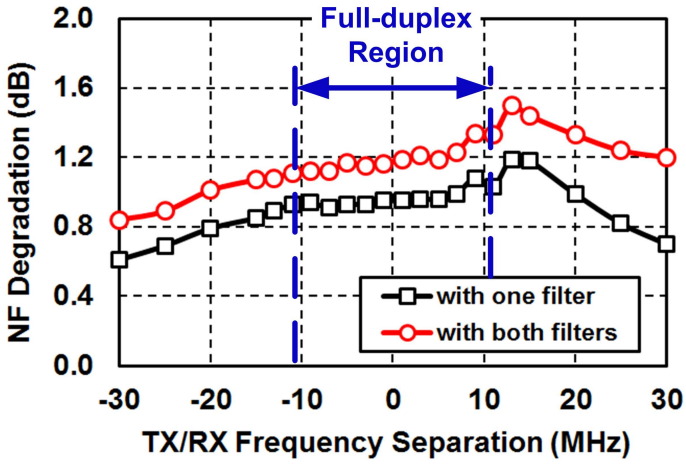

Figure 5.21: Measured RX NF degradation with one canceller filter and both canceller filters enabled versus TX/RX frequency offset. Canceller settings for the same-channel full-duplex SIC measurement in Fig. 5.20 are used.

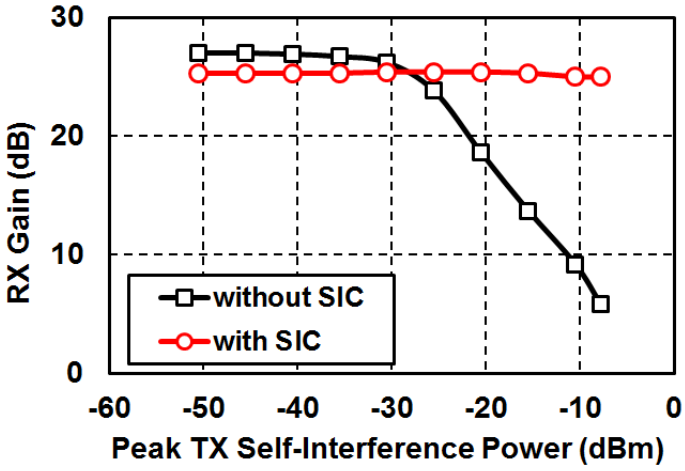

Figure 5.22: Measured RX gain compression of a weak desired signal with and without SIC versus varying full-duplex SI power level at the receiver input.

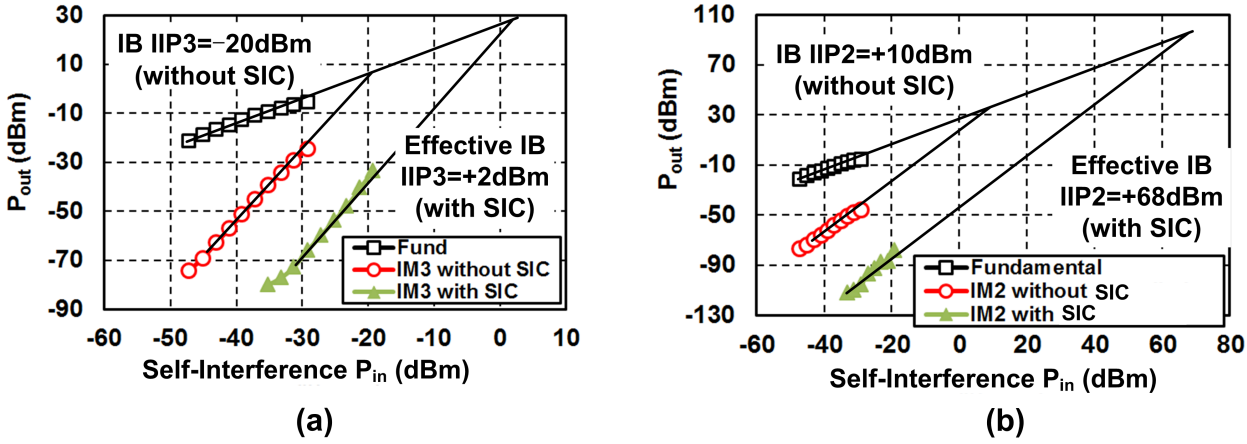

Figure 5.23: Full-duplex linearity measurement: receiver in-band (IB) IIP3 and IIP2 measurements with and without SIC for a two-tone in-band SI of varying power. To be fair, we ensure that the two-tone TX signal undergoes a cancellation of not more than 25 dB for these measurements (the average cancellation over the 25 MHz 20 dB SIC BW in Fig. 5.20(b)).

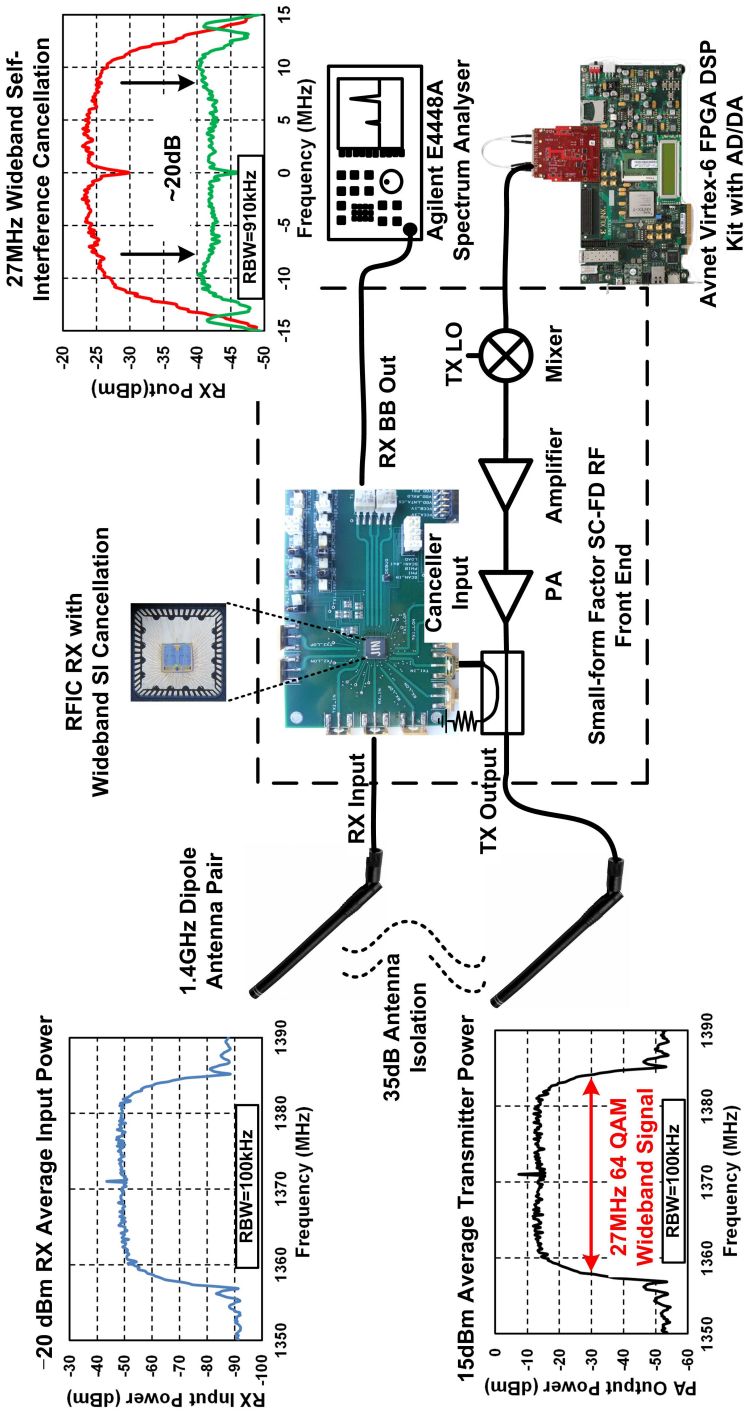

Figure 5.24: Wireless demonstration of same-channel full-duplex RF SI cancellation of a 1.37 GHz 27 MHz-BW RRC-filtered 64-QAM signal across the 1.4 GHz antenna pair showing signal spectrum at various points and 20 dB SIC across the entire 27 MHz signal BW at the receiver output. Off-the-shelf components are used to form the transmitter path.

variation over 1.36 GHz to 1.38 GHz. Please note that this is the same antenna interface assumed for the analyses presented in Section 5.1. The SI canceller achieves a 20 dB cancellation BW of 15/25 MHz (one/two filters) in Fig. 5.20. When a conventional frequency-flat amplitude-and-phase-based canceller is used, the SIC BW is about 3 MHz. Once again, in measurement, the two canceller filters share the same LO.

The associated NF increase is 0.9-to-1.1 dB/1.1-to-1.3 dB (Fig. 5.21). Measured RX gain imparted to a weak desired signal without and with SIC are shown in Fig. 5.22. SIC of up to -8 dBm of peak in-band SI at the RX input results in negligible gain compression of a desired signal (as opposed to nearly 22 dB of compression in the absence of SIC). SIC also improves the impact of receiver nonlinearity on the SI itself, improving effective in-band IIP3 from -20 dBm to $+2$ dBm and effective in-band IIP2 from $+10$ dBm to $+68$ dBm.

In the effective in-band IIP3 measurement under SIC, there is no way to separate the canceller and RX IM3 contributions. We may infer their relative contributions from the fact that RX effective in-band IIP3 should improve by the amount of SIC achieved (around 25 dB). The fact that it improves by 22 dB indicates that the RX and canceller have roughly equal IM3 contribution, which is consistent with the system-level design guideline outlined in Chapter 2. Even with both IM3 contributions, the effective in-band IIP3 under SIC of $+2$ dBm exceeds the $+0.5$ dBm specification dictated by RX IM3 alone in Section II-A. Also, while IIP3 is an extrapolated metric, consistent IM3 levels are maintained up to a single-tone SI power level of -19 dBm, which corresponds to an average two-tone TX power of $+14$ dBm assuming 30 dB ISO. At that level, under SIC, the IM3 tones are 40 dB below the incident SI, exceeding the 37 dB requirement.

While IM2 was not considered in Chapter 2, the required RX effective IIP2 under SIC is $P_{TX,main} - ISO - 3 + SIC_{RF} + SIC_{BB} = +19$ dBm so that RX SI IM2 distortion does not exceed the residual SI after RF and analog SIC. The achieved RX effective IIP2 greatly exceeds this.

Fig. 5.24 illustrates a wireless same-channel full-duplex SIC demonstration. A 27 MHz-BW 64-QAM signal is transmitted using an off-the-shelf mixer and power amplifier through one of the 1.4 GHz antennas. The modulated SI appears at the receiver input with 35 dB antenna isolation. Using the proposed canceller, 20 dB cancellation across the entire 27 MHz SI BW is measured.

Table 5.1: Summary of the specifications for a full-duplex system (see Chapter 2) and corresponding measurement results.

		Specifications		Measurement Results
		Requirements	Comments	
System Definition	$P_{TX,main}$ (TX output power)	+15 dBm		+15 dBm[1]
	Self-Interference (SI) Bandwidth	20 MHz	BW for LTE	>20 MHz[2]
	NF_{RX} (RX NF without SIC)	5 dB		4.8 to 5.8 dB
	$P_{NoiseFloor}$ (RX noise floor)	-96 dBm	Calculated from NF_{RX} and BW	-96.2 to -95.2 dBm
	P_{jam} (CW jammer power)	-33 dBm	Referred from CDMA standard [46]	-33 dBm
	Total SI Cancellation (SIC)	117 dB	To suppress SI 6 dB below RX noise floor	~52 dB over 27 MHz (ISO + RF SIC)[9]
SIC Budget	ISO (antenna isolation)	30 dB		32 dB[3]
	SIC_{RF}	20 dB	Determined by eq. (2.5)	20 dB over 27 MHz SI BW[9]
	SIC_{BB}	37 dB - SIC_{RF}	Assuming 117dB required total SIC, 30 dB ISO and 50 dB $SIC_{digital}$	Not implemented
	$SIC_{digital}$	50dB	Based on [2][3]	Not implemented
	SI Delay τ_{SI} (SI delay from the direct coupling path)	10 ns		9 ns[3]
Circuit Performance	DR_{ADC}	56 dB	Determined by DR_{ADC}= ($P_{TX,main}$−ISO−SIC_{RF}−SIC_{BB}+6) −($P_{NoiseFloor}$−6)	Not implemented
	In-band $IIP_{3,RX,effective}$ (RX IIP3 with respect to SI under SIC)	+0.5 dBm	Determined by eq. (2.3)	+2 dBm[5]
	$IIP_{3,LNA}$	+6 dBm	Typical value for LNTA.	+17 dBm[6]
	CP_{TX} (coupling strength at TX side)	-10 dB	10% reduction of TX efficiency	-10 dB
	CP_{RX} (coupling strength at RX side)	-10 dB	Determined by eq. (2.6) (2.7) (2.8).	-10 dB[4]
	$OIP_{3,Canc}$ (canceller OIP3)	+10.5 dBm	Determined by eq. (2.6).	N/A[8]
	NF_{filter} (canceller filter noise figure)	15 dB	From filter implementation.	16 dB[4]
	NF degradation under RF SIC	< 2 dB	Determined by eq. (2.7)	1.1 to 1.3 dB
	ATT+IL (total attenuation or loss from the canceller in the RF domain)	10 dB	Determined by eq. (2.8).	12 dB[7]

1. Transmitted power in the RF SIC demonstration measurement shown in Fig. 24. This is also the transmitter power at which other table parameters are reported. Note that higher levels of SI can be canceled at the RX input assuming ISO=30 dB.
2. Maximum achieved 20 dB RF SIC BW in Fig. 20(b) is 25 MHz and the wireless demonstration in Fig. 24 uses 27 MHz.
3. This represents the peak isolation magnitude and group delay of the 1.4GHz antenna pair's direct coupling path.
4. Based on the simulations of the design. 5. Includes canceller IM3 distortion as well. 6. Estimated from RX OOB IIP3 measurement.
7. Calculated as ISO+CP_{TX}+CP_{RX}=32-10-10 dB=12 dB. 8. Canceller IM3 distortion is included in the measured in-band effective IIP3 ($IIP_{3,RX,effective}$).

Table 5.2: Performance comparison with the state of the art.

	[65]	[64]	[56]	[9]	[8]	This work		
Architecture	LNA with Passive Transformer based TX Leakage Cancellation	LNA with LMS Adaptive TX Leakage Filter	Noise-Cancelling , SI Cancelling (NC-SIC) RX	Mixer-first TRX with Active Baseband Duplexing	Mixer-first receiver + SI-canceling VM-downmixer	RX with wideband SIC based on RF frequency-domain equalization		
						Without canc.	With cancellation (LC-based Duplexer for FDD)	With cancellation (Antenna Pair for FD)
RX Frequency	2.1 GHz	0.8 GHz	0.3-1.7 GHz	0.1-1.5 GHz	0.15-3.5 GHz	0.8-1.4 GHz		
RX Noise Figure	2-2.5 dB (LNA only)	1.4 dB (LNA only)	4.2-5.6 dB	5.2-7.7 dB	6.3 dB	4.8 dB		
Gain	19.8 (LNA only)	16.5 dB (LNA only)	19-34 dB	53 dB	24 dB (max.)	27-42 dB		
20dB Cancellation BW	N/R (Frequency-flat RF SI canceller)	1.23 MHz[1] (Frequency-flat RF SI canceller)	3 MHz[2]/3 MHz[3] (Frequency-flat RF SI canceller)	N/R	N/R (Frequency-flat RF SI canceller)	N/A	17MHz (one filter) 24 MHz (two filters)	15MHz (one filter) 25 MHz (two filters)
OOB IIP3	+3 dBm (LNA only)	N/R	+12	+22.5 dBm	+22.0 dBm	+17 dBm		
Effective OOB IIP3 with respect to SI	N/R	N/R	+33 dBm[4]	N/A	N/A	N/A	+25-27 dBm[4]	N/A
OOB IIP2	N/R	N/R	N/R	N/R	N/R	+61 dBm		
Effective OOB IIP2 with respect to SI	N/R	N/R	N/R	N/A	N/A	N/A	+90 dBm	N/A
IB SC-FD P1dB[5]	N/A	N/A	N/A	-52.3/-17.3[6] dBm	>+1.5[8] dBm	-30.5 dBm	N/A	>>-8 dBm[6]
IB IIP3	N/A (LNA only)	N/A (LNA only)	N/R	-32.7 dBm	+8/+16.2[9] dBm	-20 dBm		
Effective IB IIP3 with respect to SI	N/A (LNA only)	N/A (LNA only)	N/A	N/R	+19 dBm	N/A	N/A	+2 dBm
IB IIP2	N/A (LNA only)	N/A (LNA only)	N/R	N/R	N/R	+10 dBm		
Effective IB IIP2 with respect to SI	N/A (LNA only)	N/A (LNA only)	N/A	N/R	N/R	N/A	N/A	+68 dBm
Maximum Handled Peak SI Power	-25 dBm	-28 dBm	+2 dBm	-17.3 dBm[7]	-18 dBm[10]/ -10 dBm[11]/ +1.5 dBm[12]	N/A	-4 dBm	-16 dBm[13]/ -8 dBm[14]
NF Degradation due to SI Cancellation	1-1.5 dB	1.3dB	0.8 dB	N/R	4-6 dB	N/A	0.5dB (one filter) 0.6dB (two filters)	0.9-1.1dB (one filter) 1.1-1.3dB (two filters)
RX Power Consumption	10 mW (LNA only)	N/R	75-83 mW	43-56 mW	23-56 mW	63-69 mW		
Canceller Power Consumption	0 mW	43mW	13-72 mW			N/A	0-47 mW (Gm cells for one filter) 44 mW (LO at 1.35 GHz for one filter)	
SC-FD?	No	No	No	Yes	Yes	Yes		
Antenna Interface	Duplexer with single antenna	Duplexer with single antenna	Antenna pair/ Duplexer with single antenna	Single antenna	Antenna pair	Duplexer with single antenna (FDD)/ Antenna pair (FD)		
Technology	40nm CMOS	250nm CMOS	65nm CMOS	65nm CMOS	65nm CMOS	65nm CMOS		
Active Area	2.1 mm^2	N/A	1.2 mm^2	1.5 mm^2	2 mm^2	4.8 mm^2		

1. 10.8 dB average cancellation over 1.23 MHz across a CDMA SAW duplexer. 2. Across the 0.8/0.9 GHz LTE-like LC-based duplexer.
3. Across the 1.4 GHz FD antenna pair. 4. Effective IIP3 under FDD SI cancellation from triple beat measurements.
5. Power level of the FD IB TX SI that compresses a desired signal by 1dB 6. Under FD SI cancellation. N/A: Not Applicable N/R: Not Reported
7. This is also the TX power limit due to the baseband duplexing scheme. 8. 1.3 dB RX compression. 9. Negative conductance off/on.
10. SI power at which peak 69 dB SINDR is achieved.
11. SI power level that allows a full-duplex link with +10 dBm TX power (20 dB antenna isolation) and -70 dBm distortion-limited noise floor. 12. SI power@1.3 dB RX compression
13. SI power level at which the RX meets the FD link budget proposed in Section II and Table 1. 14. Peak SI power level for which SIC is demonstrated.

5.5.4 Performance Summary and Comparison

Table 5.1 summarizes the system-level analysis and specifications presented in Chapter 2 and compares them to the measurement results just described. Table 5.2 compares the measurement results with prior art. This work achieves superior SIC BW, while achieving comparable SI power handling, NF degradation and linearity enhancement under FDD SIC to [76] and supporting same-channel full-duplex wireless. When compared with [8], a recently-reported full-duplex RFIC, this work achieves lower NF degradation and incorporates equalization functionality for wideband SIC. However, [8] achieves superior in-band linearity with and without SIC due to a passive-mixer-first architecture. When compared with [9], another recently-reported full-duplex RFIC, this work exhibits superior SI power handling and in-band linearity to SI.

Canceller DC power depends on antenna interface selectivity and desired SIC BW, and must be compared with the TX power consumption, as it can be powered down when the TX is inactive, or in the absence of a CW jammer for FDD. Measured canceller LO (TX LO) feedthrough to the RX input is about -55 dBm, low enough to not affect FDD/full duplex operation. Calibration techniques can further suppress the LO leakage [114].

5.6 Summary

The concept of frequency-domain equalization (FDE) in the RF domain is introduced in this Chapter that enables wideband SIC at RF for full-duplex and frequency-division duplexing wireless communications systems. For FDE in the RF domain, reconfigurable RF bandpass filters (BPFs) are employed in the canceller. The reconfigurable BPFs enable replication of not only the magnitude and phase of the frequency-selective antenna interface isolation, but also their slopes in different sub-bands, thus greatly enhancing SIC BW. Similar to traditional FDE in digital, the RF equalizer coefficient can be derived from the SI channel transfer function. In addition, an iterative successive approach is proposed to further configure the RF BPFs in the equalizer.

FDE in the RF domains requires high-Q, widely-tunable RF BPFs. When compared to other approaches to the design of integrated RF BPFs (such as the Q-enhanced LC RF BPF), N-path filters in CMOS have advantages of being area efficient, widely tunable, and having better dynamic range performance. In the Chapter, a two-port G_m-C N-path filter with embedded variable at-

tenuation and phase shift is introduced to implement the reconfigurable canceller BPFs. Variable attenuation is introduced by reconfiguring N-path filter source and load resistance relative to each other, and phase shifting is accomplished by phase shifting the LOs driving the switches on the output side of a two-port N-path filter.

A proof-of-concept 0.8-1.4 GHz SIC receiver prototype based on RF FDE in 65 nm CMOS validates the claims and achieves >20 MHz cancellation BW (nearly 10× improvement over conventional frequency-flat amplitude- and phase-based RF cancellers) across a custom-designed LTE-like 0.780/0.895 GHz duplexer for FDD and a 1.4 GHz antenna pair for full-duplex wireless.

Chapter 6

A Full-Duplex Receiver with Integrated Non-Magnetic Passive Circulator and Baseband Self-Interference Cancellation

As discussed in Chapter 3, the progression towards short-range wireless communications relaxes SI suppression requirements in full-duplex systems. However, a full-duplex system with −6 dBm transmit power, 10 MHz signal bandwidth and 12 dB NF budget still requires 86 dB of SI suppression to reach the −92 dBm noise floor. Another fundamental challenge is related to the full-duplex antenna interface. When compared to antenna pairs, shared-antenna interfaces enable compact form factor, translate easily to MIMO, and ease system design through channel reciprocity. The realization of compact CMOS-compatible full-duplex shared-antenna interfaces with low loss, low noise, high linearity, and high TX-to-RX isolation is an important open research topic. In this Chapter, we present a full-duplex RX with an integrated non-magnetic N-path-filter-based passive circulator[1] and analog BB SI cancellation [52][42]. *This full-duplex receiver (1) enables a compact full-duplex radio with an integrated low-loss shared-antenna interface, (2) achieves 42 dB on-chip*

[1]This work was performed in collaboration with Negar Reiskarimian. The integrated non-magnetic passive circulator presented here is a research project conducted by Negar.

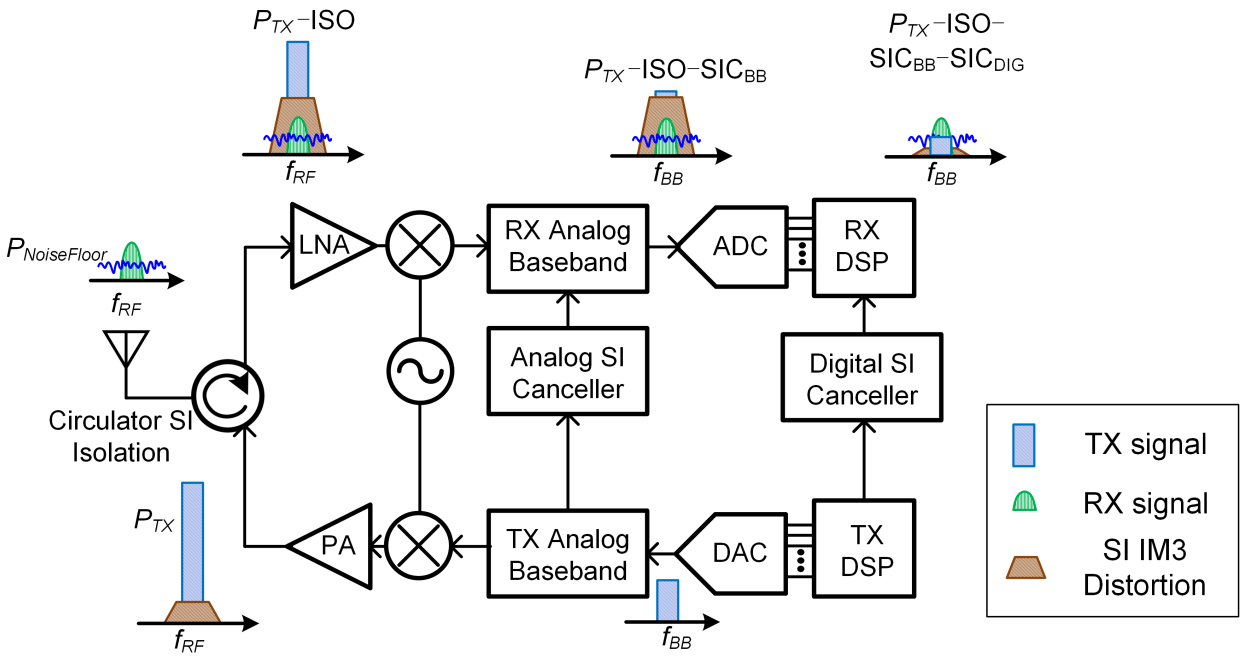

Figure 6.1: Short range full-duplex transceiver block diagram with SI suppression across the circulator, analog, and digital domains.

SI suppression across the antenna and analog BB domains over 12 MHz signal bandwidth, and (3) demonstrates 85 dB overall SI suppression in conjunction with digital SI and its IM3 distortion cancellation, enabling a full-duplex link budget of −7 dBm TX average output power and −92 dBm noise floor.

This Chapter is organized as follows. Section 6.1 discusses the specifications of the short-range full-duplex radio. Section 6.2 briefly describes the operation principle of the integrated non-magnetic N-path-filter-based passive circulator. A detailed treatment of the circulator can be found in [42][115]. A joint SIC approach across the antenna and analog domains is presented in Section 6.3. The implementation of the 65 nm CMOS 0.6-0.8 GHz full-duplex receiver with the integrated circulator and the joint SIC across the antenna and analog domains is described in Section 6.4. Measurement results are given in Section 6.5. Section 6.6 summaries the Chapter.

6.1 Short-Range Full-Duplex System Requirements

The block diagram of the short-range full-duplex wireless transceiver is depicted in Fig. 6.1. A TX baseband signal is first upconverted to RF and then amplified by a PA. The TX signal at PA output including the TX main signal (P_{TX}) and its nonlinear distortion signal leaks to the RX LNA input (becoming SI) through the integrated circulator with certain amount of TX-to-RX isolation (ISO). SIC in the analog domain taps from the TX analog baseband and cancels the SI at the RX analog baseband. Finally, SIC in the digital domain suppresses both the main SI and the associated distortion signal generated by the TX, circulator, RX, and analog SI canceller.

We assume a short-range wireless system with 10 MHz RX bandwidth and 12 dB RX NF (NF_{RX}), which results in an RX input-referred noise floor ($P_{NoiseFloor}$) of -92 dBm[2]. Given a -6 dBm P_{TX}, the required overall SIC can be calculated as -6 dBm $-$ (-92 dBm) $= 86$ dB and is distributed across the circulator, analog, and digital domains as depicted in Fig. 6.1. Assuming a required SNR of 15 dB, 2 dBi TX and RX dipole antenna gain, implementation losses of 5 dB, 15 dB margin for signal fading, and 5 dB ($3\times$) sensitivity degradation due to the residual SI and its IM3, the link budget of -6 dBm $+ 4$ dBi $-$ (-92 dBm $+ 5$ dB) $- 15$ dB $- 5$ dB $- 15$ dB $= 50$ dB translates to a transmission distance of 10 meters at a frequency of 750 MHz. The required overall SIC can be calculated as -6 dBm $-$ (-92 dBm) $= 86$ dB and is distributed across the circulator, analog, and digital domains as depicted in Fig. 6.1.

SI suppression in the antenna and analog domains is critical for relaxing the ADC DR requirement. At the ADC input, assuming an identical power level for the main SI and its associated distortion signal, the required ADC DR can be calculated as $DR_{ADC} = (P_{TX} - ISO - SIC_{BB} + 6) - (P_{NoiseFloor} - 6)$, where SIC_{BB} is the amount of SIC achieved in the analog domain and we have included a 6 dB margin at both ends[3]. Therefore, the ADC DR requirement is relaxed by the amount of SI suppression in the antenna and analog domains.

The SI suppression in the antenna and analog domains also determines the SI-cancelling RX effective in-band IIP3 (i.e. IIP3 under analog SIC). Let us assume the integrated circulator and the SI-cancelling receiver contribute equally to the SI-induced distortion signal at the ADC input.

[2] $P_{NoiseFloor}$ is the original half-duplex noise floor.

[3] The 12 dB margin accounts for the addition of the residual SI and its distortion signals, among other things.

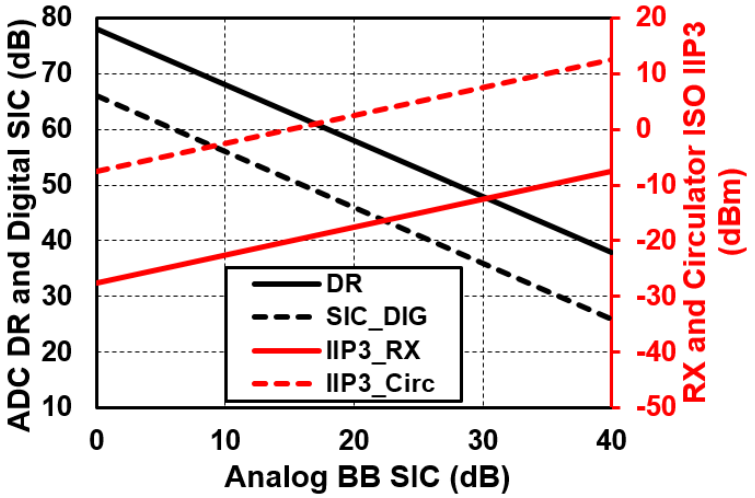

Figure 6.2: Required ADC DR, RX effective IIP3, circulator ISO IIP3, and digital SIC versus the amount of analog BB SIC.

Table 6.1: Summary of the short-range full-duplex system specifications.

		Specifications
System Definition	TX average output power	-6 dBm
	TX signal bandwidth	10 MHz
	RX NF	12 dB
	RX noise floor	-92 dBm[#]
	Total SIC	86 dB
	Link range@750MHz*	10 m
Analog/RF SIC Budget	Circulator isolation	20 dB
	Analog BB SIC	20 dB
Analog/RF Front-End Circuit Performance	DR_{ADC}	58 dB[$]
	RX Effective IIP_3	-17.5 dBm
	Circulator TX-port-referred ISO IP_3	+2.5 dBm
Digital SIC Budget	Digital SIC – Linear	46 dB
	Digital SIC – IM3	46 dB

* Assume a required SNR value of 15 dB, 2 dBi TX and RX dipole antenna gain, implementation losses of 5 dB,15 dB margin for signal fading, and 5 dB sensitivity degradation due to the residual SI and its IM3.

[#]Half-duplex noise figure.

[$]12 dB margin has been added to DR_{ADC}.

Since we've assumed that the SI-induced distortion signal at the ADC input has the same power level as the residual main SI after the circulator isolation and analog SIC, the RX effective in-band IIP3 can be calculated as:

$$IIP_{3,RX,eff} = (P_{TX} - ISO - 3) + \frac{1}{2}(SIC_{BB} + 3), \tag{6.1}$$

where the single tone power of a two-tone main SI at the RX input is $P_{TX} - ISO - 3$ and the input-referred IM3 signals are below the main SI by $SIC_{BB} + 3$. The 3 dB[4] margin is for the IM3 signals generated by the integrated circulator. Similarly, the TX-port-referred IP3 of the integrated circulator's TX-to-RX isolation can be calculated as:

$$IIP_{3,Cir,ISO} = P_{TX} - 3 + \frac{1}{2}(SIC_{BB} + 3). \tag{6.2}$$

Equations (6.1) and (6.2) indicate that enhancing SIC_{BB} beyond a certain point carries no benefit. More SIC in the analog BB relaxes the ADC DR requirement. However, more analog BB SIC results in more stringent RX and circulator ISO IIP3 requirements in order to prevent SI IM3 products from dominating the residual SI at the ADC input. It should be noted that a higher circulator isolation relaxes both the ADC DR and the SI-cancelling RX effective IIP3 requirements. Finally, the required SIC in the digital domain for the main SI and SI-induced IM3 signals can be calculated as $P_{TX} - P_{NoiseFloor} - ISO - SIC_{BB}$ each.

Assuming 20 dB isolation from the circulator, the required ADC DR, RX effective IIP3, circulator ISO IIP3, and digital SIC are plotted versus the amount of analog BB SIC in Fig. 6.2. In our design, we choose SIC_{BB}=20 dB, resulting in ADC DR of 58 dB (2×6 dB margin is included as mentioned before), RX effective IIP3 of −17.5 dBm, and circulator ISO IIP3 of +2.5 dBm. In addition, 46 dB SIC is required in the digital domain for both the main SI and SI-induced IM3 signals. Table 6.1 summaries the full-duplex system specifications. It should be mentioned that the supported TX power level is limited by the total achievable SIC across antenna, analog and digital domains (as will be seen later in this Chapter), and not by the power handling capability of the integrated circulator.

[4]The circulator generated IM3 and the RX generated IM3 are coherent, so they may add up or cancel out with each other. We assume a 3 dB increase here as the middle ground.

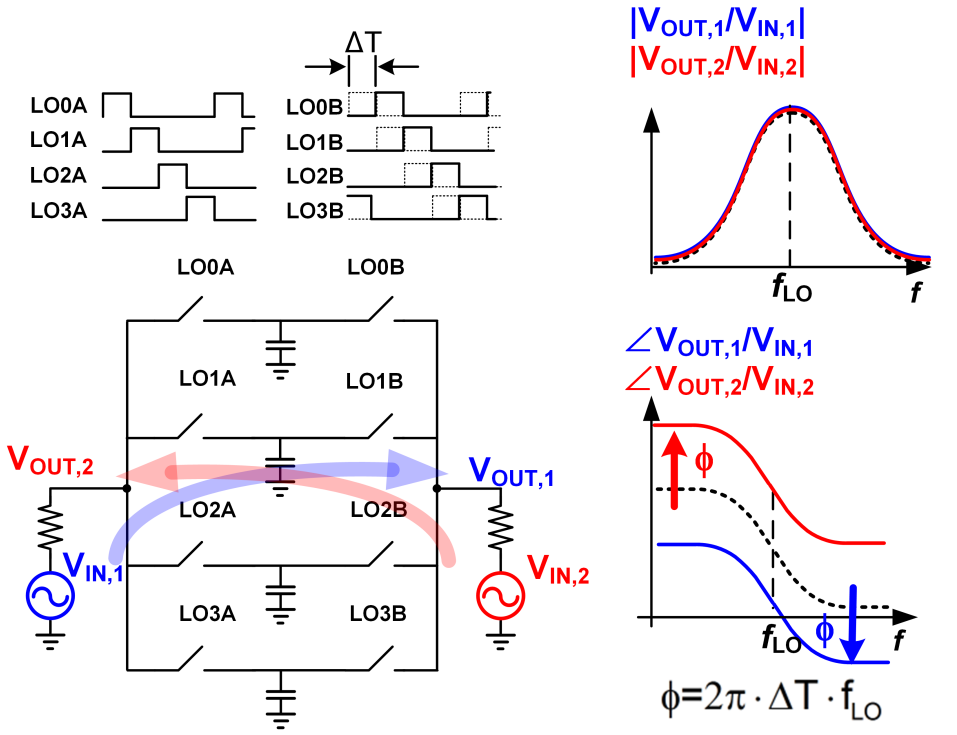

Figure 6.3: A two-port N-path filter with phase-shifted clocks driving the two switch sets at the input and output sides. Signals traveling in opposite directions experience phase shifts with identical magnitude ($2\pi\Delta T f_{LO}$) but with opposite sign as they see a different ordering of commutating N-path switches.

6.2 Integrated Non-Magnetic Passive Circulator

This Section briefly describes the operation principle of the integrated non-magnetic N-path-filter-based passive circulator. A detailed treatment regarding the circulator can be found in [42][115]. This circulator is the work of Negar Reiskarimian, and is only described briefly here to support the description of the full-duplex receiver that integrates this circulator.

Linear Time-Invariant (LTI) passive systems based on conventional materials are reciprocal. A three-port, matched, reciprocal network cannot be lossless [116]. Consequently, a three-port, matched, reciprocal antenna interface with high TX-to-RX isolation, such as electrical balance duplexers[72][73][117][118], necessarily features at least 3 dB loss between TX and antenna and between antenna and RX.

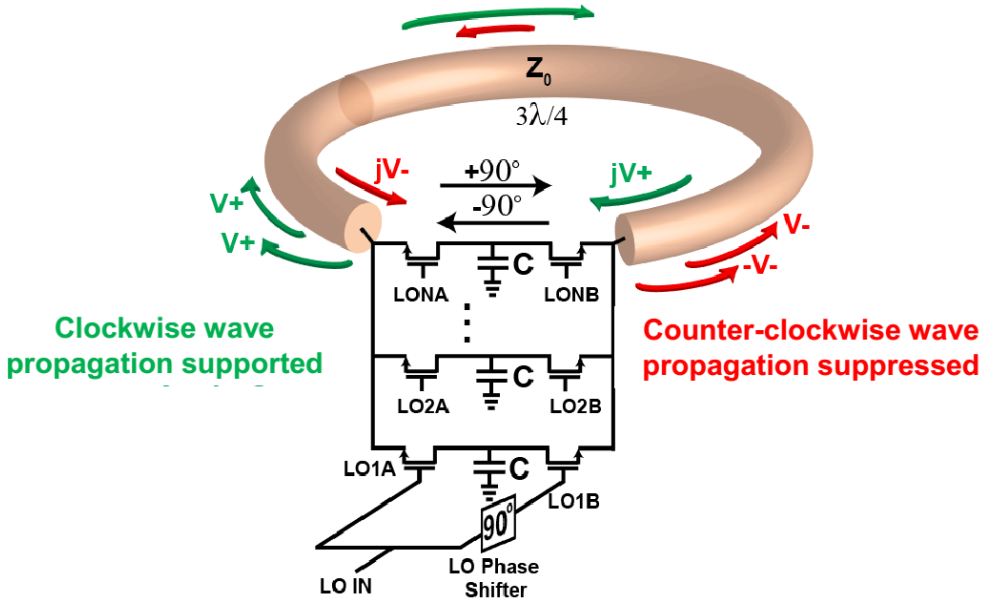

Figure 6.4: Non-reciprocal wave propagation in a ring structure where a $3\lambda/4$ transmission line is wrapped around the phase-non-reciprocal N-path filter with $+90°$ clock phase shift.

The fundamental 3 dB loss can be mitigated via non-reciprocal operation. Reciprocity can be broken by using magnetic materials, active devices, time-variant systems, or non-linear systems [42]. Based on the approaches that can break reciprocity, various circulator technologies have been reported. Conventional ferrite circulators rely on magnetic materials, and are consequently bulky and cannot be integrated on silicon [13]. Circulators using active devices can be integrated, but they have poor noise and linearity performance [75]. Non-magnetic passive circulators leveraging time-varying systems have been reported recently. Non-magnetic non-reciprocity has been achieved by modulating varactors along transmission lines in [119]. However, this technology based on distributedly modulated capacitors has large form factor and requires an extra duplexer to separate the transmit and receive signals. Parametric modulation of coupled resonator loops, resulting in angular momentum biasing, can also create non-reciprocity, and has been used to build non-magnetic circulators[120][121]. However, circulators based on parametric modulation of coupled resonators suffer from either high loss or poor linearity, primarily due to the use of varactors for modulation.

The circulator idea presented here is based on the phase-non-reciprocal behavior of two-port N-

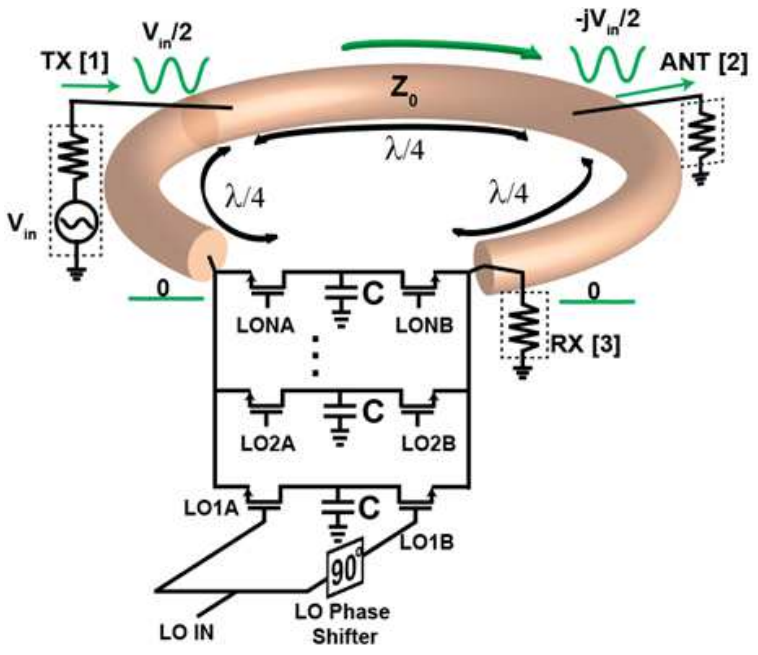

Figure 6.5: A highly-linear passive three-port circulator realization with the RX port being placed next to the N-path filter.

path filters [115]. As discussed in Chapter 5, phase shifting can be embedded in a two-port N-path filter by phase shifting the clocks driving the switches on the output side, essentially staggering the commutating action of the two-port N-path filter as shown in Fig. 6.3. LPTV analysis shows that this introduces constant phase shifts near the switching clock frequency (f_{LO}) with no other impact on the close-in magnitude response [41]. *Interestingly, as can be seen in Fig. 6.3, signals traveling in opposite directions experience phase shifts with identical magnitude ($2\pi\Delta T f_{LO}$) but with opposite sign as they see a different ordering of commutating N-path switches.* This phase non-reciprocity behavior can also be intuitively understood by viewing the two sets of switches as reciprocal quadrature mixers, and viewing the baseband capacitors together with the source resistance at the two ports as a low-pass filter. The low-pass filter attenuates the up-converted signal from the first mixer in either propagation direction. The phase non-reciprocity is achieved by the different roles that the phase-shifted clocks play in different signal propagation directions – the phase-shifted clocks act as up-conversion local oscillators in the left to right direction, and act as down-conversion local oscillators in the right to left direction.

To create non-reciprocal wave propagation, a $3\lambda/4$ transmission line is wrapped around the

N-path filter with +90° clock phase shift as depicted in Fig. 6.4. In such a ring, signals can only propagate in one direction. In the clock-wise direction, the −270° phase shift of the $3\lambda/4$ line combines with the −90° shift of the N-path filter creating constructive interference. Counter-clock-wise, the −270° shift of the line adds with the +90° shift of the N-path generating destructive interference.

A three-port circulator can be realized by introducing three ports anywhere on the transmission line, as long as they maintain a $\lambda/4$ circumferential distance between them. However, if the RX port is placed next to the N-path filter, then for TX port excitations, the RX port, and hence one end of the N-path filter, is quiet due to the isolation of the circulator. The S-parameters of the non-reciprocal N-path filter given in [42] force its two port voltages to be equal in magnitude, and consequently, its other end is quiet as well. *In other words, voltage swings across the N-path filter are suppressed, resulting in high linearity to excitations at the TX port.*

In the circuit implementation, the $3\lambda/4$ transmission line is miniaturized using three CLC sections that are each equivalent to a $\lambda/4$ transmission line. The circulator can also be configured to operate as a reciprocal T/R switch for half-duplex TDD applications as illustrated in Fig. 6.6. If the clock drive is cut and the switches are left open, the circulator simply becomes a low-loss 50 Ω transmission line from ANT to RX. Similarly, the circulator reduces to a low-loss 50 Ω line from ANT to TX if a pair of switches is held high.

6.3 Joint-SIC In the Antenna and Analog Domains

As mentioned in Section 6.1, the analog BB SIC together with the initial circulator isolation in the antenna domain relax the ADC DR and digital SIC requirements. It is known that SI suppression across different domains must be jointly optimized to obtain the best performance [57]. In this section, a joint-SIC methodology across domains is presented with enhanced performance when compared to an approach where the antenna interface and the analog BB SI canceller are configured independently.

Figure 6.7(a) illustrates the SI-cancelling full-duplex radio with the integrated circulator and an impedance tuner at the circulator antenna port. Circulators typically require an impedance tuner at their antenna ports to counter reflections due to antenna impedance mismatch [116].

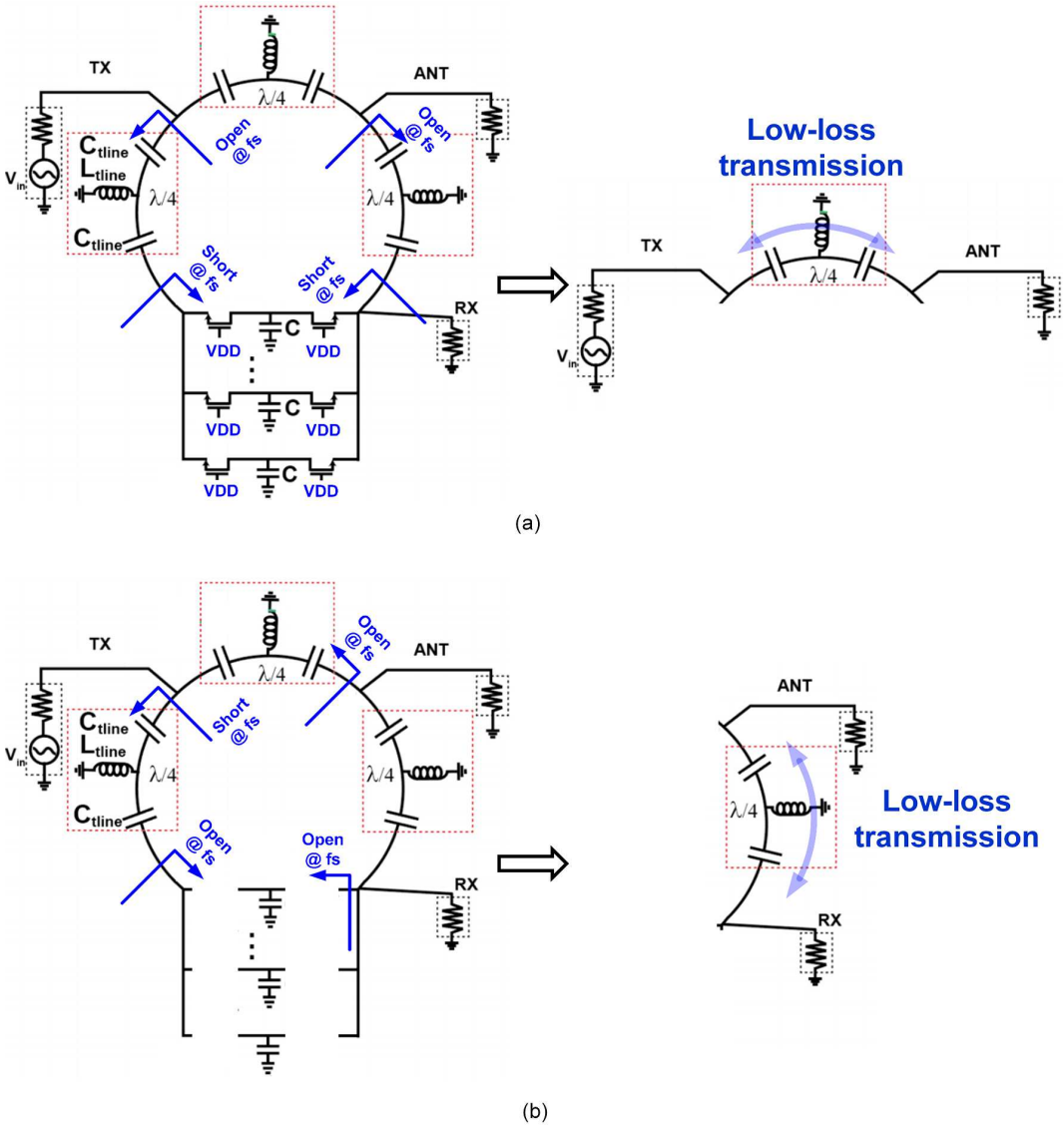

Figure 6.6: Time-division duplexing (TDD) mode of operation: (a) TX-antenna transmission mode and (b) antenna-RX transmission mode.

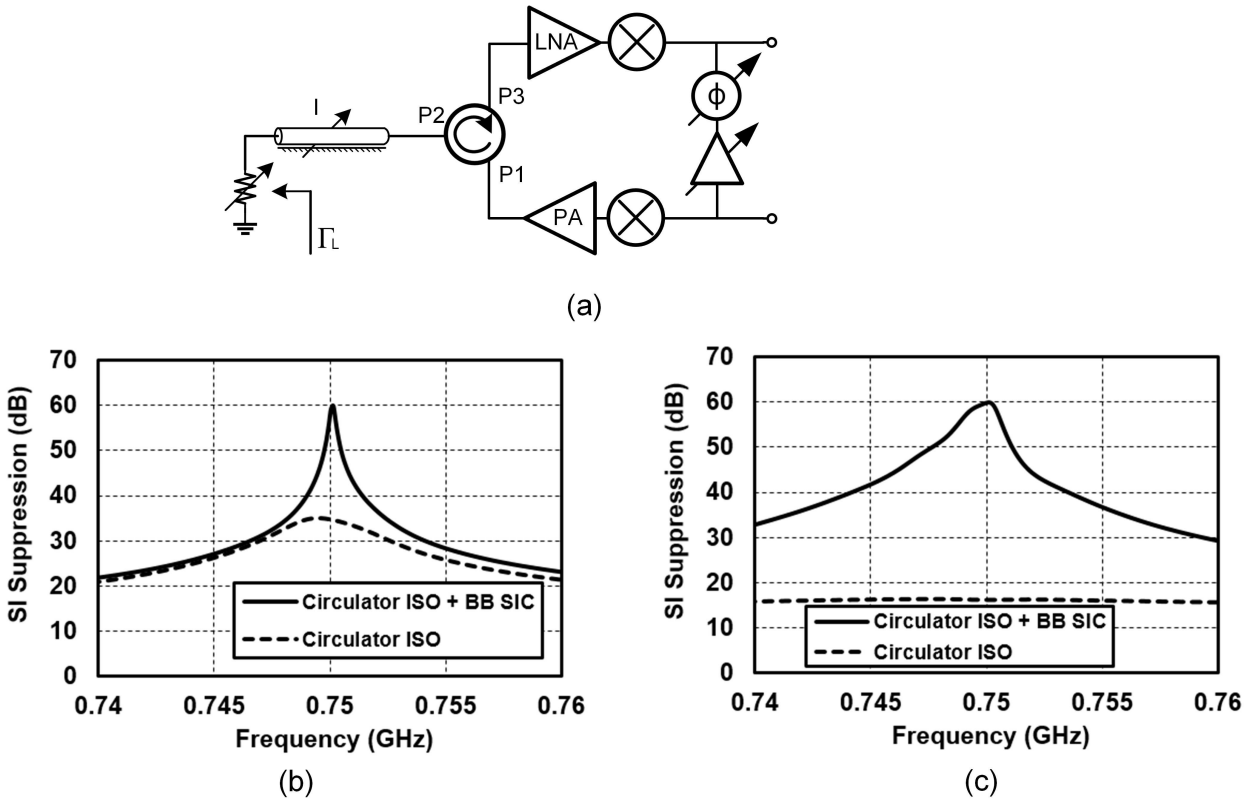

Figure 6.7: Joint SIC in the antenna and analog domains: (a) diagram, (b) overall SIC with an impedance tuner being used to provide 35 dB peak narrowband circulator isolation, (c) overall SIC with an impedance tuner being used to provide a frequency-flat circulator isolation of 16 dB.

The impedance tuner here is modeled as a transmission line with a variable length loaded with a programmable resistive termination [122]. The residual SI at the RX input after the antenna interface isolation can be written as:

$$P_R = (S_{31} + S_{21}S_{32}\Gamma_L e^{-2j\beta l})P_{TX}, \tag{6.3}$$

where S_{31}, S_{21}, and S_{32} are the S-parameters of the circulator, Γ_L is the reflection coefficient of the impedance tuner, l is the variable length of the impedance tuner transmission line, and β is the propagation constant of the impedance tuner transmission line.

In a joint-SIC approach, the residual SI after the antenna interface isolation is designed to mimic the response of the analog SI canceller. An amplitude-and-phase-based analog BB SI canceller as depicted in Fig. 6.7(a) has a relatively flat frequency response. Therefore, the residual SI after the antenna interface isolation needs to be flat across frequency. Having frequency-flat residual SI is mathematically equivalent to $\frac{d|P_R|}{df} = 0$ and $\frac{d\angle P_R}{df} = 0$, which require $\frac{dRe\{P_R\}}{df} = 0$ and $\frac{dIm\{P_R\}}{df} = 0$. Assuming $\Gamma_L \neq 0$ and $cos(\angle S_{21} + \angle S_{32} - 2\beta l) \neq 0$, we have:

$$(tan\angle P - Q)\frac{d|S_{21}||S_{32}|}{df} + (1 + Rtan\angle P)\frac{d\angle P}{df}|S_{21}||S_{32}| = 0, \tag{6.4}$$

where $P = \angle S_{21} + \angle S_{32} - 2\beta l$, $Q = \frac{d(|S_{31}|cos\angle S_{31})/df}{d(|S_{31}|sin\angle S_{31})/df}$. From (6.4), l can be solved numerically using Newton's Method. Once l is found, Γ_L can be solved explicitly as:

$$\Gamma_L = -\frac{\frac{d|S_{31}|sin\angle S_{31}}{df}}{\frac{d|S_{21}||S_{32}|}{df}sin\angle P + |S_{21}||S_{32}|cos\angle P\frac{d\angle P}{df}}. \tag{6.5}$$

To illustrate the benefit of the proposed joint-SIC approach, Figs. 6.7(b), (c) show a couple of SIC examples across the antenna and analog domains. The results in Figs. 6.7(b), (c) are based on the measured S-parameter results of the integrated circulator (see Section VI-A) and a frequency-flat amplitude-and-phase-based analog BB SI canceller. The impedance tuner is used to provide 35 dB peak narrowband circulator isolation for the example shown in Fig. 6.7(b), while it ensures frequency-flat circulator isolation of 16 dB in the other example shown in Fig. 6.7(c). With a frequency-flat analog BB SI canceller, the 40 dB SIC bandwidths in Figs. 6.7(b) and (c) are 2.3 MHz and 9.5 MHz respectively, indicating a greater-than-four-times improvement in the SIC bandwidth using the joint-SIC approach.

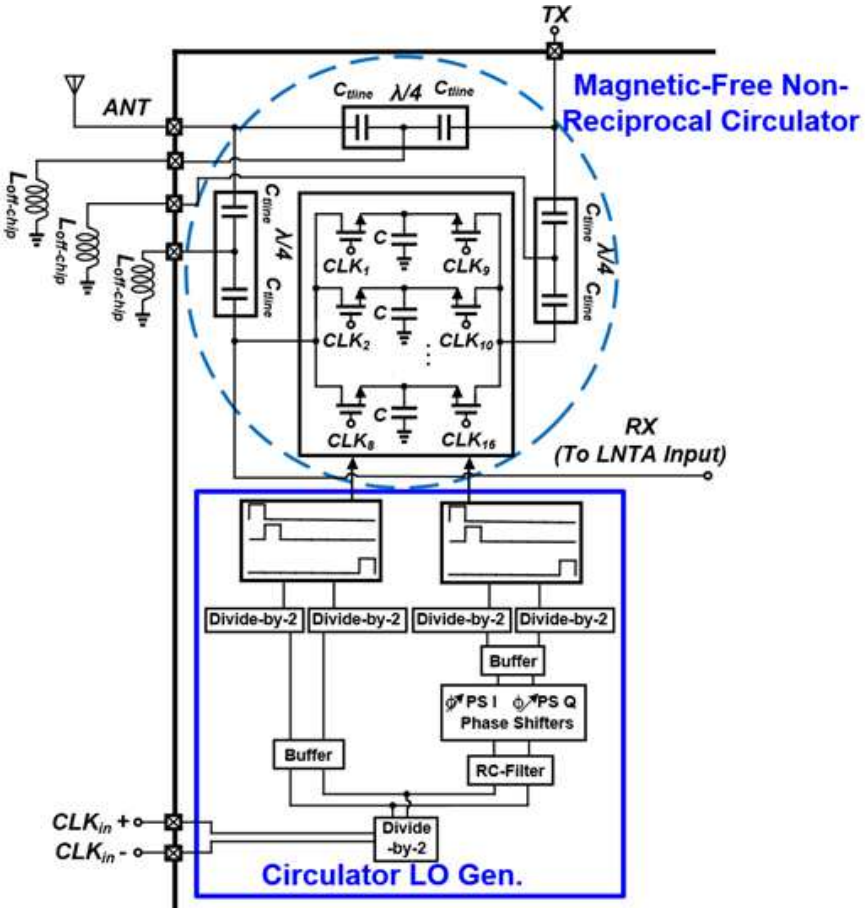

Figure 6.8: Block diagram and circuit schematic of the integrated non-magnetic passive N-path-filter-based circulator.

6.4 Implementation

6.4.1 Integrated Circulator

The circulator was designed for tunable operation around 750 MHz in 65 nm CMOS. The schematic of the circulator is depicted in Fig. 6.8. The $\frac{3\lambda}{4}$ line is miniaturized using three CLC sections implemented with on-chip MiM capacitors and off-chip air-core 8.9 nH inductors (0806SQ from Coilcraft, Q_L >100). The N-path filter uses 8-paths. Clock phase-shifting is accomplished using 4-phase vector-interpolation phase-shifters at twice the switching frequency, followed by a second frequency division to achieve 8 phases.

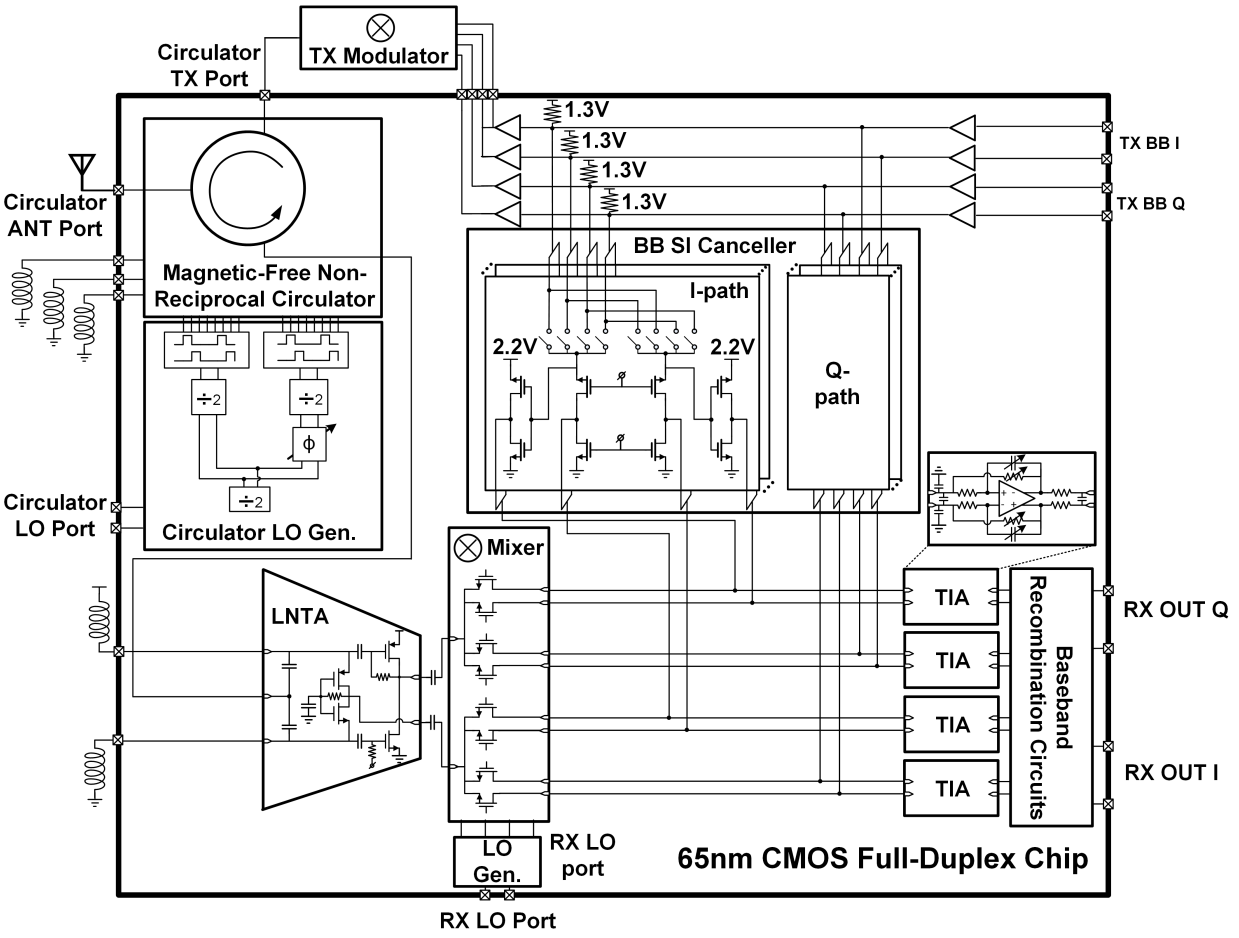

Figure 6.9: Block diagram and schematic of the implemented 65 nm CMOS full-duplex receiver with the integrated circulator and analog BB self-interference cancellation.

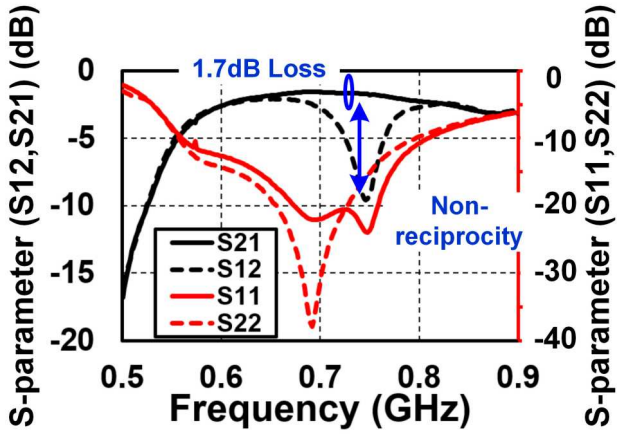

Figure 6.10: Measured circulator S-parameters in full-duplex mode between its antenna port and TX port, showing non-reciprocal operation and 1.7 dB TX-to-antenna insertion loss. (Ports 1 and 2 are TX and ANT port, respectively.)

6.4.2 Integrated Receiver and Analog Baseband SI Canceller

As depicted in Fig. 6.9, the circulator is integrated with a noise-canceling current-mode RX that is similar to the one in [4]. Both the circulator and the RX are powered from 1.2V supplies. The analog BB canceller taps from the TX BB (TX BB buffers are integrated on chip for this purpose), adjusts the amplitude and the phase, and injects the cancellation current at the TIA input. Performing BB SIC at the TIA input not only protects the RX analog BB circuits, but also enhances the RX mixer and LNTA linearity by creating a virtual ground at the passive mixer output. Amplitude and phase scaling are achieved through two 5-bit digitally-controlled phase rotators injecting into the I- and Q-paths of the RX analog BB. Each phase rotator consists of 31 identical cells with independent controls, similar to [8]. The unit cell of the phase rotator adopts a noise-canceling CG and CS topology, allowing the partial cancellation of the noise from the CG devices (dependent on the phase rotator setting). 1.3V and 2.2V supplies are used for the BB canceller as indicated in Fig. 6.9.

6.5 Measurement Results

6.5.1 Integrated Circulator

Measurements from a breakout of the circulator in full-duplex mode reveal 1.7 dB loss in TX-ANT and ANT-RX transmission and broadband isolation better than 15 dB between TX and RX (the narrowband isolation can be as high as 50 dB) as shown in Fig. 6.10. The in-band ANT-RX IIP3 is +8.7 dBm while the in-band TX-ANT IIP3 is +27.5 dBm, significantly higher due to the suppression of swing across the N-path filter. The ANT-RX NF is 4.3 dB, degraded from the expected 2 dB NF. This NF degradation is due to the implementation approach of the clock phase shifter (the square-wave digital clocks are attenuated and filtered to produce weak sine waves for linear vector interpolation, leading to susceptibility to phase noise). Elimination of the phase shifters (not necessary as only a static 90° phase shift is desired) or a redesign of the phase shifters using a purely digital topology restores the NF to around 2 dB in simulation. Comprehensive circulator characterization results can be found in [42][115].

6.5.2 Receiver with Circulator

The chip microphotograph of the 65nm CMOS SI-cancelling full-duplex receiver with the integrated circulator is shown in Fig. 6.11. The chip has an active area of 1.44 mm^2 and is mounted in a QFN56 package. The SI-cancelling full-duplex receiver with the integrated circulator operates over 610-850 MHz, with peak gain of 42 dB, IB IIP3 of −33 dBm at peak gain, and OOB IIP3 of +19 dBm at 200 MHz offset and +11 dBm at 40 MHz offset when the circulator is in full-duplex mode (Fig. 6.12). All these results are referred to the ANT port. When the circulator is configured in TDD mode, the measured peak gain and IB IIP3 at peak gain are the same as when the circulator is in full-duplex mode. The measured OOB IIP3 is +16 dBm at 200 MHz offset and +4 dBm at 40 MHz offset. The OOB IIP3 in full-duplex mode benefits from the filtering effect of the circulator's N-path filter at the RX input. The measured NF is 5.0 dB in TDD RX mode, and increases to 8.4 dB in full-duplex mode due to the circulator LO path phase noise issue described earlier [as in Fig. 6.12(b)]. The improved LO design described earlier restores the full-duplex mode NF to 5 dB in simulation.

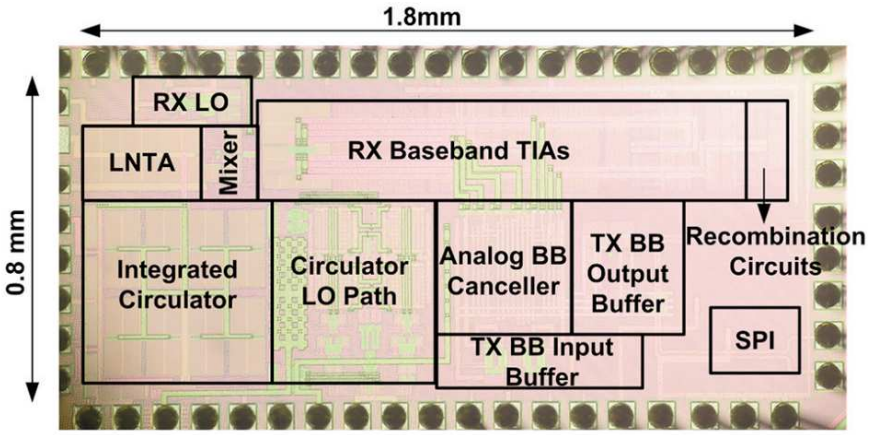

Figure 6.11: Chip microphotograph of the 65 nm CMOS full-duplex receiver with integrated circulator and analog BB self-interference cancellation.

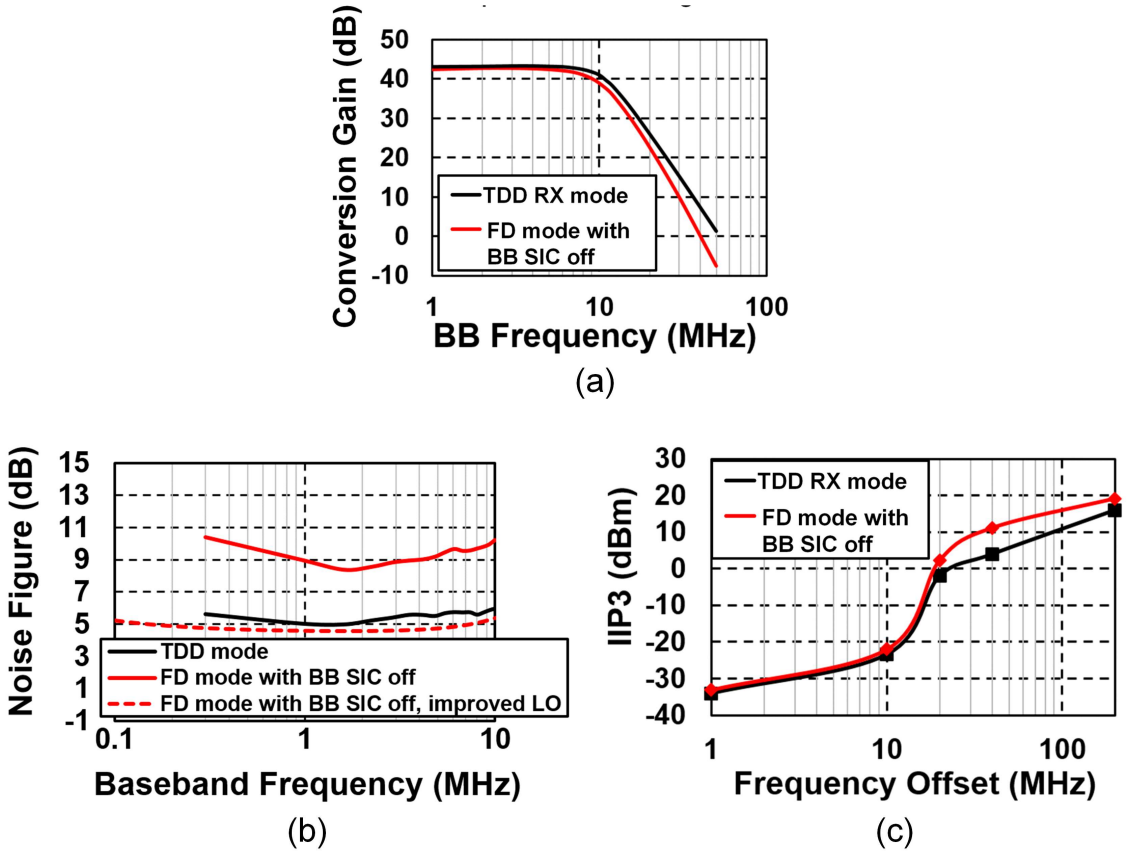

Figure 6.12: Measured circulator ANT-to-RX-BB characteristics: (a) conversion gain, (b) noise figure, and (c) IIP3.

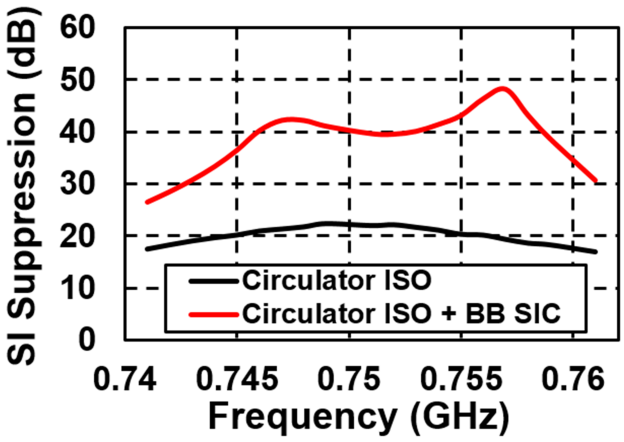

Figure 6.13: Measured small-signal SI suppression across the circulator and analog domains using the presented joint-SIC approach.

6.5.3 Transmitter and LO Path

The transmitter uses an off-the-shelf quadrature modulator from Texas Instruments [123] that is driven by the integrated TX baseband buffers, and has a measured output IP3 of +20 dBm. The TX output noise level is measured to be −145 dBm/Hz. Given 20 dB circulator isolation, the TX noise floor at the receiver input would be −165 dBm/Hz, which is 3 dB lower than the RX input-referred noise floor. The measured transmitter image rejection ratio is greater than 30 dB and thus doesn't limit the targeted 20 dB analog BB SIC.

The circulator and the full-duplex receiver receive clock inputs at four times and twice the RF carrier frequency, respectively. In the measurement, a custom-designed discrete-component-based divide-by-two divider was used in the receiver LO path allowing the circulator and the full-duplex receiver to share one LO source. The TX modulator which receives an LO at the RF carrier frequency used a separate LO source. Thanks to a relatively-low transmitter output power level and the fact that we used high-quality signal sources, the noise floor induced by the lack of correlation between TX and RX phase noise doesn't degrade the original noise floor of the receiver.

6.5.4 Full-Duplex Operation

As discussed in Section 6.3, a joint-SIC approach was used for achieving better overall SIC across the antenna and analog domains. In the measurement, an integrated overall SI suppression of 42 dB

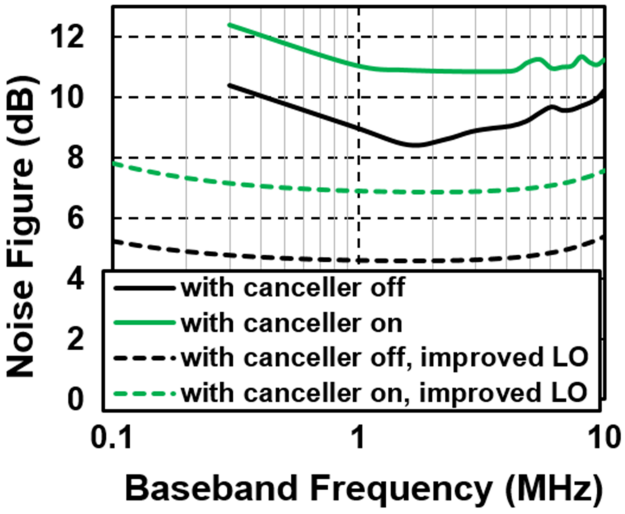

Figure 6.14: Measured and simulated impact of the analog BB SI canceller on RX NF in the full-duplex mode.

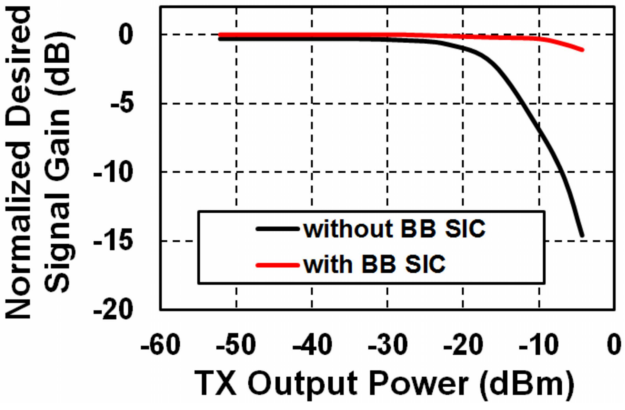

Figure 6.15: Measured ANT-to-RX-BB gain compression of a weak desired signal with and without analog BB SIC versus varying TX output power level.

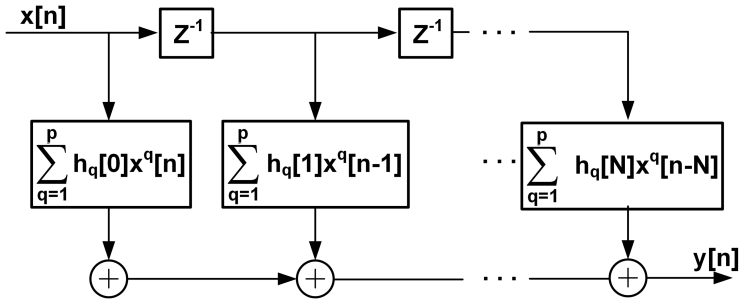

Figure 6.16: The nonlinear tapped delay line used for digital SIC.

was achieved across the circulator and analog BB SIC over a BW of 12 MHz (Fig. 6.13).

As shown in Fig. 6.14, the analog BB SI canceller further increases the RX NF to 10.9 dB (TX signal not present). With the improved LO design for the circulator as described earlier, a 7 dB NF with the BB SI canceller on is obtained in simulation. Fig. 6.15 depicts linearity tests under powerful SI with the same antenna tuning mentioned before for 42 dB average overall SIC. SIC of up to -4 dBm of TX power results in small gain compression (1 dB) of a desired signal, as opposed to nearly 15 dB of compression in the absence of analog BB SIC.

Fig. 6.17 depicts both the main two-tone SI at the RX output as well as IM3 distortion generated on the SI by the circulator, RX and BB canceller for varying TX two-tone power. All signals are referred back to the ANT port to enable comparison with the noise floor of -92 dBm. The same antenna tuning that was applied in the joint-SIC approach is used here. Analog BB SIC improves the effective in-band RX IIP3 from -33 dBm to -18 dBm. We have also implemented digital SIC in Matlab after capturing the baseband signals using an oscilloscope (an 8-bit quantizer). The digital SIC is based on a nonlinear tapped delay line (see Fig. 6.16) which essentially models the SI channel in digital as a truncated Volterra series [44][124]:

$$y[n] = \sum_{k=0}^{N} h_1[k]x[n-k] + \sum_{k=0}^{N} h_2[k]x^2[n-k] + \sum_{k=0}^{N} h_3[k]x^3[n-k] + \cdots + \sum_{k=0}^{N} h_p[k]x^p[n-k], \quad (6.6)$$

where $y[n]$ is the nonlinear tapped delay line output, $x[n]$ and $x[n-k]$ (k represents the delay index) are the current and past TX digital baseband signals, N corresponds to the maximum delay in the modeled SI channel, and $h_i[k]$ ($i = 1, 2, 3 \ldots, p$) is the i-th order digital canceller coefficient for a delay index of k. The truncation of the Volterra series helps to reduce the digital

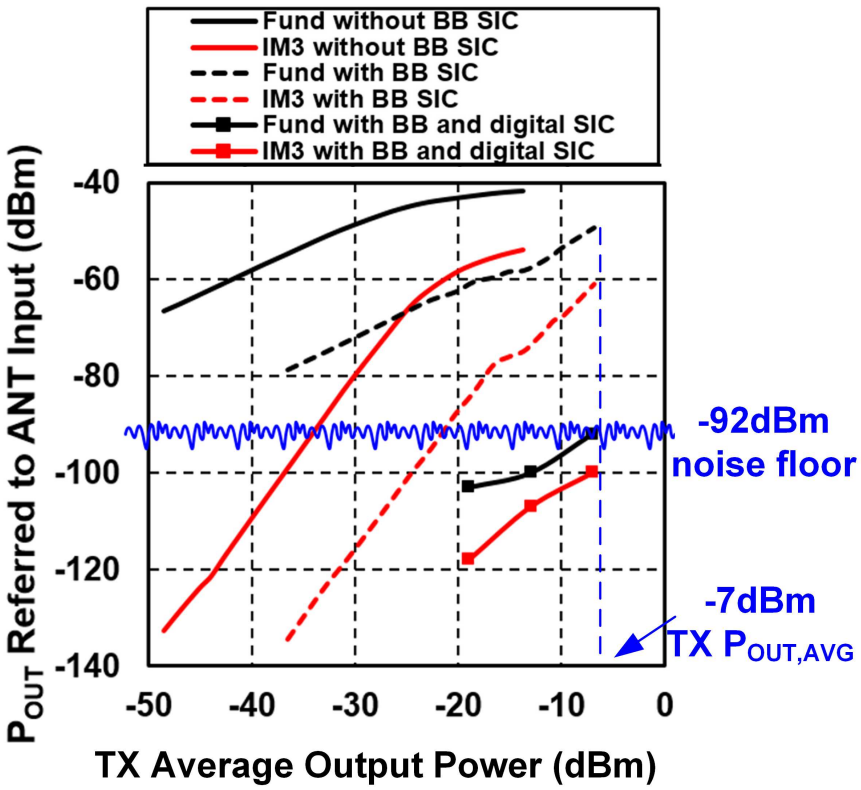

Figure 6.17: Measured two-tone linearity test with SI suppression across antenna, analog BB and digital domains, demonstrating a full-duplex link budget of −7 dBm TX average output power and −92 dBm noise floor.

Table 6.2: Performance summary and comparison.

	JSSC 2015 [4]	JSSC 2015 [8]	JSSC 2015 [9]	This work
Architecture	RX with wideband SIC based on RF frequency-domain equalization	Mixer-first RX with SI-cancelling VM-downmixer	Mixer-first TRX with Active Baseband Duplexing	RX with integrated magnetic-free N-path-filter-based circulator and BB SIC
RX Frequency	0.8-1.4 GHz	0.15-3.5 GHz	0.1-1.5 GHz	0.6-0.8 GHz
Maximum Gain	42 dB	24 dB	53 dB	42 dB
Noise Figure	4.8 dB	6.3 dB	5-8 dB	5.0 dB (TDD mode)
OOB IIP3	+ 17 dBm	+22.0 dBm	+22.5 dBm	+19 dBm
IB IIP3	-20 dBm at 27 dB gain	+9 / +19 dBm at 24dB gain (Neg. conductance off/on)	-38.7 dBm at 53 dB gain	-33 dBm at 42 dB gain
Integrated Antenna Interface	No	No	Yes (baseband duplexing LNA)	Yes (magnetic-free non-reciprocal circulator)
Integrated SI Suppression Domains	RF	RF	Analog BB	Antenna + Analog BB
Amount of Integrated SI Suppression	20 dB SIC across 25 MHz BW	21 dB integrated SIC across ~16 MHz BW	33 dB across 300kHz TX BB BW	42 dB SIC across 12 MHz BW (incl. integrated circulator)
Effective IIP3 with respect to RX/ANT Input	+2 dBm at 27 dB gain	+21.5 dBm at 24dB gain	N/A	-18 dBm at 42 dB gain
Effective IIP3 with respect to TX Power	N/A	N/A	~0 dBm at 43/53 dB gain[1]	+1 dBm at 42 dB gain
NF Degradation in Full-Duplex Mode	0.9/1.3 dB[4]	4-6 dB[5]	N/R	6.5 dB[2] (incl. circulator in FD mode)
Overall SI Suppression	56 dB (incl. 34 dB isolation from antenna pair)	46 dB (incl. 25 dB isolation from antenna pair)	N/A	85 dB (incl. digital SIC)
RX Power	63-69 mW	22-46 mW	43-56 mW (incl. TX)	60 mW signal path + 10 mW LO path (at 0.7GHz)
SI Canceller Power	0-182 mW	1-10 mW		30 mW
Antenna Interface Power	N/A	N/A	N/A	59mW[3] (at 0.7GHz)
Technology	65 nm CMOS	65 nm CMOS	65 nm CMOS	65 nm CMOS
Active Area	4.8 mm^2	2 mm^2	1.5 mm^2	1.4 mm^2

1. From Fig. 31(a) in the paper. 2. Includes circulator 4.3dB NF, which is degraded from the expected 2dB NF due to LO phase noise. Elimination of the phase shifters (not necessary as only a static 90°phase shift is desired) restores the circulator NF to 2dB in simulation.
3. Circulator power consumption can be significantly reduced if the phase shifters are removed as only a static 90°phase shift is desired.
4. One/two canceller filters enabled. 5. Across VM settings. N/A: Not Applicable N/R: Not Reported

SI canceller complexity to a manageable level. In our measurement, nonlinear terms up to 4^{th} order are considered (i.e., $p = 4$) with a delay spread length of 41 samples, resulting in 164 total unknown canceller coefficients. The digital SI canceller coefficients are determined using a two-tone pilot signal. By taking into account both the delay spread and the nonlinearities of the SI channel, the digital SIC cancels not only the main SI but also the IM3 distortion generated on the SI . After digital SIC, the main SI tones are at the noise floor, while the SI IM3 tones are 8 dB below for -7 dBm TX average power. This corresponds to a total SI suppression of 85 dB. The -7 dBm TX average power is not limited by the power handling of the circulator, but rather by the need to cancel the main SI down to the noise floor in our measurement (in other words, by the achieved total SI suppression).

Table 6.2 compares this work to prior integrated full-duplex receivers. The novel aspects of this work include the integrated non-magnetic non-reciprocal passive circulator with very low TX-ANT loss (1.7 dB) and 85 dB total SI suppression in conjunction with digital SIC.

6.6 Summary

This Chapter introduced a self-interference-cancelling full-duplex receiver with an integrated non-magnetic passive N-path-filter-based non-reciprocal circulator and analog baseband SIC that achieves 42 dB on-chip SI suppression across the antenna and analog BB domains over a 12 MHz signal BW using a joint-SIC approach. In conjunction with digital SI and its IM3 distortion cancellation, the full-duplex receiver demonstrates 85 dB overall SI suppression, enabling a full-duplex link budget of -7 dBm TX average output power and -92 dBm noise floor.

Chapter 7

Cross-Layer Analysis and Design of Full-Duplex Wireless Systems

To fully utilize the benefits of full-duplex communication, wireless systems will require a careful redesign of not only the PHY layer but also the MAC layer. While the focus of this thesis is on integrated radios for full-duplex wireless at the PHY layer, cross-layer investigations have been performed in our collaborative efforts with researchers at higher layers of the stack and has allowed us to make concrete steps towards practical full-duplex wireless networks. This larger cross-layer project has been dubbed the Columbia FlexICoN (The Full-duplex Wireless: From Integrated Circuits to Networks) project [125].

As outlined in Fig. 8.1, our full-duplex cross-layer research is based on integrated self-interference-cancelling radios presented in the previous Chapters at the PHY layer. Based on our model of the remaining SI in integrated full-duplex radios, power control algorithms are derived and rate gains are characterized for full-duplex wireless communication systems in [21][126]. Section 7.1 discusses the model of the remaining SI for integrated full-duplex radios and touches upon some of the key results from [21][126]. To enable experimental characterization of full-duplex MAC layer algorithms, we have developed a cross-layered software-defined full-duplex radio testbed. Section 7.2 discusses the full-duplex radio testbed and a practical real-time full-duplex wireless demonstration [22]. At the end of this Chapter (Section 7.3), a multi-band FDD demonstration using a tunable duplexer based on microwave cavity filters [43][127] and our integrated widely-tunable SI-cancelling receiver

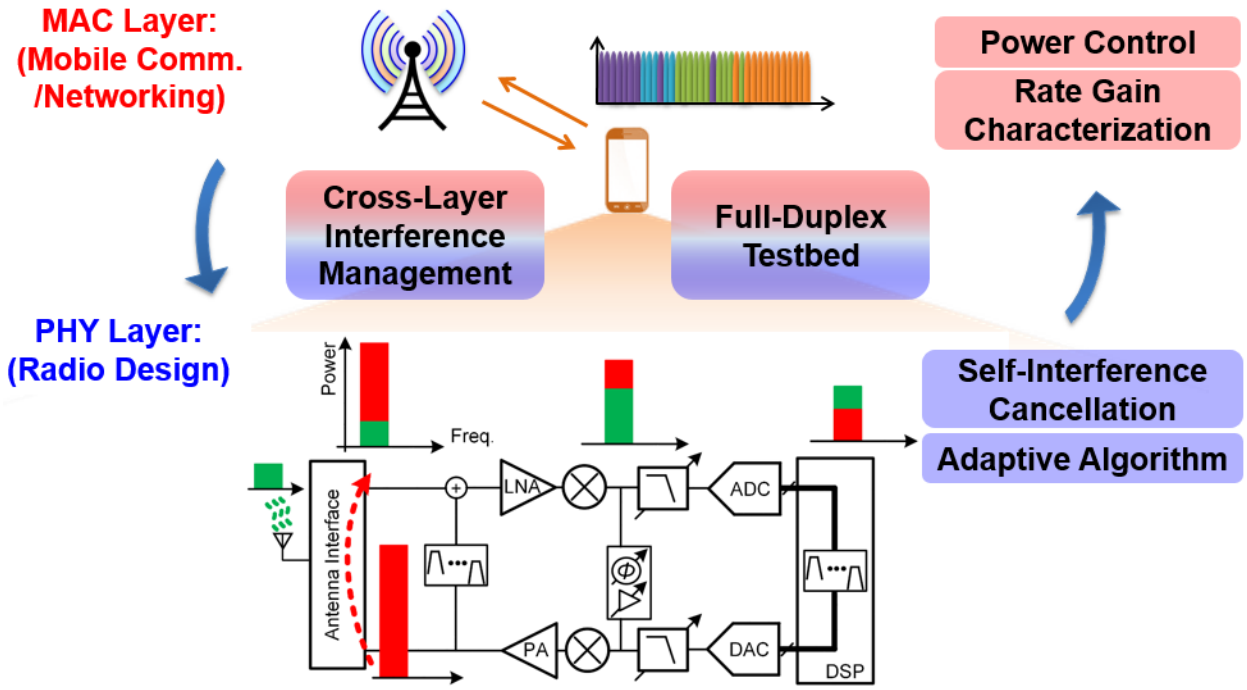

Figure 7.1: Outline of our full-duplex cross-layer research in collaboration with Profs. Gil Zussman and Yuan Zhong, Dr. Jelena Marasevic, and Tingjun Chen from Columbia University.

in [4] is presented.

The full-duplex cross-layer research was performed in collaboration with Professors Gil Zussman and Yuan Zhong, Dr. Jelena Marašević, and Tingjun Chen from Columbia University. The model of the remaining SI for integrated full-duplex radios was developed in collaboration with Jelena. Based on the model, power control algorithms and rate gains were derived and characterized exclusively by Jelena. The full-duplex radio testbed and the practical real-time full-duplex wireless demonstration (including our RF and real-time digital SIC algorithms) were developed in collaboration with Tingjun. The realization of our RF and real-time digital SIC algorithms and data communications in commercial software-defined radios were performed exclusively by Tingjun. The FDD demonstration was performed in collaboration with Professor Dimitrios Peroulis, Dr. Mohammad Abu Khater, and Yu-Chen Wu from Purdue University, and the tunable duplexer based on microwave cavity filters was developed exclusively by Dr. Mohammad Abu Khater, Yu-Chen Wu, and Professor Dimitrios Peroulis.

7.1 Resource Allocation and Rate Gains in Full-Duplex Networks

Much existing work on full-duplex rate improvement assumes perfect SIC [128][129][130][131] – SIC that suppresses SI to at least the RX noise floor and is flat across frequencies. However, such SIC has been only reported in discrete-component-based full-duplex radios (e.g., [2]). For integrated full-duplex radios, SIC can be frequency selective as we discussed in Chapter 3. Note that the realization of integrated full-duplex radios is critical if we are to bring full-duplex functionality to handheld devices such as smartphones.

The frequency selectivity of SIC using integrated full-duplex radios has not been considered in any analytical work regarding full-duplex rate improvement. This is an important feature that is inherent in integrated full-duplex radios, where frequency selectivity is mainly a consequence of the cancellation in the analog/RF domain [64][56][65]. While continued research progress will improve the quality of the SIC that can be achieved in integrated radios, the technology constraints associated with integrated implementations and the form factor and power consumption constraints associated with mobile devices will always render SIC in such implementations more challenging than implementations based on discrete components or laboratory bench-top equipment.

Hence, one of the main contributions of the work presented in [21] is a thorough analytical study of rate gains from full-duplex under non-negligible SI based on a mathematical model that captures the practical frequency-dependent SIC at mobile stations using integrated full-duplex radios.

7.1.1 Model of the Remaining SI in Integrated Full-Duplex Radios with Frequency-Flat RF Canceller

A mathematical model of the remaining SI in integrated full-duplex radios with frequency-flat amplitude- and phase-based RF SI cancellers is derived here.

Figure 7.2 depicts the block diagram of a full-duplex radio employing SI suppression in the antenna, RF, and digital domains. The magnitude and phase response of the RF SI canceller is assumed to be frequency flat and is denoted by $|H_{C,R}|$ and $\angle H_{C,R}$. In addition, the magnitude and phase response of the canceller is assumed to be programmable. For the antenna interface's SI isolation, we assume a flat magnitude response $|H_A(f)| = const = |H_A|$ and a constant group delay equal to τ, so that $H_A(f) = |H_A|e^{-j2\pi f\tau}$. For the digital SIC, we assume that the amount

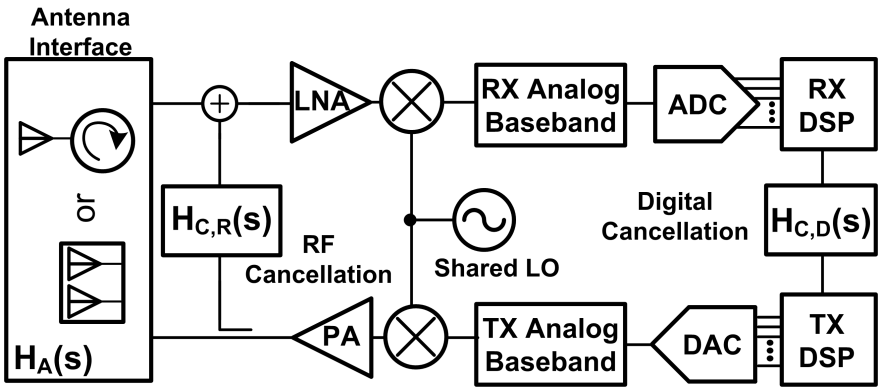

Figure 7.2: Block diagram of a full-duplex radio employing RF and digital self-interference cancellation with a frequency-selective antenna interface.

of cancellation, denoted by SIC_D, is constant across frequency, as delay can be easily generated in the digital domain.

We assume that the network bandwidth of size B is subdivided into K orthogonal frequency channels of width B/K each, and index the frequency channels with $k \in \{1, ..., K\}$. An example of such sub-channelization is Orthogonal Frequency-Division Multiplexing (OFDM) with each frequency channel consisting of an integral number of subcarriers. Let f_k denote the central frequency of the k^{th} channel, so that $f_k = f_1 + (k-1)B/K$. Then, the remaining SI after cancellation can be written as:

$$\begin{aligned} RSI_{m,k} &= |P_{m,k}(H_A - H_{C,R})SIC_D^{-1}| \\ &= P_{m,k}||H_A|e^{-j\angle H_A(f_k)} - |H_{C,R}|e^{-j\angle H_{C,R}}|SIC_D^{-1} \\ &= P_{m,k}||H_A|^2 + |H_{C,R}|^2 - 2|H_A||H_{C,R}| \cdot \cos(\angle H_A(f_k) + \angle H_{C,R})|SIC_D^{-1}, \end{aligned} \tag{7.1}$$

where $P_{m,k}$ is the Mobile Station (MS) transmission power on channel k, $P_{m,k}(H_A - H_{C,R})$ is the remaining SI after the RF SIC, and $P_{m,k}(H_A - H_{C,R})SIC_D^{-1}$ is the remaining SI after both the RF and digital SIC. We assume a common oscillator for the TX and RX, with the phase noise of the oscillator being good enough so that it does not affect the remaining SI.

The RF canceller's settings can be programmed in the field to adjust the frequency at which peak SIC is achieved. With the amplitude ($|H_{C,R}|$) and the phase ($\angle H_{C,R}$) of the RF canceller set to $|H_A|$ and $-\angle H_A(f_c)$, respectively, peak SIC is achieved at frequency f_c. Therefore, the total

remaining SI on channel k can be written as:

$$RSI_{m,k} = 2|H_A|^2 P_{m,k}(1 - \cos(2\pi\tau(f_k - f_c)))SIC_D^{-1}, \tag{7.2}$$

where τ is the group delay from the antenna interface with a typical value at the order of nanoseconds. Frequency bands used by commercial wireless systems are at most 10s of MHz wide. It follows that $2\pi\tau(f_k - f_c) << 1$, and using the standard approximation $\cos(x) \approx 1 - x^2/2$ for $x << 1$, we further get:

$$RSI_{m,k} \approx |H_A|^2 P_{m,k}(2\pi\tau)^2(f_k - f_c)^2 SIC_D^{-1}. \tag{7.3}$$

Recalling that $f_k = f_1 + (k-1)B/K = f_0 + kB/K$ for $f_0 = f_1 - B/K$, and writing f_c as $f_c = f_0 + cB/K$, for $c \in \mathbb{R}$, we can combine all the constant terms and represent the remaining SI as:

$$RSI_{m,k} = g_m P_{m,k}(k - c)^2, \tag{7.4}$$

where $g_m = |H_A|^2(2\pi\tau)^2(B/K)^2 SIC_D^{-1}$.

Fig. 7.3 shows the SI suppression based on (7.4) and based on measurement results using a commercial 2110-2170 MHz miniature circulator [13] and an integrated RF canceller with flat magnitude and phase response. The parameter g_m in Eq. (7.4) was determined via a least square estimation. As Fig. 7.3 shows, our model of the remaining SI closely matches the remaining SI that we measured.

7.1.2 Power Control and Rate Gain

Based on the model presented in Section 7.1.1, our collaborators have derived power control algorithms and characterized rate gains for full-duplex wireless links [21]. Here, we briefly discuss some of the numerical results given in [21].

The numerical evaluation setup assumes a bidirectional full-duplex link between an MS that uses an integrated full-duplex radio and a discrete-component-based Base Station (BS) (see Fig. 7.4). We further consider a total bandwidth of 20 MHz being subdivided into 33 orthogonal frequency channels (i.e. B=20 MHz and K=33). Since measurement-based modeling was performed only for

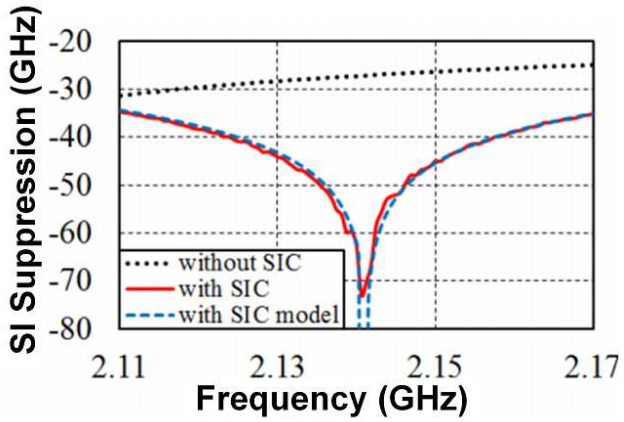

Figure 7.3: Self-inference suppression profile using a commercial 2110-2170 MHz miniature circulator [13] and an integrated RF canceller with flat magnitude and phase response. Our model of the remaining SI closely matches the remaining SI in the measurement.

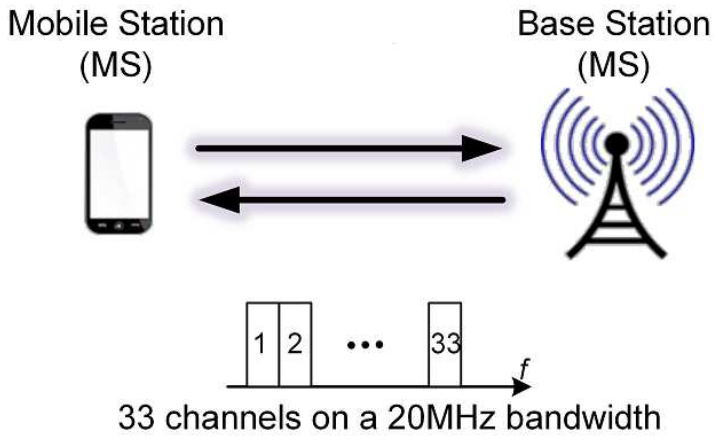

Figure 7.4: A bidirectional full-duplex link between an MS that uses an integrated full-duplex radio (featuring a frequency-flat RF SI canceller) and a discrete-component-based BS. We assume a total bandwidth of 20 MHz is subdivided into 33 orthogonal frequency channels.

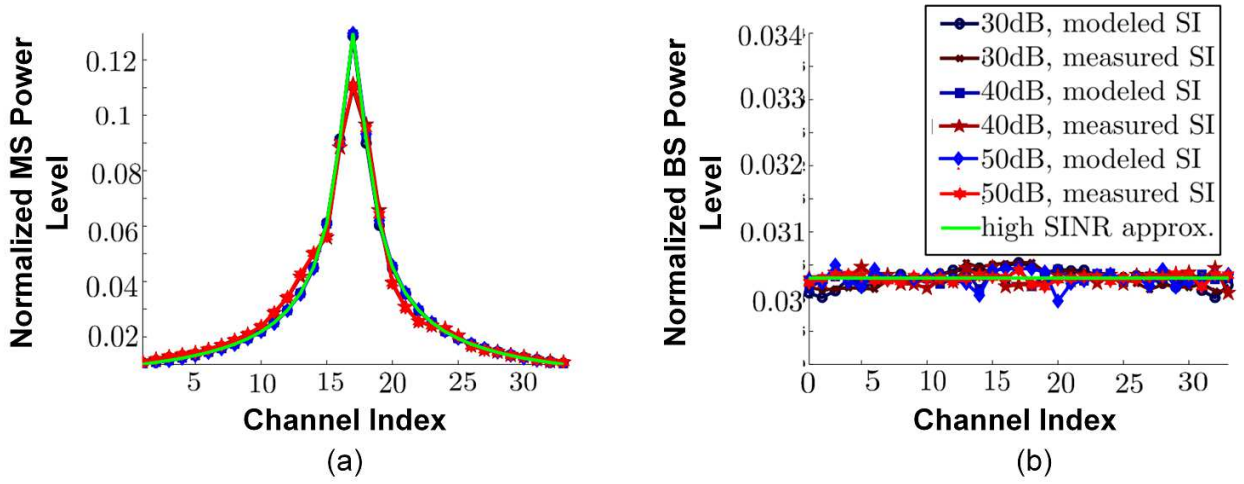

Figure 7.5: Full-duplex power allocation across 33 channels over a 20 MHz bandwidth at the (a) mobile station and (b) base station. The TX power is normalized to 1.

the RF part of the integrated full-duplex transceiver, we assume additional 50 dB of broadband cancellation from the digital domain (SIC_D=50 dB). At BS, we assume SI gets suppressed evenly across the entire frequency band based on the reported discrete-component-based implementations (such as the one in [2]). Similar to [2], we assume that when either station transmits at maximum total power that is equally allocated across channels, the noise on each channel is 110 dB below the transmitted power level. In addition, we consider flat frequency fading, and perform numerical evaluations for the same SNR at the MS and BS.

Fig. 7.5 shows the power allocation at the MS and at the BS computed by MaximumRate, a full-duplex power control algorithm developed in [21] that maximizes the sum of rates on uplink and downlink, for both measured and modeled SI and for different values of average SNR (from 30 dB to 50 dB). In Fig. 7.5, the total transmitted power has been normalized to 1. As we can see from Fig. 7.5, at the BS side, the transmit power is allocated evenly across all channels. At the MS side, the power is concentrated at a few channels. These power control results make intuitive sense, as they resemble the corresponding cancellation profiles at the BS and MS sides. Regarding full-duplex rate gain improvement, the analysis presented in [21] shows that in the high SNR regime (30-50 dB SNR), more than 60% throughput gain gain over conventional TDD can be achieved from full-duplex operation (Fig. 7.6). Higher throughput gains can be obtained with a narrower

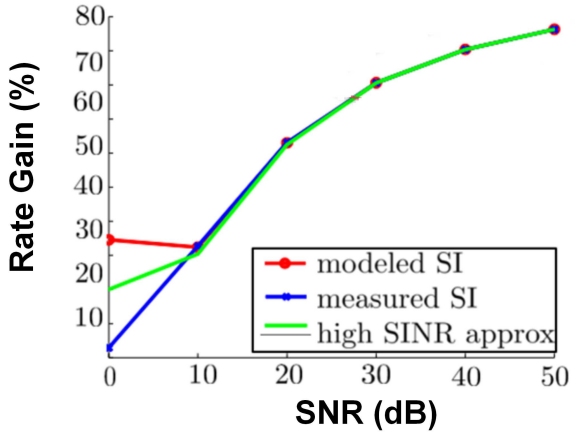

Figure 7.6: Evaluated full-duplex rate gain for 33 channels versus SNR. With 30-50 dB SNR, 60-80% throughput gain can be achieved from full-duplex operation using a frequency-flat amplitude- and phase-based integrated RF SI canceller.

bandwidth or by using the more advanced frequency-domain-equalization-based integrated RF SI canceller described in Chapter 5. It should be noted that the results in [21] use the Shannon capacity formula for the rates, so they give the upper bound on the achievable rates under any modulation and coding scheme (no particular modulation and coding schemes are assumed). The aforementioned 60% improvement is comparing the rates achievable in half-duplex and full-duplex cases *considering the highest achievable rates under any modulation and coding scheme for both cases with the given SNR*. In addition, the high SNR required here is mainly due to the limited achievable SIC especially at the MS side using a frequency-flat amplitude-and-phase-based RF canceller. Full-duplex radios with higher SIC across wide bandwidths are critical for a relaxed SNR requirement and are a part of important future research plans.

While the work in [21] aims to maximize the sum of uplink and downlink rates, our collaborators have subsequently developed algorithms in [132] that maximize one of the (uplink and downlink) rates when the other is fixed using the frequency-domain-equalization-based integrated RF SI canceller described in Chapter 5. These algorithms can be used in scenarios with asymmetric data rates on the uplink and downlink.

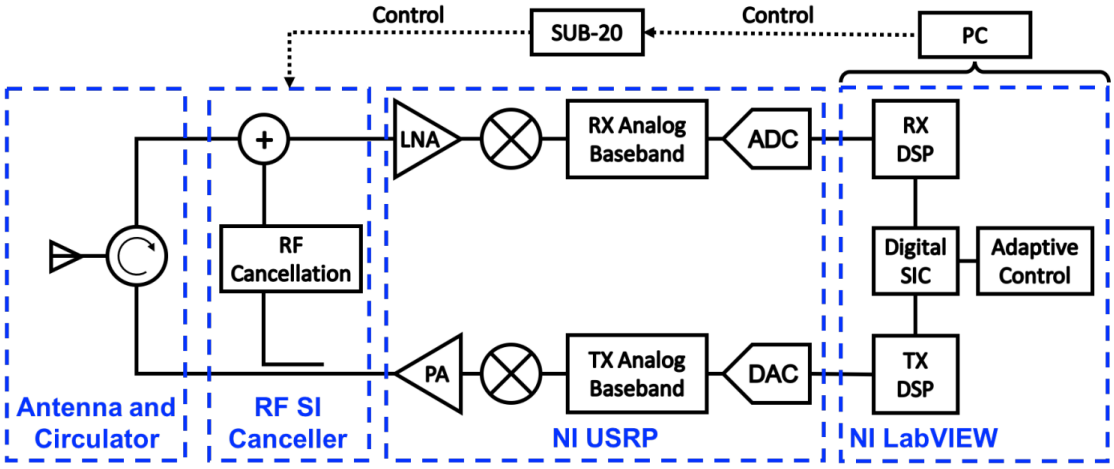

Figure 7.7: Block diagram of the full-duplex transceiver used in our cross-layered full-duplex testbed.

7.2 Cross-Layered Full-Duplex Testbed

To enable experimental performance evaluation of MAC algorithms, we have fabricated discrete-component-based prototype RF cancellers that emulate the integrated canceller in [56], and integrated them in a cross-layered software-defined testbed. In the testbed, these SI cancellers are used in a full-duplex transceiver (see Fig. 7.7) that consists of an antenna, a ferrite circulator, the custom-designed RF SI canceller, and an NI Universal Software Radio Peripheral (USRP) [133]. The RF SI canceller taps a reference signal at the output of the PA and performs SIC at the input of the LNA at the RX side. An adaptive RF SIC control algorithm and digital SIC are implemented in NI LabVIEW.

The implementations of the full-duplex transceiver and the RF SI canceller are shown in Fig. 7.8. The implemented RF SI canceller depicted in Fig. 7.8(b) operates from 0.8 GHz to 1.3 GHz. The TX input and output ports of the canceller connect to the PA output and the circulator's TX port, respectively. The RX input and output ports of the canceller connect to the circulator's RX port and the USRP's RX input, respectively. A portion of the TX signal is coupled from the PA output through a 6 dB directional coupler. The TX reference signal is then adjusted in amplitude and phase using a passive phase shifter and an attenuator, which are software-controlled from a PC (see Fig. 7.7). The passive phase shifter covers full 360° and is controlled by a control circuit

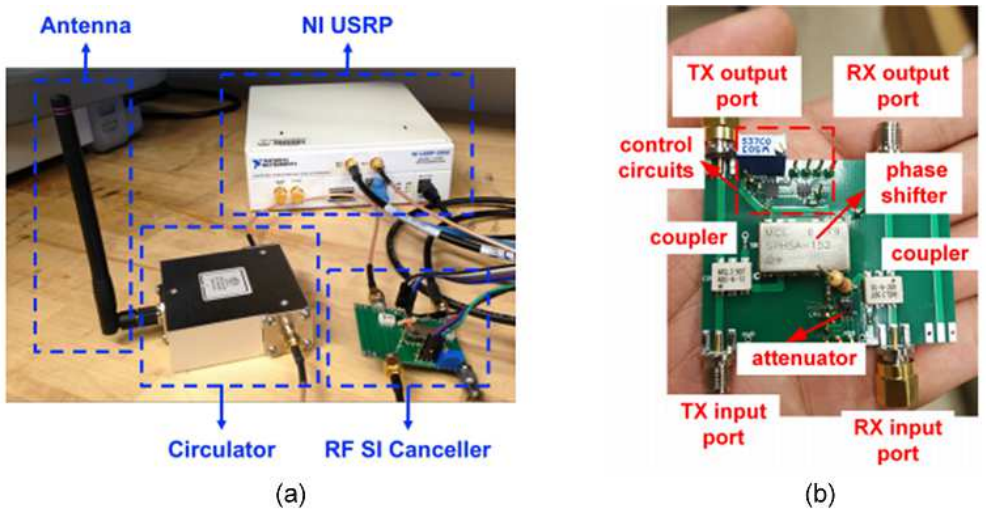

Figure 7.8: (a) The implementation of the full-duplex transceiver, and (b) the 0.8-1.3 GHz frequency-flat amplitude- and phase-based RF SI canceller.

that consists of an 8-bit digital-to-analog converter (DAC), resulting in a resolution of about 1.5°. The attenuator provides an attenuation range from 0 dB to 15.5 dB with a 0.5 dB resolution. The attenuation and phase control resolution result in a worst-case peak SIC of about 28 dB.

7.2.1 Adaptive RF SIC Algorithm

The SI channel response varies as the environment changes. Therefore, an algorithm that can adaptively configure RF SI canceller amplitude and phase settings is required. An iterative gradient descent algorithm has been reported to adaptively control an RF SI canceller [134]. However, this algorithm can be extremely slow due to a large number of canceller setting combinations [1], imposing huge overhead for using this algorithm for full-duplex wireless communications [2].

In [22], an algorithm that can be significantly faster than an iterative gradient descent search is presented [2]. The insight behind this algorithm is that the unknown RF SI canceller amplitude and phase settings can be solved using trigonometric equations based on inputs from a few SIC measurements with pilot signals. We found experimentally that this algorithm provides about

[1]Given the 8-bit phase shifter and the 5-bit variable attenuator in our design, there are 31×255=7905 canceller amplitude and phase combinations.

[2]This algorithm was developed in collaboration with Tingjun Chen from Columbia University.

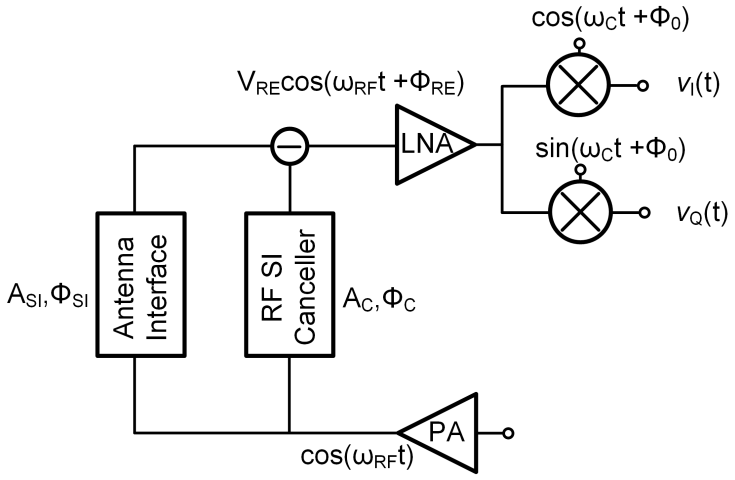

Figure 7.9: Block diagram and mathematical model of a full-duplex transceiver with a frequency-flat amplitude- and phase-based RF SI canceller used in deriving our adaptive RF SIC algorithm.

10 dB RF SIC. Therefore, a local search is performed to obtain at least 20 dB RF SIC. It should be noted that even with the local tuning, the entire adaptive algorithm converges within about 10 attempts which is still significantly faster than a brute-force iterative gradient descent algorithm.

The RF SI canceller amplitude and phase settings can be solved as follows. Fig. 7.9 shows a mathematical model of a full-duplex transceiver with a frequency-flat amplitude- and phase-based RF SI canceller. The signal at the PA output is $\cos(\omega_{RF}t)$ with normalized amplitude and phase for simplicity. The SI channel has a magnitude and phase response of A_{SI} and ϕ_{SI} at ω_{RF}, and the canceller has a magnitude and phase response of A_C and ϕ_C at ω_{RF}. We assume the antenna interface and the RF SI canceller are linear due to their purely-passive implementations. The residual SI present at the LNA input is $V_{RE}\cos(\omega_{RF}t + \phi_{RE})$ with V_{RE} and ϕ_{RE} being calculated as:

$$V_{RE}^2 = (A_{SI}\cos(\phi_{SI}) - A_C\cos(\phi_C))^2 + (A_{SI}\sin(\phi_{SI}) - A_C\sin(\phi_C))^2, \tag{7.5}$$

$$\cos\phi_{RE} = \frac{A_{SI}\cos(\phi_{SI}) - A_C\cos(\phi_C)}{|V_{RE}|}, \tag{7.6}$$

and

$$\sin\phi_{RE} = \frac{A_{SI}\sin(\phi_{SI}) - A_C\sin(\phi_C)}{|V_{RE}|}. \tag{7.7}$$

The receiver mixer is driven by the local oscillator signals $\cos(\omega_C t+\phi_0)$ and $\sin(\omega_C t+\phi_0)$, resulting in baseband signals $v_I(t)$ and $v_Q(t)$ at I and Q channels, respectively. $v_I(t)$ and $v_Q(t)$ are given as below:

$$\begin{aligned} v_I(t) &= A_I \cos((\omega_{RF}-\omega_C)t+\phi_{RE}-\phi_0) \\ &= A_I \cos(\phi_{RE}-\phi_0), \text{when } \omega_{RF}=\omega_C, \end{aligned} \tag{7.8}$$

$$\begin{aligned} v_Q(t) &= -A_Q \sin((\omega_{RF}-\omega_C)t+\phi_{RE}-\phi_0) \\ &= -A_Q \sin(\phi_{RE}-\phi_0), \text{when } \omega_{RF}=\omega_C, \end{aligned} \tag{7.9}$$

where ω_C is the local oscillator frequency, ϕ_0 denotes the local oscillator clock phase, and A_I and A_Q are gains from the LNA input to the baseband I and Q outputs, respectively. Finally, substituting (7.8) and (7.9) into (7.5)(7.6)(7.7), we have:

$$(A_{SI}\cos(\phi_{SI})-A_C\cos(\phi_C))^2+(A_{SI}\sin(\phi_{SI})-A_C\sin(\phi_C))^2=\frac{v_I^2(t)+v_Q^2(t)}{A_{RX}^2}, \tag{7.10}$$

and

$$\begin{aligned} \cos^{-1}\frac{A_{RX}^2(A_{SI}\cos(\phi_{SI})-A_C\cos(\phi_C))}{v_I^2(t)+v_Q^2(t)} &= \sin^{-1}\frac{A_{RX}^2(A_{SI}\sin(\phi_{SI})-A_C\sin(\phi_C))}{v_I^2(t)+v_Q^2(t)} \\ &= \phi_0-\tan^{-1}\frac{v_Q(t)}{v_I(t)}, \end{aligned} \tag{7.11}$$

where we have assumed $A_I = A_Q = A_{RX}$. In (7.10) and (7.11) we have total four unknowns including the SI channel amplitude and phase settings A_{SI} and ϕ_{SI}, the receiver gain A_{RX}, and the receiver clock phase ϕ_0. $v_I(t)$ and $v_Q(t)$ are known measurement outputs, and two sets of SIC measurements with the pilot sinusoidal signal $\cos(\omega_C t)$ using different RF SI canceller settings A_C and ϕ_C can generate four equations based on (7.10) and (7.11) which should be sufficient to solve for the four unknowns.

We implemented this adaptive RF SIC algorithm in our full-duplex wireless demonstration (discussed later). We found experimentally that this algorithm provides about 10 dB RF SIC. Therefore, a local search is performed to obtain at least 20 dB RF SIC. To enhance the performance, our next steps include understanding the factors that limit the achievable RF SIC using the adaptive algorithm.

7.2.2 Digital SIC

In Chapter 6 (Section 6.5.4), we discussed the implementation of our digital SI canceller and the digital SIC results with a two-tone signal. Here, we focus on the approach that is used to configure the digital SI canceller in a real-time fashion and factors that can fundamentally limit the amount of digital SIC in full-duplex systems.

The SI channel can be modeled in the digital domain by a truncated discrete Volterra series [135]. At the RX digital baseband, the received residual discrete-time SI $y[n]$ can be expressed as:

$$y[n] = \sum_{k=0}^{N} h_1[k]x[n-k] + \sum_{k=0}^{N} h_2[k]x^2[n-k] + \sum_{k=0}^{N} h_3[k]x^3[n-k] + \cdots + \sum_{k=0}^{N} h_p[k]x^p[n-k] + w[n], \quad (7.12)$$

where $x[n]$ and $x[n-k]$ (k represents the delay index) are the current and past TX digital baseband signals, N corresponds to the maximum delay in the modeled SI channel, $h_i[k]$ ($i = 1, 2, 3 \ldots, p$) is the i-th order Volterra series coefficient for a delay index of k, and $w[n]$ represents the noise along with the received residual SI. Equation (7.12) can also be written as:

$$\mathbf{Y} = \mathbf{XH} + \mathbf{W}, \quad (7.13)$$

where $\mathbf{H} = (h_1[0], h_1[1], \cdots, h_1[N], \cdots, h_p[0], h_p[1], \cdots, h_p[N])^T$ is a $Q \times 1$ vector ($Q = pN$), $\mathbf{W}$ and $\mathbf{Y} = (y[0], y[1], \cdots, y[M])^T$ are $M \times 1$ vectors (M is the length of the training sequence used in the digital SIC and needs to be larger than Q to avoid an under-determined system), and $\mathbf{X}$ is the corresponding $M \times Q$ matrix.

The digital SI canceller presented in Section 6.5.4 is realized based on a nonlinear tapped delay line [44][124], and the goal of the digital SIC is to minimize the residual SI power $||\mathbf{Y} - \mathbf{X}\hat{\mathbf{H}}||^2$ by adjusting the digital SI canceller coefficients $\hat{\mathbf{H}} = (\hat{h}_1[0], \hat{h}_1[1], \cdots, \hat{h}_1[N], \cdots, \hat{h}_p[0], \hat{h}_p[1], \cdots, \hat{h}_p[N])^T$. This essentially becomes a least-squares problem with the optimal solution being given as $\hat{\mathbf{H}} = \mathbf{X}^+\mathbf{Y}$, where $\mathbf{X}^+$ is the pseudo-inverse of $\mathbf{X}$ [136][2]. Since $\mathbf{X}$ is a known sequence based on the TX digital baseband signal, $\mathbf{X}^+$ can be pre-computed and does not need to be calculated on the fly. Therefore, given an M-length pilot sequence, we have implemented a real-time digital SI canceller and computed its coefficients as $\hat{\mathbf{H}} = \mathbf{X}^+\mathbf{Y}$ in NI LabVIEW as presented in [22].

There are several factors that can fundamentally limit the amount of digital SIC achievable in full duplex systems, including ADC DR and LO phase noise [57]. The required ADC DR needs to

be no less than the budgeted amount of digital SIC, while the required TX and RX phase noise performance depend on the system implementation and the RF SI channel delay spread [57].

If a common LO is shared between TX and RX, phase noise in the TX and the RX path are nominally fully correlated and will not limit the digital SIC. In practical scenarios, however, there will be some delay between the transmission and reception of the SI introduced by the wireless channel. This delay reduces the correlation between the phase noise in the transmitted SI signal and the phase noise in the RX local oscillator and hence limits the subsequent digital cancellation [57]. In Section 2.2.3.3, we have derived the resultant noise floor power spectral density $\frac{p_n(\Delta f)}{Hz}$ due to phase noise as:

$$\frac{p_n(\Delta f)}{Hz} = \frac{2\pi^2 \mathcal{L}\{\Delta f\} \Delta f^2 \tau_{SI}^2 P_{TX,main}}{ISO \times SIC_{RF}}, \tag{7.14}$$

where $P_{TX,main}$ is the TX output power, ISO is the amount of isolation achieved at the antenna interface, SIC_{RF} is the amount of SIC in the RF domain, and τ_{SI} is the time delay in the antenna interface. We have assumed a common LO being shared between TX and RX, and the LO phase noise is $\mathcal{L}\{\Delta f\}$ at an offset frequency of Δf. As we can see from (7.14), given fixed TX output power $P_{TX,main}$ and LO phase noise performance $\mathcal{L}\{\Delta f\}$, to prevent digital SIC from being limited by phase noise, sufficient amount of antenna interface isolation ISO and RF SIC SIC_{RF} before down-conversion is important.

In some commodity software-defined radios (such as the NI USRP [133]), separate LOs are used for TX and RX, resulting in a noise floor as follows:

$$\frac{p_n(\Delta f)}{Hz} = \frac{2\mathcal{L}\{\Delta f\} P_{TX,main}}{ISO \times SIC_{RF}}, \tag{7.15}$$

where we have assumed the TX and RX LOs have the same but uncorrelated phase noise of $\mathcal{L}\{\Delta f\}$. This noise floor can be much higher than that given in (7.14) and can significantly limit the overall achievable SIC [57].

In the full-duplex transceiver implementation shown in Fig. 7.8, the USRP uses a 14-bit ADC with an Spurious-Free Dynamic Range (SFDR) of 88 dB which is significantly higher than the typical amount of digital SIC. However, the separate LOs in the USRP can limit the digital SIC as we will see in the following section.

7.2.3 A Real-Time Full-Duplex Demonstration

A demonstration of real-time full-duplex wireless communication is presented in [22], in which a pair of the full-duplex transceivers described at the beginning of Section 7.2 performs simultaneous transmission and reception on the same frequency channel as depicted in Fig. 7.10(a).

In this demonstration, the full-duplex transceiver operates at 0.9 GHz. The USRP is controlled from a PC that runs NI LabVIEW, which both performs digital signal processing and provides a graphical user interface. Through the panel of NI LabVIEW [Fig. 7.10(b)], the transmitted and received signals in both time and frequency domains can be visualized. Furthermore, the amount of SIC in each domain is constantly updated and displayed. The transmitted multi-tone signal has a bandwidth of 5 MHz with a peak output power of 10 dBm and an average output power of 0 dBm. The desired signal is a single-tone signal at 2.5 MHz baseband frequency as shown in Fig. 7.10(b). The received signal is shown after each SIC phase. Without performing SIC, the SI signal is too strong for the desired signal to be detected. Once the SI signal is suppressed close to the -90 dBm noise floor, the desired signal is revealed. The circulator and the RF SI canceller together provide 40 dB SIC before the USRP RX, of which around 20 dB is obtained from the RF SI canceller. The additional 50 dB suppression comes from the digital SIC which eventually allows us to detect the desired signal under the powerful SI. The digital SI canceller has a maximum delay of 80 samples with a nonlinear order of 3. 5000 samples from the pilot signal are used to train the digital SI canceller.

The adaptive RF SIC algorithm described before in Section 7.2.1 is employed here. We found experimentally that the control algorithm based on solving trigonometric equations provides about 10 dB RF SIC. A further automatic local fine tuning is performed to obtain >20 dB RF SIC. The run time of our adaptive RF SIC algorithm is currently limited by our canceller control interface. The development of a much faster control interface is one of our on-going projects.

Using the same full-duplex transceiver, we have also demonstrated SIC using modulated waveforms with higher average TX power. Binary Phase-Shift Keying (BPSK) waveforms are generated using NI LabVIEW modulation toolkits with root-raised-cosine filtering, a sampling rate of 5 MS/s, and a symbol rate of 625k symbol/s. The symbol rate is limited by the computation capability of the PC that runs NI labVIEW for both the real-time digital SIC and the high-speed data link. Migrating digital SIC to the Field-Programmable Gate Array (FPGA) inside the USRP can signif-

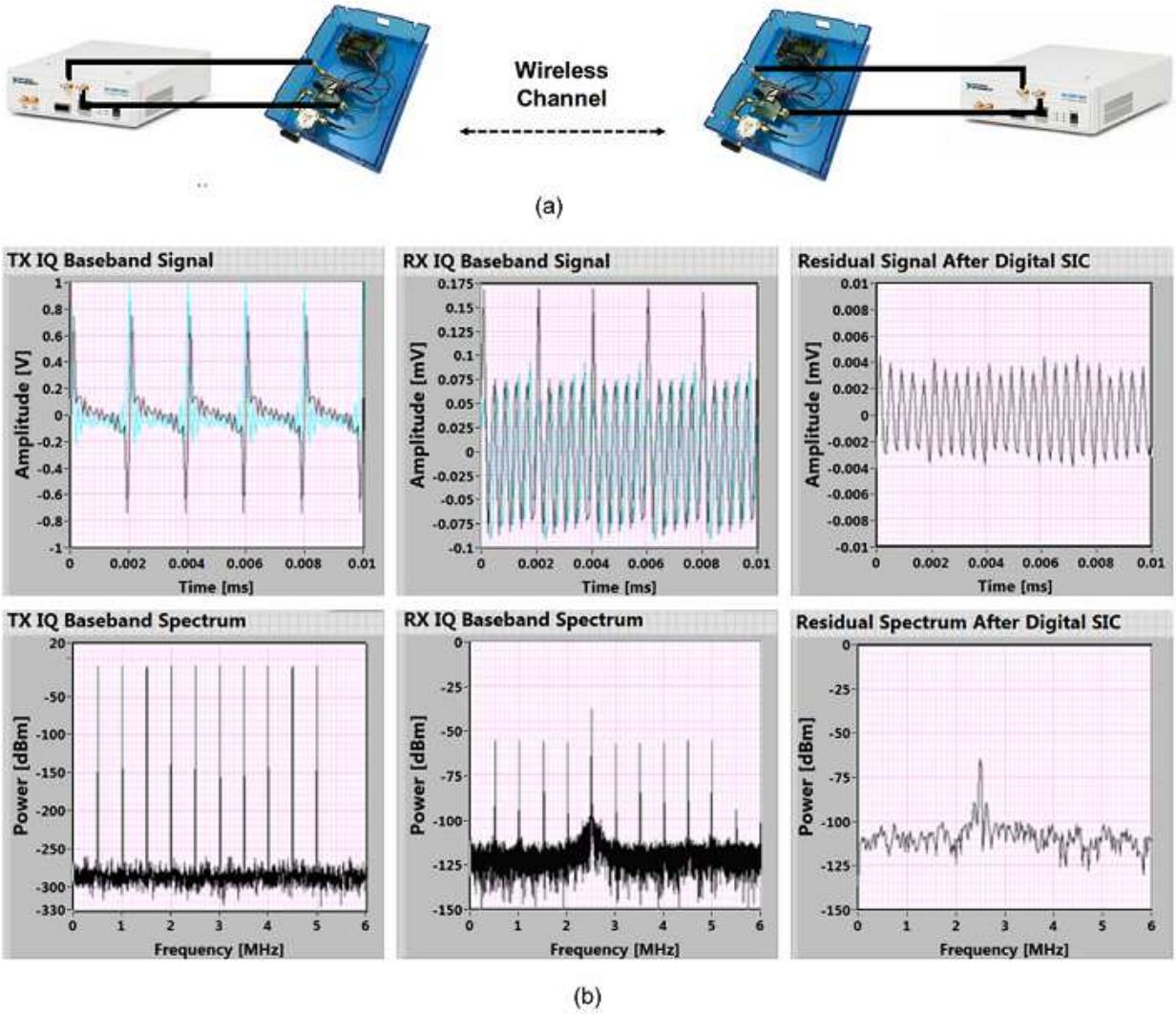

Figure 7.10: (a) Two full-duplex transceivers that transmit and receive simultaneously on the same frequency channel around 0.9 GHz, and (b) NI LabVIEW user interface showing the transmitted signal (left column), residual SI with the desired signal after circulator isolation and RF SIC (middle column), and recovered desired signal after digital SIC (right column). The transmitted multi-tone signal has a bandwidth of 5 MHz with a peak output power of 10 dBm and an average output power of 0 dBm. The RX is configured to have a noise floor of -90 dBm. The circulator and the RF SI canceller together provide 40 dB SIC before the RX, of which around 20 dB is obtained from the RF SI canceller. An additional 50 dB suppression comes from the digital SIC which eventually allows us to detect the desired signal under the powerful SI.

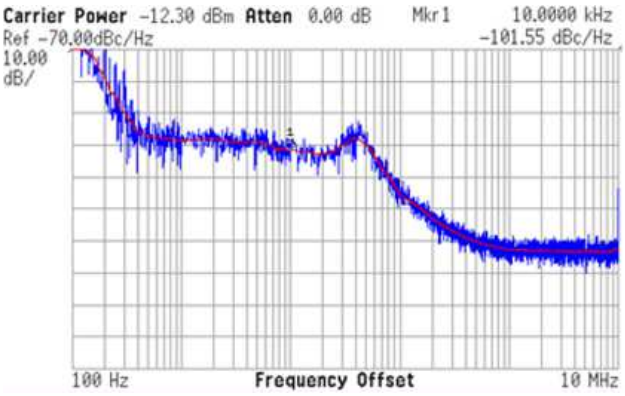

Figure 7.11: Measured USRP TX LO phase noise at 900 MHz carrier frequency.

icantly reduce the computational load on the PC, allowing higher symbol rates. This is part of our on-going efforts. The measured average TX output power is +9 dBm, and the RX has a noise floor of −95 dBm. Therefore, +9 −(−95) dBm=104 dB overall SIC from the antenna, RF, and digital domains is required to suppress the SI to the noise floor.

In our measurements, 43 dB SI suppression was achieved from the circulator and the RF SI canceller. As discussed in Section 7.2.2, the NI USRP uses separate local oscillators for its TX and RX, resulting in a relatively high noise floor due to phase noise. Fig. 7.11 shows the measured USRP TX LO phase noise at 900 MHz carrier frequency. The integrated phase noise from 1 kHz to 2.5 MHz is −51 dBc, resulting in an RX noise floor of +9 dBm −43 dB +(−51+3) dBc = −82 dBm based on (7.15). This means that phase noise will limit the overall SIC to be +9 dBm − (−82 dBm) = 91 dB.

The received residual SI at the USRP RX digital baseband after the 43 dB SI suppression in the antenna and RF domains is plotted in Fig. 7.12 with and without digital SIC. To ensure that digital SIC is not limited by the SI channel delay spread and nonlinearity, or the estimation error, the amount of digital SIC is plotted versus the maximum delay in the modeled SI channel [N in (7.12)], the digital SI canceller nonlinear order [p in (7.12)], and the number of points in the training sequence [M in (7.13)], respectively, in Fig. 7.13. From Fig. 7.13, we can see that the digital SIC achieved is limited to 45 dB, resulting in an overall SIC of 43 + 45 dB=88 dB. This matches reasonably well with our analysis based on (7.15) which predicted an achievable overall SIC of 91 dB. In order to suppress the SI to the RX noise floor, more isolation and cancellation are

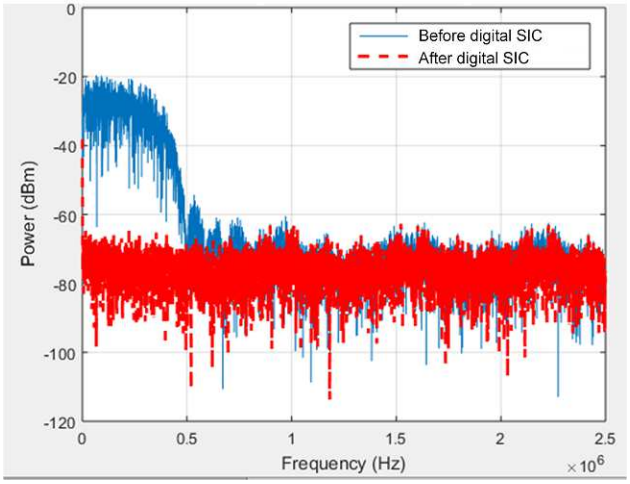

Figure 7.12: Received residual BPSK SI at the USRP RX digital baseband after 43 dB SI suppression from the circulator and RF SI canceller. The average transmit signal power is +9 dBm and the RX noise floor is −95 dBm. 45 dB subsequent digital SIC is achieved and is limited by the USRP phase noise.

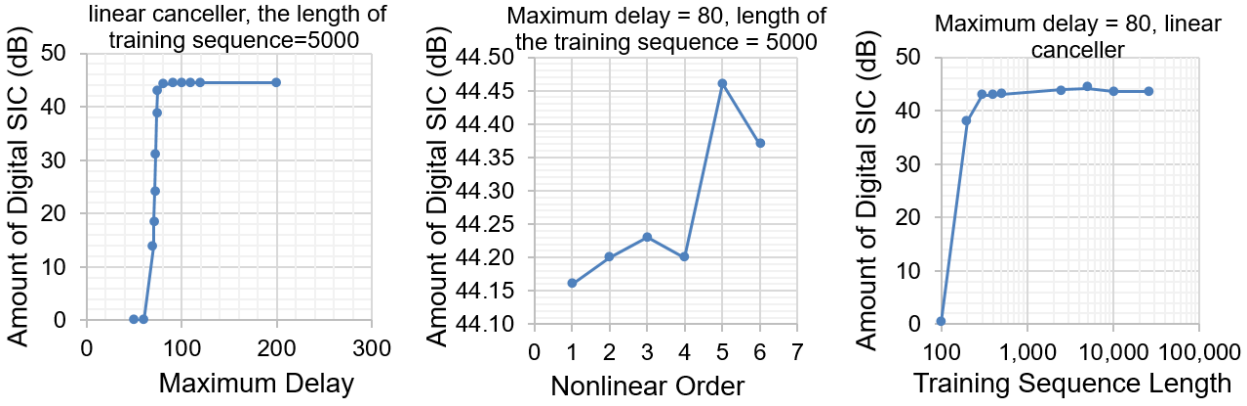

Figure 7.13: The amount of digital SIC versus the maximum delay in the modeled SI channel [N in (7.12)], the digital SI canceller nonlinear order [p in (7.12)], and the number of points in the training sequence [M in (7.13)].

required in the antenna and RF domains before frequency down-conversion. Alternatively, finding a way to use a common LO in the USRP would greatly improve digital SIC, and consequently, the overall SIC. It should also be mentioned that while nonlinear digital SIC is essential for our integrated full-duplex radios, the USRP RX is sufficiently linear at these power levels that a linear digital SI canceller (p=1) performs as well as a nonlinear canceller (Fig. 7.13).

7.3 A Multi-Band Frequency-Division Duplexing Demonstration

Modern wireless communication standards support numerous frequency bands as mentioned in Chapter 1. Consequently, wireless devices (e.g., smartphones) need to support FDD operation across transmit-receive band pairs that range from several hundreds of megahertz to several gigahertz. Multiband FDD operation requires numerous off-chip duplexers which limit the system form factor. Research efforts have been making progress toward tunable duplexers [34][35][36]. However, the incorporation of tunability is typically associated with an increase in loss. Consequently, tunable duplexers tend to have less TX-to-RX isolation for the same insertion loss when compared with fixed-frequency duplexers. To relax TX-to-RX isolation, SIC is required.

Using the SI-cancelling RX presented in Chapter 5 together with a tunable duplexer based on cavity filters with a real-time feedback control system [43][127], we demonstrated a multi-band FDD system as shown in Fig. 7.14 [3]. The SI-cancelling RX and the duplexer support tunable operation from 0.8 GHz to 1.1 GHz, covering multiple cellular frequency bands [33]. Fig. 7.14 shows the block diagram and the implementation of the multi-band FDD system that consists of the cavity-filter-based tunable duplexer and our SI-canceller RX RFIC sitting on a demonstration board. The measured duplexer insertion loss results are shown in Fig. 7.15(a). The filter's frequency tuning and real-time feedback control operation can be found in [127] and [43], respectively. As shown in Fig. 7.15(b), the tunable duplexer provides 38-40 dB initial TX-to-RX isolation, and the self-interference cancelling receiver further improves the isolation to >50dB across a 5 MHz bandwidth which is comparable to the isolation of existing fixed-frequency commercial acoustic-technology-based duplexers. It should be noted that being able to design the tunable duplexer to only have

[3]This demonstration was performed in collaboration with Prof. Dimitrios Peroulis, Dr. Mohammad Abu Khater, and Yu-Chen Wu from Purdue University.

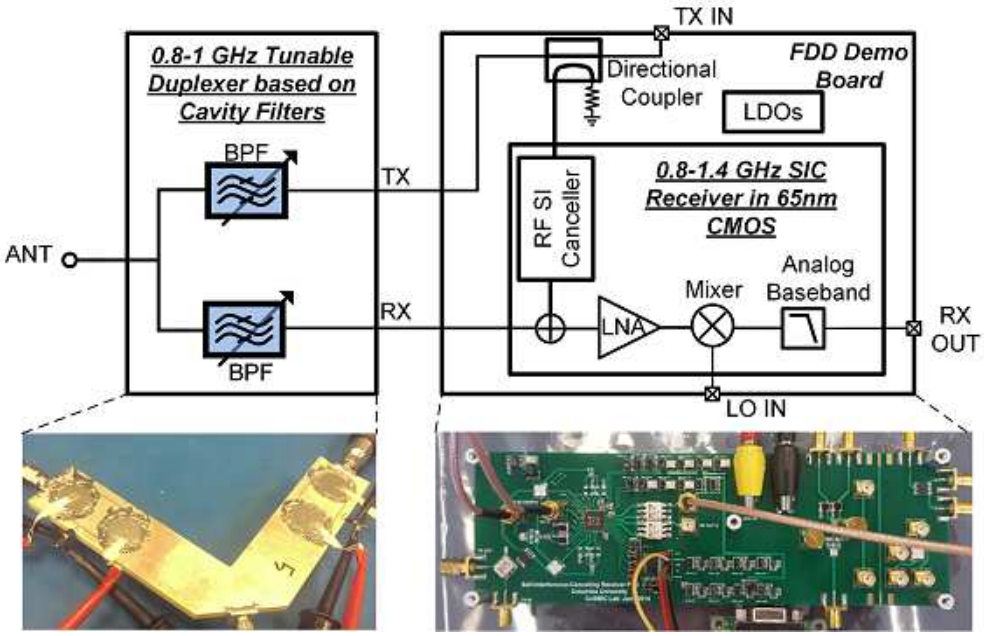

Figure 7.14: Block diagram and implementation of a multi-band FDD system that consists of a cavity-filter-based tunable duplexer and our SI-canceller RX RFIC sitting on a demonstration board.

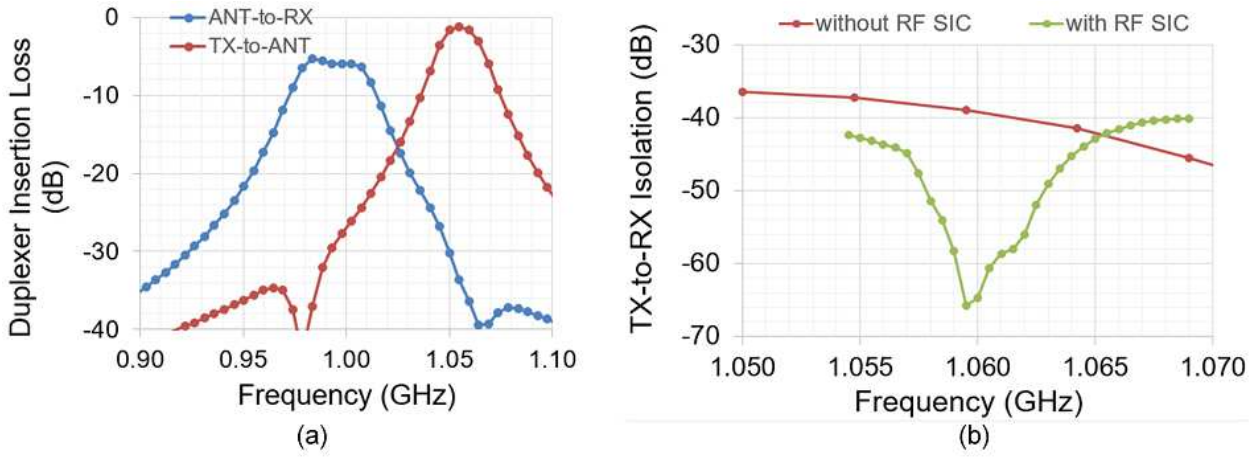

Figure 7.15: (a) Measured tunable duplexer insertion loss for TX and RX band center frequencies of 1.06 and 0.99 GHz, and (b) measured tunable duplexer TX-to-RX isolation with and without RF SIC.

around 40 dB isolation enabled a lower order filter design in the duplexer, thus relaxing insertion loss.

Further measurements that target wider SIC bandwidths and use modulated waveforms with higher power levels are ongoing. An adaptive tuning mechanism that dynamically adjust the cavity-filter-based tunable duplexer and the SI-cancelling RX in a joint fashion is also an important topic for future research.

7.4 Summary

Our cross-layer analysis and design of full-duplex wireless systems has been presented in this Chapter. A mathematical model of the remaining SI in integrated full-duplex radios with frequency-flat amplitue- and phase-based RF cancellers is derived, enabling the derivation of power control algorithms and the characterization of rate gains in practical full-duplex links. A cross-layered software-defined full-duplex testbed is introduced with details related to our RF and digital SIC algorithms. A real-time full-duplex link demonstration is presented using a 5 MHz multi-tone signal with +10 dBm peak and 0 dBm average power. In our full-duplex demo, the SI is cancelled to the −90 dBm noise floor by applying our RF and digital SIC algorithms. Finally, we discussed a

multi-band frequency-division duplexing demonstration using a tunable duplexer based on cavity filters together with our integrated self-interference-cancelling full-duplex receiver.

Chapter 8

Conclusion

Full-duplex wireless, an emergent wireless communication paradigm, has been revolutionizing the concept of duplexing in existing wireless systems and networks, and requires extensive interactions between the MAC and PHY layer designs. Allowing simultaneous transmission and reception at the same frequency, full-duplex operation can result in significant improvement in wireless network performance, such as spectral efficiency, link capacity, and network latency.

The biggest challenge associated with full-duplex wireless is the tremendous amount of TX SI right on top of the desired signal. This thesis presents a study of TX SIC in wireless communications systems. New approaches, at both system and circuit levels, of suppressing SI are introduced that enable future *integrated full-duplex radios* and tunable multi-band frequency-division duplexing systems. A number of prototype self-interference-cancelling receivers in CMOS are implemented to validate the theoretical findings.

To fully utilize the benefits of full-duplex communication, wireless systems will require a careful redesign of the PHY layer and the MAC layer. In collaboration with researchers at higher layers of the stack, concrete steps towards practical full-duplex wireless networks have been made.

8.1 Summary

SI mitigation strategies and SIC architectures strongly depend on the performance and specifications of the corresponding wireless systems. This dissertation starts with a briefly review of the wireless transceiver basics and a qualitative discussion about SI and its mitigation in full-duplex

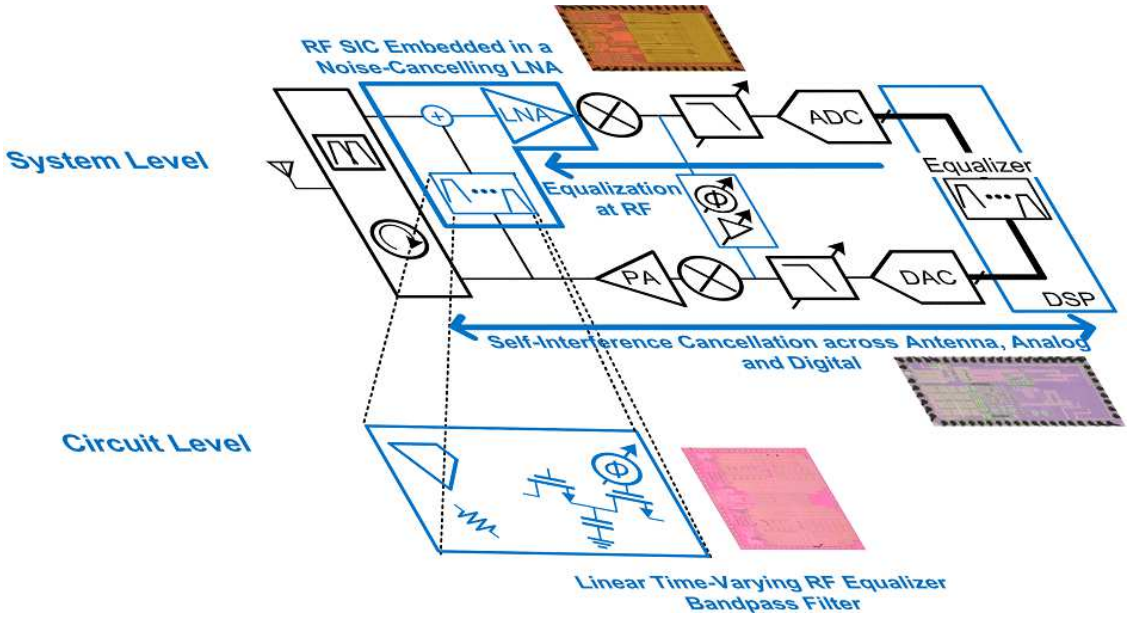

Figure 8.1: High-level illustration of the presented innovations at both system and circuit levels. Implemented prototype self-interference-cancelling receivers in CMOS are placed next to the corresponding innovations.

systems. This is followed by a quantitative example full-duplex system-level analysis. The impact of SI under reduced TX-to-RX isolation at the antenna interface in multi-band FDD systems is also discussed, and a fundamental benefit of performing RF SIC over having an ultra-linear RX for FDD systems is unveiled.

After an overview of existing SI mitigation architectures and techniques, several fundamental challenges associated with SIC are identified, motivating the need of innovative solutions at both system and circuit levels.

Many RF system designs adopt a block-by-block partitioned design methodology which allows the experimental determination of input and output port parameters without the need to know the internal block details. However, this methodology misses many degrees of design freedom as it ignores the low-level device/component characteristics, resulting in fundamental design trade-offs. An integrated implementation of RF systems enables easy access and utilization of device internal nodes, opening doors to co-design opportunities that can substantially enhance the system performance. In this dissertation, a noise-cancelling, self-interference-cancelling receiver is introduced

where an active canceller that is integrated with a receiver on the radio-frequency integrated circuits is co-designed with the receiver (see Fig. 8.1), breaking a fundamental trade-off between support for low antenna interface isolation levels (or equivalently, power of TX SI being cancelled) and RX sensitivity degradation.

Traditional RF systems are divided into several functional domains, namely the antenna interface, RF front-end, analog baseband, and digital baseband. One reason for this classical system division is that historically, different technologies have been used in the different domains. Today's ultra-scaled CMOS technology allows increasing functional integration onto a single silicon platform. This integration potential opens up a plethora of new design spaces, where a holistic approach that unifies the different functional blocks in a traditional RF system is emerging. This approach manifests itself in this work. In order to emulate SI channels at RF over a wide frequency range for wideband SIC, we introduce FDE at RF, a technique and functionality that is traditionally implemented in the digital signal-processing block (see Fig. 8.1). In addition, we demonstrate joint-SIC with nearly one part-per-billion accuracy across the antenna interface, analog baseband, and digital baseband that suppresses the SI to the RX noise floor as depicted in Fig. 8.1.

At the circuit level, ultra-scaled CMOS technology with transistors that can be efficiently switched at high frequencies enables Linear Time-Varying (LTV) circuits at RF. Recently, high-quality-factor (high-Q) RF filtering has been demonstrated using LTV circuits. By leveraging this RF filtering, N-path filters, to a preliminary level, enable the unification of high-Q antenna-interface filters and RF front-end circuits [39][40]. In this work, we find that RF LTV circuits can enable many new features (such as RF FDE) that go beyond RF filtering and would be extremely challenging, if not impossible, to achieve using a traditional LTI approach. As is illustrated in Fig. Fig. 8.1, LTV switched-capacitor circuits together with transconductors, resistors, and clock-path phase shifters form the integrated high-Q programmable BPF that is the core building block of the RF frequency-domain equalizer. While LTI passive systems based on conventional materials are reciprocal following the Lorentz reciprocity theorem, RF LTV circuits enable non-magnetic non-reciprocity and the realization of integrated high-performance RF circulators[1] [42][115].

Finally, a cross-layer approach used in our collaborative research with theoreticians at higher

[1]The integrated non-magnetic passive circulator mentioned here is a research project conducted by Negar Reiskarimian from Columbia University.

layers of the stack has allowed us to make concrete steps towards practical full-duplex wireless networks: based on the model of the proposed integrated fullduplex radios, the power control algorithms and the full-duplex rate gains have been derived and characterized [21]; to enable experimental characterization of full-duplex MAC layer algorithms, cross-layered software-defined testbeds have been developed and a practical real-time full-duplex wireless demonstration has been demonstrated [22]. In collaboration with researchers from the field of micro-electro-mechanical systems, we demonstrate a multi-band frequency-division duplexing system using a cavity-filter-based tunable duplexer and our integrated widely-tunable self-interference-cancelling RX.

8.2 Future Research

The study presented in this dissertation leads to several topics for future research.

For wireless systems adopt LTV N-path filters, phase noise can degrade the system performance through spectral spreading or reciprocal mixing. The FDE-based RF canceller presented in this dissertation relies on two-port N-path filters for the realization of the high-Q widely tunable canceller filters. Therefore, phase noise mitigation technique is an important future research topic.

While we have developed a set of mathematical equations and an iterative successive approach to configure the FDE-based RF SI canceller for wide SIC bandwidths, how to automate this configuration process fast enough so that it changes accordingly as the environment changes is an important problem for practical full-duplex systems. In addition, research regarding an algorithm that optimizes total SIC jointly between the FDE-based RF SIC and the tapped-delay-line-based (essentially time-domain-based) digital SIC is desirable.

FDE has been used in digital for single-carrier broadband wireless systems to avoid inter-symbol interference [137]. When compared with time domain equalization, FDE can offer a better performance/complexity trade-off for large multipath spread [138]. Therefore, it is worthwhile to investigate FDE-based SIC in digital, especially in conjunction with the FDE-based RF SIC presented in this work for a joint frequency-domain SIC across the RF and digital domains.

In a full-duplex network, an in-band unknown interference from another user can greatly affect the overall performance as it cannot be canceled. To address this challenge, simultaneous unknown interference suppression and SIC across antenna and RF/analog domains are required.

The unknown interference can be mitigated through spatial- and frequency-domain filtering at the antenna input using a phased-array receiver with RF channel selection. But, how to cancel SI in a phased-array receiver remains an interesting research topic. In addition, it is important to consider interference management in OFDM networks jointly at the PHY and MAC layers.

In order to bring the full-duplex technology to wireless applications that have higher TX power levels and more stringent RX sensitivity requirements (e.g., cellular applications), integrated full-duplex transceivers need to have increased total SIC over wide bandwidths. In addition, improved linearity is necessary for integrated RXs and SI cancellers to handle the higher TX power levels.

A synergy between full duplex and MIMO can dramatically increase spectral efficiency. When compared with a single-input and single-output (SISO) full-duplex radio, the challenge associated with MIMO full-duplex radios is that the output signals from all transmitting elements can all couple to one receiving element, requiring multiple SIC paths. A brute force solution is to use as many SIC paths as the number of transmitting elements in each receiver. However, this approach results in a system complexity that grows quadratically with the number of antennas, limiting the size of the antenna array. A lot of circuit and architecture innovations are needed towards MIMO full-duplex using integrated circuit technology.

Regarding multi-band frequency-division duplexing systems, development of small-form-factor tunable duplexers that can benefit from the presented SIC techniques can be a promising topic for further research. An adaptive tuning mechanism that can dynamically adjust the tunable duplexer and the SI-cancelling RX in a joint fashion for optimized SIC over wide bandwidths is also of high interest.

Part I

Bibliography

Bibliography

[1] T. Sawanobori and R. Roche, "Mobile data demand: growth forecast met," June 2015, [accessed 18-July-2016]. [Online]. Available: http://www.ctia.org/docs/default-source/default-document-library/062115mobile-data-demands-white-paper-new.pdf

[2] D. Bharadia, E. McMilin, and S. Katti, "Full duplex radios," in *Proc. ACM SIGCOMM'13*, October 2013, pp. 375–386.

[3] J. Zhou, T.-H. Chuang, T. Dinc, and H. Krishnaswamy, "A receiver with reconfigurable self-interference cancellation based on RF frequency-domain equalization supporting >20MHz cancellation bandwidth for FDD, co-existence and same-channel full duplex applications," in *Solid-State Circuits Conference Digest of Technical Papers (ISSCC), 2015 IEEE International*, Feb. 2015, pp. 342–343.

[4] ——, "Integrated wideband self-interference cancellation in the RF domain for FDD and full-duplex wireless," *IEEE Journal of Solid-State Circuits*, vol. 50, no. 12, pp. 3015–3031, Dec 2015.

[5] T. Georgantas, K. Vavelidis, N. Haralabidis, S. Bouras, I. Vassiliou, C. Kapnistis, Y. Kokolakis, H. Peyravi, G. Theodoratos, K. Vryssas, N. Kanakaris, C. Kokozidis, S. Kavadias, S. Plevridis, P. Mudge, I. Elgorriaga, A. Kyranas, S. Liolis, E. Kytonaki, G. Konstantopoulos, P. Robogiannakis, K. Tsilipanos, M. Margaras, P. Betzios, R. Magoon, N. Bouras, M. Rofougaran, and R. Rofougaran, "A 13mm^2 40nm multiband GSM/EDGE/HSPA+/TDSCDMA/LTE transceiver," in *Solid- State Circuits Conference - (ISSCC), 2015 IEEE International*, Feb 2015, pp. 1–3.

[6] J. W. Lai, C. H. Wu, A. Lin, W. K. Hong, C. Y. Wang, C. H. Shen, Y. H. Lin, Y. H. Cho, Y. C. Chen, and Y. H. Chung, "A World-Band Triple-Mode 802.11a/b/g SOC in 130-nm CMOS," *IEEE Journal of Solid-State Circuits*, vol. 44, no. 11, pp. 2911–2921, Nov 2009.

[7] M. Chung, M. S. Sim, J. Kim, D. K. Kim, and C. b. Chae, "Prototyping real-time full duplex radios," *IEEE Communications Magazine*, vol. 53, no. 9, pp. 56–63, September 2015.

[8] D. J. van den Broek, E. A. M. Klumperink, and B. Nauta, "An in-band full-duplex radio receiver with a passive vector modulator downmixer for self-interference cancellation," *IEEE Journal of Solid-State Circuits*, vol. 50, no. 12, pp. 3003–3014, Dec 2015.

[9] D. Yang, H. Yuksel, and A. Molnar, "A wideband highly integrated and widely tunable transceiver for in-band full-duplex communication," *Solid-State Circuits, IEEE Journal of*, vol. PP, no. 99, pp. 1–14, 2015.

[10] F. Bruccoleri, E. Klumperink, and B. Nauta, "Wide-band CMOS low-noise amplifier exploiting thermal noise canceling," *IEEE J. Solid-State Circuits*, vol. 39, no. 2, pp. 275–282, Feb 2004.

[11] W. B. Kuhn, N. K. Yanduru, and A. S. Wyszynski, "Q-enhanced LC bandpass filters for integrated wireless applications," *IEEE Transactions on Microwave Theory and Techniques*, vol. 46, no. 12, pp. 2577–2586, Dec 1998.

[12] H. Busignies and M. Dishal, "Some relations between speed of indication, bandwidth, and signal-to-random-noise ratio in radio navigation and direction finding," *Proceedings of the IRE*, vol. 37, no. 5, pp. 478–488, May 1949.

[13] "SKYFR-000709 Miniature 2110-2170MHz Single Junction Robust Lead Circulator Data Sheet," Skyworks Solutions, Woburn, MA, USA.

[14] R. Jones, "Telecoms next goal: Defining 5G," March 2015, [accessed 18-July-2016]. [Online]. Available: http://www.wsj.com/articles/telecom-industry-bets-on-5g-1425895320

[15] S. Onoe, "1.3 evolution of 5G mobile technology toward 2020 and beyond," in *2016 IEEE International Solid-State Circuits Conference (ISSCC)*, Jan 2016, pp. 23–28.

[16] L. Larson, "RF and microwave hardware challenges for future radio spectrum access," *Proceedings of the IEEE*, vol. 102, no. 3, pp. 321–333, March 2014.

[17] L. Young, "Telecom experts plot a path to 5G," October 2015, [posted 5-October-2015]. [Online]. Available: http://spectrum.ieee.org/telecom/wireless/telecom-experts-plot-a-path-to-5g

[18] T. L. Marzetta, "Noncooperative cellular wireless with unlimited numbers of base station antennas," *IEEE Transactions on Wireless Communications*, vol. 9, no. 11, pp. 3590–3600, November 2010.

[19] E. G. Larsson, O. Edfors, F. Tufvesson, and T. L. Marzetta, "Massive MIMO for next generation wireless systems," *IEEE Communications Magazine*, vol. 52, no. 2, pp. 186–195, February 2014.

[20] T. S. Rappaport, S. Sun, R. Mayzus, H. Zhao, Y. Azar, K. Wang, G. N. Wong, J. K. Schulz, M. Samimi, and F. Gutierrez, "Millimeter wave mobile communications for 5G cellular: It will work!" *IEEE Access*, vol. 1, pp. 335–349, 2013.

[21] J. Marasevic, J. Zhou, H. Krishnaswamy, Y. Zhong, and G. Zussman, "Resource allocation and rate gains in practical full-duplex systems," in *Proc. ACM SIGMETRICS'15*, June 2015.

[22] T. Chen, J. Zhou, N. Grimwood, R. Fogel, J. Marašević, H. Krishnaswamy, and G. Zussman, "Full-duplex wireless based on a small-form-factor analog self-interference canceller: Demo," in *Proceedings of the 17th ACM International Symposium on Mobile Ad Hoc Networking and Computing*, ser. MobiHoc '16. New York, NY, USA: ACM, 2016, pp. 357–358. [Online]. Available: http://doi.acm.org/10.1145/2942358.2942397

[23] T. H. Lee, *Planar Microwave Engineering: A Practical Guide to Theory, Measurement, and Circuits*. Cambridge University Press, August 30, 2004.

[24] A. Goldsmith, *Wireless Communications*. Cambridge University Press, August 8, 2005.

[25] B. Razavi, *RF Microelectronics*, 2nd ed. Prentice Hall, October 2, 2011.

[26] A. Sabharwal, P. Schniter, D. Guo, D. Bliss, S. Rangarajan, and R. Wichman, "In-band full-duplex wireless: Challenges and opportunities," *Selected Areas in Communications, IEEE Journal on*, vol. 32, no. 9, pp. 1637–1652, Sept 2014.

[27] B. Debaillie, D. van den Broek, C. Lavin, B. van Liempd, E. Klumperink, C. Palacios, J. Craninckx, and A. Parssinen, "Analog/RF solutions enabling compact full-duplex radios," *IEEE J. Sel. Areas Commun.*, vol. 32, no. 9, pp. 1662–1673, Sept 2014.

[28] J. I. Choi, M. Jain, K. Srinivasan, P. Levis, and S. Katti, "Achieving single channel, full duplex wireless communication," in *Proc. ACM MobiCom'10*, 2010.

[29] M. Duarte, C. Dick, and A. Sabharwal, "Experiment-driven characterization of full-duplex wireless systems," *IEEE Transactions on Wireless Communications*, vol. 11, no. 12, pp. 4296–4307, December 2012.

[30] "WARP Project," http://warpproject.org, 2008, [Online; accessed 21-June-2016].

[31] V. P. Tse, D., *Fundamentals of Wireless Communication*. Cambridge University Press, July 11, 2005.

[32] "TriQuint-856879 miniature LTE band 13 duplexer data sheet," TriQuint Semiconductor, Hillsboro, OR, USA.

[33] "LTE-Advanced (3GPP rel.11) technology introduction," Rohde and Schwarz, Munich, Germany.

[34] H. Joshi, H. H. Sigmarsson, S. Moon, D. Peroulis, and W. Chappell, "Tunable high Q narrowband triplexer," in *IEEE MTT'09*, 2009.

[35] A. S. Morris and V. Steel, "Integrated tunable systems for scalable 4G radios," in *Microwave Symposium Digest (IMS), 2013 IEEE MTT-S International*, June 2013, pp. 1–4.

[36] M. Pourakbar, L. Linton, M. Trmnen, and M. Faulkner, "Tunable duplex filter for adaptive duplexers of advanced LTE handsets," in *Microwave Symposium Digest (IMS), 2013 IEEE MTT-S International*, June 2013, pp. 1–4.

[37] L. Franks and I. Sandberg, "An alternative approach to the realization of network transfer functions: The N-path filter," *Bell System Technical Journal, The*, vol. 39, no. 5, pp. 1321–1350, Sept 1960.

[38] M. Soer, E. Klumperink, P.-T. de Boer, F. van Vliet, and B. Nauta, "Unified Frequency-Domain Analysis of Switched-Series-RC Passive Mixers and Samplers," *Circuits and Systems I: Regular Papers, IEEE Transactions on*, vol. 57, no. 10, pp. 2618–2631, Oct 2010.

[39] A. Ghaffari, E. Klumperink, M. C. M. Soer, and B. Nauta, "Tunable High-Q N-Path Band-Pass Filters: Modeling and Verification," *IEEE J. Solid-State Circuits*, vol. 46, no. 5, pp. 998–1010, 2011.

[40] A. Mirzaei, H. Darabi, A. Yazdi, Z. Zhou, E. Chang, and P. Suri, "A 65 nm CMOS Quad-Band SAW-Less Receiver SoC for GSM/GPRS/EDGE," *Solid-State Circuits, IEEE Journal of*, vol. 46, no. 4, pp. 950–964, April 2011.

[41] N. Reiskarimian, J. Zhou, T. H. Chuang, and H. Krishnaswamy, "Analysis and design of two-port N-path bandpass filters with embedded phase shifting," *IEEE Transactions on Circuits and Systems II: Express Briefs*, vol. 63, no. 8, pp. 728–732, Aug 2016.

[42] N. Reiskarimian and H. Krishnaswamy, "Magnetic-free non-reciprocity based on staggered commutation," in *Nature Communications*, vol. 7, no. 4, Apr. 2016.

[43] M. A. Khater and D. Peroulis, "Real-time feedback control system for tuning evanescent-mode cavity filters," *IEEE Transactions on Microwave Theory and Techniques*, vol. PP, no. 99, pp. 1–10, 2016.

[44] M. A. Nizamuddin, P. J. Balister, W. H. Tranter, and J. H. Reed, "Nonlinear tapped delay line digital predistorter for power amplifiers with memory," in *Wireless Communications and Networking, 2003. WCNC 2003. 2003 IEEE*, vol. 1, March 2003, pp. 607–611 vol.1.

[45] B. Mohammadi, M. Kahrizi, A. Mirzaei, S. Zhou, A. Hadji-Abdolhamid, J. C. Leete, B. Pregardier, M. Nariman, B. Saeidi, Y. Chang, D. Rozenblit, M. Mikhemar, A. T. Mehrabani, R. Magoon, M. Rofougaran, and A. Rofougaran, "A Rel-12 2G/3G/LTE-Advanced 2CC Transmitter," *IEEE Journal of Solid-State Circuits*, vol. 51, no. 5, pp. 1080–1095, May 2016.

[46] H. Khatri, P. Gudem, and L. Larson, "An Active Transmitter Leakage Suppression Technique for CMOS SAW-Less CDMA Receivers," *IEEE J. Solid-State Circuits*, vol. 45, no. 8, pp. 1590–1601, 2010.

[47] N. Kim, L. Larson, and V. Aparin, "A Highly Linear SAW-Less CMOS Receiver Using a Mixer With Embedded Tx Filtering for CDMA," *IEEE J. Solid-State Circuits*, vol. 44, no. 8, pp. 2126–2137, 2009.

[48] T. G. Schreier, R., *Understanding Delta-Sigma Data Converters*. Wiley-IEEE Press, 2005.

[49] A. A. Abidi, "RF CMOS comes of age," *IEEE Journal of Solid-State Circuits*, vol. 39, no. 4, pp. 549–561, Apr 2004.

[50] A. Hajimiri and T. Lee, "A general theory of phase noise in electrical oscillators," *Solid-State Circuits, IEEE Journal of*, vol. 33, no. 2, pp. 179–194, Feb 1998.

[51] C. Fulton, M. Yeary, D. Thompson, J. Lake, and A. Mitchell, "Digital phased arrays: Challenges and opportunities," *Proceedings of the IEEE*, vol. 104, no. 3, pp. 487–503, March 2016.

[52] J. Zhou, N. Reiskarimian, and H. Krishnaswamy, "9.8 Receiver with integrated magnetic-free N-path-filter-based non-reciprocal circulator and baseband self-interference cancellation for full-duplex wireless," in *2016 IEEE International Solid-State Circuits Conference (ISSCC)*, Jan 2016, pp. 178–180.

[53] M. Soer, E. Klumperink, Z. Ru, F. van Vliet, and B. Nauta, "A 0.2-to-2.0GHz 65nm CMOS receiver without LNA achieving >11dBm IIP3 and <6.5 dB NF," in *Proc. IEEE ISSCC'09*, 2009.

[54] C. Andrews and A. Molnar, "A Passive Mixer-First Receiver With Digitally Controlled and Widely Tunable RF Interface," *IEEE J. Solid-State Circuits*, vol. 45, no. 12, pp. 2696–2708, 2010.

[55] T. Dinc and H. Krishnaswamy, "A T/R antenna pair with polarization-based wideband reconfigurable self-interference cancellation for simultaneous transmit and receive," in *Proc. IEEE IMS'15*, 2015.

[56] J. Zhou, A. Chakrabarti, P. Kinget, and H. Krishnaswamy, "Low-Noise Active Cancellation of Transmitter Leakage and Transmitter Noise in Broadband Wireless Receivers for FDD/Co-Existence," *IEEE J. Solid-State Circuits*, vol. 49, no. 12, pp. 3046–3062, December 2014.

[57] A. Sahai, G. Patel, C. Dick, and A. Sabharwal, "On the impact of phase noise on active cancelation in wireless full-duplex," *Vehicular Technology, IEEE Transactions on*, vol. 62, no. 9, pp. 4494–4510, Nov 2013.

[58] S. Min, T. Copani, S. Kiaei, and B. Bakkaloglu, "A 90-nm CMOS 5-GHz Ring-Oscillator PLL With Delay-Discriminator-Based Active Phase-Noise Cancellation," *Solid-State Circuits, IEEE Journal of*, vol. 48, no. 5, pp. 1151–1160, May 2013.

[59] N. Fong, J.-O. Plouchart, N. Zamdmer, D. Liu, L. Wagner, C. Plett, and N. Tarr, "Design of wide-band cmos vco for multiband wireless lan applications," *Solid-State Circuits, IEEE Journal of*, vol. 38, no. 8, pp. 1333–1342, Aug 2003.

[60] V. Aparin and L. Larson, "Analysis and reduction of cross-modulation distortion in cdma receivers," *IEEE Trans. Microw. Theory Techn.*, vol. 51, no. 5, pp. 1591–1602, May 2003.

[61] N. Swanberg, J. Phelps, and M. Recouly, "WCDMA cross modulation effects and implications for receiver linearity requirements," in *IEEE RAWCON'02*, 2002.

[62] F. Zhang and P. R. Kinget, "Low-power programmable gain CMOS distributed LNA," *IEEE Journal of Solid-State Circuits*, vol. 41, no. 6, pp. 1333–1343, June 2006.

[63] M. Omer, R. Rimini, P. Heidmann, and J. S. Kenney, "A PA-noise cancellation technique for next generation highly integrated RF front-ends," in *Proc. IEEE RFIC'12*, 2012.

[64] V. Aparin, G. Ballantyne, C. Persico, and A. Cicalini, "An integrated LMS adaptive filter of TX leakage for CDMA receiver front ends," *IEEE J. Solid-State Circuits*, vol. 41, no. 5, pp. 1171–1182, 2006.

[65] T. Zhang, A. R. Suvarna, V. Bhagavatula, and J. C. Rudell, "An integrated CMOS passive self-interference mitigation technique for FDD radios," *IEEE Journal of Solid-State Circuits*, vol. 50, no. 5, pp. 1176–1188, May 2015.

[66] A. Goel, B. Analui, and H. Hashemi, "Tunable duplexer with passive feed-forward cancellation to improve the RX-TX isolation," *Circuits and Systems I: Regular Papers, IEEE Transactions on*, vol. 62, no. 2, pp. 536–544, Feb 2015.

[67] H. Kim, S. Woo, S. Jung, and K. H. Lee, "A CMOS transmitter leakage canceller for WCDMA applications," *IEEE Transactions on Microwave Theory and Techniques*, vol. 61, no. 9, pp. 3373–3380, Sept 2013.

[68] Y.-H. Kuo, J.-H. Tsai, and T.-W. Huang, "A digital-calibrated transmitter-to-receiver isolator in radar applications," *IEEE Microw. Compon. Lett.*, vol. 22, no. 12, pp. 651–653, Dec 2012.

[69] H. Hashemi, T.-S. Chu, and J. Roderick, "Integrated true-time-delay-based ultra-wideband array processing," *Communications Magazine, IEEE*, vol. 46, no. 9, pp. 162–172, September 2008.

[70] "ACMD-7612 Miniature UMTS Band I Duplexer Data Sheet," Avago Technologies, San Jose, CA, USA.

[71] T. Dinc, A. Chakrabarti, and H. Krishnaswamy, "A 60GHz Same-Channel Full-Duplex CMOS Transceiver and Link Based on Reconfigurable Polarization-Based Antenna Cancellation," in *Proc. IEEE RFIC'15*, 2015.

[72] M. Mikhemar, H. Darabi, and A. A. Abidi, "A Multiband RF Antenna Duplexer on CMOS: Design and Performance," *IEEE Journal of Solid-State Circuits*, vol. 48, no. 9, pp. 2067–2077, Sept 2013.

[73] B. van Liempd, B. Hershberg, B. Debaillie, P. Wambacq, and J. Craninckx, "An electrical-balance duplexer for in-band full-duplex with < -85dBm in-band distortion at +10dBm TX-power," in *European Solid-State Circuits Conference (ESSCIRC), ESSCIRC 2015 - 41st*, Sept 2015, pp. 176–179.

[74] S. Tanaka, N. Shimomura, and K. Ohtake, "Active circulators - the realization of circulators using transistors," *Proceedings of the IEEE*, vol. 53, no. 3, pp. 260–267, March 1965.

[75] G. Carchon and B. Nanwelaers, "Power and noise limitations of active circulators," *IEEE T-MTT*, vol. 48, no. 2, pp. 316–319, Feb 2000.

[76] J. Zhou, P. Kinget, and H. Krishnaswamy, "A Blocker-Resilient Wideband Receiver with Low-Noise Active Two-Point Cancellation of >0dBm TX Leakage and TX noise in RX band for FDD/Co-Existence," in *Solid-State Circuits Conference Digest of Technical Papers (ISSCC), 2014 IEEE International*, Feb. 2014, pp. 352–353.

[77] P. B. Reinhold Ludwig, *RF Circuit Design: Theory and Applications*. Prentice Hall, January 28, 2000.

[78] S. Blaakmeer, E. Klumperink, D. Leenaerts, and B. Nauta, "Wideband Balun-LNA With Simultaneous Output Balancing, Noise-Canceling and Distortion-Canceling," *IEEE J. Solid-State Circuits*, vol. 43, no. 6, pp. 1341–1350, 2008.

[79] J. Zhu, H. Krishnaswamy, and P. R. Kinget, "Field-Programmable LNAs With Interferer-Reflecting Loop for Input Linearity Enhancement," *IEEE Journal of Solid-State Circuits*, vol. 50, no. 2, pp. 556–572, Feb 2015.

[80] W.-H. Chen, G. Liu, B. Zdravko, and A. Niknejad, "A Highly Linear Broadband CMOS LNA Employing Noise and Distortion Cancellation," *IEEE J. Solid-State Circuits*, vol. 43, no. 5, pp. 1164–1176, May 2008.

[81] S. Jain, Y. Wang, and A. Natarajan, "A 10GHz CMOS RX frontend with spatial cancellation of co-channel interferers for MIMO/digital beamforming arrays," in *2016 IEEE Radio Frequency Integrated Circuits Symposium (RFIC)*, May 2016, pp. 99–102.

[82] D. Kaczman, M. Shah, M. Alam, M. Rachedine, D. Cashen, L. Han, and A. Raghavan, "A Single Chip 10-Band WCDMA/HSDPA 4-Band GSM/EDGE SAW-less CMOS Receiver With DigRF 3G Interface and + 90 dBm IIP2," *IEEE J. Solid-State Circuits*, vol. 44, no. 3, pp. 718–739, March 2009.

[83] Y. Feng, G. Takemura, S. Kawaguchi, N. Itoh, and P. Kinget, "Digitally Assisted IIP2 Calibration for CMOS Direct-Conversion Receivers," *IEEE J. Solid-State Circuits*, vol. 46, no. 10, pp. 2253–2267, Oct 2011.

[84] D. Murphy, H. Darabi, A. Abidi, A. Hafez, A. Mirzaei, M. Mikhemar, and M.-C. Chang, "A blocker-tolerant, noise-cancelling receiver suitable for wideband wireless applications," *IEEE J. Solid-State Circuits*, vol. 47, no. 12, pp. 2943–2963, 2012.

[85] H. Zhang and E. Sanchez-Sinencio, "Linearization Techniques for CMOS Low Noise Amplifiers: A Tutorial," *Circuits and Systems I: Regular Papers, IEEE Transactions on*, vol. 58, no. 1, pp. 22–36, Jan 2011.

[86] Z. Ru, E. Klumperink, G. Wienk, and B. Nauta, "A software-defined radio receiver architecture robust to out-of-band interference," in *Proc. IEEE ISSCC'09*, 2009.

[87] D. Murphy, A. Mirzaei, H. Darabi, M.-C. Chang, and A. Abidi, "An ltv analysis of the frequency translational noise-cancelling receiver," *Circuits and Systems I: Regular Papers, IEEE Transactions on*, vol. 61, no. 1, pp. 266–279, Jan 2014.

[88] J. Zhu and P. R. Kinget, "A field-programmable noise-canceling wideband receiver with high-linearity hybrid class-AB-C LNTAs," in *Custom Integrated Circuits Conference (CICC), 2015 IEEE*, Sept 2015, pp. 1–4.

[89] W. J. Rugh, *Nonlinear System Theory: The Volterra / Wiener Approach.* The Johns Hopkins University Press, 1981.

[90] P.Wambacq and W.Sansen, *Distortion Analysis of Analog Integrated Circuits.* Kluwer Academic Publishers, 1998.

[91] H. Khatri, P. Gudem, and L. Larson, "Distortion in current commutating passive cmos down-conversion mixers," *Microwave Theory and Techniques, IEEE Transactions on*, vol. 57, no. 11, pp. 2671–2681, Nov 2009.

[92] S. Rabii and B. Wooley, "A 1.8-V digital-audio sigma-delta modulator in 0.8um CMOS," *Solid-State Circuits, IEEE Journal of*, vol. 32, no. 6, pp. 783–796, Jun 1997.

[93] I. Fabiano, M. Sosio, A. Liscidini, and R. Castello, "SAW-Less Analog Front-End Receivers for TDD and FDD," *IEEE J. Solid-State Circuits*, vol. 48, no. 12, pp. 1–13, 2013.

[94] A. Perez-Carrillo, S. Taylor, J. Silva-Martinez, and A. Karsilayan, "A large-signal blocker robust transimpedance amplifier for coexisting radio receivers in 45nm cmos," in *Radio Frequency Integrated Circuits Symposium (RFIC), 2011 IEEE*, June 2011, pp. 1–4.

[95] S. Youssef, R. van der Zee, and B. Nauta, "Active feedback technique for rf channel selection in front-end receivers," *Solid-State Circuits, IEEE Journal of*, vol. 47, no. 12, pp. 3130–3144, Dec 2012.

[96] N. Kim, L. Larson, and V. Aparin, "A highly linear saw-less cmos receiver using a mixer with embedded tx filtering for cdma," *Solid-State Circuits, IEEE Journal of*, vol. 44, no. 8, pp. 2126–2137, Aug 2009.

[97] M. Kaltiokallio and J. Ryynnen, "A 1 to 5GHz adjustable active polyphase filter for LO quadrature generation," in *Proc. IEEE RFIC'11*, 2011.

[98] J. Kaukovuori, K. Stadius, J. Ryynanen, and K. A. I. Halonen, "Analysis and Design of Passive Polyphase Filters," *IEEE Trans. Circuits Syst. I, Reg. Papers*, vol. 55, no. 10, pp. 3023–3037, Nov 2008.

[99] Z. N. Low, J. H. Cheong, and C. L. Law, "Low-cost PCB antenna for Low-cost PCB antenna for UWB applications," *IEEE Antennas Wireless Propag. Lett.*, vol. 4, no. 1, pp. 237–239, December 2005.

[100] M. de Jongh, A. van Bezooijen, T. Bakker, K. Boyle, and J. Stulemeijer, "A low-cost closed-loop antenna tuner module for mobile phone single-feed multi-band antennas," in *Proc. EuMC'13*, 2013.

[101] D. Mahrof, E. Klumperink, M. Oude Alink, and B. Nauta, "A receiver with in-band IIP3 >20dBm, exploiting cancelling of OpAmp finite-gain-induced distortion via negative conductance," in *Proc. IEEE RFIC'13*, 2013.

[102] B. Razavi, "Translational circuits [a circuit for all seasons]," *IEEE Solid-State Circuits Magazine*, vol. 8, no. 1, pp. 8–13, winter 2016.

[103] P. M. Asbeck, M. F. Chang, K. C. Wang, D. L. Miller, G. J. Sullivan, N. H. Sheng, E. Sovero, and J. A. Higgins, "Heterojunction Bipolar Transistors for Microwave and Millimeter-Wave

Integrated Circuits," *IEEE Transactions on Microwave Theory and Techniques*, vol. 35, no. 12, pp. 1462–1468, Dec 1987.

[104] K. W. Kobayashi, A. K. Oki, L. T. Tran, and D. C. Streit, "Ultra-low dc power GaAs HBT S- and C-band low noise amplifiers for portable wireless applications," *IEEE Transactions on Microwave Theory and Techniques*, vol. 43, no. 12, pp. 3055–3061, Dec 1995.

[105] J. O. Voorman, W. H. A. Bruls, and P. J. Barth, "Integration of analog filters in a bipolar process," *IEEE Journal of Solid-State Circuits*, vol. 17, no. 4, pp. 713–722, Aug 1982.

[106] O. E. Agazzi, T. Koh, S. S. Haider, R. W. Walden, D. R. Cassiday, G. A. Wilson, T. M. Lalumia, C. M. Gerveshi, J. Kumar, R. E. Crochiere, R. F. Shaw, R. A. Wilson, W. R. McDonald, N. L. Gottfried, N. S. Ramesh, and R. B. Blake, "A digital signal processor for an ANSI standard ISDN transceiver," *IEEE Journal of Solid-State Circuits*, vol. 24, no. 6, pp. 1605–1613, Dec 1989.

[107] J. W. Park and B. Razavi, "Channel selection at rf using miller bandpass filters," *IEEE Journal of Solid-State Circuits*, vol. 49, no. 12, pp. 3063–3078, Dec 2014.

[108] L. Martoyo, T. Weiss, F. Capar, and F. K. Jondral, "Low complexity CDMA downlink receiver based on frequency domain equalization," in *Vehicular Technology Conference, 2003. VTC 2003-Fall. 2003 IEEE 58th*, vol. 2, Oct 2003, pp. 987–991 Vol.2.

[109] W. B. Kuhn, F. W. Stephenson, and A. Elshabini-Riad, "A 200 MHz CMOS Q-enhanced LC bandpass filter," *IEEE Journal of Solid-State Circuits*, vol. 31, no. 8, pp. 1112–1122, Aug 1996.

[110] D. Li and Y. Tsividis, "A 1.9 GHz Si active LC filter with on-chip automatic tuning," in *Solid-State Circuits Conference, 2001. Digest of Technical Papers. ISSCC. 2001 IEEE International*, Feb 2001, pp. 368–369.

[111] N. Testi, R. Berenguer, X. Zhang, S. Munoz, and Y. Xu, "A 2.4GHz 72dB-variable-gain 100dB-DR 7.8mW 4th-order tunable Q-enhanced LC band-pass filter," in *Radio Frequency Integrated Circuits Symposium (RFIC), 2015 IEEE*, May 2015, pp. 87–90.

[112] M. Darvishi, "Active N-path filters: Theory and design," Ph.D. dissertation, University of Twente, 2013.

[113] M. Darvishi, R. van der Zee, E. Klumperink, and B. Nauta, "Widely Tunable 4th Order Switched G_m-C Band-Pass Filter Based on N-Path Filters," *IEEE J. Solid-State Circuits*, vol. 47, no. 12, pp. 3105–3119, Dec 2012.

[114] S. Jayasuriya, D. Yang, and A. Molnar, "A baseband technique for automated lo leakage suppression achieving < -80dbm in wideband passive mixer-first receivers," in *Custom Integrated Circuits Conference (CICC), 2014 IEEE Proceedings of the*, Sept 2014, pp. 1–4.

[115] N. Reiskarimian, J. Zhou, and H. Krishnaswamy, "A CMOS Passive LPTV Non-Magnetic Circulator and Its Application in a Full-Duplex Receiver," *IEEE J. Solid-State Circuits*, August 2016, submitted and under review.

[116] D. Pozar, *Microwave Engineering*, 4th ed. Wiley, November 22, 2011.

[117] S. H. Abdelhalem, P. S. Gudem, and L. E. Larson, "Tunable CMOS Integrated Duplexer With Antenna Impedance Tracking and High Isolation in the Transmit and Receive Bands," *IEEE Transactions on Microwave Theory and Techniques*, vol. 62, no. 9, pp. 2092–2104, Sept 2014.

[118] M. Elkholy, M. Mikhemar, H. Darabi, and K. Entesari, "Low-Loss Integrated Passive CMOS Electrical Balance Duplexers With Single-Ended LNA," *IEEE Transactions on Microwave Theory and Techniques*, vol. 64, no. 5, pp. 1544–1559, May 2016.

[119] S. Qin, Q. Xu, and Y. Wang, "Nonreciprocal components with distributedly modulated capacitors," *IEEE T-MTT*, vol. 62, no. 10, pp. 2260–2272, Oct 2014.

[120] N. A. Estep, D. L. Sounas, J. Soric, and A. Alu, "Magnetic-free non-reciprocity and isolation based on parametrically modulated coupled resonator loops," *Nature Phys.*, vol. 10, p. 923927, Dec. 2016.

[121] N. A. Estep, D. L. Sounas, and A. Alu, "Magnetless microwave circulators based on spatiotemporally modulated rings of coupled resonators," *IEEE Trans. Microw. Theory Techn.*, vol. 64, no. 2, pp. 502–518, Feb. 2016.

[122] "Data Sheet: Wide matching range slide screw tuners," Maury Microwave, Ontario, CA, USA.

[123] "Data sheet: TRF370417 50-MHz to 6-GHz Quadrature Modulator," Texas Instruments, Dallas, TX, USA.

[124] J. Marašević, T. Chen, J. Zhou, N. Reiskarimian, H. Krishnaswamy, and G. Zussman, "Full-Duplex Wireless: Algorithms and Rate Improvement Bounds for Integrated Circuit Implementations," in *Proc. ACM HotWireless'16*, 2016. To appear.

[125] "The Full-duplex Wireless: From Integrated Circuits to Networks (FlexICoN) project," [accessed 2-October-2016]. [Online]. Available: http://flexicon.ee.columbia.edu/

[126] J. Marasevic, J. Zhou, H. Krishnaswamy, Y. Zhong, and G. Zussman, "Resource allocation and rate gains in practical full-duplex systems," *IEEE/ACM Trans. Netw.*, 2016. To appear.

[127] D. Peroulis, E. Naglich, M. Sinani, and M. Hickle, "Tuned to resonance: Transfer-function-adaptive filters in evanescent-mode cavity-resonator technology," *IEEE Microwave Magazine*, vol. 15, no. 5, pp. 55–69, July 2014.

[128] A. Sahai, S. Diggavi, and A. Sabharwal, "On uplink/downlink full-duplex networks," in *Proc. IEEE Asilomar'13*, 2013.

[129] J. Bai and A. Sabharwal, "Distributed full-duplex via wireless side-channels: Bounds and protocols," *IEEE Trans. Wireless Commun.*, vol. 12, no. 8, pp. 4162–4173, Aug. 2013.

[130] S. Goyal, P. Liu, S. Panwar, R. DiFazio, R. Yang, J. Li, and E. Bala, "Improving small cell capacity with common-carrier full duplex radios," in *Proc. IEEE ICC'14*, 2014.

[131] X. Xie and X. Zhang, "Does full-duplex double the capacity of wireless networks?" in *Proc. IEEE INFOCOM'14*, 2014.

[132] J. Marasevic and G. Zussman, "On the capacity regions of single-channel and multi-channel full-duplex links," in *Proc. ACM MobiHoc16*, 2016.

[133] "NI USRP-292x/293x Datasheet," http://www.ni.com/datasheet/pdf/en/ds-355.

[134] M. Jain, J. Choi, T. Kim, D. Bharadia, S. Seth, K. Srinivasan, P. Levis, S. Katti, and P. Sinha, "Practical, real-time, full duplex wireless," in *Proc. ACM MobiCom'11*, 2011.

[135] G. Sicuranza, A. Bucconi, and P. Mitri, "Adaptive echo cancellation with nonlinear digital filters," in *Acoustics, Speech, and Signal Processing, IEEE International Conference on ICASSP '84.*, vol. 9, Mar 1984, pp. 130–133.

[136] L. E. Ghaoui, *Optimization Models and Applications.* UC Berkeley, [accessed 18-July-2016]. [Online]. Available: https://inst.eecs.berkeley.edu/~ee127a/book/login/index.html

[137] H. Sari, G. Karam, and I. Jeanclaud, "Frequency-domain equalization of mobile radio and terrestrial broadcast channels," in *Global Telecommunications Conference, 1994. GLOBECOM '94. Communications: The Global Bridge., IEEE*, Nov 1994, pp. 1–5 vol.1.

[138] D. Falconer, S. L. Ariyavisitakul, A. Benyamin-Seeyar, and B. Eidson, "Frequency domain equalization for single-carrier broadband wireless systems," *IEEE Communications Magazine*, vol. 40, no. 4, pp. 58–66, Apr 2002.

[139] C.-Y. Yu, I. Lu, Y.-H. Chen, L.-C. Cho, C. Sun, C.-C. Tang, H.-H. Chang, W.-C. Lee, S.-J. Huang, T.-H. Wu, C.-S. Chiu, and G. Chien, "A SAW-Less GSM/GPRS/EDGE Receiver Embedded in 65-nm SoC," *IEEE J. Solid-State Circuits*, vol. 46, no. 12, pp. 3047–3060, 2011.

[140] J. Bussgang, L. Ehrman, and J. Graham, "Analysis of nonlinear systems with multiple inputs," *Proceedings of the IEEE*, vol. 62, no. 8, pp. 1088–1119, Aug 1974.

[141] B. Razavi, *Design of Analog CMOS Integrated Circuits.* McGraw-Hill Science/Engineering/Math, August 15, 2000.

Part II

Appendices

Appendix A

Out-of-Band Linearity Analysis for Current-Mode Receivers

Following the linearity analysis in Chapter 4, we first find the expressions for the LNTA's output current, and then derive the TIA's Volterra kernels. Finally, the RX TB is derived.

A.0.1 Broadband LNTA Distortion Analysis

As depicted in Fig. 4.6, we assume the magnitude of the LNTA output impedance is much larger than the magnitude of the input impedance of the passive mixer. Thus, the LNTA's output current i_{CG} and i_{CS} can be found with short circuit output terminations. DC blocking capacitors in Fig. 4.6 are assumed to be large. Memory elements such as capacitive parasitics as well as off-chip biasing inductors and capacitors in a practical implementation of the LNTA (see Fig. 4.8) have been ignored. Consequently, the analysis is valid within the RF bandwidth of the LNTA where these memory elements are ineffectual.

In order to perform the LNTA linearity analysis under TX leakage cancellation, two excitations are included - v_s at the input of the LNTA , and v_g at the gate of the LNTA CG device. We expand the input voltage v_{in} into a 2-variable power series of v_g and v_s.

$$\begin{aligned} v_{in}(t) =& \beta_{1G} v_g + \beta_{2G^2} v_g^2 + \beta_{3G^3} v_g^3 + \beta_{1S} v_s + \beta_{2S^2} v_s^2 + \beta_{3S^3} v_s^3 \\ &+ \beta_{2GS} v_g v_s + \beta_{3G^2S} v_g^2 v_s + \beta_{3GS^2} v_g v_s^2 + \cdots . \end{aligned} \tag{A.1}$$

These nonlinearity coefficients represent the nonlinearity of the CG device. Cross-modulation distortion is quantified using TB where the modulated TX signal is modeled using an OOB two-tone signal (v_{SI}) and an in-band continuous-wave jammer (v_{jam}) is assumed to be present. Substituting $v_s = v_{SI} + v_{jam}$ and $v_g = kv_{SI}$ into (A.1), we have the following expression. Note that k represents the scaling factor for injection at the gate to achieve TX leakage cancellation at the input v_{in}. Setting $k = 0$ allows this formulation to model an FTNC-RX, i.e. a noise-cancelling current-mode RX without leakage cancellation.

$$\begin{aligned} v_{in}(t) =& \alpha_{1T} v_{SI} + \alpha_{2T^2} v_{SI}^2 + \alpha_{3T^3} v_{SI}^3 + \\ & \alpha_{1S} v_{jam} + \alpha_{2S^2} v_{jam}^2 + \alpha_{3S^3} v_{jam}^3 + \\ & \alpha_{2TS} v_{SI} v_{jam} + \alpha_{3T^2S} v_{SI}^2 v_{jam} + \alpha_{3TS^2} v_{SI} v_{jam}^2 \\ & + \cdots , \end{aligned} \tag{A.2}$$

where $\alpha_{1S} = \beta_{1S}$, $\alpha_{2S} = \beta_{2S}$, $\alpha_{3S} = \beta_{3S}$, $\alpha_{1T} = k\beta_{1G} + \alpha_{1S}$, $\alpha_{2T} = k^2\beta_{2G} + \alpha_{2S} + k\beta_{2GS}$, $\alpha_{3T} = k^3\beta_{3G} + \beta_{3S} + k^2\beta_{3G^2S} + k\beta_{3GS^2}$, $\alpha_{2TS} = 2\beta_{2S} + k\beta_{2GS}$, $\alpha_{3T^2S} = 3\beta_{3S} + k^2\beta_{3G^2S} + 2k\beta_{3GS^2}$, $\alpha_{3TS^2} = 3\beta_{3S} + k\beta_{3GS^2}$. Applying KCL in Fig. 4.6 gives,

$$i_{CG}(t) = -\frac{1}{R_S}\left[v_{in} - (v_{SI} + v_{jam})\right]. \tag{A.3}$$

Setting $v_{SI} = V_{tx}\cos(\omega_2 t) + V_{tx}\cos(\omega_3 t)$, $v_{jam} = V_j\cos(\omega_1 t)$, and assuming that cross-modulation products only come from the $v_{SI}^2 v_{jam}$ term in (A.4), we have:

$$\begin{aligned} i_{CG}(t) =& \frac{1-\alpha_{1T}}{2R_S} V_{tx}\left(e^{j\omega_2 t} + e^{-j\omega_2 t} + e^{j\omega_3 t} + e^{-j\omega_3 t}\right) + \\ & \frac{1-\alpha_{1S}}{2R_S} V_j\left(e^{j\omega_1 t} + e^{-j\omega_1 t}\right) + \cdots \\ & - \frac{\alpha_{3T^2S}}{4R_S} V_j V_{tx}^2\left(e^{j\omega_x t} + e^{-j\omega_x t}\right) + \cdots , \end{aligned} \tag{A.4}$$

where $\omega_x = \omega_1 + \omega_2 - \omega_3$[1]. In not considering the compression of main leakage and jammer signal, we've further assumed that the power level of the TX leakage and jammer are below the LNTA compression point.

[1]Cross-modulation products will appear on both sides of the jammer, i.e. at $\omega_1 + \omega_2 - \omega_3$ and $\omega_1 - \omega_2 + \omega_3$. ω_x represents one of the sidebands and the other sideband can be computed in a similar fashion.

To model the CS device nonlinearity, its drain current is expanded into a power series of its gate voltage.

$$i_d = g_{m,CS} v_{in} + \frac{1}{2} g'_{m,CS} v_{in}^2 + \frac{1}{6} g''_{m,CS} v_{in}^3 + \cdots . \tag{A.5}$$

Similarly, we assume that cross-modulation products only arise from the $v_{SI}^2 v_{jam}$ term. Thus, the current output of the LNTA's CS device is:

$$\begin{aligned} i_{CS}(t) = {} & A_1 \left(e^{j\omega_1 t} + e^{-j\omega_1 t} \right) + \\ & A_2 \left(e^{j\omega_2 t} + e^{-j\omega_2 t} + e^{j\omega_3 t} + e^{-j\omega_3 t} \right) + \cdots \\ & + A_x \left(e^{j\omega_x t} + e^{-j\omega_x t} \right) + \cdots , \end{aligned}$$

where

$$\begin{aligned} A_1 &= -\frac{1}{2} g_{m,CS} \alpha_{1S} V_j, \\ A_2 &= -\frac{1}{2} g_{m,CS} \alpha_{1T} V_{tx}, \\ A_x &= -[g_{m,CS} \alpha_{3T^2S} + g'_{m,CS} (\alpha_{2T^2} \alpha_{1S} + \alpha_{2TS} \alpha_{1T}) + \\ &\qquad \frac{1}{2} g''_{m,CS} \alpha_{1T}^2 \alpha_{1S}] \frac{V_j V_{tx}^2}{4}. \end{aligned} \tag{A.6}$$

A.0.2 TIA Volterra Series based Distortion Analysis

A 1^{st}-order TIA is depicted in Fig. A.1, with a two-stage Miller-compensated operational transconductance amplifier (OTA)[86; 139; 56]. The evolution of the TIA model for the distortion analysis is shown in Fig. A.2. In Fig. A.2(a), the RC feedback network (R_F and C_F) of the TIA is modeled using its Y-parameter equivalent circuits. The forward path of the feedback network is ignored by setting $Y_{12} = 0$, as the OTA forward gain is large[**?**]. The OTA first stage is modeled with a nonlinear voltage-controlled current source (VCCS) in parallel with the output resistance of the first stage (R_1) and a loading capacitor C_1. C_1 captures the Miller effect on the intermediary dominant pole, as $C_1 = (1 + A_{v2})C_C$, where A_{v2} is magnitude of the OTA second stage voltage gain at low frequency. We've ignored the drain side nonlinearity for the first stage, as the OOB signal will be suppressed by the dominate pole of the OTA. The OTA second stage is modeled with a nonlinear VCCS controlled by both input and output voltages (v_1 and v_{out}). Pole splitting and

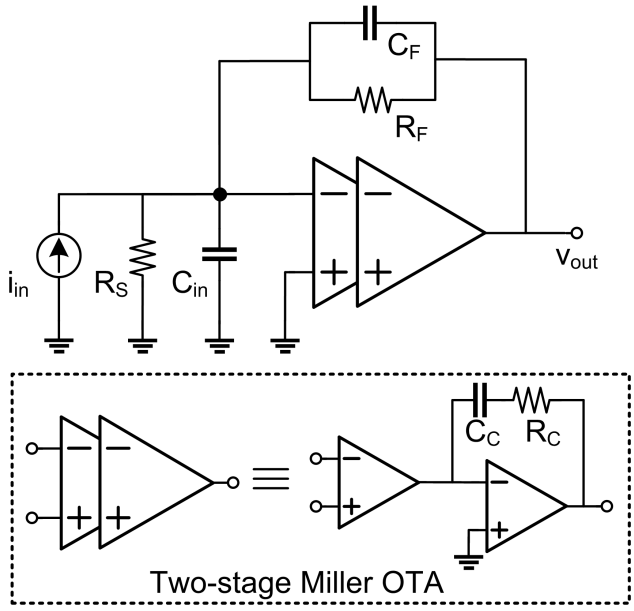

Figure A.1: Diagram of a 1^{st}-order TIA with a two-stage Miller-compensated operational transconductance amplifier.

pole-zero compensation of the two-stage OTA are indirectly captured by eliminating the compensation R_C-C_C and ignoring any capacitive loading at its output (i.e. C_F). Finally, the nonlinear VCCS i_{d2} together with its load R_F can be modeled as a voltage-controlled voltage source shown in Fig. A.2(b). In Fig. A.2(b), $Y_{21} = -sC_F - R_F^{-1}$, $R_0 = R_F||R_S$, and $C_0 = C_{in} + C_F$.

If the Volterra operators of the system $\mathbf{Q}$ with input i_{in} and output v_{out} are known, then v_{out} can be written as in (4.9) as we mentioned before. Furthermore, the first, second, and third order nonlinear transfer function (or Volterra kernel transform) can be found as [90]:

$$\begin{aligned}
Q_1(s) &= H_1(s)R(s), \\
Q_2(s_1, s_2) &= H_2(s_1, s_2)R(s_1)R(s_2)R(s_1 + s_2), \\
Q_3(s_1, s_2, s_3) &= R(s_1)R(s_2)R(s_3)[H_3(s_1, s_2, s_3) - \\
&\qquad 2H_2(s_1, s_2)F(s_1 + s_2)R(s_1 + s_2)H_2(s_3, s_1 + s_2)] \cdot R(s_1 + s_2 + s_3), \\
Q_{3,sym}(s_1, s_2, s_3) &= \frac{1}{3}[Q_3(s_1, s_2, s_3) + Q_3(s_1, s_3, s_2) + Q_3(s_2, s_3, s_1)].
\end{aligned} \tag{A.7}$$

In (A.7), $R(s) = ((1 + H_1(s)F(s)))^{-1}$ is a shorthand notation. Q_1, Q_2, and Q_3 can also be considered as the multi-dimensional Laplace transform of Volterra kernels q_1, q_2, and q_3 in (4.9).

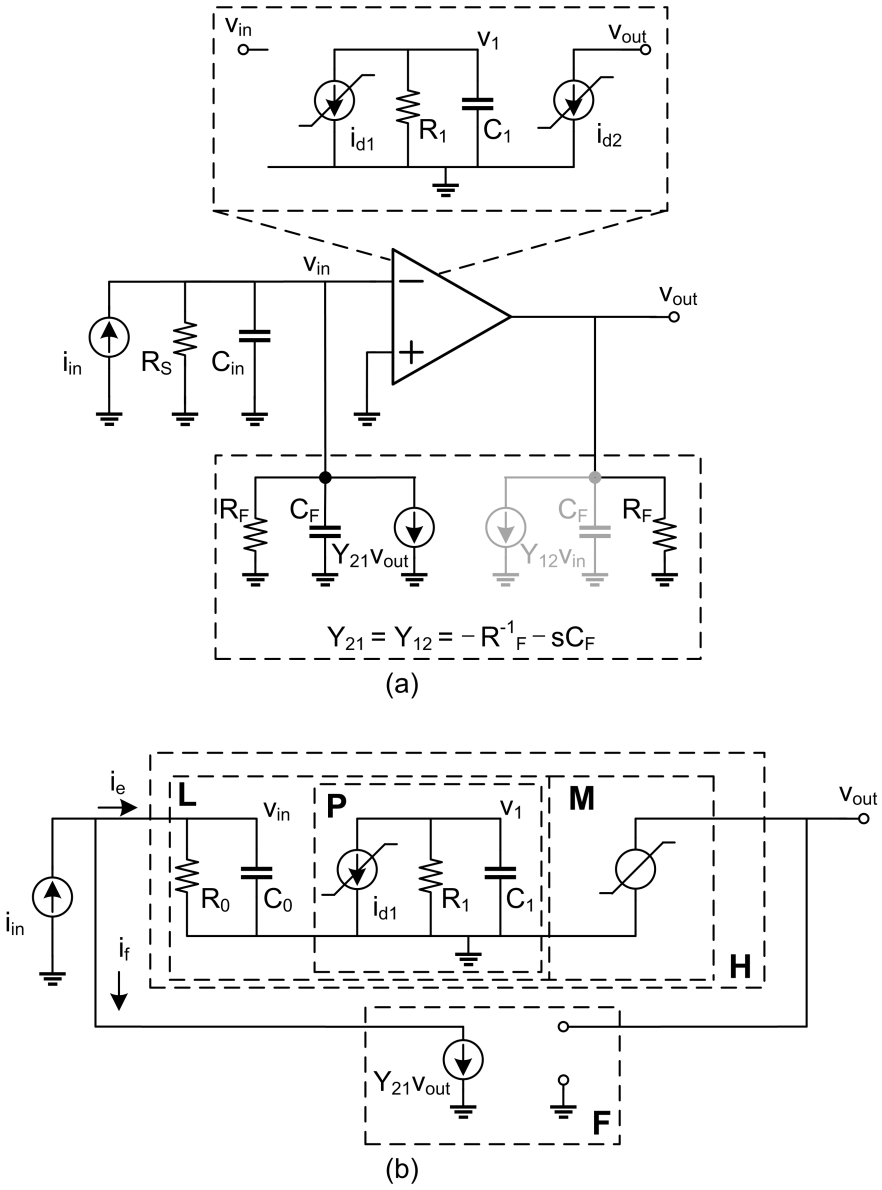

Figure A.2: Evolution of the TIA model for the distortion analysis.

H_1, H_2, and H_3 are the first, second, and third order nonlinear transfer functions of the system H depicted in Fig. A.2. Note that, we've forced the symmetry for Q_3, resulting in a symmetric transform $Q_{3,sym}$ with respect to all its 3 arguments[140]. Finally, $F(s) = Y_{21} = -sC_F - R_F^{-1}$.

Next, we'll find the nonlinear transfer functions of the system **H**. In Fig. A.2, the drain current of the first stage (i_{d1} is expanded into a power series as:

$$i_{d1}(t) = g_{m1}v_{in} + g_{1,2g}v_{in}^2 + g_{1,3g}v_{in}^3 + \cdots , \tag{A.8}$$

we've ignored the drain side nonlinearity for the first stage, since the OOB signal will be suppressed by the dominate pole of the OTA. For the second stage, the voltage output v'_{out} of the nonlinear voltage-controlled voltage source in Fig. A.2(b) is written as a power series as:

$$v'_{out}(t) = A_{v2}v_1 + A_{v2,2}v_1^2 + A_{v2,3}v_1^3 + \cdots , \tag{A.9}$$

The nonlinear transfer functions of the sub-system **P** indicated in Fig. A.2, a cascade system of a nonlinear VCCS and a LTI RC load, can be calculated as[90]:

$$\begin{aligned} P_1(s) &= -\frac{g_{m1}R_1}{1+sR_1C_1}, \\ P_2(s_1,s_2) &= -\frac{g_{1,2g}R_1}{1+(s_1+s_2)R_1C_1}, \\ P_3(s_1,s_2,s_3) &= -\frac{g_{1,3g}R_1}{1+(s_1+s_2+s_3)R_1C_1}. \end{aligned} \tag{A.10}$$

The sub-system **L** indicated in Fig. A.2 is a cascade system of a LTI system (R_0 and C_0) and a nonlinear system P. This gives:

$$\begin{aligned} L_1(s) =& \frac{R_0}{1+sR_0C_0}P_1(s), \\ L_2(s_1,s_2) =& \frac{R_0}{1+s_1R_0C_0}\frac{R_0}{1+s_2R_0C_0}P_2(s_1,s_2), \\ L_3(s_1,s_2,s_3) =& \frac{R_0}{1+s_1R_0C_0}\frac{R_0}{1+s_2R_0C_0}\frac{R_0}{1+s_3R_0C_0} \\ & \cdot P_3(s_1,s_2,s_3). \end{aligned} \tag{A.11}$$

The system **H** is a cascade of system **L** and **M**, and its nonlinear transfer functions can be written as [90]:

$$\begin{aligned} H_1(s) =& A_{v2}L_1(s), \\ H_2(s_1,s_2) =& A_{v2}L_2(s_1,s_2) + A_{v2,2}L_1(s_1)L_1(s_2), \\ H_3(s_1,s_2,s_3) =& A_{v2,3}L_1(s_1)L_1(s_2)L_1(s_3) + A_{v2}L_3(s_1,s_2,s_3) \\ &+ \frac{2}{3}A_{v2,2}[L_1(s_1)L_2(s_2,s_3) + L_1(s_2)L_2(s_1,s_3) \\ &\qquad + L_1(s_3)L_2(s_1,s_2)]. \end{aligned} \tag{A.12}$$

Finally, the nonlinear transfer functions of system **Q** can be found by substituting (A.12) into (A.7).

A.0.3 RX Cross-modulation Distortion Analysis and Calculated TB

Now, we know both the LNTA output current (i_{CG} and i_{CS}) and the nonlinear transfer functions of the TIA, the cross-modulation distortion (and its resulting TB) of the entire RX can be found using (4.10)(4.15)(4.16).

From (4.15) and (A.4), we have:

$$\begin{aligned} i_{CG}M_I = \frac{1}{4}\text{sinc}\frac{\pi}{4}(e^{j\omega_C t} + e^{-j\omega_C t})\cdot \\ [K_0V_j(e^{j\omega_1 t} + e^{-j\omega_1 t}) + \\ K_2V_{tx}(e^{j\omega_2 t} + e^{-j\omega_2 t} + e^{j\omega_3 t} + e^{-j\omega_3 t})]. \end{aligned} \tag{A.13}$$

Therefore, by the definition of the Volterra operator in (4.9), $\mathbf{Q_1}(i_{CG}M_I)$ can be calculated as,

$$\begin{aligned}\mathbf{Q_1}(i_{CG}M_I) &= \frac{1}{4}\text{sinc}\frac{\pi}{4}V_j\cdot \\ &[K_0(Q_1(\omega_{1B})e^{j\omega_{1B}t} + Q_1(-\omega_{1B})e^{-j\omega_{1B}t})+ \\ &K_1V_{tx}^2(Q_1(\omega_{xB})e^{j\omega_{xB}t} + Q_1(-\omega_{xB})e^{-j\omega_{xB}t})]+ \\ &\cdots, \\ &= \frac{1}{4}\text{sinc}\frac{\pi}{4}V_j\cdot \\ &[K_0(Q_1(\omega_{1B})e^{j\omega_{1B}t} + Q_1^*(\omega_{1B})e^{-j\omega_{1B}t})+ \\ &K_1V_{tx}^2(Q_1(\omega_{xB})e^{j\omega_{xB}t} + Q_1^*(\omega_{xB})e^{-j\omega_{xB}t})]+ \\ &\cdots,\end{aligned} \tag{A.14}$$

where $K_0 = \frac{1-\alpha_{1S}}{2R_S}$, $K_1 = -\frac{\alpha_{3T^2S}}{4R_S}$, $\omega_{1B} = \omega_1 - \omega_C$, $\omega_{xB} = \omega_x - \omega_C$. $Q_1(s) = \int_{-\infty}^{\infty} q_1(\tau)e^{-s\tau}d\tau$ is the 1st-order transfer function of system $\mathbf{Q}$, which can be found using (A.7). To arrive at (A.14), we've applied that for symmetric nth-order transfer functions, its complex conjugate can be obtained by changing the sign of the frequency arguments[90]. Note that, in (A.14), $\mathbf{Q_1}(i_{CG}M_I)$ is a linear combination of components at multiple frequencies, and we only write components at the jammer frequency (ω_{1B}) and one of two cross-modulation distortion frequencies (ω_{xB}). Similarly, we have,

$$\begin{aligned}\mathbf{Q_1}(i_{CG}M_Q) &= j\frac{1}{4}\text{sinc}\frac{\pi}{4}V_j\cdot \\ &[K_0(Q_1(\omega_{1B})e^{j\omega_{1B}t} - Q_1^*(\omega_{1B})e^{-j\omega_{1B}t})+ \\ &K_1V_{tx}^2(Q_1(\omega_{xB})e^{j\omega_{xB}t} - Q_1^*(\omega_{xB})e^{-j\omega_{xB}t})]+ \\ &\cdots.\end{aligned} \tag{A.15}$$

Next, $\mathbf{Q_1}(i_{CS}M_I)$ and $\mathbf{Q_1}(i_{CS}M_Q)$ can be found as:

$$\begin{aligned}\mathbf{Q_1}(i_{CS}M_I) &= \frac{1}{8}\text{sinc}\frac{\pi}{4}\cdot \\ &[A_x(Q_1(\omega_{xB})e^{j\omega_{xB}t} + Q_1^*(\omega_{xB})e^{-j\omega_{xB}t})+ \\ &A_y(Q_1(\omega_{1B})e^{j\omega_{1B}t} + Q_1^*(\omega_{1B})e^{-j\omega_{1B}t})]+ \\ &\cdots.\end{aligned} \tag{A.16}$$

$$\begin{aligned}\mathbf{Q_1}(i_{CS}M_Q) = j\frac{1}{8}\mathrm{sinc}\frac{\pi}{4}\cdot \\ [A_x(Q_1(\omega_{xB})e^{j\omega_{xB}t} - Q_1^*(\omega_{xB})e^{-j\omega_{xB}t})+ \\ A_y(Q_1(\omega_{1B})e^{j\omega_{1B}t} - Q_1^*(\omega_{1B})e^{-j\omega_{1B}t})]+ \\ \cdots .\end{aligned} \tag{A.17}$$

To calculate $\mathbf{Q_3}(i_{CG}M_I)$ and $\mathbf{Q_3}(i_{CG}M_Q)$, we ignore the cross-modulation components in i_{CG} since they are weak in power. By doing this, we've also ignored the cross-modulation components coming from $Q_3(\omega_x, \omega_2, -\omega_2)$, $Q_3(\omega_x, \omega_3, -\omega_3)$, and $Q_3(\omega_x, \omega_1, -\omega_1)$. Furthermore, due to the low-pass filtering in $\mathbf{Q_3}[\cdot]$, high frequency components (e.g. component at frequency $\omega_1 + \omega_C$) are ignored. This gives,

$$\begin{aligned}\mathbf{Q_3}(i_{CG}M_I) \approx \mathbf{Q_3}[\frac{1}{4}\mathrm{sinc}\frac{\pi}{4}V_j\cdot \\ (K_2V_{tx}(e^{j\omega_{2B}t} + e^{-j\omega_{2B}t} + e^{j\omega_{3B}t} + e^{-j\omega_{3B}t})+ \\ K_0V_j(e^{j\omega_{1B}t} + e^{-j\omega_{1B}t}))],\end{aligned} \tag{A.18}$$

where $K_2 = \frac{1-\alpha_1\tau}{2R_S}$. Using the definition of the Volterra operator in (4.9), (A.18) can be calcuated as:

$$\begin{aligned}\mathbf{Q_3}(i_{CG}M_I) \approx \frac{3}{32}(\mathrm{sinc}\frac{\pi}{4})^3K_0V_jK_2^2V_{tx}^2\cdot \\ [Q_{3,sym}(\omega_{1B}, \omega_{2B}, -\omega_{3B})e^{j\omega_{xB}t}+ \\ Q_{3,sym}^*(\omega_{1B}, \omega_{2B}, -\omega_{3B})e^{-j\omega_{xB}t}].\end{aligned} \tag{A.19}$$

Similar, we can find $\mathbf{Q_3}(i_{CG}M_Q)$, $\mathbf{Q_3}\left(\frac{i_{CS}M_I}{r}\right)$, and $\mathbf{Q_3}\left(\frac{i_{CS}M_Q}{r}\right)$ as:

$$\begin{aligned}\mathbf{Q_3}(i_{CG}M_Q) \approx j\frac{3}{32}(\mathrm{sinc}\frac{\pi}{4})^3K_0V_jK_2^2V_{tx}^2\cdot \\ [Q_{3,sym}(\omega_{1B}, \omega_{2B}, -\omega_{3B})e^{j\omega_{xB}t}- \\ Q_{3,sym}^*(\omega_{1B}, \omega_{2B}, -\omega_{3B})e^{-j\omega_{xB}t}],\end{aligned} \tag{A.20}$$

$$\mathbf{Q_3}\left(\frac{i_{CS}M_I}{r}\right) \approx \frac{3}{32r^3}(\mathrm{sinc}\frac{\pi}{4})^3 A_y A_z^2 \cdot [Q_{3,sym}(\omega_{1B},\omega_{2B},-\omega_{3B})e^{j\omega_{xB}t} + Q^*_{3,sym}(\omega_{1B},\omega_{2B},-\omega_{3B})e^{-j\omega_{xB}t}], \tag{A.21}$$

$$\mathbf{Q_3}\left(\frac{i_{CS}M_Q}{r}\right) \approx j\frac{3}{32r^3}(\mathrm{sinc}\frac{\pi}{4})^3 A_y A_z^2 \cdot [Q_{3,sym}(\omega_{1B},\omega_{2B},-\omega_{3B})e^{j\omega_{xB}t} - Q^*_{3,sym}(\omega_{1B},\omega_{2B},-\omega_{3B})e^{-j\omega_{xB}t}], \tag{A.22}$$

where $K_0 = \frac{1-\alpha_{1S}}{2R_S}$, $K_2 = \frac{1-\alpha_{1T}}{2R_S}$, $A_y = -\frac{1}{2}g_{m,CS}\alpha_{1S}V_j$, and $A_z = -\frac{1}{2}g_{m,CS}\alpha_{1T}V_{tx}$.

Finally, the RX TB can be calculated by substituting (A.14)(A.15)(A.16)(A.17)(A.19)(A.20)(A.21)(A.22) into (4.18), and grouping components at jammer frequency and at cross-modulation product frequency:

$$TB^{-1} = |\frac{(g_{m,CS}R_S - r\delta)\alpha_{3T^2S} + XR_S}{2(1-\alpha_{1S})r\delta + 2g_{m,CS}R_S\alpha_{1S}} + \frac{rY\left[(1-\alpha_{1S})(1-\alpha_{1T})^2\delta + \left(\frac{g_{m,CS}R_S}{r}\right)^3\alpha_{1S}\alpha_{1T}^2\right]e^{j\phi}}{32[(1-\alpha_{1S})r\delta + g_{m,CS}R_S\alpha_{1S}]|Q_1(\omega_{1B})|R_S^2}| \cdot V_{SI}^2, \tag{A.23}$$

where $X = g'_{m,CS}(\alpha_{2T^2}\alpha_{1S} + \alpha_{2TS}\alpha_{1T}) + \frac{1}{2}g''_{m,CS}\alpha_{1T}^2\alpha_{1S}$, $Y = 3(\mathrm{sinc}\frac{\pi}{4})^2|Q_{3,sym}(\omega_{1B},\omega_{2B},-\omega_{3B})|$, $\phi = \angle Q_{3,sym}(\omega_{1B},\omega_{2B},-\omega_{3B}) - \angle Q_1(\omega_{xB})$, $\delta = \frac{g_{CGI}-jg_{CGQ}}{g_{CSI}-jg_{CSQ}}$, ω_{1B}, ω_{2B}, ω_{3B} are the baseband frequencies of a CW jammer and a two-tone SI, and ω_{xB} is the baseband frequency of the cross-modulation distortion.

A.0.4 TIA Distortion Simulation Results

The TIA described in Section 4.5 is characterized here and is driven by a current source with TIA input capacitor C_{in} being its source impedance. Fig. A.3 plots the simulated and calculated TB at TIA output versus normalized TX/RX frequency separation. The jammer current is 45 μA at 4 MHz, while a two-tone TX leakage locates at "Normalized TX/RX frequency separation"×"TIA

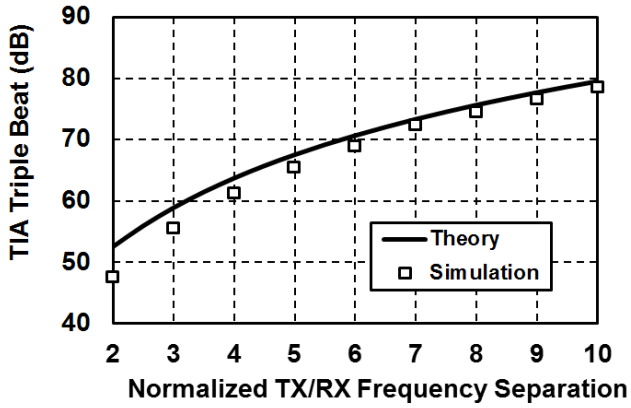

Figure A.3: Simulated and calculated TIA TB across normalized TX/RX frequency separation. The TIA BW is 20 MHz. The TX leakage current is 0.72 mA for each tone of the two-tone signal, and the TX signal has a BW of 2.5 MHz. The jammer located at 4 MHz has a current of 45 μA .

BW=20 MHz" with 2.5 MHz signal BW. The current is 0.72 mA for each tone of the two-tone signal. As can be seen from Fig. A.3, the TIA TB improves as the normalized TX/RX frequency separation increases. This can be intuitively understood as the input capacitor of the TIA (C_{in}) sinks more TX leakage at larger TX/RX frequency offset.

Interestingly, the TIA TB highly depends on the jammer frequency location, given fixed normalized TX/RX frequency offset, fixed TX-leakage signal current, and fixed TX-leakage signal BW. Fig. A.4 plots the TIA TB across various jammer frequencies. The TIA BW is 20 MHz, while the normalized TX/RX frequency separation is set to be 5. The TX-leakage signal current and BW are 0.72 mA for each tone of the two-tone signal and 2.5 MHz, respectively. From Fig. A.4, we can find that the TIA TB drops rapidly starting at <1.5 MHz, but decreases much gradually at larger frequency locations. The behavior of the TIA TB over jammer frequencies is closely related to the TIA loop gain as plotted on the auxiliary y-axis in Fig. A.4. This can be intuitively understood as any feedback system is linearized by its loop gain [141]. The less the loop gain, the stronger the nonlinearity of the system would be. The of the TIA calculated as $LG = H_1(s)F(s)$ has a dominant pole set by the OTA's internal node R_1 and C_1. This pole is typically at very low frequency for the stability of a two-stage Miller OTA [141], resulting the TIA linearity decreases starting from very low frequency. The LG drops more gradually after the TIA BW set by the feedback network R_F and C_F, so as the TIA TB. To avoid the very low frequency dominant pole of a two-stage Miller

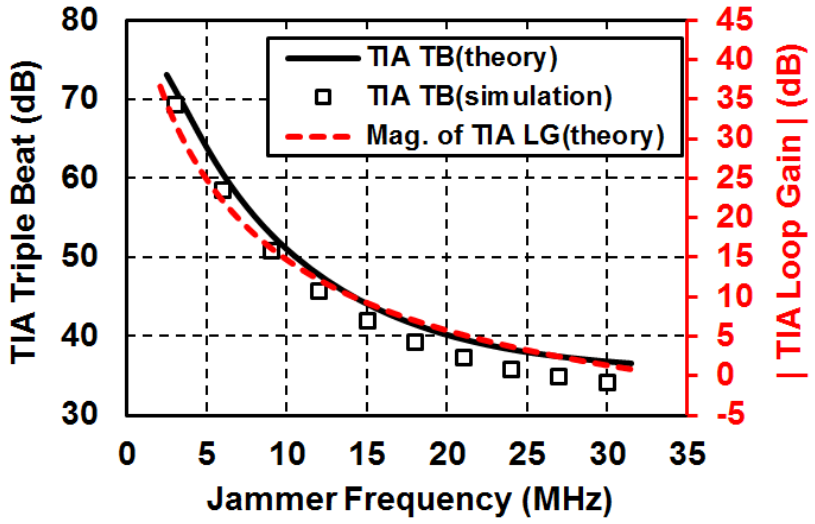

Figure A.4: Simulated and calculated TIA TB across various jammer frequencies. The loop gain of the TIA calculated as $LG = H_1(s)F(s)$ is plotted on top of the TIA TB at the auxiliary y-axis. The TIA BW is 20 MHz, while the normalized TX/RX frequency separation is set to be 5. The TX leakage current is 0.72 mA for each tone of the two-tone signal, and the TX signal has a BW of 2.5 MHz. The jammer current is 45 μA.

OTA, single stage OTAs can be used [84].

Appendix B

List of Acronyms

ADCs Analog-to-Digital Converters

BB baseband

BPSK Binary Phase-Shift Keying

BS Base Station

BW Bandwidth

CDMA Code-Division Multiple Access

CMOS Complementary Metal-Oxide-Semiconductor

CG Common-Gate

CS Common-Source

CW Continuous-Wave

DACs Digital-to-Analog Converters

DSP Digital Signal Processing

FDE Frequency-Domain Equalization

FDD Frequency-Division Duplexing

FIR Finite Impulse Response

FPGA Field-Programmable Gate Array

FSK Frequency-Shift Keying

FTNC Frequency-Translational Noise Cancelling

IB In-Band

IIP3 input third-order intercept point

IM3 third-order inter-modulation

IM2 second-order inter-modulation

IP3 third-order intercept point

LNA Low-Noise Amplifier

LNTA Low-Noise Transconductance Amplifier

LO Local Oscillator

LPTV Linear Periodically Time-Varying

LPFs Low-Pass Filters

LTI Linear Time-Invariant

LTE Long-Term Evolution

LTV Linear Time-Varying

MAC Medium-Access Control

MIMO Multi-In-Multi-Out

MS Mobile Station

NC-SIC Noise-Cancelling, Self-Interference-Cancelling

NF Noise Figure

NI National Instruments

OFDM Orthogonal Frequency-Division Multiplexing

OFDMA Orthogonal-Frequency-Division Multiple Access

OIP3 output third-order intercept point

OOB Out-Of-Band

PA Power Amplifier

PHY Physical

PPFs Polyphase Filters

QAM Quadrature Amplitude Modulation

QPSK Quadrature Phase-Shift Keying

RF Radio Frequency

RX Receiver

SAW Surface Acoustic Wave

SFDR Spurious-Free Dynamic Range

SIC Self-Interference Cancellation

SI Self-Interference

SNR Signal-to-Noise Ratio

TB Triple Beat

TDMA Time-Division Multiple Access

TDD Time-Division Duplexing

TF Transfer Function

TIAs transimpedance amplifiers

TX Transmitter

USRP Universal Software Radio Peripheral

VGAs Variable-Gain Amplifiers

VM Vector Modulator

WCDMA Wideband Code Division Multiple Access